Summer 8-15-2018

Radiological Pathological Correlations in Chronic Traumatic Encephalopathy

Mihika Gangolli
Washington University in St. Louis

WASHINGTON UNIVERSITY IN ST. LOUIS

School of Engineering and Applied Science
Department of Biomedical Engineering

Dissertation Examination Committee:
David L. Brody, Chair
Joseph Ackerman
Dennis Barbour
Philip Bayly
Michael Bruchas

Radiological-Pathological Correlations in Chronic Traumatic Encephalopathy

by
Mihika Gangolli

A dissertation presented to
The Graduate School
of Washington University in
partial fulfillment of the
requirements for the degree
of Doctor of Philosophy

August 2018
St. Louis, Missouri

Table of Contents

List of Tables

List of Figures

Abstract of the Dissertation

Radiological-Pathological Correlations in Chronic Traumatic Encephalopathy

Mihika Gangolli

Doctor of Philosophy in Biomedical Engineering

Washington University in St. Louis, 2018

Thesis Mentor: David L. Brody, MD, PhD

Chronic traumatic encephalopathy (CTE) is a progressive neurodegenerative disease that has been increasingly linked to traumatic brain injury. The neuropathology that distinguishes CTE from other tauopathies includes hyperphosphorylated tau (pTau) tangles and tau positive astrocytes irregularly distributed in cortical sulcal depths and clustered around perivascular foci. These features are clearly identified using immunohistochemistry, but are undetectable to current clinical imaging methods. Diffusion imaging has been proposed as a noninvasive method to detect the pathognomonic lesion of CTE *in vivo* because of its high sensitivity to microstructural alterations in tissue structure. While several diffusion imaging approaches, ranging from diffusion tensor imaging (DTI) to more advanced schemes such as generalized q-sampling imaging (GQI) and diffusion kurtosis imaging (DKI) may prove useful, the relationship between changes in diffusion-derived metrics and the underlying pathology remains unknown. We have developed and implemented a method of perform radiological-pathological correlations in tissues with diagnoses of CTE, aimed to determine whether high spatial resolution diffusion imaging is capable of sensitively detecting pTau pathology.

Human *ex vivo* cortical tissues diagnoses with Stage III/IV CTE, Alzheimer's disease (AD) or frontotemporal lobar dementia (FTLD) were scanned in an 11.74T Agilent MRI scanner using DTI, GQI and DKI acquisition schemes with isotropic in-plane spatial resolution of 250μm and 500μm slice thickness. Following image acquisition, tissues were sectioned and stained for histopathological markers including AT8 (pTau), GFAP (astrocytes) and Myelin Black Gold II (myelinated white matter). A custom script was used to co-register histological to MRI images, allowing for the ability to perform high spatial resolution correlations of histological with diffusion metrics. Using this approach, we found no relationship between pTau in sulcal depths and any of our DTI, GQI and DKI based measures. Interestingly, we found that white matter underlying sulcal depths in CTE tissues showed signs of disruption, a finding that we did not observe in AD or FTLD tissues. Furthermore, white matter integrity in these regions was correlated with fractional anisotropy. These findings demonstrate that high spatial resolution diffusion imaging is capable of detecting white matter disorganization closely related to pTau pathology in CTE, and may provide a more sensitive and specific means of diagnosing CTE.

Acknowledgements

This work would not have been possible without the guidance and support of a large network of individuals. First, I would like to thank my thesis mentor, Dr. David Brody. Without his support, the work in this project would not have been possible. He has encouraged me to venture beyond my comfort zone to learn wet lab skills that were essential in this project, along with working to refine my presentation skills. His philosophy of "how will this help my patient" has provided a focus in my research that has been essential to asking and answering the important questions when it is often easy to travel down the rabbit hole of possible experiments. Moreover, his reminder that a negative outcome to an experiment is not detrimental, and in fact can lead to a new direction in research provided me with motivation to continue not only with radiological-pathological correlations, but also in animal studies that I have additionally been pursuing.

Second, I am incredibly grateful to the members of the Brody, Kummer and Friess labs, current and former who have advised me and provided me with constructive critique during my time in lab. Specifically, the team members working together on this project, Laurena Holleran and Joong Hee "Caleb" Kim who taught me so much about histology and MRI. This has truly been a collaborative project and is a culmination of a diverse set of both wet lab and computational skills that I could not have dreamed of approaching on my own. They are co-authors on the work detailed in Chapter 3, which was accepted for publication in NeuroImage in 2016. I would also like to thank TJ Esparza and Terrance Kummer for always being open to discussing questions regarding histology, data analysis and troubleshooting when my experiments were not going as planned. Everyone in the lab has made me feel welcome and

excited to come to lab everyday, providing important intellectual and emotional support. A talented undergraduate, Eric Hsu has shown particular initiative in his work not only on the rad-path project, but also to further investigate serendipitous findings of astrocyte degeneration, a research direction I hope will continue. Detailed consent, pathological diagnoses and tissue information was provided by our collaborators Ann McKee, Thor Stein and Victor Alvarez from Boston University who ensured we obtained a ready supply of tissue in excellent conditions. Most importantly, this work would not have been possible without the precious gift of tissue and the donors and their families. Their donation is key not only in the current work, but in future studies going forward.

I would also like to thank the members of my thesis committee for their thoughtful advice in which research questions I should focus on, as well as their flexibility in meeting to discuss updates. Their input has provided much needed fresh perspective to this work.

Finally, I cannot say enough to thank my parents. They have been never ending in their love and support during the long and winding road from Denver, to my undergraduate career in Cleveland to pursuing graduate work in St. Louis. No matter what direction I chose to take, they have been encouraging of my every decision while still making sure I am practicing self-care, allowing me to pursue new opportunities going forward.

Mihika Gangolli

Washington University in St. Louis

August 2018

Chapter 1. Introduction to chronic traumatic encephalopathy

1.1 Traumatic brain injury

Traumatic brain injury (TBI) affects approximately 2.5 million individuals in the United States every year (Centers for Disease Control and Prevention, 2015). An estimated 75 percent of these patients suffer from concussive impacts (Centers for Disease Control and Prevention, 2015). Clinically, a concussion is diagnosed by a score of 13-15 on the Glasgow coma scale, with acute symptoms including headache, irritability, anxiety, attention and cognitive deficits, and depression (Alexander, 1995; McCrory et al., 2009). While these symptoms typically resolve within three months post injury (Alexander, 1995), they can persist for over six months in up to a third of patients (Kashluba et al., 2004; Stulemeijer et al., 2008). Furthermore, patients who sustain multiple concussive injuries are at increased risk of developing progressive neurodegenerative conditions. These injuries can be sustained by a blunt impact to the head, or a high-pressure blast wave, but injury mechanism appears most closely related to the rotational forces experienced during injury (McCrory et al., 2009; Zhang et al., 2006). Microscopically, during a concussive injury, the mismatch of rotational and accelerative forces results in shear strain, particularly at tissue interfaces such as the gray-white matter boundary and perivascular regions (Gennarelli and Graham, 1998; Margulies et al., 1990; Povlishock and Katz, 2005). Acutely, this shear strain causes impaired axonal transport, while in the chronic phase there is

often increased abundance of microglia, astrocytes, and evidence of fiber disruption of white matter fiber tracts (Blumbergs et al., 1989).

1.2 Chronic traumatic encephalopathy

Long-term effects of repetitive concussions were first observed in 1928 by neuropathologist Harrison Martland, who used the term "punch drunk" to describe the array of symptoms that included confusion, memory loss, and deterioration of motor skills seen in boxers who had sustained multiple head impacts, which were later more formally categorized as *dementia puglistica* (Martland, 1928). Since then, the observed population exhibiting these symptoms has expanded to include athletes participating in contact sports such as football, ice hockey, rugby and soccer, as well as military service members who have a history of exposure to blast related TBI (Hales et al., 2014; Maroon et al., 2015). Consequently, the observations of *dementia pugilistica* have evolved into a formal diagnosis of chronic traumatic encephalopathy, or CTE (McKee et al., 2013). A recent study by Stern et al found that patients who were diagnosed post mortem with CTE presented clinically in two separate manners. The first subset presented with symptoms of anxiety, irritability and depression at an early age (~35 years old) followed by subsequent cognitive deterioration (Stern et al., 2013). Patients in the second subset show signs of severe cognitive dysfunction relatively late in life (~60 years old) followed by further progression into dementia (Stern et al., 2013). Unfortunately, the spectrum of symptoms in both categories could easily be misdiagnosed, as patients with frontotemporal dementia (FTD) present with a similar array of mood and behavioral symptoms as patients who manifest early behavioral signs of CTE. The second subset also remains indistinguishable behaviorally, as the symptoms of late onset cognitive decline overlap with patients who have Alzheimer's Disease

(AD). Moreover, in the largest reported cohort of football players to date, Mez et al reported that patients with mild (Stage I/II) CTE presented with deficits in attention, impulsivity, and depression despite relatively limited tau pathology, indicating poor correlation between tau pathology and behavioral symptoms (Mez et al., 2017). Therefore, the only method to provide a specific diagnosis of CTE is to identify its characteristic pathology post mortem using gold standard immunohistochemistry. A 2016 consensus panel has provided a preliminary definition of the pathognomonic lesion of CTE as consisting of hyperphosphorylated tau (pTau) accumulated in neurons, astrocytes and cell processes in perivascular regions and the depths of cortical sulci. This tau pathology progresses in severity with a stereotypical manner. In stages I-II of CTE, tau tangles and astroglial tau are found in the frontal lobe. Cases of stage III CTE exhibit tau pathology not only in the frontal lobe, but also in the medial temporal and parietal cortices. Finally, in the most severe stage IV of CTE, tau pathology is found in the thalamus and hypothalamus as well as in white matter tracts.

Although CTE pathology has typically been found in patients with a history of repetitive concussive injuries, the mechanistic role between the axonal injury experienced during TBI and the accumulation of hyperphosphorylated tau in neurons and astrocytes remains unclear. In the uninjured brain, tau is a microtubule associated protein found mostly in neurons and oligodendrocytes with roles in cytoskeletal organization and axonal transport (Drechsel et al., 1992). It is hypothesized that disruption and damage to axons during TBI results in the tau protein to become hyperphosphorylated, first folding as toxic oligomers and later aggregating as neurofibrillary tangles (Gerson et al., 2016; Guzman-Martinez et al., 2013). A study by Adams et al found that diffuse axonal injury commonly seen in concussive TBI resulted in histological evidence of axonal injury in the cerebral white matter and corpus callosum (Adams et al., 1989).

Most recently, a computational model based study has shown that cortical sulcal depths experience the highest amounts of strain during injury (Ghajari et al., 2017). In a cohort of schizophrenic patients who had undergone bilateral frontal leucotomy and survived at least 40 years post-surgery, Shively et al found evidence of neurofibrillary tangles in the gray matter associated with the sites of severe axonal injury (Shively et al., 2017). Because these locations correspond to regions where the tau pathology characteristic of CTE is most commonly observed, these data support the hypothesized relationship between TBI related white matter injury and aggregation of pTau tangles. Studies in animal models of TBI would provide the most direct approach to investigate this relationship. Unfortunately, animal studies of repetitive brain injury at a truly chronic time point (over nine months post injury) are rare. Behavioral deficits including depressive-like behavior, cognitive dysfunction and increased risk-taking behaviors have been reported at six months post injury, along with increased pTau and astrogliosis indicated by AT8 and GFAP immunoreactivity respectively (**Table A.1**). However, the pathology observed in these animal studies is not consistent with the widespread neurofibrillary tangles, neuritic threads and astroglial tau found in the later stages of CTE. Consequently, the only means of validating proposed diagnostic biomarkers for CTE is to perform studies in humans.

1.3 Detection of tau in humans

Modalities proposed as candidates to detect tau in humans currently include blood and cerebrospinal fluid (CSF) based biomarkers and positron emission tomography (PET) ligands targeted to bind to pTau. Preliminary work to develop antibodies recognizing TBI related posttranslationally modified tau was performed by Zemlan et al, who found that patients

sustaining severe TBI had elevated levels of tau in the CSF relative to both neurologic and healthy controls (Zemlan et al., 1999). Assessments of tau in CSF by Zetterberg and colleagues found that amateur boxers had significantly elevated levels of total tau, but no differences in pTau in the acute phase following a bout compared to the same athletes following a three month rest period (Zetterberg et al., 2006). Furthermore, levels of total tau were increased in boxers sustaining hits to the head with increased frequency or severity. More recently in a cohort of hockey players acute tau-A levels measuring A Disintegren fragments of tau (Henriksen et al., 2013), have been found to correlate with duration of post concussive symptoms while tau-C levels, which measure caspase cleaved tau fragments (Rissman et al., 2004), were increased in the same players relative to pre-season (Shahim et al., 2016). While these results are encouraging, changes in blood and CSF based biomarkers also reflect axonal injury and astrocytosis (Shahim et al., 2015; Siman et al., 2015). Alternatively, while several active studies using PET ligands claim binding specificity to pTau, autoradiography and *in vivo* validations appear to show off-target binding and high signal in regions that do not correspond to the stereotypical distribution of pTau pathology ascribed to CTE (Barrio et al., 2015; Coughlin et al., 2015; Mitsis et al., 2014; Scholl et al., 2016).

1.4 Summary

In summary, there is an increasing unmet need to noninvasively detect and monitor the neuropathology of CTE *in vivo*. Diffusion MRI may be a means of detecting pTau related changes in brain tissue. However, similar to PET studies, changes in the diffusion signal remain challenging to interpret in the context of complex pathology of CTE. Without an animal model of CTE, imaging and subsequent histological validation require the development and

implementation of a method to perform radiological-pathological correlations in *ex vivo* human tissues. Because the pathology associated with CTE is often found along tissue interface boundaries and sulcal depths, which are both prone to partial voluming errors, such a method have validated voxel-based accuracy in order to identify how changes in axonal integrity, hyperphosphorylated tau tangles and tau positive astrocytes are related to changes in imaging metrics. The primary hypothesis of this thesis was that chronic white matter disruption underlying sulcal depths is related to pTau pathology in CTE and can be detected using diffusion MRI. In order to test this hypothesis, I have aimed to (1) develop a voxel-based histology-MRI coregistration framework applicable to human *ex vivo* tissues (2) implement this method to perform correlations of white matter integrity and phosphorylated tau pathology in CTE with high spatial resolution diffusion MRI measures and (3) determine whether any observed changes were specific to CTE or generalized across tauopathies. In addition, I sought to investigate whether repetitive head injuries was associated with behavioral and histopathological abnormalities at chronic time points post-injury. The overarching intent of this work was to determine whether diffusion MRI is a feasible technique to detect phosphorylated tau pathology and ultimately provide an *in vivo* diagnosis of CTE.

Chapter 2. Imaging of ex vivo human brain tissue

2.1 Introduction to diffusion MRI

Diffusion MRI has the ability to noninvasively probe microstructural changes in brain tissue by measuring the Brownian motion of water molecules and their interactions with cellular membranes (Basser and Özarslan, 2014; Le Bihan, 1995; Stejskal and Tanner, 1965). A typical spin echo pulse sequence consists of an initial 90° radiofrequency (RF) pulse that flips the proton spins into the transverse plane, perpendicular to the magnetic field of the scanner (**Figure 2.1**). As time progresses, the initially synchronized spins begin to experience small changes in phase due to inhomogeneities of the magnetic field and precess at varying rates. A second 180° RF pulse is then applied in order to reverse the dephasing process by flipping the spins such that protons previously precessing at a higher rate following the 90° excitation pulse are now behind protons that were initially precessing at a lower rate (Pipe, 2014). An echo is detected once all spins have reached coherence (Pipe, 2014). Water diffusion is measured by the addition of a set of gradient pulses, the first timed after the initial 90° flip meant to provide additional dephasing of the proton spins, and the second following the 180° flip that reverses any changes in phase spin. Protons that have not moved between the pulses will experience a complete reversal in phase shift of their spins. However, protons in water that have moved due to diffusion experience a different magnetic field, resulting in a phase shift that is not reversed by the refocusing RF pulse (Stejskal and Tanner, 1965). Degree of diffusion sensitization is determined by the

duration of each pulse (δ), time between pulses (Δ), and the gradient strength (G). Each pulse should have Δ >> δ such that the majority of water diffusion occurs after the proton spins have been dephased, rather than during the applied duration of the gradient pulse (Basser, 2002). The combined phase shifts of the population of moving water molecules due to application of the gradients results in an attenuated, or diffusion weighted, signal (Le Bihan et al., 2006). Degree of signal attenuation for a fixed amount of diffusion can therefore be described by a parameter called the b-value which is proportional to the strength and timing of these diffusion sensitizing gradients is calculated as

$$\boldsymbol{b} = \boldsymbol{\gamma^2 G^2 \delta^2 (\Delta - \frac{\delta}{3})} \qquad \text{(Eq. 2.1)}$$

where γ is the gyromagnetic ratio of 4256 Hz/gauss for protons (Pipe, 2014).

Figure 2.1 Schematic of a typical pulse sequence used in to acquire diffusion data. 90° RF pulse excitation flips the protons perpendicular to applied magnetic field (B_0). The protons precess about B_0 at varying frequencies, with the precession occurring along the transverse (T2) and longitudinal axes (T1) of the spins. Application of a gradient short after the excitation pulse adds to the phase of each spin. Following the refocusing 180° RF pulse, a second gradient pulse is applied, designed to reverse any phase shifts that occurred due to the first pulse. Water molecules that have moved during the time between the two gradient pulses will not experience a reversal in phase shifts, resulting in a signal decay caused by diffusion. Application of crusher gradients is meant to eliminate any extraneous free induction decay signals if the refocusing RF pulse does not completely reverse phase shifts induced by the excitation pulse.

While *ex vivo* diffusion data acquisition allows for collection of high spatial resolution data and provides the ideal radiological dataset to perform correlations with histology, there are also several associated limitations. First, post-mortem interval (PMI) is known to have a

deleterious effect on tissue microstructure and alters diffusivity of water in fixed tissue (Pfefferbaum et al., 2004; Srinivasan et al., 2002; Verwer et al., 2002). D'Arceuil and de Crespigny found that diffusion metrics such as fractional anisotropy and apparent diffusion coefficient decreased in the mouse brain with increased time between animal death and fixation in formalin (D'Arceuil and de Crespigny, 2007). A PMI of fourteen days also resulted in reduced white matter tract integrity (D'Arceuil and de Crespigny, 2007). Diffusion studies in the rat spinal cord have also shown that fractional anisotropy decreased even when PMI was restricted to four hours. Furthermore, changing from perfusion fixation method to immersion fixation also resulted in reductions of water diffusivity (Shepherd et al., 2009). In fixed human brains with PMI ranging from twenty to eighty hours, DTI derived measures of mean diffusivity, axial diffusivity and radial diffusivity showed strong and significant dependence on PMI, while PMI did not appear to drive changes in fractional anisotropy (Miller et al., 2011). Ideally, tissue samples for *ex vivo* imaging should be perfusion fixed, such that formalin is able directly permeates all parts of the brain through capillary beds. For human tissues, the more popular method of immersion fixation results in inevitable tissue degradation during the time required for formalin to diffuse from the superficial layers to deeper cortical regions (de Guzman et al., 2016). Therefore, *ex vivo* studies should be performed in tissues with minimal post mortem intervals, and absolute values of diffusion measures cannot be directly compared with their *in vivo* counterparts.

A second challenge when imaging *ex vivo* tissues is the problem of tissue fixation. Fixation not only results in decreased T2 relaxation time but also reduces water diffusivity compared to tissues *in vivo* (D'Arceuil et al., 2007). In order to counteract these effects and preserve signal to noise quality, gradients with increased power are necessary and require

increased data acquisition times of over twenty four hours (McNab et al., 2009; Miller et al., 2011).

With these considerations, experiments were conducted on formalin-fixed human *ex vivo* tissue samples to optimize MRI sequence parameters, allowing for efficient collection of diffusion data with high spatial resolution and maximized signal to noise.

2.2 Preparation of fixed tissue for imaging

All imaging studies were performed on an 11.74T Agilent MR scanner at Washington University School of Medicine. Formalin-fixed, human *ex vivo* tissue samples were sampled from cortical regions. Tissue samples had dimensions of 1x2x3cm. Imaging studies were performed with the direction and supervision of Joong Hee Kim, PhD, research instructor.

Equilibration of tissues in 1xPBS has previously been proposed as a strategy to compensate for fixation induced reductions in T2 relaxation time (Miller et al., 2011). T2 weighted imaging data (16 echoes, TR/TE = 4000/11ms) with 400 μm isotropic in-plane spatial resolution and 500 μm slice thickness was collected on a sample first incubated in 10% formalin for a minimum of seven days (**Figure 2.2A**). The tissue block was then transferred to a solution of 1xPBS and 0.1% sodium azide. T2 weighted imaging data was then collected after three, ten, fifteen, eighteen, and sixty days of incubation in the 1xPBS solution. Because we were interested in performing correlations in both gray and white matter, it was necessary to determine rehydration conditions that resulted in maximal T2 relaxation time in both tissue types. Therefore, T2 relaxation time was measured in regions of interest (ROIs) selected from both gray and white matter. While the T2 relaxation time increased after three and ten days in 1xPBS, the signal in gray and white matter reached steady state after fifteen days of incubation in 1xPBS

(**Figure 2.2B**). Therefore, optimal rehydration to achieve maximal T2 relaxation time was empirically determined to be fifteen days.

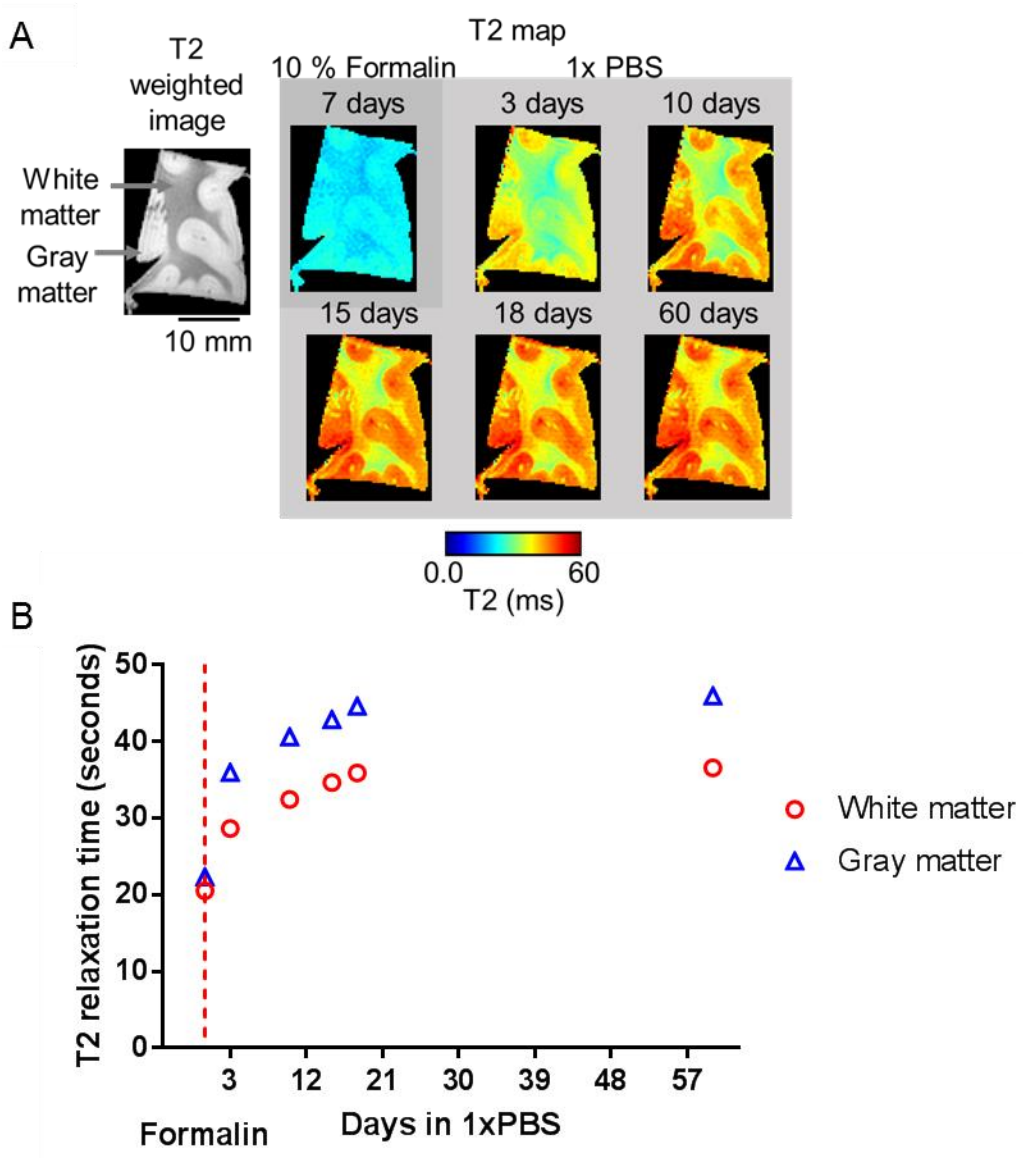

Figure 2.2 Optimization of tissue rehydration. A. T2 map of a sample of human *ex vivo* tissue rehydrated in 1x PBS over the course of 60 days. T2 relaxation time was measured in both gray and white matter. **B.** The steady state of the T2 signal was measured at each time point for both gray and white matter. Tissues were initially stored in formalin (dashed red line) and then transferred to a solution of 1xPBS and sodium azide. By the 15 day time point, the T2 relaxation time does not increase any further, shown by steady-state relaxation times at up to 60 days in 1xPBS.

2.3 Optimization of imaging parameters

An additional strategy to compensate for fixation related reduction in signal quality is to increase repetition time (TR). Maximizing TR allows for full recovery of spins to their initial precession states, but results in long scan times and therefore must be optimized prior to imaging *ex vivo* tissues. MR data from formalin-fixed human *ex* vivo cortical tissue was collected with varying TR times (0.5, 1.0, 1.5, 2.0, 2.5, 3.0, 4.0 seconds) with fixed echo time (TE = 11ms). MR signal intensity was then measured in both gray and white matter as a function of TR time (Figure 2.3). Increasing TR time from 0.5 to 1 second resulted in the largest increase of MR signal intensity in both tissue types. Repetition times greater than one second did not show changes in MR signal intensity. These results indicate that optimal TR time can be limited to one second such that signal intensity in gray and white matter is maximized , thereby increasing efficiency of scan times.

We next sought to optimize the number of slices that would be used to collect MR data of human *ex vivo* tissues. Each slice collected directly corresponded to an increase in the number of RF pulses, resulting in tissue heating and subsequent increases in water diffusivity in tissue during imaging (Delannoy et al., 1991). Therefore, to maintain consistency when imaging tissue blocks and to empirically determine the effects of increase RF pulses on tissue temperature, a single tissue block, equilibrated in 1xPBS was imaged with a b-value of 4 ms/μm^2. Data was collected with either three RF pulses (three slices) or thirteen RF pulses (thirteen slices). The apparent diffusion coefficient was then use to determine the tissue temperature using the relationship between water diffusivity and temperature (Delannoy et al., 1991). Imaging using three RF pulses resulted in a mean tissue diffusivity of 1.8 ms/μm^2 , while imaging using thirteen

RF pulses increased tissue diffusivity to 2.3 ms/μm^2 (**Figure 2.4**). This translated to an increase in tissue temperature by 8°C, a direct consequence of increase number of RF pulses. Based on the outcomes of this study, thirteen slices were prespecified in subsequent imaging setup in order to maintain consistent tissue temperature.

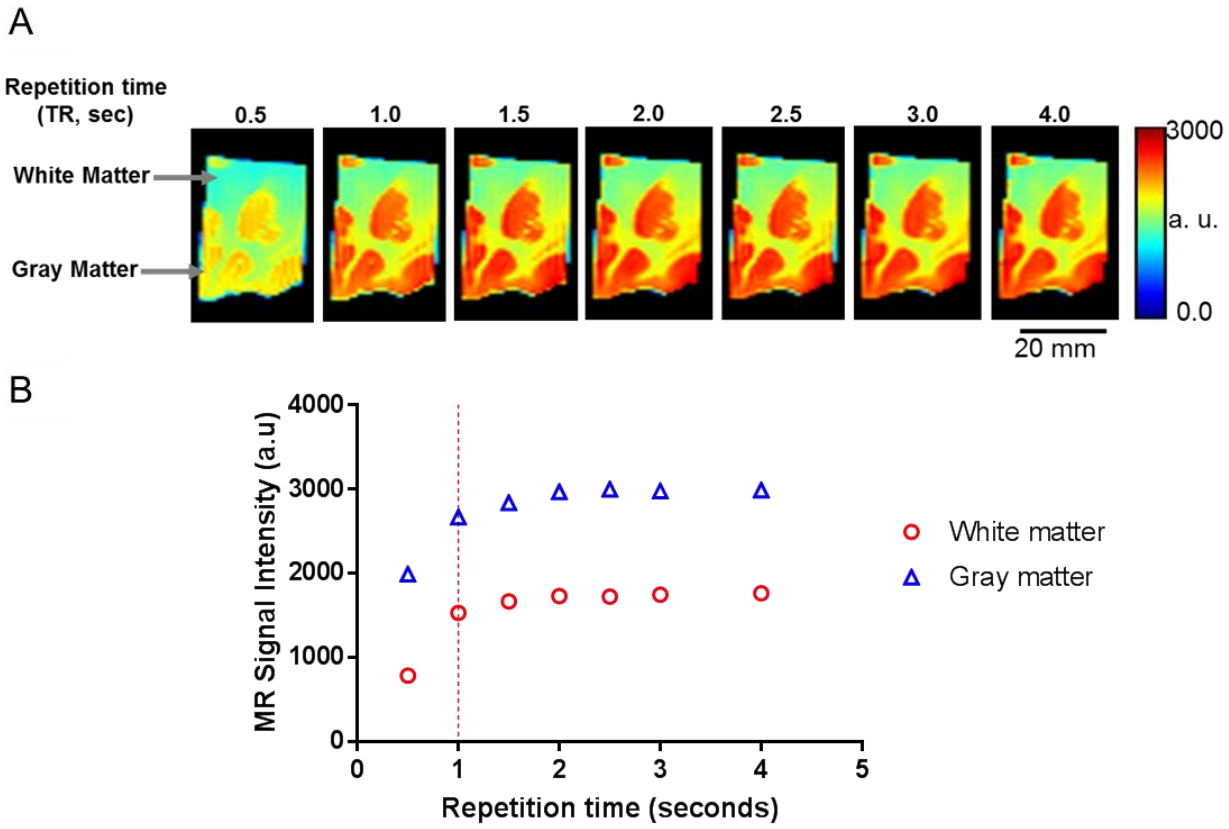

Figure 2.3 Optimization of repetition time. MRI data was collected with isotropic in plane resolution of 400 μm and a slice thickness of 500 μm. MR signal intensity was quantified as a function of repetition time (TR, seconds) in both gray and white matter. Increasing the TR time from 0.5 to 1.0 seconds had the greatest effect on MR signal intensity in both tissue types, with signal intensity reaching steady state at TR times greater than 1.0 second (dashed red line).

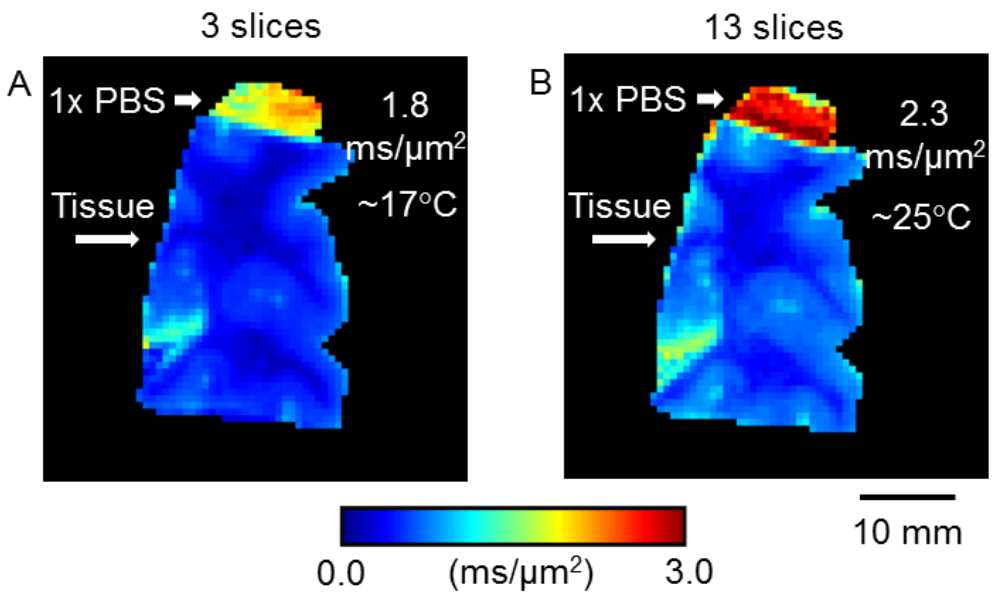

Figure 2.4 Effects of slice number on diffusivity. A. B. The apparent diffusion coefficient (ADC) maps are shown of data collected using 3 slices and 13 slices, both collected using a b-value of 4 ms/μm^2. Increasing the number of slices from 3 to 13 results in an average increase in the temperature of 1x PBS by 8° Celsius. This indicates that the number of RF pulses (resulting in the number of MRI slices) affects tissue temperature.

Choice of imaging medium can also significantly alter signal quality of *ex* vivo tissues. While incubation in 1xPBS demonstrably increased signal to noise quality in gray and white matter, imaging of tissues in a protonated fluid has been shown to result in susceptibility artifact, particularly at tissue interfaces (Nolte et al., 2000). SNR can be further improved by imaging tissues in a proton-free fluid, most commonly perfluoropolyether (PFPE, commercial name: Fomblin/Fluorinert) (Benveniste et al., 2000; Miller et al., 2011). We tested whether imaging tissues in Fluorinert would provide much needed increases in signal quality.

A spin echo sequence optimized to produce maximized signal (TR/TE = 1400/30ms) was used to collect images of tissues incubated either in 1xPBS or Fluorinert (**Figure 2.5**). SNR was calculated by dividing the signal magnitude by the standard deviation of background noise and then dividing by 0.66 (Rayleigh ratio). Tissues imaged in Fluorinert had 20-30% greater

SNR compared to tissues imaged in 1xPBS. The results of this experiment determined that imaging tissues in an imaging media such as Fluorinert would further increase SNR.

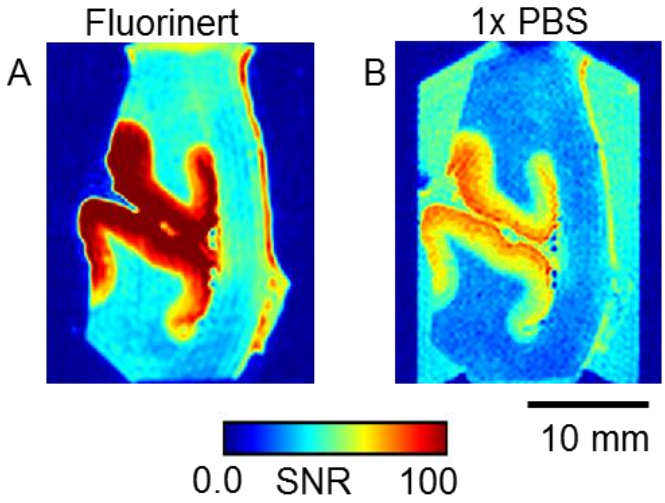

Figure 2.5 Effects of protonation on signal quality. A. The signal to noise ratio (SNR) of the spin echo images was tested while *ex vivo* tissue was stored in Fluorinert. MRI data collected of tissue stored in Fluorinert showed 20-30% higher SNR than tissue stored in 1xPBS. **B.** Tissues imaged in 1xPBS had high signal artifact due to the highly protonated nature of PBS, as opposed to magnetically inert Fluorinert.

2.4 Optimization of coil shape

Coil shape, has been demonstrated to impact signal to noise ratio (SNR). Specifically, a parameter termed “filling factor”, uses the ratio of tissue sample volume to coil volume to measure the magnetic field energy stored by the tissue sample relative to the total magnetic energy of the RF coil (Hoult and Richards, 2011). In order to improve SNR in our *ex vivo* tissues, an additional parameter to be optimized was the volume of the RF coil used to hold tissue samples.

A custom built cylindrical radiofrequency (RF) coil 4cm in length was used to collect all MRI data. A tunable dielectric copper capacitor (1-5 pf) was used to tune the coil (**Figure 2.6A**). A custom made pickup coil made from 16G copper wire 4cm in diameter was permanently fixed

to the RF coil, with a matching capacitor (1-5 pf) allowing to match signal frequency of the coil with the scanner frequency (499.7 MHz). Tissue was then placed with imaging medium in a syringe container cut to fit within the RF coil (**Figure 2.6B**). A sandwich of magnetically inert polyvinylfloride inserts was used to prevent movement of the tissue sample during MR data acquisition. A spin echo imaging sequence (TR/TE = 1400/30ms) was used to collect data with isotropic in-plane resolution of 250µm and slice thickness of 500µm. SNR was measured for the same tissue sample with varying RF coil diameters (**Figure 2.6C-E**), and calculated as the magnitude of the image signal divided by the standard deviation, and then divided by the Rayleigh ratio (0.66). Signal quality increased as the coil diameter decreased. A coil diameter of 2.6cm produced data with the highest SNR in both gray and white matter. Based on these data, RF coil diameter of 2.6cm was determined to provide the highest tissue: coil filling factor and thereby maximize signal to noise.

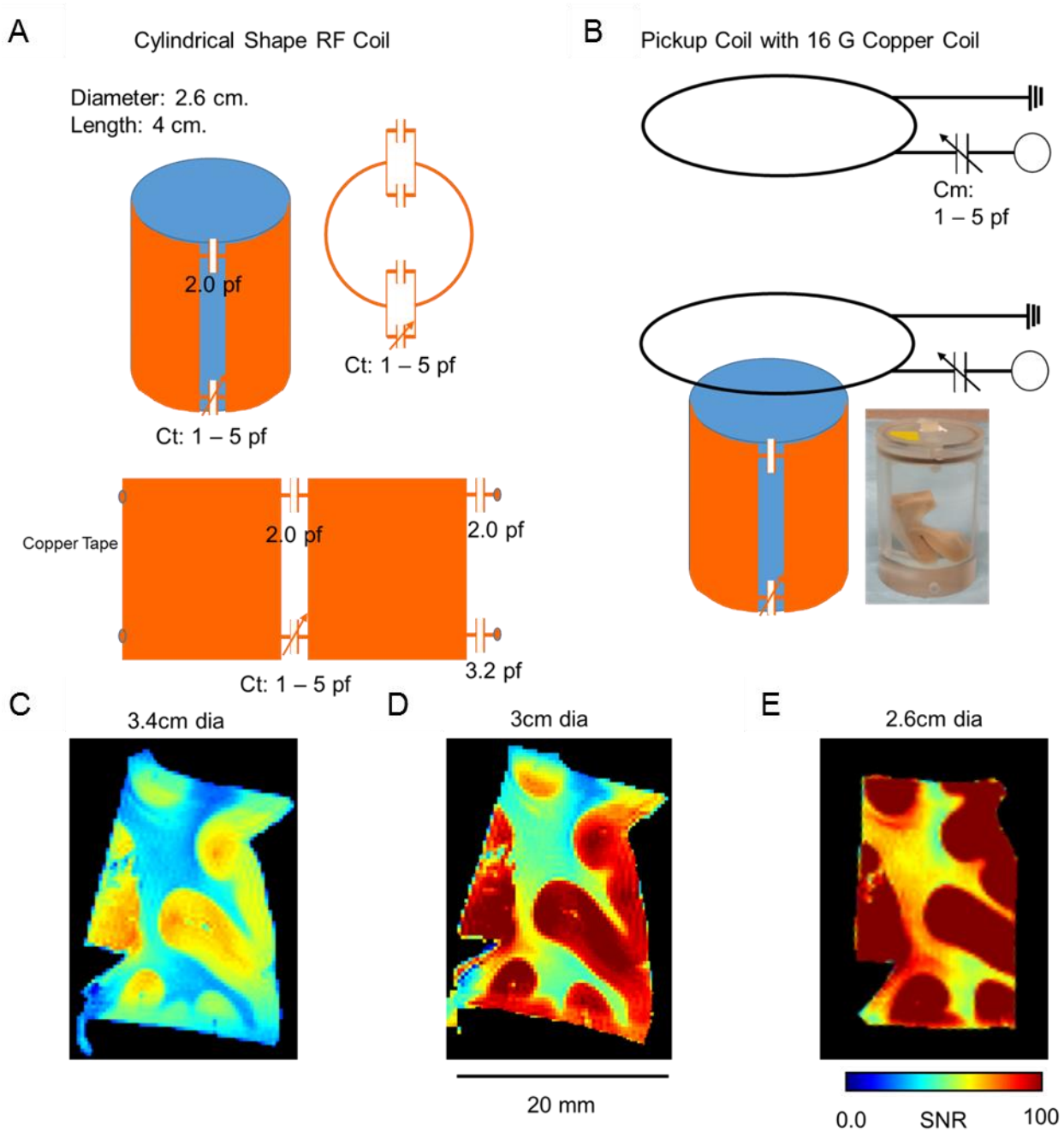

Figure 2.6 Configuration of RF and pickup coil. A. A custom built cylindrical radiofrequency (RF) coil 4 cm in length and 2.6 cm in diameter made from copper tape was used to collect all MRI data. **B.** A custom pickup coil was permanently fixed to the RF coil with a matching capacitor allowing for precise control of frequency matching. **C.** SNR map of data collected using a 3.4 cm diameter RF coil. **D.** SNR map of data collected using a 3 cm diameter RF coil. **E.** SNR ratio of data collected using a 2.6 cm RF coil. The 2.6 cm diameter allowed for an optimal filling factor, and therefore had the best SNR. All images have a voxel size of 250 x 250 x 500 μm^3.

2.5 Post-processing of diffusion data

Although our aim was to acquire MR data with maximum spatial resolution and high tissue contrast between gray and white matter, such data is susceptible to Gibbs ringing artifact. This artifact, caused by truncation of the Fourier series that comprises the MR image signal can produce false morphological features in otherwise healthy tissue (Veraart et al., 2016). Furthermore, when considering diffusion data, Gibbs ringing has been found to produce significant bias in diffusion tensor estimates (Perrone et al., 2015). Filtering the k-space data with a sloped, decreasing windowing function is one solution to correct distortion caused by Gibbs ringing, but application of this filter comes at the expense of spatial resolution (Veraart et al., 2016). We tested whether filtering high spatial resolution diffusion data would remove Gibbs ringing artifact while still preserving true tissue architecture.

Diffusion data of human *ex* vivo cortical tissue was collected using thirty non-collinear directions with a b-value of 4 ms/μm^2 and with 400 μm isotropic voxel size. The resulting data was filtered with a Hamming window using a customized Matlab script (Mathworks 2017a). Although complex white matter architecture, indicated by reduced fractional anisotropy was visible in unfiltered data, there was also evidence of Gibbs ringing (**Figure 2.7A**). In contrast, data smoothed with a Hamming window did not show this artifact (**Figure 2.7B**), but showed morphological sensitivity to complex tissue architecture at relatively voxel sizes compared to our target in-plane spatial resolution (250 μm isotropic). Therefore, the additional post-processing step of filtering diffusion data using a Hamming window was added to the data processing workflow to minimize the possibility of biases tensor estimates in diffusion calculations.

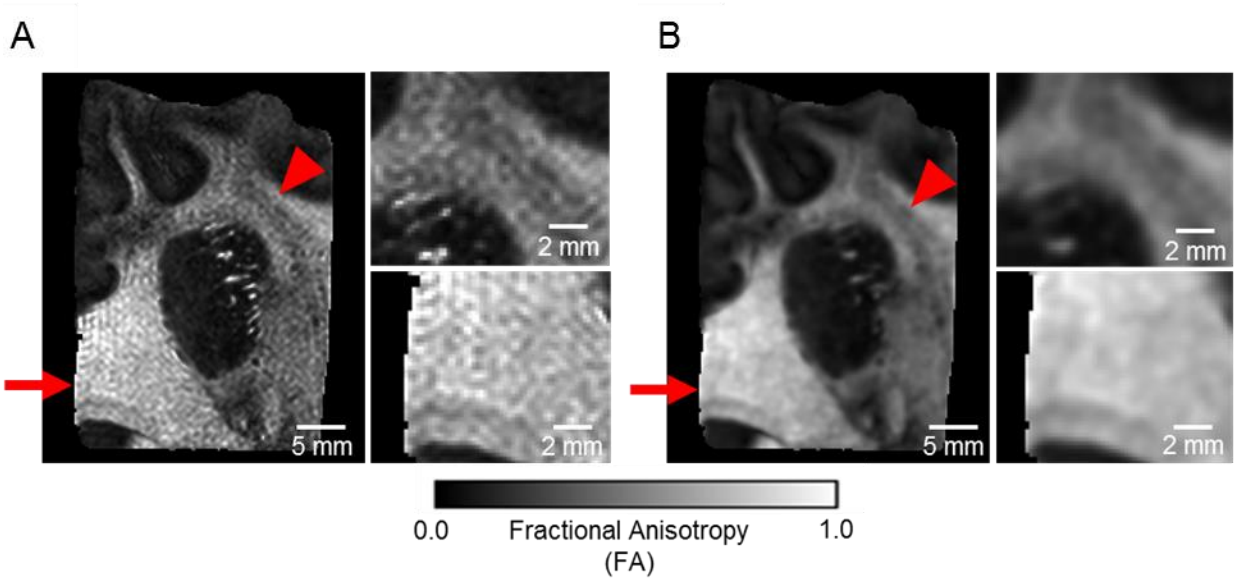

Figure 2.7 Removal of Gibbs ringing artifact. A. Fractional anisotropy (FA) map of cortical tissue (400 μm isotropic voxels with b = 4 ms/μm^2 and 30 non-collinear directions). The FA map shows significant Gibbs ringing (red arrow), but the small voxel size allows for high morphological sensitivity (red arrowhead). **B.** FA map filtered using a Hamming filter removes the Gibbs ringing (red arrow) while preserving the morphological sensitivity necessary when imaging the complex white matter structures in cortical tissue (red arrowhead).

2.6 Conclusions

While the goal of this work is to perform correlations of histology with diffusion metrics in *ex* vivo tissues, there were several associated challenges we needed to consider when acquiring MR data. In addition to concerns of post-mortem interval and effects of fixation on water diffusivity in tissues, diffusion imaging is associated with reduced signal to noise quality relative to traditional structural scans (Tournier et al., 2011). Based on the outcomes of our experimental data, we were able to determine optimal conditions to acquire high spatial resolution diffusion data with high signal to noise ratio. Although we were unable to control for the effects of post mortem interval on tissue quality and water diffusivity in tissues, several steps were established as part of the acquisition of *ex vivo* MRI data. First, equilibration of tissue blocks in 1xPBS for a minimum of two weeks, followed by imaging in Fluorinert using an RF

coil optimized for the tissue block shape was sufficient to increase T2 relaxation time to its maximal state, while further reducing background signal to improve SNR. Second, optimized repetition time and RF pulse number allowed us to not only maximize the MR signal, but also maintain consistent tissue temperature and reduce signal variability. Finally, post-processing of data using a Hamming window corrected diffusion data for Gibbs ringing artifact, reducing the possibility of false signal dropout. With these parameters, we expect that our diffusion data is of reasonable quality to perform radiological-pathological correlations in human cortical tissues.

Chapter 3. Quantitative validation of a nonlinear histology-MRI coregistration methods using generalized Q-sampling imaging in complex human cortical white matter

3.1 Introduction

Chronic traumatic encephalopathy (CTE) is a progressive neurodegenerative disease that has been increasingly linked to patients who have been exposed to repetitive mild brain trauma in sports or blast related injuries (McKee et al., 2009b; McKee et al., 2013). While the initial injuries that trigger CTE are often sustained earlier in life, behavioral symptoms of CTE manifest at later stages, including mood changes, cognitive impairment, and dementia (McKee et al., 2009b; McKee et al., 2015b; Stern et al., 2013). Neuropathological features of CTE include irregularly distributed hyperphosphorylated tau (p-tau) neurofibrillary tangles and astrocytic tangles prominently distributed in the depths of cortical sulci and around cortical blood vessels (McKee et al., 2016; McKee et al., 2009b; McKee et al., 2015b; McKee et al., 2013). These features, which increase in quantity and severity through stages I-IV, classify CTE as a tauopathy, can only be definitively detected at the present time by post-mortem examination. In

addition to characteristic tau pathology, there is also evidence of axonopathy in CTE (McKee et al., 2015b; McKee et al., 2013). There is a concerted effort to develop methods to diagnose CTE and impact related axon injury *in vivo* using blood based or imaging biomarkers (Barrio et al., 2015; Bogoslovsky et al., 2016; Mitsis et al., 2014). One potential imaging modality that is currently under consideration as a means to noninvasively detect axon injury and diagnose CTE *in vivo* is diffusion MRI (Arfanakis et al., 2002; Niogi et al., 2008; Rutgers et al., 2008). Diffusion MRI is widely used for fiber tracking, brain connectivity, and the diagnosis of neurological diseases, however, the underlying interpretation of diffusion MRI signals is often unknown especially in complex white matter. The diffusion MRI signal is based on the microscopic movement of water in brain tissue (Le Bihan, 1995). Water molecules in fluid such as CSF are free to move in any direction, while diffusion of water in gray matter is hindered by cellular components such as neuronal and glial membranes (Edgar and Griffiths, 2014; Le Bihan, 1995). In simple white matter tracts, the high density of axons restricts water diffusion to the preferential axes of the fiber tracts (Behrens et al., 2014; Le Bihan, 1995; Pierpaoli et al., 2001). This property of water diffusion has opened the door to use diffusion MRI to map and assess the fiber integrity of large brain white matter tracts. Regardless of the algorithm, diffusion MRI based tracking relies on the assumption that water diffusion is least hindered on a path parallel to white matter fiber tracts (Behrens et al., 2014). For example, in the streamline tractography method, local fiber orientation is modeled on a voxel-wise level. The tract is then reconstructed by starting with a seed point and then following local fiber orientation (Behrens et al., 2014). Another strategy which can reduce the error propagations commonly encountered in streamline tractography is to use a probabilistic method (Behrens et al., 2014). Such methods are often more successful when attempting to track white matter fibers where there is a higher degree of

uncertainty of the local directionality of the track, a situation where streamline tractography can fail (Hubbard and Parker, 2014).

Fundamentally, all approaches implementing models such as diffusion tensor imaging (DTI) that use a single tensor estimation inevitably fail when there are multiple fiber populations within a single voxel (Behrens et al., 2014; Hubbard and Parker, 2014; Wiegell et al., 2000). White matter in the healthy human brain is estimated to consist of at least 63% complex fiber populations, defined as crossing, bending, branching or kissing fibers (Jeurissen et al., 2013). Therefore, DTI is inadequate when used to model diffusion in the majority of human brain white matter. For example, Reveley et al. (2015) demonstrated that probabilistic tractography based on DTI data could not be performed in approximately 50% of cortical surface structures, most commonly in sulci and gyri (Reveley et al., 2015) due to the rapidly changing fiber orientation, a finding that they further supported using injected dyes to trace axonal projections. In the context of CTE and impact related axonal injury, the white matter regions most susceptible to injury may be adjacent to cortical sulci (Blumbergs et al., 1994; McKee et al., 2009b), though the exact patterns in concussive injury have not yet been fully investigated. These white matter tracts are classified as complex due to the high prevalence of curving U-fibers. Modeling diffusion as an orientation distribution function (ODF) has been proposed as an alternative solution to the multiple fiber populations dilemma, but such models require data collection in more directions, are prone to loss of signal and increased noise due the higher degree of diffusion weighting and require small voxel sizes for precise ODFs (Jones and Cercignani, 2010; Jones et al., 1999). Validation of the fiber directionality central to diffusion tractography has proven successful in radiological-pathological correlations of large relatively simple white matter tracts, but remains under investigated in complex white matter regions (Behrens et al., 2014; Budde and Annese,

2013; Hubbard and Parker, 2014; Kier et al., 2004). Furthermore, the complexity of white matter directionality can confound the interpretation of quantitative diffusion imaging parameters if the issue of directionality is not adequately addressed (Hubbard and Parker, 2014). Specifically, without accurate interpretation of directionality, complex but intact white matter cannot be distinguished from white matter with disrupted microstructural integrity. A radiological pathological correlation approach which accounts for complex white matter architecture would therefore be highly useful when interpreting the sensitivity and specificity of changes in the diffusion MRI signal.

A key component and challenge in performing radiological-pathological correlations lies in the area of coregistration of histology to MRI data. First, coregistration is highly dependent on the placement of fiducials that are clear in both the MRI and histology data. Initial studies typically involved drawing regions of interest based on the anatomical locations of the suspected pathology of interest in corresponding locations for both MRI and histology datasets using a brain atlas or clear anatomical boundaries as reference (Donahue et al., 2016; Herrera et al., 2016; Mac Donald et al., 2007b; Weiss et al., 2015). However, in the more general case for arbitrary neuropathological features of interest, such as white matter underlying a specific sulcus, regions of interest that are visually distinguishable based on anatomical landmarks would not provide sufficient specificity. Another option is the use of exogeneous fiducial markers that can be injected into the tissue prior to imaging, and used as reference points following sectioning and staining however, this approach is highly vulnerable to inaccurate injections and subsequent migration of the markers resulting in displacement errors as high as 600 μm (Lazebnik et al., 2003; White et al., 2011; Zemmoura et al., 2014). Strategies to perform automated feature extraction have been successful in cases where the gradient of the histological image has a high

degree of correspondence with the structural MRI image (Goubran et al., 2013; Goubran et al., 2015). However, an edge detection based approach often fails when coregistering tissue stained for pathological markers which are only localized to specific regions, such as AT8 for tau tangles in sulcal depths, because of high reliance on similar contrast properties of MRI and histology data (Goubran et al., 2013; Goubran et al., 2015).

Second, the choice of method to warp the histology data to the MRI image can also drastically change the accuracy of registration. Linear transformations such as similarity or affine transforms lead to high registration errors at the curving cortical sulci, due to the sudden change in tissue architecture and potential histological processing differences in the adjacent gray and white matter (Breen et al., 2005a; Breen et al., 2005b; Choe et al., 2011; Goubran et al., 2015). Importantly, registration errors in these areas, the primary locations of CTE related pathology, would create a further loss of sensitivity while performing radiological pathological correlations. A nonlinear approach can provide higher accuracy of registration in cases where a single transformation function does not describe the geometry across all of the tissue, particularly in local changes of tissue architecture (Choe et al., 2011; Dauguet et al., 2007; Goshtasby, 1988; Zagorchev and Goshtasby, 2006). Finally, most automated registration algorithms typically involve downsampling histological data to match MRI data resolution (Wang et al., 2015), or upsampling MRI data to match the high resolution histology (Schilling et al., 2016). Thus, typical coregistration approaches result in a loss of sensitivity in situations where the MRI signal may be affected by changes in the tissue microstructure that are not reflected by measures available in downsampled data, most commonly area fraction of positive staining. Because of the technical challenges listed above, validations of radiological pathological coregistration on a

voxel wise level have yet to be performed, resulting in a lack of knowledge of how quantitative histological measures directly reflect corresponding MRI metrics.

In the course of our radiological-pathological investigations of brain tissue from subjects with CTE (Gangolli et al., 2015; Holleran et al., 2015) we have recently developed a method to coregister histology and MRI data at a voxel-by-voxel level so that correlations can be performed between high spatial resolution diffusion MRI and quantitative histological data. We validated the method using a variety of measures, most notably an initial radiological pathological correlation of fiber directionality in complex white matter regions. The registration workflow is not restricted to high contrast stains, thus providing a means of assessing subtle morphological changes in histology, and can be applied to perform highly sensitive and specific radiological pathological correlations in CTE and potentially other applications to extract ground truth relationships between the MRI signal and underlying tissue pathology.

3.2 Methods

3.2.1 Diffusion MRI Acquisition

Ex vivo human brain tissue blocks of superior frontal cortex (Brodmann Area 8/9), approximately 1x2x3 cm, with a confirmed neuropathological diagnosis of Stage III or IV CTE (ACM,TDS,VEA) were obtained through the VA-BU-CLF brain bank. All brain tissue samples were stored in periodate-lysine-paraformaldehyde (PLP) fixative, but then refixed in 10% neutral buffered formalin and refrigerated for one week (**Figure 3.1**). Meninges and blood vessels were trimmed from the cortical surface to remove potential artifacts in the MRI data acquisition, such as blood iron and air bubble induced artifacts. Image artifacts were examined using the T2*

images. Tissue blocks were rehydrated in 1x phosphate buffer solution (1x PBS) with 0.01% NaN_3 for two weeks prior to MRI data acquisition and stored at 4° Celsius, changing the solution every three days to assure equilibrated rehydration. This rehydration time was determined empirically by finding the time during rehydration at which the T2 relaxation time reached steady state. The volume ratio of tissue and 1xPBS was 1:40.

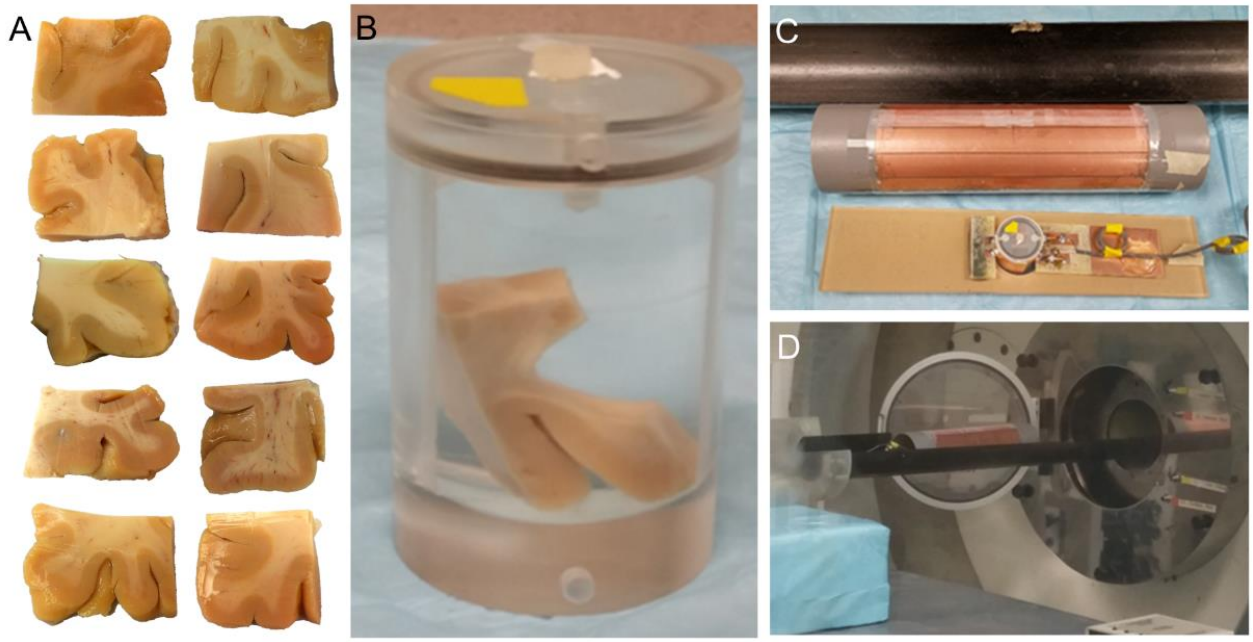

Figure 3.1 MRI data acquisition. A. Ten human *ex vivo* tissue samples from the superior frontal cortex (BA 8/9) were requilibrated at 4° Celsius in 1xPBS with 0.01% NaN_3 for two weeks after being received from Boston University. Prior to MRI data acquisition, tissue was stored overnight at room temperature in Fluorinert. **B.** Tissue was placed in a container which optimized filling factor thereby maximizing the tissue signal. **C.** An inductive coupling coil was used to in order to better tune the coil and tissue contained contents to the resonant frequency of the MRI scanner. **D.** GQI data were acquired in an 11.74 T Agilent MRI scanner, requiring a total scan time of 11 hours per tissue sample.

Diffusion MRI data were acquired using an 11.74 T MRI scanner with 120 G/cm gradient (Agilent, Palo Alto, CA), using a two dimensional standard spin echo sequence, which was optimized to produce high spatial resolution data with an in plane resolution of 250 μm x 250 μm and slice thickness of 500 μm. An in-house built cylindrical radio frequency (RF) coil with 2.60 cm diameter and 4.0 cm length was used to obtain diffusion MR data. The main axis of the RF

coil (resonant) was parallel to the longest axis of each tissue block to improve B1 field inhomogeneity. While a long repetition time (TR) is typically preferred to collect MRI data with high SNR, this also results in longer scan times and therefore requires optimization of the TR time. Optimal TR times were empirically found to be greater than one second. To minimize artifactual MR signal (Miller et al., 2011; Thelwall et al., 2006), tissue blocks were stored in a proton free solution (Fluorinert) prior to scanning. The tissue samples were stored at room temperature twenty-four hours prior to scanning to reduce temperature related diffusion artifacts (D'Arceuil et al., 2007; Kim et al., 2007; Thelwall et al., 2006). Furthermore, multiple slice collection requires multiple RF pulse excitations that heat the tissue can increase diffusivity. Therefore, each MRI data acquisition consisted of 13 slices irrespective of the tissue block thickness to maintain consistent temperature throughout the study. Approximately seven MRI slices per tissue of the collected data were used for analysis to ensure minimal artifacts caused by partial voluming near the top and bottom of the often irregularly shaped tissues.

With these parameters, both DTI (Jones et al., 1999) and Generalized Q-Sampling Imaging (GQI) (Yeh et al., 2010) data were collected. DTI data were acquired using 30 diffusion sensitized gradients (**Table A.2**), a b value of 4,000 s/mm^2, four non-diffusion weighted images (b = 0 s/mm^2) and TR/TE = 1400/30 ms with a total scan time of 1.5 hours. Fixed *ex vivo* tissue has reduced water diffusivity compared to *in vivo* tissue, thus requiring higher b values to compensate for the reduced diffusivity (D'Arceuil et al., 2007; Thelwall et al., 2006). GQI data were acquired using 202 diffusion sensitized gradients (**Table A.3**), a maximum b value of 8,000 s/mm^2, ten non-diffusion weighted images (b = 0 s/mm^2) and TR/TE = 1400/30 ms, resulting in a total scan time of 11 hours. The data was filtered using a standard periodic Hamming window to filter any Gibbs ringing artifact of size 160-point x 128-point to match the readout encoding and

phase encoding directions. DTI data were reconstructed using the BrainSuitev16a1 diffusion pipeline (Shattuck and Leahy, 2002) to generate eigenvalue and eigenvector files. GQI data were reconstructed in DSI studio (http://dsi-studio.labsolver.org/) using a diffusion sampling length ratio (L_{Δ}) of 0.70, a 4-fold tessellated icosahedron resulting in 162 sampling directions, a maximum of three resolved fibers per voxel, and a balanced full sphere scheme. The orientation distribution function (ODF) calculation was weighted by the square of the diffusion displacement. These parameters were chosen empirically in order to maximize the sharpness of calculated ODFs, which were then exported into MATLAB (Mathworks 2014a) for remaining analysis. As an additional comparison, the DTI data were also reconstructed in DSI studio based on the higher angular resolution data.

3.2.2 Histology

Following diffusion MRI data acquisition, tissue blocks were refixed in 4% paraformaldehyde, incubated for a minimum of three days in 30% sucrose solution, sectioned into sequential 50 μm sections on a freezing sliding microtome and stored in individual wells to preserve slice location. The tissue blocks were placed on the platform in the same orientation as the acquired MRI images, with the MRI image planning used as a reference to slicing plane and orientation. Every sixth section (250 μm interslice interval) was stained using the Myelin Black Gold II stain for myelinated fibers (Millipore, Billerica, MA), resulting in two Black Gold II sections for each MRI slice. Free floating sections were incubated in six well plates (Corning) filled with Black Gold II solution (Black Gold II powder, resuspended in 0.9% saline solution) pre-heated to 60 °Celsius and monitored until they had reached the optimum amount of staining, approximately eight minutes, which was determined by assessing whether fibers could be readily distinguished at x5 magnification. To maintain uniform quality of staining across tissue sections,

fresh Black Gold II solution was used for each section. Sections were washed with MilliQ water for two minutes and then incubated in 1% sodium thiosulfate pre-heated to 60 °Celsius for three minutes to remove excess staining. After three washes in 1xTBS, stained sections were mounted on Superfrost-Plus microscope slides (Fisher, Houston, TX) in an orientation matching that of the corresponding MRI slices and allowed to dry at room temperature overnight. The mounted sections were dehydrated in a series of graded ethanol solutions (50%-70%-95%-95%-100% for two minutes each), and then incubated in two treatments of Xylene for three minutes each. Slides were coverslipped with Cytoseal 60 (Richard Allan Scientific, Kalamazoo, MI), and digital images of the slides were acquired with a Hamamatsu NanoZoomer 2.0 HT System (Hamamatsu) with an x20 objective and stored in an NDPI file format.

3.2.3 Co-Registration of Histology to MRI

Due to the large files sizes of the originally acquired x20 magnification images, where the linear dimension of the image pixels was 0.52 μm, the NDPI images of the stained sections were downsampled in ImageJ (NIH, Bethesda, MD) using the NDPI tools plugin (Deroulers et al., 2013) to x5 magnification. This magnification preserved morphological details for quantification where the linear dimension of image pixels was 1.84 microns, and the smaller file size allowed for more efficient registration and quantification. Because this downsampled image was still at a higher resolution than the MRI image, co-registration was then performed to warp the histological data to the MRI space. A minimum of 55 anatomical landmarks were manually placed on the x5 image of the Myelin Black Gold II stained section and the same landmarks were placed on the corresponding non-diffusion weighted ($b = 0$ s/mm^2) diffusion MRI slice which had T2 contrast characteristics. Landmarks were placed at readily identifiable locations along the tissue edges, border between gray and white matter, and at matching features in both gray and

white matter. A forward nonlinear moving least squares transformation (Goshtasby, 1988) was applied to transform the MBGII section to the MRI data. An inverse transform was then applied to transform each MRI voxel of the histological data, resulting in a warped grid of regions of interest (each region of interest corresponding to one MRI voxel) that was used to quantify the higher resolution x5 histological image in ImageJ (**Figure 3.2**). Both forward and inverse transforms were performed using a custom script written in Matlab.

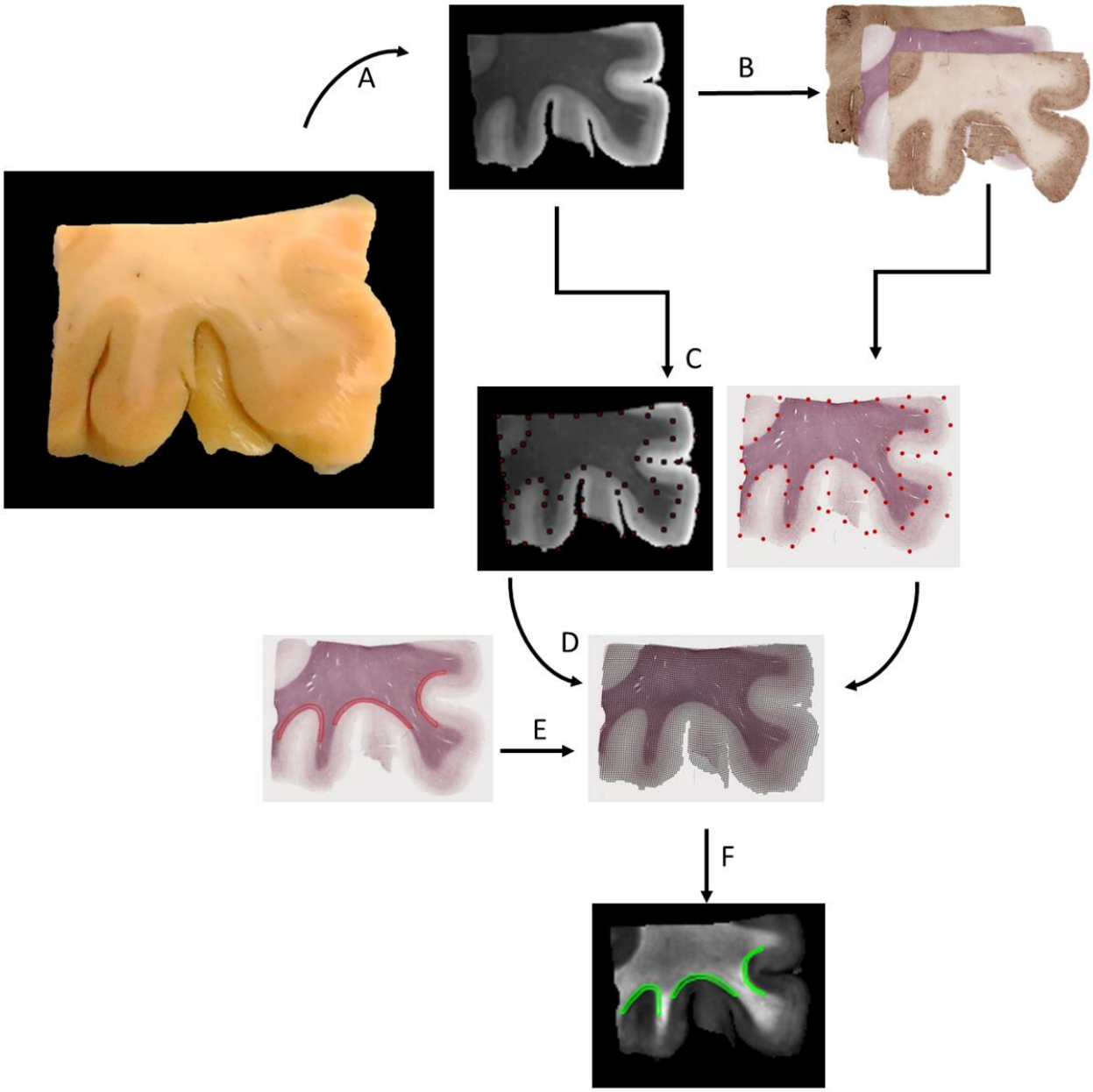

Figure 3.2 Workflow of histology to MRI registration. A. Fixed blocks of human cortical tissue were scanned using a spin echo sequence to collect GQI data. **B.** Tissue was sectioned into serial 50 μm thick sections and stained for neuropathological markers. Every sixth section (250 μm spacing) was stained for myelin using Black Gold II, and digital images of histology were acquired for quantification. **C.** Landmarks were manually placed on the digital image (downsampled to x5 magnification) of the Black Gold II image and associated slice on the unweighted diffusion ($b = 0$ s/mm^2) data in corresponding locations. **C.** A nonlinear least squares registration was applied to warp the histological image to the same orientation and dimensions as MRI space. **D.** To preserve high resolution needed for further quantitative histology, an inverse transformation was applied to each warped histological voxel to generate a grid of ROIs where each region of interest represents a voxel of the diffusion data. **E.** ROIs were then able to be drawn on the high resolution (x5 magnification) histology. **F.** Using the voxel based grid as a reference, the corresponding ROIs were automatically selected on the MRI data for other investigations of radiological-pathological correlations in specific zones such as sub-sulcal white matter.

3.2.4 Validation of Registration

Following co-registration, and generation of voxel-based grids, the accuracy of registration was validated using tools in ImageJ. First, the agreement between MRI and histology to classify voxels into tissue categories was evaluated. To classify Black Gold II registered voxels, a histologically derived trinary white matter mask was generated (**Figure 3.3**). Each Black Gold II image was converted to a 32 bit (grayscale) image, manually thresholded based on staining intensity and blurred using a Gaussian filter with a radius that matched the in plane resolution of the MRI data (250 μm). The coregistered grid obtained from the inverse transformation was then overlaid onto the white matter mask, and the mean intensity within each voxel-based ROI was measured. ROIs with a mean intensity of zero were classified as gray matter, while voxels with a mean intensity of one were classified as white matter. Finally, voxels with a mean intensity that was between zero and one reflected the partial voluming of white and gray matter and were classified as boundary voxels. The gradient of the non-diffusion weighted ($b = 0$ s/mm^2) MRI image was used to classify MRI voxels into the same three categories. To compare the efficacy of a nonlinear approach to linear transformations which have typically been applied in previous radiological-pathological correlation studies (Choe et al., 2011; Wang et al., 2015), voxel-based grids were generated using an affine transformation included in Matlab. The kappa coefficients of the grids resulting from nonlinear moving least squares vs affine transformations were then compared to determine whether our registration approach provides superior sensitivity when parceling tissue into gray, white, and gray/white matter boundary regions.

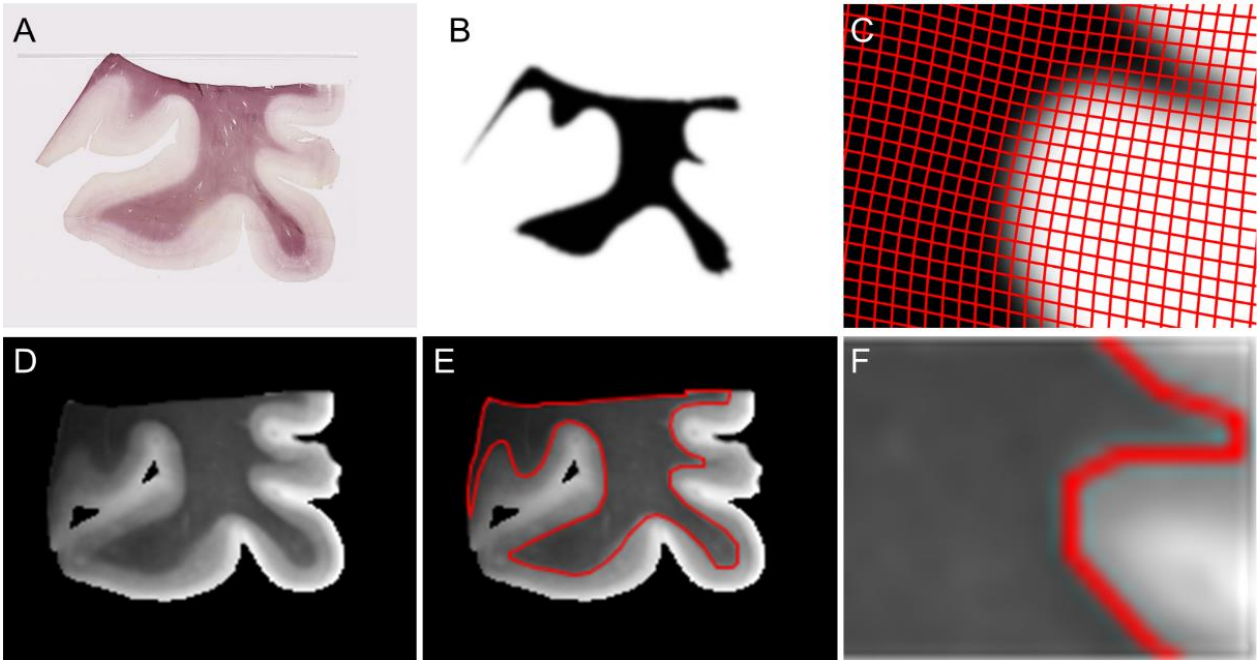

Figure 3.3 Automated generation of white matter masks. A. Histologically derived white matter masks were automatically generated using the high gray white matter contrast of the Black Gold II stain. **B.** Sections were thresholded and blurred using a Gaussian filter with a radius matching the MRI in plane resolution (250 μm). **C.** The corresponding voxel-based grid was then overlaid onto the blurred mask. Voxel equivalent ROIs with a mean value of 1 (darkest intensity) were classified as white matter, while voxels with a mean value of 0 (lightest intensity) were classified as gray matter. Voxels with a mean intensity between 0 and 1 were classified as gray/white matter boundary. **D.** MRI voxel classification was based on the unweighted diffusion image ($b = 0$ s/mm^2). **E.** The boundary between gray and white matter was selected using the edge detection feature available in ImageJ. **F.** Voxels within this boundary were classified as white matter, voxels outside of this boundary were classified as gray matter, and voxels selected during edge detection were classified as boundary voxels.

Because the registration algorithm relies on user defined landmarks, we carefully tested the susceptibility of nonlinear registration to variability when presented with landmarks with small shifts of their in plane locations. Intra-user and inter-user reliability was tested by comparing the shift of each registered voxel between two pairs of grids generated by landmarks placed by the same user at two different time points (five days apart). Inter-user reliability was tested by performing the same procedure for landmarks placed by two different users. The shift was calculated as the Euclidean distance between the centroid of corresponding voxels from the

first and second grid. A computer simulation was additionally used to test the effects of shifting landmarks between 0 to 1000 μm along both the x and y direction. Random numbers were selected from a uniform distribution and applied to a baseline set of landmarks in Matlab. The total number of registered voxels from the resulting registrations that had not shifted more than the in plane MRI voxel resolution (250 μm isotropic) was then calculated for each interval.

The final validation was a test of the registration method to perform a radiological pathological correlation for a parameter where the relationship between histology and diffusion measure is expected to be very strong. This parameter of interest was fiber directionality, which can be calculated from both the histological data and the diffusion data. Fiber directionality of each ROI corresponding to each white matter voxel was derived from the Myelin Black Gold II data using a custom written macro in ImageJ (NIH, Bethesda, MD). Each voxel was zero mean normalized and multiplied with a Tukey window ($\alpha = 0.5$) to reduce background and Gibbs ringing artifacts (**Figure 3.4**). A two dimensional discrete Fourier transformation was then applied to each voxel-corresponding ROI to calculate the associated power spectrum, which contains information about fiber directionality and the degree of fiber coherency within an equivalent voxel. Fiber directionality and coherency were extracted by fitting two ellipses to the power spectrum, where each ellipse represented a fiber population. The angle of the preferential axis of each ellipse relative to the main axis of each registered histological voxel was used as the primary orientation of fibers within each voxel. The degree of coherency of each fiber population was calculated as the ratio of the radial (minor axis) to preferential axes to obtain a measure between zero and one, where a higher coherency measure (closer to one) was thought to represent high fiber integrity. For example, a power coherency of 0.17 indicates two fitted ellipses, where the major and minor axes of both ellipses are relatively equal in length, making the ellipses nearly circular.

Conversely, a power coherency of 0.81 indicates two ellipses that both have minor axes which are much smaller than their respective major axes. In parallel, the diffusion based fiber directionality was extracted in Matlab from the generalized q-sampling imaging (GQI) data based on the orientation distribution function (ODF) of each MRI voxel. The ODF was stored as a series of three dimensional directional vectors of size 3 x N, where N is the number of fiber directions at a subvoxel level, here defined as two. After obtaining the directional vectors of the primary and secondary major fiber components, the orientation angles, θ_n, along the xy plane were calculated using

$$a \cdot b_n = |a||b_n| \sin\theta_n \qquad \text{(Eq. 3.1)}$$

$$\theta_n = \sin^{-1} \frac{a \cdot b_n}{|a||b_n|} \qquad \text{(Eq. 3.2)}$$

where a is the equation of the xy plane (0,0,1) and b_n is the directional vector of either the primary (n = 1) or secondary (n = 2) orientation. White matter voxels were classified as simple (n = 1) or complex (n = 2) for all analysis. Furthermore, because the two-dimensional Fourier transformation can only be used to quantify fibers that are in the histological plane, all analysis was restricted to only include voxels where the primary and secondary major fiber components were either fully in plane or made an angle with the z-axis that was less than 45°.

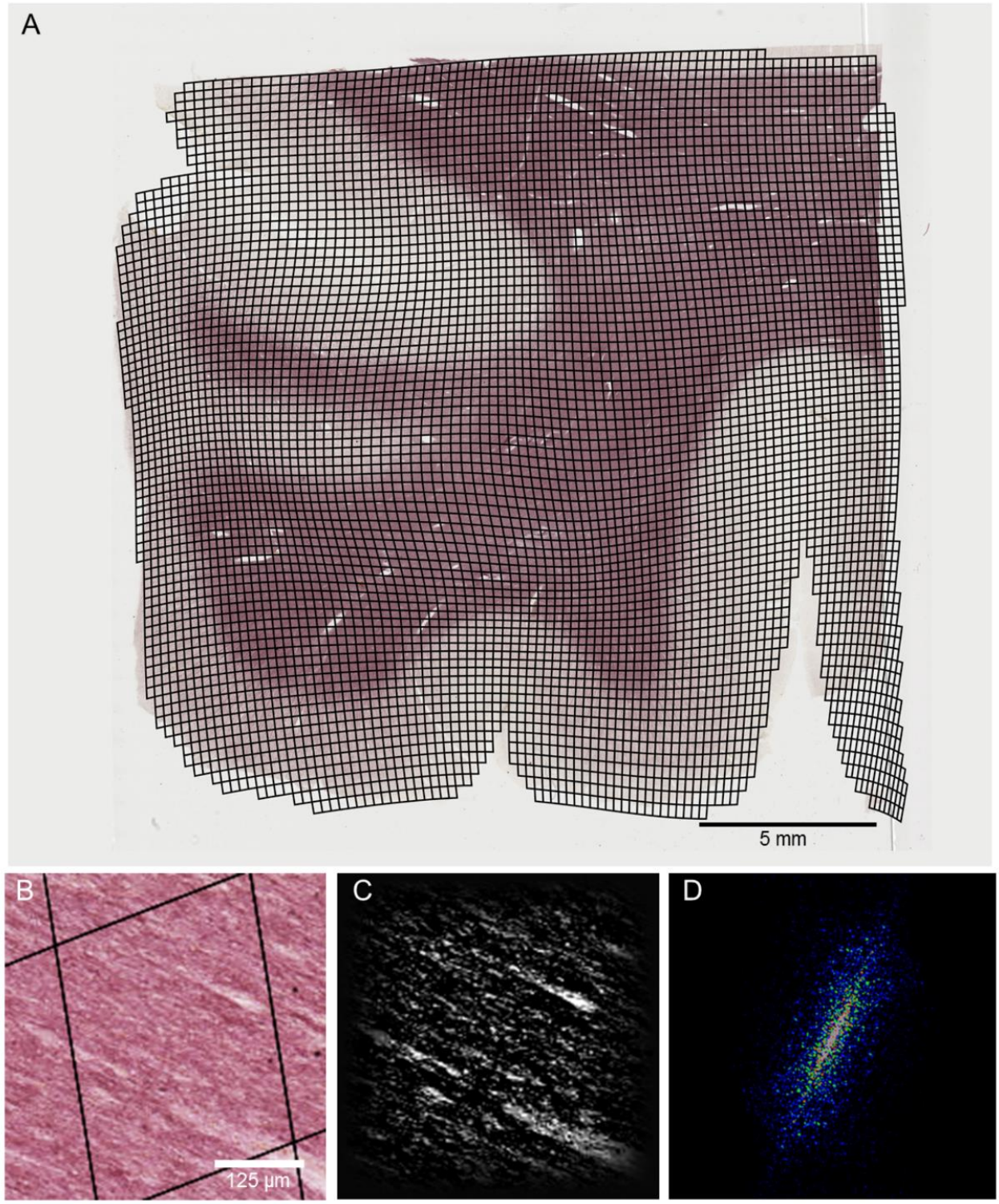

Figure 3.4 Derivation of fiber orientation from histology. A. Voxel-based grids derived from nonlinear least squares registration were overlaid onto the corresponding Black Gold II stained tissue sections in ImageJ. **B.** Each white matter voxel was used as a region of interest. **C.** The ROI equivalent to each voxel was converted to grayscale, zero mean normalized and windowed to remove edge and center spike artifacts. **D.** The power spectrum

resulting from a two dimensional discrete Fourier transformation shows high amplitude peaks perpendicular to fiber orientation stained by Black Gold II. Intensity of the power spectrum corresponds to the amplitude in dB at each spatial frequency. In this example, the power spectrum has greatest amplitude at approximately 60 degrees from the horizontal, perpendicular to the fibers in the spatial domain which are oriented at approximately -30 degrees; the direction of maximum change in signal amplitude is perpendicular to the fiber orientation.

To test the effects of lower in plane voxel resolution on the histological measure of voxel based power coherency, the open source software MIPAV (NIH, Bethesda, Maryland) was used to downsample the raw diffusion data voxels to 500 µm and 1000 µm isotropic resolution. In accordance with the methods described in section 2.3 landmarks were placed on the x5 histology image and the associated slice of the downsampled unweighted ($b = 0$ s/mm^2) diffusion dataset to generate voxel based grids corresponding to these lower resolutions. A region of interest starting at the gray/white matter boundary and extending 2 mm into adjacent white matter of a sulcus with known fiber disruption was assessed for power coherence on a voxel wise basis using grids with isotropic in plane resolutions of 250 µm, 500 µm, and 1000 µm. ODFs were reconstructed in DSI studio with the parameters described in Section 2.1for the downsampled diffusion data. A two tensor fit was applied on a voxel wise basis to each corresponding Black Gold II sections to calculate fiber orientation. A correlation between GQI based and Black Gold II based fiber orientation was performed, only on white matter voxels that did not have a z-axis angle greater than 45°.

Similarly, the effects of implementing a DTI model with both coarse angular resolution and high angular resolution matching that of the GQI data were tested. DTI based fiber orientation was calculated on a voxel-wise basis. The eigenvector corresponding the largest eigenvalue for each calculated tensor was used as the measure of fiber orientation of each MRI voxel. The orientation angle θ was calculated using

$$a \cdot b = |a||b| \sin\theta \qquad \text{(Eq. 3.3)}$$

$$\theta = \sin^{-1} \frac{a \cdot b}{|a||b|} \qquad \text{(Eq. 3.4)}$$

where a is the equation of the xy plane $(0,0,1)$ and b is the eigenvector corresponding to the largest eigenvalue of the diffusion tensor. The same landmarks used to coregister GQI data to Black Gold II data were used to coregister the DTI data.

To test that power coherence is indeed a measure of white matter disruption, a 2 mm controlled cortical impact (CCI) injury was applied to a male mouse, as previously described (Brody et al., 2007). This level of injury is known to result in thinning of hippocampal and cortical layers, along with positive staining for amyloid precursor protein (APP) and other markers of axonal injury in the acute phase following injury. Twenty-four hours after injury, the mouse was transaortically perfused and the brain was surgically removed from the skull and fixed in 4% paraformaldefyde (PFA) in 1x PBS overnight. The whole brain was then incubated in 30% sucrose for three days, sectioned on a freezing sliding microtome into 50 μm thick sections, and stained for myelinated white matter using Myelin Black Gold II.

3.2.4 Statistical Analysis

All statistical analysis was performed in Statistica 13.1 (Statsoft Inc., Tulsa, OK). A one-tailed Spearman's correlation coefficient was calculated to measure the correlation between GQI based and Black Gold II based primary and secondary fiber orientations. A one-tailed F-test was used to determine whether there was a significant reduction in power coherence variation across samples when comparing voxels with isotropic in plane resolutions of 250 μm vs 500 μm and 250 μm vs 1000 μm.

3.3 Results

3.3.1 Agreement between MRI and histology based tissue classification

A total of 113 Myelin Black Gold II stained sections from ten tissue blocks were registered to their corresponding MRI slices. Every registered voxel was classified as gray matter, white matter, or gray/white matter boundary, and a Cohen's kappa coefficient was calculated for each registered section to determine the agreement between MRI based and Myelin Black Gold II based voxel classification. Nonlinear transformations resulted in higher kappa coefficients compared with affine transformations (**Table 3.1**), measured by calculating the mean kappa coefficient across sections for each tissue block. The difference in registration methods could also be qualitatively observed, in particular at sulci and gray/white matter boundaries (**Figure 3.5**). A linear affine transformation applied the same transformation to each registered voxel, whereas our nonlinear method better compensates for tissue warping and shrinkage that is not uniform across heterogeneous tissue regions. Notably, nonlinear registration results in a high classification agreement of boundary voxels. This indicates that a nonlinear registration method is more reliable than a linear (affine) method when coregistering tissue sections in regions characterized by abrupt in-plane changes in tissue architecture.

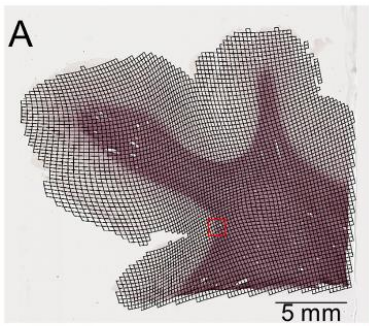

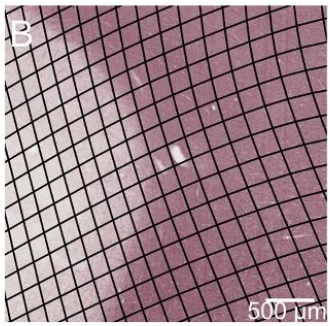

C

Observed kappa = 0.98	MRI white matter	MRI boundary	MRI gray matter
MBGII white matter	2025 voxels	17 voxels	7 voxels
MBGII boundary	33 voxels	295 voxels	15 voxels
MBGII gray matter	3 voxels	3 voxels	2031 voxels

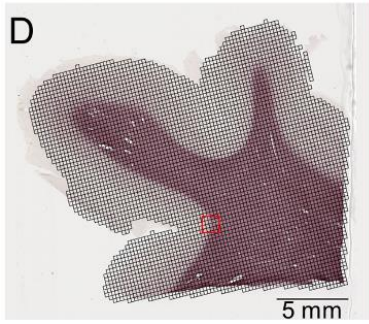

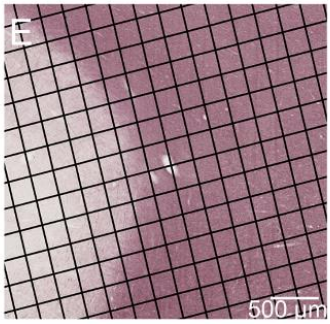

F

Observed kappa = 0.77	MRI white matter	MRI boundary	MRI gray matter
MBGII white matter	1908 voxels	141 voxels	76 voxels
MBGII boundary	123 voxels	126 voxels	57 voxels
MBGII gray matter	25 voxels	157 voxels	1816 voxels

Figure 3.5 Comparison of nonlinear vs linear transformation methods. A. A nonlinear moving last squares transformation was used to generate voxel-based grids corresponding to Black Gold II sections. **B.** Variation in tissue warping is apparent by the non-uniform shape of the grid in gray and matter regions. **C.** An unweighted Cohen's kappa coefficient was used to evaluate the agreement of voxels classified as white matter, gray matter, or boundary voxels using histology and MRI, resulting in very strong agreement (kappa = 0.98). **D.** An affine transformation was used to generate voxel-based grids using the same manually placed landmarks as the nonlinear transformations. **E.** Uniform warping across gray and white matter is apparent, particularly at the gray/white matter boundary. **F.** The unweighted kappa coefficient was calculated, resulting in good agreement (kappa = 0.77), but there is a large discrepancy in the agreement between boundary voxels, indicating that a linear transformation may not be able to account for sudden variations in tissue.

		Nonlinear transformation		Affine transformation	
Sample #	CTE Stage	mean κ	± std dev	mean κ	± std dev
Case 1	IV	0.92	0.05	0.78	0.13
Case 2	III	0.94	0.06	0.81	0.22
Case 3	IV	0.91	0.02	0.65	0.17
Case 4	III	0.96	0.08	0.72	0.09
Case 5	IV	0.97	0.08	0.76	0.11
Case 6	III	0.92	0.04	0.67	0.24
Case 7	III	0.93	0.05	0.71	0.23
Case 8	IV	0.94	0.02	0.80	0.19

Case 9	IV	0.95	0.07	0.62	0.08
Case 10	III	0.93	0.03	0.77	0.29

Table 3.1 Performance of transformation method evaluated using tissue classification. Unweighted kappa coefficients for all ten human cortical tissue samples were calculated for grids generated using the nonlinear vs. affine transformation methods. The kappa coefficient was used to determine the agreement between MRI and Black Gold II histology classified as white matter, gray matter, or boundary tissue on a voxel-wise basis. Nonlinear transformation results in improved tissue classification, reflected by higher kappa coefficients, all higher than 0.90, while the implementation of an affine transformation results in less agreement between MRI and histology based tissue classification, reflected by lower kappa coefficients which are less than 0.90.

3.3.2 Robustness of landmark placement-based registration

Two sets of registered grids were generated for a subset of registered Myelin Black Gold II sections for each of the ten human *ex vivo* cortical tissue blocks. The nonlinear registration algorithm remained consistent between the two sets of landmarks, so any variability of the grids and registration would be due to a change in the in plane position of the manually placed landmarks. The Euclidian distance was used as a metric of voxel-wise shift and reliability of registration was determined by plotting the cumulative histogram of the shift of all voxels (**Figure 3.6A-B**). Because the MRI in plane resolution was 250 μm x 250 μm, the percentage of voxels that had shifted less than 250 μm was used as a metric of inter and intra-rater reliability of landmark placement. To maintain registration quality control, a minimum intra-user and inter-user reliability was set to 90%. All investigators placing landmarks showed inter and intra-reliability of landmark placement that was above this threshold.

An additional simulation was performed on established sets of landmarks to determine the robustness of registration, or the tendency of voxels to shift due to increasing changes in landmark placement (**Figure 3.6C**). Landmarks placed on Myelin Black Gold II were shifted along both the x and y axis by drawing random numbers from a uniform distribution where the interval of the distribution reflected the maximum amount of shift. For each distribution and

maximum landmark shift, the percentage of registered ROIs equivalent to MRI voxels that had shifted more than 250 μm was calculated and plotted as a function of the distribution interval. As expected, larger amounts of shift in landmarks decreased the percentage of registered ROIs that were below this threshold. However, landmark shifts below 350 μm did not cause the percentage of registered ROIs to fall below 80%. These results indicated a high degree of reliability for our manual landmark-based coregistration method.

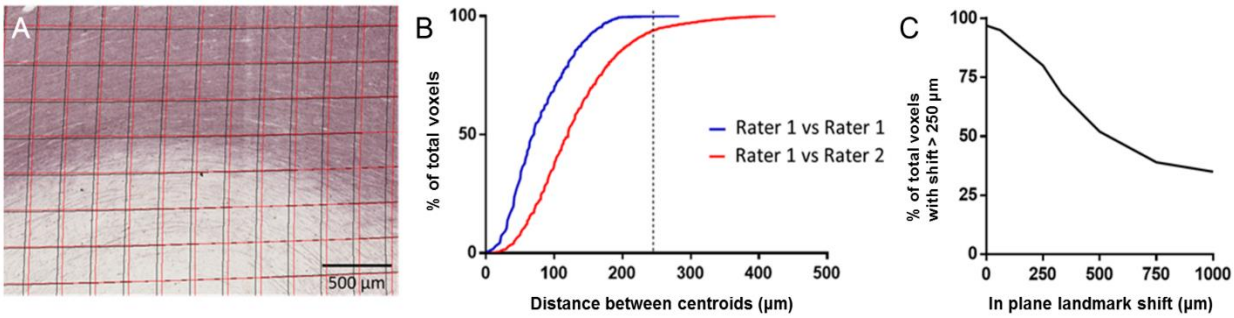

Figure 3.6 Reliability testing. A. Two grids were generated and overlaid onto the corresponding histological images based on two sets of landmarks placed by either the same or two different users. **B.** The cumulative histogram of the distance the centroid of each voxel has shifted shows that even when two different users have placed separate sets of fiducials based on anatomical landmarks, less than 25% of voxels have shifted more than 250 μm, a threshold determined using the MRI in plane resolution. **C.** A simulation was carried out to test the robustness of nonlinear registration to variations in landmark placement. The percentage of voxels that had shifted less than the MRI in plane resolution (250 μm) was then plotted as a function of the maximum distance the landmarks had been shifted. Registration is less prone to variability when landmarks have been shifted less than 350 μm, with 80% of voxels having shifted less than 250 μm.

3.3.3 Correlation of diffusion derived and histologically derived fiber orientations

The strength of the relationship between diffusion based and histologically based primary and secondary fiber orientations was used to determine the accuracy of histology to MRI co-registration. Fiber orientations derived from the Myelin Black Gold II data were compared on a voxel wise basis with fiber orientations of corresponding voxels derived from the diffusion data.

Because the GQI data had higher angular resolution compared to DTI data, GQI data were the basis for comparison. Strong edges in gray/white matter boundary regions could not be removed by zero mean normalization or windowing, consequently, only registered regions of interest classified as white matter were included in analysis. = When plotting the Myelin Black Gold II based fiber orientations as a function of the corresponding GQI based fiber orientations (**Figure 3.7**), there was nearly a one to one linear relationship between both primary ($p < 0.0001$, $r = 0.94$) and secondary ($p<0.0001$, $r = 0.88$) fiber populations. The agreement between primary fiber directionality was then compared utilizing an affine transformation (**Figure 3.8**). The spread of Black Gold II based fiber orientations for each GQI fiber orientation bin was much broader when comparing primary fiber orientation, but the affine still provided reasonable agreement ($p < 0.0001$, $r^2 = 0.87$). When comparing the correlations of affine vs nonlinear transformations using a difference test, there was a significant difference between the two correlation coefficients ($p = 0.0026$). The results of the linear regression showed that there was a bias in the nonlinear transformation ($y = 1.0x + 10.47$), compared to the affine transformation ($y = 1.0x + 1.952$). Fiber orientation correlations based on nonlinear coregistration had small variance and large bias, while correlations based on the affine transformation had large variance and small bias. However, while addition of more sample voxels would reduce the variance of fiber orientation correlation, this would not be feasible when performing correlations in human tissue, where each sample only has a finite number of voxels.

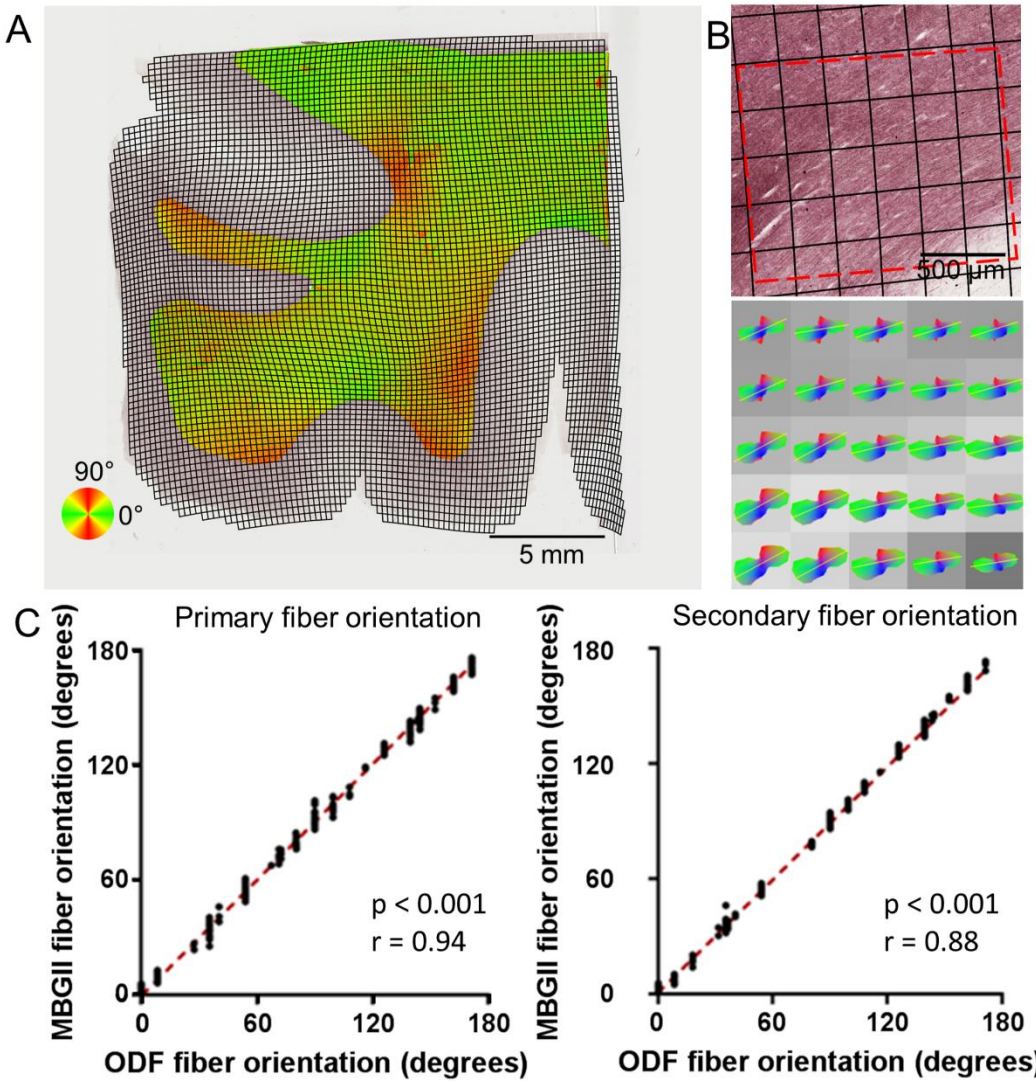

Figure 3.7 Correlation of diffusion based and histologically based fiber orientation. A. Fitting two tensors to the power spectrum of each white matter voxel-registered ROI resulted in a directionality map, where the color of each registered region of interest represents the orientation of the primary fiber population. **B.** Directionality comparisons could then be directly made by comparing the histologically derived fiber orientation from the Myelin Black Gold II with the GQI derived orientation. **C.** There was a strong nearly one-to-one linear relationship between the quantitative histological metric and the GQI data (red line indicates line of identity). Orientations calculated from the ODFs resulted in discrete bins due to the finite angular resolution of the GQI data (202 directions) on the x-axis, while the Black Gold II based fiber orientations were a continuous measure. Therefore, a one-tailed Spearman's correlation was used, resulting in p values < 0.001 for both primary and secondary major fiber components.

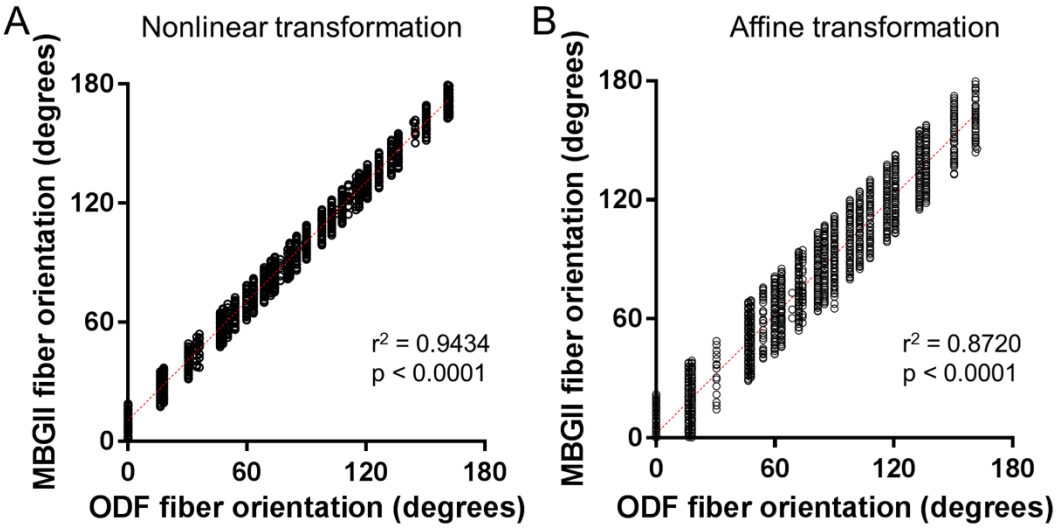

Figure 3.8 Performance of nonlinear vs affine transformations when correlating fiber orientation. A. Nonlinear transformation results in a strong correlation ($p < 0.0001$, $r = 0.94$) of ODF derived vs Black Gold II derived primary fiber orientations. Red line indicates line of identity. **B.** Affine transformation of the same data results in a strong correlation ($p < 0.001$, $r = 0.86$), but the distribution of Black Gold II fiber orientation in each ODF bin is wider compared to the results of the nonlinear transformation. A difference test shows that the correlation of the primary fiber orientations resulting from a nonlinear transformation is superior to the correlation resulting from an affine transformation. The maximum difference between the primary in plane peak of the ODF and the secondary in plane peak of the ODF was 153.73°.

3.3.4 Limitations of spatial and angular resolution on radiological-pathological correlations

To assess the effects of spatial resolution on the correlation between diffusion derived and histologically derived fiber orientation, Black Gold II stained sections were registered to corresponding GQI diffusion data that was downsampled to either 500 µm or 1000 µm isotropic resolution. At these spatial resolutions, the relationship between GQI based and Black Gold II based primary fiber orientations using the two tensor fit resulted in limitations when calculating histologically based fiber orientation (**Figure 3.9**), particularly at 1000 µm isotropic resolution with a low correlation ($r = 0.35$).

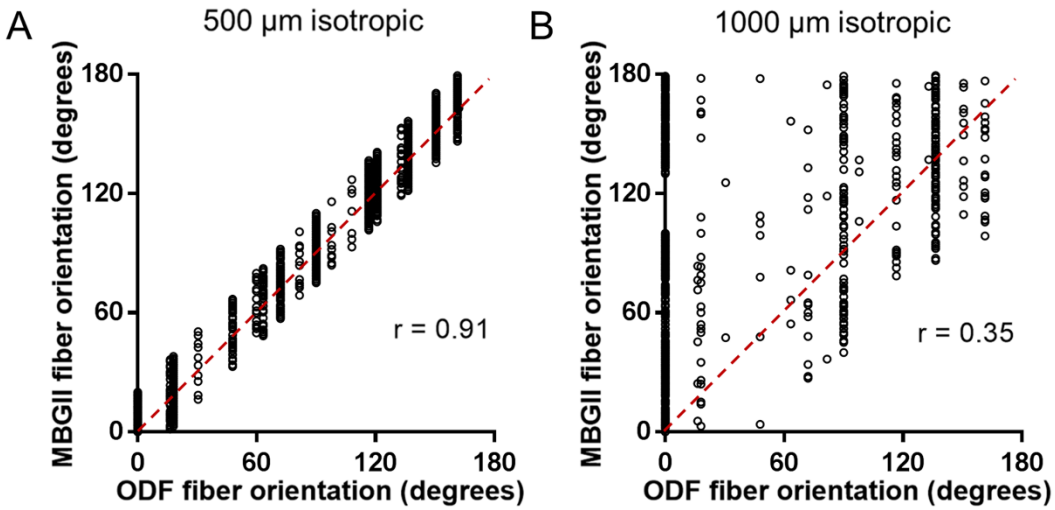

Figure 3.9 Relationship between spatial resolution and fiber direction correlations. A. Comparison of ODF derived and Black Gold II derived fiber orientations at 500 µm isotropic resolution in complex cortical white matter continues to show a strong correlation (r = 0.91) but the distribution of histologically based fiber orientations is broader for each bin, indicating that a two tensor fit may not be able to account for the increased voxel wise white matter heterogeneity. Red line indicates line of identity. **B.** Comparison of ODF derived and Black Gold II derived fiber orientations at 1000 µm isotropic resolution shows a low correlation (r = 0.35), where the ability to implement the 2D FFT to discern between simple, crossing, and disrupted white matter is lost, showing the limitations of a two tensor model. Red line indicates line of identity.

The importance of angular resolution was tested by coregistering Black Gold II stained sections to corresponding DTI data using the original MRI spatial resolution (250 µm in plane). The DTI based fiber orientations were calculated on a voxel-wise basis and compared with fiber orientations derived from corresponding histological data. The tissue block used for this analysis was composed of 4.40% simple white matter and 22.6% complex white matter only with in plane fiber components. 12.11% of the voxels in the tissue block were classified as having one or more major 3D fiber components, and the remaining 60.89% voxels were classified as gray matter. Assessments of the relationship between fiber orientation derived from a low angular resolution diffusion tensor model (30 directions) resulted in low correlations in both simple (r=0.41) and complex (r=0.53) white matter (**Figure 3.10A-B**). Similarly, correlations of DTI based and Black Gold II based fiber orientations resulted in low correlations in both simple (r=0.42) and complex

(r=0.54) white matter (**Fig. 10C-D**) when implementing DTI reconstruction using diffusion data with an angular resolution matching that of the GQI data.

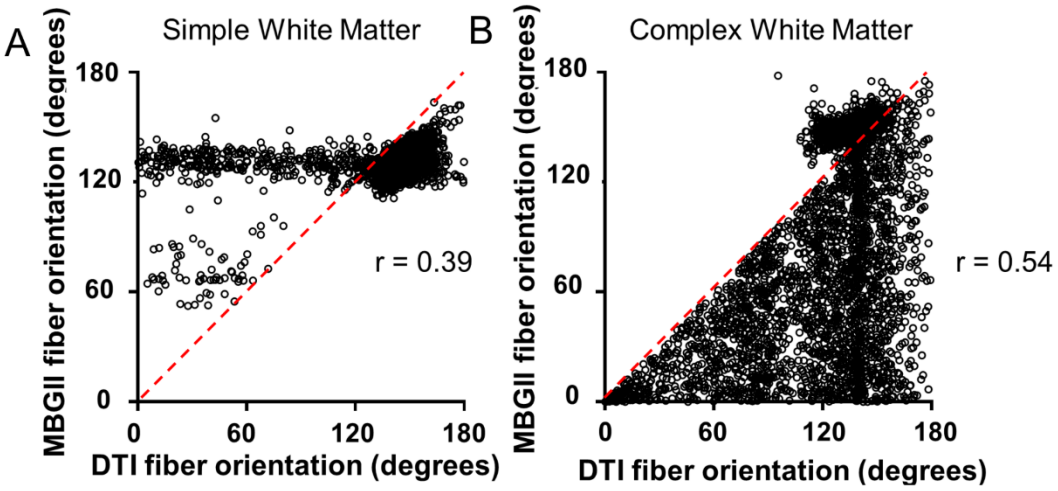

Figure 3.10 Fiber direction correlations in a single tensor model. A. DTI derived fiber orientation based on low angular resolution diffusion data (30 directions) vs. Black Gold II derived fiber orientation shows a low correlation (r=0.41) in simple white matter, defined based on GQI data as having only one fiber population. 4.40% of the total voxels in the tissue block were classified as simple white matter. Red line indicates line of identity. **B.** Comparison of DTI and Black Gold II derived fiber orientations in complex white matter, defined based on GQI data as having two fiber populations shows a modest correlation (r=0.53). 22.60% of the total voxels in the tissue block were classified as complex white matter.. **C.** DTI derived fiber orientation based on high angular resolution diffusion data (202 directions) shows a low correlation (r=0.42) with Black Gold II derived fiber orientation in simple white matter. **D.** DTI derived fiber orientation shows a modest (r = 0.54) correlation with Black Gold II derived fiber orientation in complex white matter. The correlations are not affected by using increasing angular resolution, indicating that the single tensor assumption of DTI is not sufficient when modeling voxels with more than one fiber population.

3.3.5 Assessment of fiber integrity using power coherence

To demonstrate the potential utility of the fully coregistered approach, the power spectrum calculated from the voxel-wise two dimensional Fourier transformation was also used to assess the degree of fiber organization, and whether fiber disorganization could be quantitatively distinguished from crossing fibers. The measure of power coherency was calculated for each voxel classified as white matter based on Myelin Black Gold II staining. Power coherency was calibrated to remain between 0 and 1, where a higher power coherency

reflects increased fiber organization. Conversely, decreased power coherency reflects decreased directionality within a registered ROI, and therefore decreased fiber organization. In voxels where fiber components were either fully in plane or had a primary z axis component of less than 45°, we were able to readily distinguish regions of simple, crossing, and disrupted fibers when analyzing white matter adjacent to cortical sulcal depths (**Figure 3.11**). Voxels with simple and crossing fibers had power spectra that spread across narrow ranges of spatial frequencies, reflecting intact fiber integrity with strong directional components. Voxels with disrupted fibers had power spectra that spread across a broad range of spatial frequencies, reflecting reduced fiber integrity with fibers distributed in random orientations.

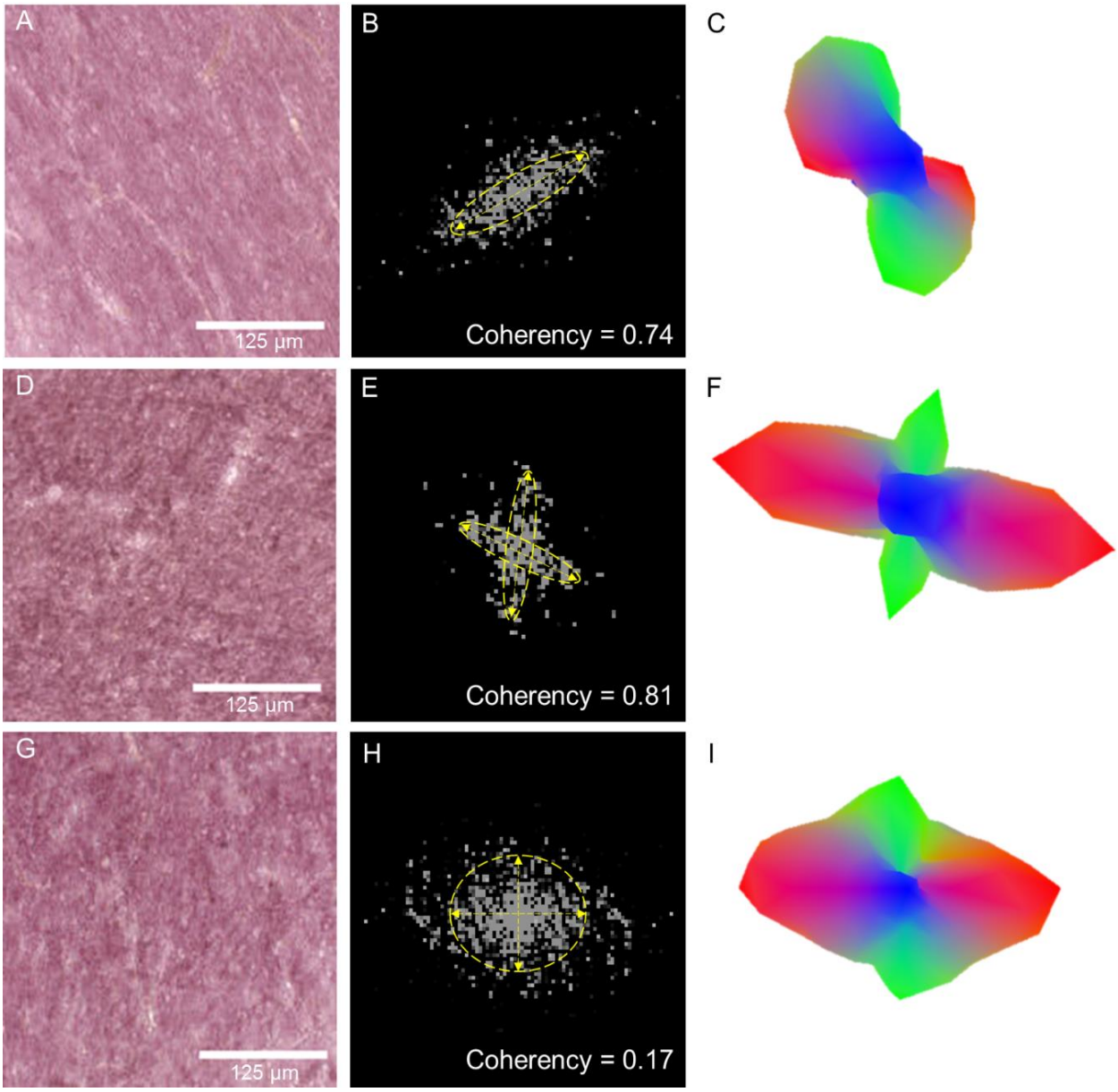

Figure 3.11 Power coherence distinguishes between complex vs. disrupted white matter. A. Black Gold II stains myelinated fibers aligned in one orientation. **B.** The power spectrum reflects the strong directional component and coherent fiber architecture (power coherency = 0.74). **C.** The ODF of the coregistered voxel from GQI shows that the white matter fibers in this tract all lie along one direction. **D.** Black Gold II stained examples of crossing fibers. **E.** The power spectrum of these crossing fibers shows two strong directional components, each fitted with two narrow tensors (power coherency = 0.81). **F.** The crossing tracts are apparent in the voxel coregistered to this region, reflected by the two sharp peaks of the function. **G.** Black Gold II stain in a region with disrupted fibers. **H.** The disorganization of the fibers is reflected in the power spectrum, where there is no strong directional component in any direction, resulting in low coherency (power coherency = 0.17). **I.** The ODF from the coregistered voxel reflects the broader spread of directionalities that is observed in the power spectrum of the histological data.

Because the human tissue used for this study had known CTE pathology with prior history of concussive injury, we also tested whether power coherence would be able to distinguish between uninjured white matter and a positive control of axon injury. This was performed in a mouse model using a 2 mm controlled cortical impact (CCI) injury as previously described by Brody et al. (2007) (Brody et al., 2007). White matter in the corpus callosum ipsilateral to the injury site showed reduced power coherence compared to the corresponding region of interest in an uninjured animal (**Figure 3.12**).

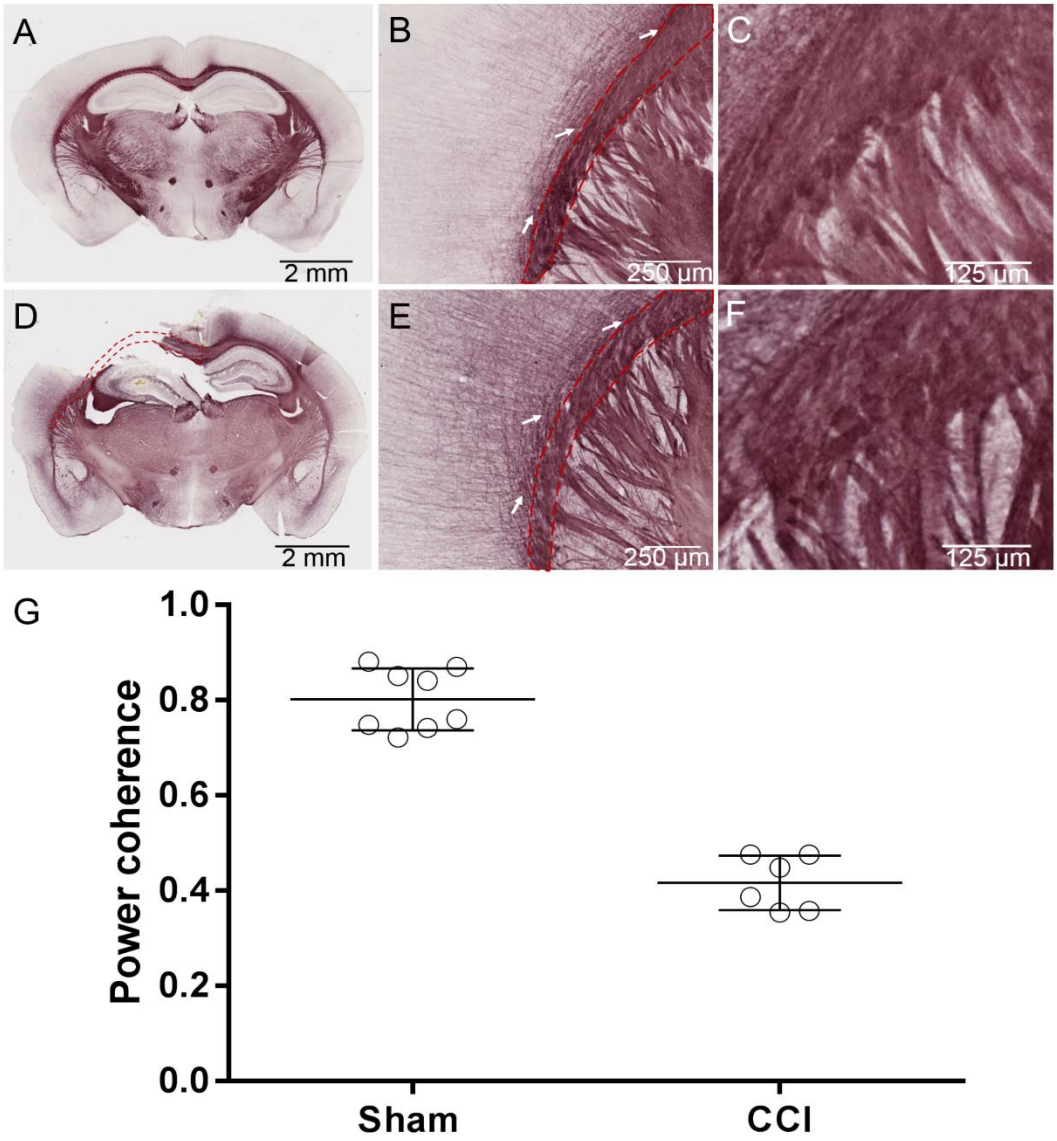

Figure 3.12 Power coherence in a mouse model of traumatic brain injury as a positive control. A. 50 µm thick sections from an uninjured mouse brain were stained for myelin using Black Gold II. A region of interest was drawn to include the corpus callosum, restricted to the genu, anterior forceps and external capsule bound by the midline and the lateral edge of the cingulum on the hemisphere ipsilateral to injury for multiple sections (red line). **B.** Fibers, indicated by white arrows, appear to be curving normally throughout the region. **C.** A high power view of the white matter in the corpus callosum shows that there are no irregularities in fiber organization. **D.** 50 µm thick sections from a positive control (2 mm CCI injury) mouse model of traumatic brain injury were stained for myelin using Black Gold II. A region of interest ipsilateral to the injury site that includes the corpus callosum was drawn for each section (red line). **E.** Fibers, indicated by white arrows, show signs of disruption both in the corpus callosum and as they branch into cortical gray matter. **F.** The high power view of the white matter adjacent to the injury site shows disruption of the underlying fibers. **G.** Power coherence of regions of interest from adjacent sections of both the uninjured and CCI injured mouse was calculated as described in Appendix I. As expected, white matter ipsilateral and close to the injury site in the injured mouse shows signs of disruption, reflected by reduced power coherence. In contrast, white matter in the corresponding region of interest of the uninjured mouse shows consistently high power coherence, reflecting preserved fiber integrity.

To test whether spatial resolution limits the ability to measure power coherence in complex human white matter, Black Gold II stained sections were registered to corresponding diffusion data that was downsampled to either 500 µm or 1000 µm isotropic resolution. Power coherence was calculated in regions of interest defined as extending 2 mm into white matter adjacent to sulcal gray matter. At 250 µm, the heterogeneity of these white matter regions was apparent by the large variance of the voxel wise measures of power coherence (**Figure 3.13**). However, as spatial resolution was decreased, both to 500 µm and 1000 µm, there was an observed reduction in the amount of variance of voxel based power coherence, while the mean power coherence did not change. A one-tailed F-test to assess a decrease in variance resulted in significance both when comparing a decrease from 250 µm to 500 µm ($F_{(1185,395)} = 5.43$, $p < 0.001$) and 250 µm to 1000 µm ($F_{(1185,79)} = 1.53$, $p< 0.001$).

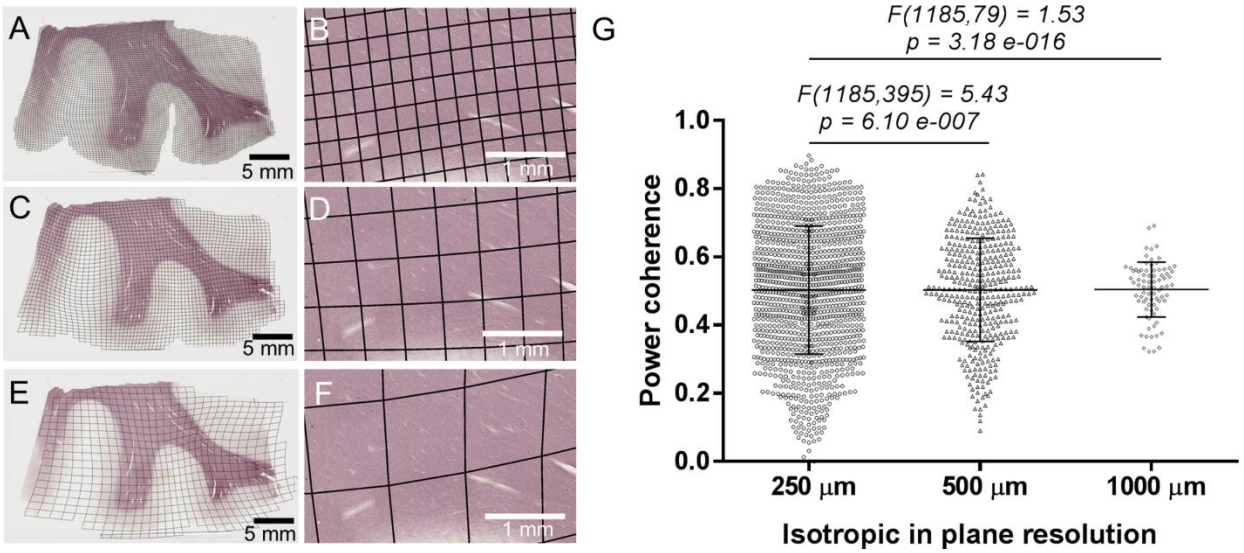

Figure 3.13 Effect of voxel size on estimations of white matter heterogeneity. A. Voxel-based grids were generated at 250 µm isotropic in plane resolution. **B.** White matter adjacent to sulcal gray matter within a region of interest extending 2 mm into white matter was analyzed for voxel-wise power coherence. **C.** Voxel-based grids were generated at 500 µm isotropic in plane resolution based on landmarks placed on downsampled MRI data. **D.** A 2 mm region of interest of white matter adjacent to sulcal gray matter was analyzed for voxel-wise power coherence. **E.** Voxel based grids were generated at 1000 µm isotropic in plane resolution based on landmarks placed on downsampled MRI data. **F.** The same 2 mm region of interest was analyzed for voxel-wise power coherence. **G.**

High in plane spatial resolutions of 250 µm show a large variation in power coherence in white matter adjacent to sulcal gray matter. This region of interest may contain a range of severities of disrupted vs. intact fibers, which should span the range (0-1) of power coherence. As isotropic in plane spatial resolution decreases to 1000 µm, the variation in power coherence is reduced ($F = 1.53$, $p<0.001$), indicating that low spatial resolutions may underestimate the heterogeneity of complex white matter regions.

3.4 Discussion

In summary, we have developed a histology to MRI image coregistration workflow that can be applied to explore the neuropathological features that drive MRI signal changes in the brain. This method is not limited to diffusion MRI, and could be applied to various other imaging modalities, provided that there is a corresponding structural image dataset for the basis of registration. Registration results in voxel-based grids that are highly robust due to shifting landmarks, highly sensitive when parceling tissue types, and show strong accuracy when correlating histologically derived measures with MRI parameters. Furthermore, our registration provides an efficient approach to perform arbitrary region of interest based analysis, with manually drawn regions from histology automatically referenced to corresponding MRI voxels. In this study, the agreement between histological and diffusion based fiber orientations was used throughout as the primary means of validating coregistration accuracy on a voxel wise basis. Prior comparisons of directionality have been performed both in human and mouse tissue, calculating histologically based fiber direction using a Fourier transformation or gradient based approach (Budde and Annese, 2013; Budde and Frank, 2012; Budde et al., 2011; Nazaran et al., 2016), and validating DTI based tractography at high resolutions. At similar spatial resolution, we found that the fiber orientation derived from DTI tensors did not reflect underlying fiber architecture, particularly in complex white matter regions, at both coarse and high angular resolutions. This finding indicates that alternative local reconstruction methods that do not rely

on a single tensor assumption are necessary to accurately perform tractography. Because our intent is to perform correlations primarily in cortical tissue which has a complex fiber architecture, we turned to more advanced diffusion methods which could still produce measures of fiber orientation. GQI based ODF peaks were used here as this metric because in white matter, each ODF is been directly calculated based on water displacement (Yeh et al., 2010) compared to alternative q-space methods such as diffusion spectrum imaging, which often requires additional filtering to counter cutoff effects in the frequency domain (Hagmann et al., 2006). The GQI reconstruction method is therefore able to compensate for rapid changes in fiber orientation in complex white matter between voxels. Consequently, correlations proved to be most robust when comparing fiber orientations calculated using the GQI reconstruction method. Fundamentally, these correlational studies would not have been successful without careful optimization of the method parameters, such as spatial resolution and choice of histology-MRI transformation.

A primary advantage of our coregistration approach is that histological parameters for correlation can be based on high resolution digital image of histology, so analysis is not limited to area fraction of positive staining. For example, in this study, we compared fiber orientation on a voxel-wise basis in both simple and complex white matter regions to validate the registration technique, which would not have been possible in downsampled histological data that is compressed to match MRI resolution. When applied to analysis of additional histological markers, such as immunostaining for hyperphosphorylated tau, injured axons, and activated astrocytes or microglia, we can explore morphological features of neuropathological markers, such as circularity, and randomness of cells within regions of interest that correspond to voxels in MRI space. This may provide increased specificity in radiological-pathological correlations

for both gray and white matter pathology which contain multiple cellular components that may contribute to the diffusion MRI signal (Edgar and Griffiths, 2014; Le Bihan, 1995).

Our derived measure of power coherence also reflects an advantage of high resolution histological analysis. When exploring axon injury at acute time points, markers such as Myelin Basic Protein (MBP) and β-APP have been successful (Blumbergs et al., 1989; Blumbergs et al., 1994; Johnson et al., 2013; Ryu et al., 2014) while chronic white matter demyelination has been used as a metric of injury in severe cases of traumatic brain injury (Strich, 1956), and multiple sclerosis (Wang et al., 2015). For both cases, the primary quantitative metric is area fraction of positive staining. In the CTE cases that we have examined, there was no detectable staining for markers such as β-APP or compacted neurofilament (not shown); such staining may not be detectable in the chronic phase of injury which is years after the initial insults to tissue (McKee et al., 2009b; Stern et al., 2013). Similarly, Bennett et al. determined that β-APP was unable to distinguish between uninjured and injured mice in a mouse model of repetitive concussive injury, suggesting a different mechanism of axonal injury (Bennett et al., 2012). Stains such as Black Gold II for myelin do show demyelination, again in severe cases of white matter injury (Savaskan et al., 2009). As an alternative to demyelination and decreased area fraction of staining, power coherence is applicable when examining fibers that are disrupted due to residual effects of axon injury. Coherence shows evidence of chronic white matter injury, which has been found as late as 60 days following repetitive traumatic brain injury in a mouse model (Donovan et al., 2014). Furthermore, coherence is advantageous because of its ability to differentiate between complex fibers and injured fibers, a well-known dilemma encountered in the single tensor model of diffusion imaging (Arfanakis et al., 2002; Behrens et al., 2014; Pierpaoli et al., 1996). The single tensor model used in DTI results in complex fibers and injured fibers being

indistinguishable by metrics such as fractional anisotropy (Arfanakis et al., 2002; Behrens et al., 2014; Yeh et al., 2010) but readily addressed with GQI and other more advanced diffusion imaging methods (Yeh et al., 2010). Application of power coherence to histological measures may be able help to resolve the interpretation of diffusion imaging signals in otherwise ambiguous situations, particularly in regions where injury occurs in white matter regions that have crossing fibers.

A second major advantage of this study is the high quality of the diffusion MRI data, notably the high spatial resolution (250 μm x 250 μm in plane) and high angular resolution of the GQI data (202 directions). The optimized spatial and angular resolutions were key during the validation by comparing fiber orientation on a voxel-wise basis. Our method of calculating fiber orientation using the two dimensional Fourier transform was successful because of its ability to discern between crossing and simple fiber populations at these high spatial resolutions. Implementation of a two dimensional Fourier transformation, which does not take into account the fiber orientation of the surrounding voxels was also complementary to the GQI reconstruction method, where fiber orientations within a single MRI voxel are based solely on the diffusion of water within that single voxel. At lower spatial resolutions, such as those approaching clinically feasible levels, application of the Fourier transformation to validate tractography would be challenging in complex white matter regions (Budde and Frank, 2012; Budde et al., 2011). Furthermore, the measure of power coherence used here to distinguish between disrupted and crossing fibers would no longer be applicable due to signal averaging within a larger voxel volume. We have shown that the true heterogeneity of cortical white matter is lost at lower resolutions, a factor which must be considered if performing radiological pathological correlations in a disease where the primary pathology is located in such complex

white matter regions. While this finding is not surprising, it does make explicit the need for either alternative imaging modalities that can provide clinically achievable high spatial resolutions, or the development of an injury specific imaging marker which would allow for more sensitive diagnostic imaging at current spatial resolutions.

We must also consider the limitations of our registration method. First, manual landmark placement is an inherent source of variability in registration, and would be increasingly difficult at low resolutions where the gray/white matter boundary and anatomical features become less visually salient (Choe et al., 2011). An additional confound of our landmark based registration method is that registration is most accurate in a region with a high density of landmarks, and may be more prone to errors in regions with sparse landmark placement, or in regions far away from the landmarks. Therefore, further validation steps should be considered, such as evaluating the accuracy of registration as a function of distance from landmarks placed along the gray/white matter boundary and tissue boundary. Second, because the workflow is a two dimensional registration, any correlation analysis that uses our technique is limited to in plane histological features. When considering three dimensional histology to MRI registration, parameters such as inter-slice sampling interval and tissue sectioning thickness would need to be optimized (Absinta et al., 2014; Breen et al., 2005b; Goubran et al., 2013; Zarow et al., 2004) because of rapid changes in tissue architecture between slices. At high spatial resolutions and small slice thicknesses, validation of three dimensional histological registration could then be performed using three dimensional structure tensor analysis (Schilling et al., 2016). Despite this possibility, the z-axis changes between MRI slices may not be able to be sufficiently accounted for using current imaging resolutions, particularly in human cortical tissue where sulci change or even disappear within our current 500 μm slice thickness. These rapid z-axis changes would create

challenges when attempting to register and match histological sections with the associated MRI slices. Our current validation method of determining the correlation of fiber direction is therefore only valid when considering features that are in the histological plane. While there may be agreement between in plane fiber orientations, the strongest evidence of robust 3D coregistration would be correlation of fibers that have a primary directional component along the z-axis. Aligned to the issue of three dimensional coregistration and validation is the application power coherence to distinguish between disrupted white matter and fibers that are perpendicular to the plane of histology. In this study, we limited our analyses to voxels with in plane major fiber components, using GQI data to identify voxels with primary or secondary fiber components perpendicular to the plane of histology. Without this exclusionary criteria, using power coherence is not sufficient to distinguish between disrupted and intact white matter which is out of plane. Using a technique such as serial two photon microscopy, where the tissue section is imaged below the block surface before sectioning would prevent the issues of z-axis warping that commonly occurs in the serial sectioning method that we have used here (Amato et al., 2016). Alternatively, an approach such as CLARITY (Chung and Deisseroth, 2013) combined with a stain for myelinated fibers would be able to distinguish between out of plane, intact and disrupted white matter. Third, while we have been able to show that complex fiber orientations can be discerned using quantitative histology methods, there may be a dependency, yet to be characterized, on the quality of the *ex vivo* tissue, fixation methods, and post-mortem interval. Finally, while our coregistration has been extensively validated in white matter, this approach has not been fully validated for complex gray matter.

The most immediate applications of our registration method are in the field of radiological-pathological correlations in CTE (Holleran et al., 2015), exploring the relationship

between multiple immunohistochemistry stained markers and associated advanced diffusion MRI metrics. The workflow is also applicable to analysis *in vivo* using animal models of concussive injury, by scanning living animals and performing registration and subsequent correlation after sacrificing the animals. Because we have shown that histology-MRI registration is highly robust in human tissue, *ex vivo* correlation studies may potentially be conducted in cases of acute traumatic brain injury, where pathology is drastically different compared to chronic cases. Further applications of this method could be extended to *ex vivo* correlations in Alzheimer's Disease, frontotemporal dementia, or Parkinson's disease (Suri et al., 2014), where the neuropathology is distinct but the effect on traditional and advanced diffusion MRI metrics needs to be further elucidated.

Acknowledgements

We would like to acknowledge the donors and their families who have made this work possible. The studies presented in this work were carried out, in part, using Small-Animal MR Facility of the Mallinckrodt Institute of Radiology, Washington University. We would also like to thank Tao Ju and Terrance Kummer for helpful discussion when developing thorough validation methods for the proposed coregistration technique. We also thank Justin P. Haldar for his implementation of the Hamming filter using Matlab.

Funding Sources

This work is supported by the National Institutes of Health [NIHUO1 NS086659]; the Hope Center Alafi Neuroimaging Laboratory at Washington University in St. Louis [P30 NS057105].

Chapter 4. Reduced white matter disruption correlates with fractional anisotropy in chronic traumatic encephalopathy

4.1 Introduction

Chronic traumatic encephalopathy (CTE) is a progressive tauopathy that has been increasingly diagnosed in patients who have a history of repetitive brain trauma (Mez et al., 2017). A definitive diagnosis of CTE can only be performed using gold standard immunohistochemistry methods to identify phosphorylated tau (pTau) accumulated as neurofibrillary tangles (NFTs) and tau positive astrocytes (McKee et al., 2016; McKee et al., 2009a). However, identification of these features alone is insufficient to provide a specific diagnosis; the distribution of pTau pathology is used to distinguish CTE from other tauopathies such as Alzheimer ’s disease (AD) and frontotemporal lobar dementia (FTLD). In early stages of CTE, NFTs and tau positive astrocytes are typically found aggregated locally in perivascular regions and in the depths of cortical sulci, most commonly in the frontal, temporal and parietal cortices (McKee et al., 2015a). This pTau pathology progressively spreads, and in late stages, NFTs and astroglial tau are found increasingly in the superficial cortical layers in the superior and inferior regions of the frontal, temporal and parietal cortices as well as in the hippocampus, amygdala and hypothalamus (McKee et al., 2015a). In contrast, astroglial tau is rarely found in cases of AD, and neurofibrillary tangles are diffusely distributed in both superficial and deep

layers of the entorhinal cortex, later spreading to inferior frontal and parietal cortices (Braak and Braak, 1995; Hof et al., 1992). Astroglial tau is more commonly found in cases of FTLD, but similar to AD, these tau positive cells are diffusely distributed in cortical layers (Cairns et al., 2007).

Although the morphology and distribution of pTau pathology clearly distinguishes between tauopathies, such investigations can only currently be performed post-mortem. Therefore, a noninvasive biomarker specific for pTau pathology would prove to be valuable not only in providing a specific diagnosis of CTE, but also to provide prognostic information in living patients. While multiple imaging modalities are being explored for this purpose, diffusion MRI has been proposed as an attractive candidate because of its potential to detect specific microstructural changes in brain tissue. The most established model, diffusion tensor imaging (DTI) has revealed abnormalities in the white matter tracts of patients with a history of concussive brain trauma (Mac Donald et al., 2017; Manning et al., 2017; Multani et al., 2016). However, the primary downfall of DTI, particularly in complex cortical tissue and gray matter structures, is the assumption that water diffuses in a Gaussian manner along a single direction, driving the need for more advanced diffusion models. Techniques such as generalized q-sampling space imaging (GQI) directly quantify the direction and diffusivity of water along multiple directions within a single voxel. Such imaging methods are capable of resolving complex white matter structures, both in living patients and in post mortem studies of human brain tissue (Fan et al., 2014; Gangolli et al., 2017; Mollink et al., 2017). While GQI would provide useful information about changes in complex white matter, the most direct approach to diagnosis CTE *in vivo* would be a biomarker of pTau pathology, most commonly present in gray matter. Diffusion kurtosis imaging (DKI), which uses high b-values to quantify the non-

monoexponential decay of the diffusion signal, has been proposed as a potential tool to more sensitively quantify microstructural alterations in gray matter (Helpern et al., 2011; Jensen and Helpern, 2010; Jensen et al., 2005). DKI in patients who had previously sustained a concussive brain injury revealed reductions in mean kurtosis of the thalamus at time points up to nine years post injury (Grossman et al., 2012; Naess-Schmidt et al., 2017). Despite these advances in diffusion imaging, the exact relationship between changes in DTI, GQI or DKI based metrics and CTE related tau pathology remains unclear. Studies to better understand this relationship must be performed in humans because there is currently no animal model that consistently recapitulates the progressively worsening pTau lesions that are pathognomic of CTE (Turner et al., 2015b). Therefore, radiological-pathological correlations in tissues with known pTau pathology would answer the question of whether diffusion imaging methods are capable not only of sensitively detecting such lesions, but also of providing a specific diagnosis of CTE.

We previously performed high spatial resolution radiological-pathological correlations in *ex vivo* tissues with a definitive diagnosis of Stage III/Stage IV CTE (Holleran et al., 2017). In this study, there was no correlation of tau pathology with diffusion-based metrics. However, we found that fractional anisotropy was modestly correlated with microstructural white matter disruption measured using power coherence. Moreover, white matter adjacent to tau laden cortical sulci had reduced fiber integrity, indicating a possible relationship between white matter injury and aggregation of tau in nearby gray matter. These findings, while compelling, require additional investigation in tissues with reduced post mortem intervals and repetition in a cohort where the investigators are blinded to the tissue diagnosis. Furthermore, it remains unknown whether the white matter fiber disruption is an exclusive result of chronic axonal injury, or is also related to chronic astrogliosis in white matter. To provide further evidence of our

hypothesis, we have performed similar radiological-pathological correlations in tissues with post mortem intervals less than twenty four hours. These correlations were also performed in tissues with a diagnosis of AD or FTLD to investigate the hypothesis that white matter disruption is linked to specifically to CTE tau pathology and does not generalize across tauopathies.

4.2 Methods

4.2.1 Tissue samples

Ten tissue samples from the superior frontal cortex (Brodmann Area 8/9) with confirmed pathological diagnoses of Stage III/IV CTE, FTLD, or AD were obtained from the VA-BU-CLF bank (**Table 4.1**). Neuropathological evaluation was performed at the Boston University School of Medicine. Next of kin provided written consent for study participation and brain donation. All tissue samples were stored in periodate-lysine-paraformaldehyde (PLP) fixative. Investigators performing MRI data acquisition, histopathology, and correlation analyses were blinded to the tissue pathological diagnoses of all tissue blocks.

4.2.2 Magnetic resonance image acquisition

Prior to data acquisition, meningeal layers and blood vessels were removed from each tissue sample to prevent air bubble formation as well as to prevent iron-induced artifact from residual blood in the bloods vessels. In order to minimize formalin induced reduction of T2 relaxation times, excess fixative was removed by equilibrating the tissue blocks in 1x PBS with 0.1% sodium azide at 4°C for two weeks, changing the PBS solution every three days. One day prior to MRI data collection, tissue blocks were placed in a custom made syringe with Fluorinert to prevent proton induced imaging artifact and stored overnight at room temperature.

MRI data was acquired using an 11.74T Agilent MRI scanner as previously described (Gangolli et al., 2017; Holleran et al., 2017). Briefly, a 2D spin echo sequence was implemented to provide 250 μm isotropic in-plane spatial resolution with 500 μm slice thickness. Diffusion gradient δ was 5ms and diffusion time Δ was 15ms. Gibbs ringing artifact was removed by applying Hamming filtering to all datasets. TR times greater than 1000 ms were empirically determined to result in steady state signal in white matter (Gangolli et al., 2017).

DTI data was collected using 30 diffusion weighted gradients with a b value of 4000 s/mm^2 and four images with a b value of 0 s/mm^2, TR/TE = 1200/30 ms, resulting in a total scan time of 1.5 hours (**Table A.2**). DTI image processing was performed in Brain Suite (Shattuck and Leahy, 2002), using a weighted log-linear estimation.

GQI data was collected using 202 diffusion weighted directions, with a maximum b value of 8,000 s/mm^2 and ten non-diffusion weighted images (b = 0 s/mm^2) and TR/TE of 1400/30ms for a total scan time of 11 hours (**Table A.3**). GQI data was reconstructed using DSI studio (http://dsi-studio.labsolver.org) and thresholded to remove background noise using the non-diffusion weighted image. GQI based parameters were calculated using a balanced scheme (0.7 diffusion sampling length ratio, three fiber orientations in a voxel).

DKI data was collected using 30 diffusion weighted directions across five b-values (2000, 4000, 6000, 8000 and 10,000 s/mm^2) with TR/TE = 2000/30ms for a total scan time of 11 hours (**Table A.4**). Kurtosis parameters were calculated using DKE estimator (Tabesh et al., 2011). For all diffusion datasets, thresholding to remove background noise was performed by using the unweighted (b = 0/mm^2) diffusion dataset. MRI slices selected for coregistration and correlation analyses were examined for partial volume artifact; slices in which sulcal depths were prone to partial voluming were excluded from analyses.

4.2.3 Tissue sectioning

Following MRI data acquisition, tissue blocks were stored at 4°C in 10% neutral buffered formalin for one week. To prevent ice crystallization during sectioning, tissue blocks were then placed in 30% sucrose solution for an additional week. Tissue sectioning was performed on a freezing sliding microtome, with the gradient echo multi-slice image planning used to guide tissue block placement and orientation. Tissues were sectioned into 50 µm thick sections in a 1:5 series and stored in individual wells to maintain order of z-axis location. This eliminated the potential of data bias (250 µm inter-section distance) when quantifying histology while preserving the ability to perform correlations with the thicker MRI slice (500 µm).

4.2.4 Histopathology

Monoclonal antibody AT8 (pSer202, Thre205 mouse anti-human, ThermoFisher Scientific) was used as previously described (Holleran et al., 2017) to stain for phosphorylated tau immunoreactivity (**Figure 4.1**). Monoclonal GFAP was used to stain for reactive astrocytes (mouse anti-human Millipore, MA). Tissue sections were washed of excess cryprotectant using 1xTBS, followed by antigen retrieval (pTau: five minutes in 70% formic acid, GFAP: three minutes in 90°C sodium citrate buffer pH 6.0). Endogenous peroxidase activity was quenched using 3% hydrogen peroxide. Sections were blocked in 3% normal goat serum diluted in TBS-X, followed by overnight incubation in primary antibody diluted 1:1000 in 3% normal goat serum at 4°C. The next day, sections were incubated for one hour in biotinylated goat anti-mouse secondary antibody at 1:1000 dilution, followed by another hour in avidin-biotin horseradish peroxidase complex (Vectastain Elite ABC HRP Kit, Vector Laboratories, Burlingame, CA), diluted 1:400 in 1xTBS. Incubation of sections for five minutes in a solution of 3-3’

diaminobenzidine (Sigma-Aldrich, USA), hydrogen peroxide and 4% nickel chloride was used to visualize pTau and astrocytes. Cell nuclei were detected by incubating sections in Harris Hematoxylin counterstain followed by differentiation in 0.25% acid alcohol to remove excess staining. A negative control for each tissue block was performed by excluding primary antibody and incubating overnight in blocking serum.

Myelin Black Gold II was used to stain for myelinated white matter in tissues as previously described (Gangolli et al., 2017). Free floating tissue sections were washed of excess cryoprotectant in 1xTBS, followed by incubation in 3% Black Gold II solution (Millipore, MA) heated to 60°C for 8-12 minutes until staining was complete. Excess staining was removed by incubation of sections for three minutes in 1% sodium thiosulfate also heated to 60°C

All tissue sections were mounted on positively charged glass slides and allowed to dry overnight at room temperature. Slides were then dehydrated in a series of graded ethanols, cleared using xylenes, and coverslipped with glass slips using mounting medium.

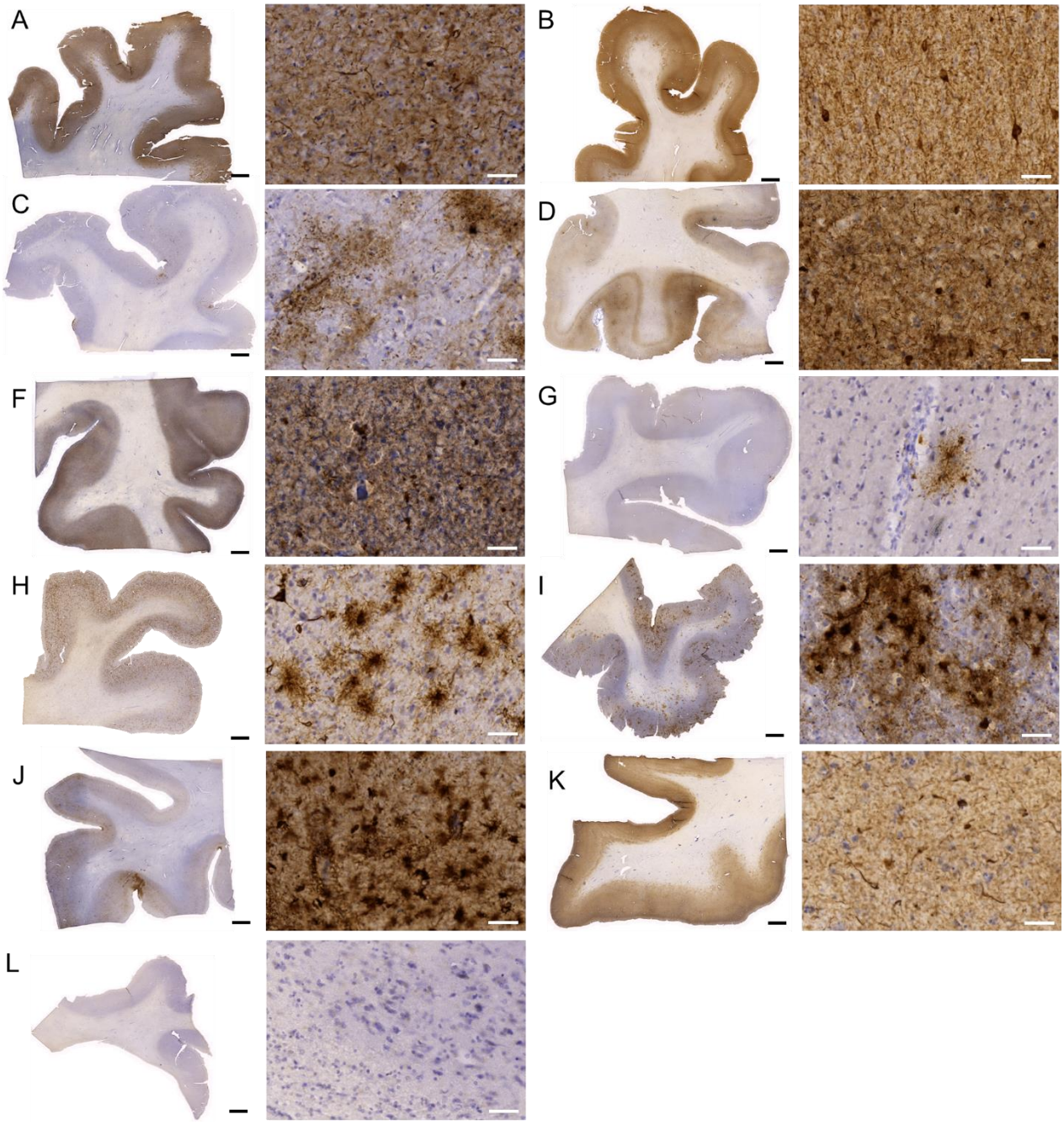

Figure 4.1 Immunohistochemical detection of phosphorylated tau. A-K. Hyperphosphorylated tau was detected using monoclonal AT8 in 50 µm sections. Following staining and visualization with DAB, tissues were mounted on positively charged slides and allowed to air dry overnight. Once dry, sections were counterstained with Harris Hematoxylin. **L.** A negative control, with no overnight incubation in primary antibody was included for each tissue block to control for off-target binding. Low power scale bar = 2mm, high power scale bar = 500 µm.

4.2.5 Acquisition of histopathological images

Digital images of all stained tissue sectioned were acquired on a Zeiss Axioscan Z1 automated slide scanning system (Zeiss Microscopy) using a 20x objective. These images were then converted from CZI to tiff format using Zen (Zeiss Microscopy), downsampling to 30% of the original image resolution. Color deconvolution was performed in FIJI (NIH, Bethesda MD), producing DAB and hematoxylin based images for each tissue section.

MRI-histology coregistered grids were derived for each tissue section as previously described (Gangolli et al., 2017; Holleran et al., 2017). Briefly, a minimum of 55 landmarks were placed on tissue edges and the gray/white matter boundary of histological images (AT8, GFAP, Myelin Black Gold II). Landmarks were placed by raters blinded to pathological tissue diagnosis. Furthermore, for AT8 and GFAP stained tissue sections, raters were blinded to the presence of pTau or reactive astrocytes by using the corresponding hematoxylin images for landmark placement. A custom Matlab script (Mathworks 2017b) was implemented to apply a nonlinear least squares transformation, converting the histological image to MRI space. An inverse transformation was then applied to each voxel of the transformed histological image, resulting in a grid of regions of interest (ROIs), with each region corresponding to a single MRI voxel.

ROIs were drawn on the hematoxylin component of each image by raters blinded to the pathological tissue diagnoses. ROIs included (1) depths of cortical sulci, defined as extending 1 mm from the deepest point of the sulcus, extending to the gray/white matter boundary, and (2) white matter adjacent to sulcal depths, defined by starting at the gray/white matter boundary and extending 0.5 mm into the adjacent white matter (**Figure 4.2A-C**).

4.2.6 Quantification of histopathology

Phosphorylated tau pathology was quantified by implementing an automated thresholding method on the deconvolved DAB component of AT8 stained tissue sections. Briefly, cell bodies of neurofibrillary tangles and tau positive astrocytes were identified using the Sauvola thresholding method (radius = 50 pixels) available in FIJI (NIH, Bethesda MD), followed by size inclusion criterion (50-10,000 pixels) to remove artifacts caused by out of focus structures, tissue edges and folded regions (**Figure 4.2A**). Total astrogliosis was quantified by manual thresholding applied to the DAB component of GFAP stained tissue sections, followed by size exclusion analysis. Astrocytes in white matter were identified in these thresholded regions by a size inclusion criteria of 0-10,000 pixels (**Figure 4.2C**). Because of dense GFAP staining and increased astroglial size in gray matter, astrocytes in gray matter were identified in thresholded regions using a size inclusion criteria of 0-20,000 pixels. The MRI-histology coregistered grids were then overlaid onto each tissue section and the percent area of thresholded particles was measured for each element of the grid.

White matter disruption was quantified as previously described (Gangolli et al., 2017). Briefly, the MRI-histology coregistered grid was overlaid onto the image of each Myelin Black Gold II tissue section. A two dimensional Fourier transformation was applied within every element of the grid to obtain a power spectrum representing directional frequencies. A two tensor model was then fit to this power spectrum, where each elliptical tensor represented a fiber population (**Figure 4.2B**). Power coherence was calculated as the ratio of the radial to preferential axes of the tensors, subtracted from one to obtain a coherence metric that ranged from 0 (lowest coherence) to 1 (highest coherence). Fiber orientations of the first and second major fiber components were calculated from the angle of the preferential axes of each tensor relative to the two dimensional sectioning plane.

Finally, because there were two 50 µm histological sections for each 500 µm MRI slice, the resulting measures of percent areas of staining (AT8 and GFAP) or power coherence (Myelin Black Gold II) were averaged across the two histological sections, obtaining a single measure of pTau, GFAP staining, or power coherence corresponding to each MRI voxel. Regions (sulcal depths, adjacent white matter) where the sulcal depth was not aligned with the two dimensional sectioning plane, or where fibers made an angle larger than 45° relative to the sectioning plane were excluded a priori from all analyses.

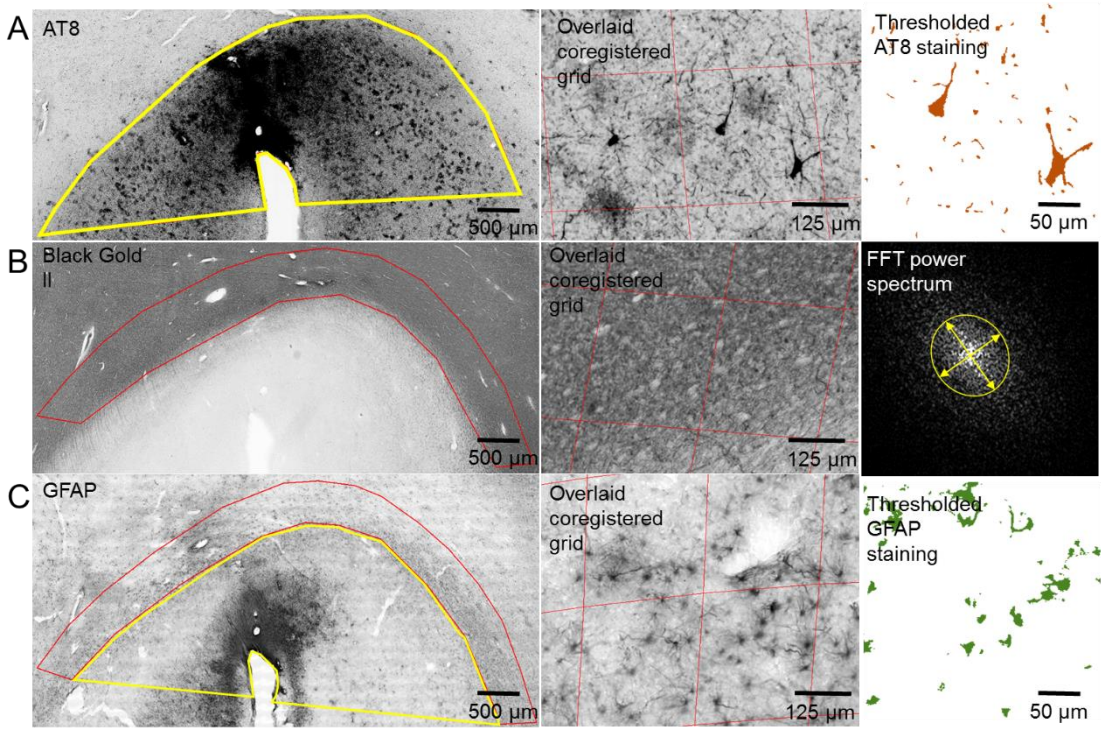

Figure 4.2 Automated quantification of histopathology. A. Left panel: Sulcal depth ROIs (yellow line) were drawn on the DAB component of the AT8 stained image to quantify pTau tangles. Middle panel: The voxel-based grid was overlaid onto the image. Right panel: Thresholding and size exclusion were then used to quantify threads, neurofibrillary tangles, and astroglial tau. **B.** Left panel: Sulcus adjacent ROIs (red line) were drawn on the Myelin Black Gold II stained image. Middle panel: For each component of the voxel based grid in the spatial domain, zero mean subtraction followed by Tukey windowing ($\alpha = 0.5$) was used to remove ringing due to cutoff effects. Right panel: A two tensor was then fit to the spatial distribution in the frequency domain to obtain a measure of power coherence. **C.** Left panel: Sulcal depth (yellow line) and sulcus adjacent white matter ROIs (red line) were drawn on the GFAP stained image. Middle panel: The voxel-based grid was overlaid onto the image. Right panel: Thresholding and size exclusion were used to identify astrocytes and obtain a quantitative measure of each region in the voxel-based grid.

4.2.7 Statistical methods

Statistical analysis of all data was performed in Statistica (Tibco Software Inc., Palo Alto, CA, USA). All data were tested for normality using the Shapiro-Wilk normality test. For all analyses, ROIs from sulcal depths and adjacent white matter were classified either as CTE or non-CTE tauopathy (FTLD/AD). Two-tailed Mann Whitney-U tests, followed by Bonferroni correction for multiple comparisons were used to detect differences in power coherence, astrogliosis, and pTau accumulation between tauopathy groups (CTE, non-CTE tauopathy). Spearman's rank correlations were used to determine the relationship between sulcal pTau and white matter power coherence as well as white matter power coherence and white matter astrogliosis. Spearman's rank correlation tests were also used to determine the relationships between histopathological measures of sulcal pTau, white matter power coherence, and diffusion metrics. To account for variability of diffusion and histological metrics due to differences in post mortem interval, measures for radiological-pathological correlations were adjusted by dividing each value by the mean value of the tissue block (Holleran et al., 2017). In this study, there were 8-10 valid sulcal depths (aligned with sectioning plane) per tauopathy group (CTE (8), FTLD/AD (10)). With this sample size, only correlations of 0.88 or greater with $p<0.05$ were considered to be significant in order to power this study at 0.88 (increased to account for non-parametric Spearman's correlations). Correlations that reached a strength of $r>0.88$ were tested for significance and corrected using Bonferroni correction for multiple comparisons, with the effective number of measures adjusted by eigenvalue decomposition to account for potential correlation between measures (Cheverud, 2001). All correlation coefficients are reported as $r_{(ll,ul)} = r_{spearman}$, indicating the lower and upper 95% confidence intervals of the Spearman's r coefficient. These intervals were calculated with Fisher's z' transformation method, but using the

Fieler estimate of standard error to account for variability due to non-normally distributed data (Bishara and Hittner, 2017).

Case #	Age	Post mortem interval	Tauopathy group	Pathological diagnosis	Number of valid sulcal depths
1	80-89	6 hours 40 min	CTE	CTE IV; diffuse LBD; VaD	1
2	50-59	10 hours 23 min	CTE	CTE III	2
3	60-69	9 hours 10 min	CTE	CTE IV; white matter rarification	1
4	70-79	15 hours 26 min	CTE	CTE IV; LBD; VaD	3
5	70-79	12 hours 30 min	CTE	CTE III: VaD	1
6	90-99	10 hours	FTD	FTLD; tangles only	1
7	80-89	9 hours	FTD	FTLD-PSP; VaD	2
8	70-79	14 hours 20 min	FTD	Picks; AD; VaD	4
9	80-89	4 hours 42 min	AD	AD (A2B3C3); VaD	2
10	90-99	7 hours 15 min	AD	AD (A2B3C3); VaD	1

Table 4.1 Tissue information for CTE/FTLD/AD cases. LBD: lewy body disease; VaD: vascular disease; AD pathology: A0 (no Aß or plaques), A1 (Thal phases 1 or 2), A2 (Thal phase 3), A3: (Thal phases 4 or 5); NFT stage: B0 (no NFTs), B1 (Braak stage I or II), B2 (Braak stage III or IV), B3 (Braak stage V or VI); Neuritic plaque score: C0 (no neuritic plaques), C1 (sparse CERAD score), C2 (moderate CERAD score), C3 (frequent CERAD score).

4.3 Results

4.3.1 No correlation of age or post mortem interval and histopathology

Spearman's rank analyses showed weak correlations between sulcal pTau and age ($r_{(-0.71,0.53)}$ = -0.143, **Figure 4.3A**) as well as sulcal pTau and post mortem interval ($r_{(-0.53,0.71)}$ = 0.155, **Figure 4.3B**). Power coherence in white matter adjacent to sulcal depths was modestly correlated with age ($r_{(-0.069,0.89)}$ = 0.586, **Figure 4.3C**) and post mortem interval ($r_{(-0.75,0.46)}$ = -0.236, **Figure 4.3D).** Because these correlations were too weak to warrant testing for statistical significant,, we

concluded that age and post mortem interval did not have a strong effect on histopathological measures in our tissue samples.

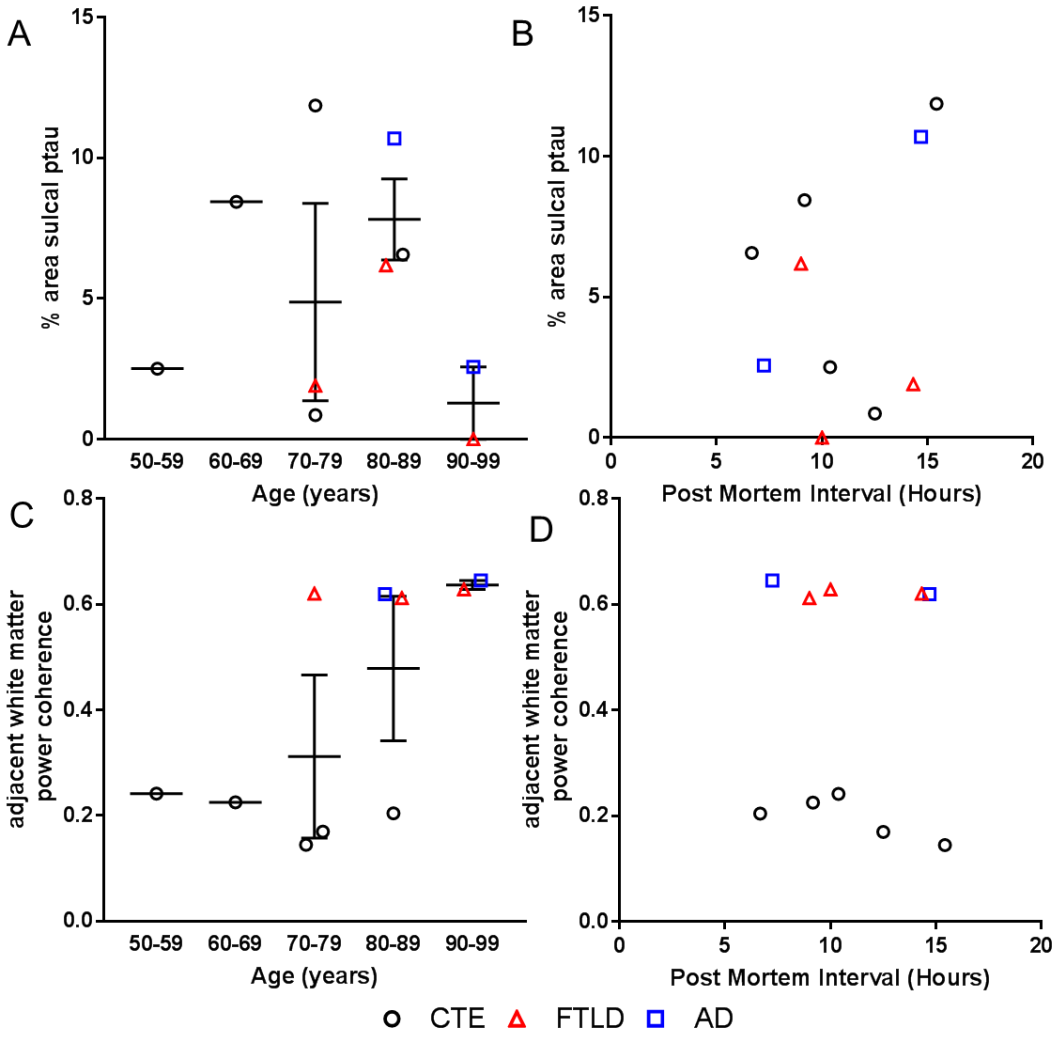

Figure 4.3 Effects of age and post mortem interval on pTau and white matter coherence. A. Spearman's rank analysis showed a weak correlation between age (grouped by decade) and the mean percent area of sulcal tau in tissues with CTE, AD, or FTLD ($r_{(-0.71,0.53)}$ = 0.143) **B.** Post mortem interval was weakly correlated with mean percent area of sulcal tau in tissues ($r_{(-0.53,0.71)}$ = 0.155). **C.** Power coherence in white matter adjacent to cortical sulci was modestly correlated with age (grouped by decade, in tissues with CTE, AD or FTLD ($r_{(-0.069,0.89)}$ = 0.586) **D.** There was a similar, modest correlation between power coherence and post mortem interval ($r_{(-0.75,0.46)}$ = -0.236). Each datapoint represents a single tissue block.

4.3.2 Relationship between pTau and power coherence in CTE and non-CTE tauopathies

Differences in sulcal and gyral phosphorylated tau between CTE and non-CTE tauopathies were analyzed using Mann-Whitney U tests. (**Figure 4.4**). There were no differences in AT8 staining between CTE and non-CTE tauopathies in either sulcal or gyral regions. While tissues with Stage III CTE tended to have increased pTau tangles and glial tau in sulcal depths relative to superficial gray matter and gyri, Stage IV CTE tissues showed and abundance of pTau staining in both regions. Similarly, Mann-Whitney U testing showed no differences in GFAP staining when analyzing sulcal gray matter, or white matter underlying sulcal depths (**Figure 4.5**). In general, gray matter in both CTE and non-CTE tauopathy tissues tended to have an abundance of astrocytes with large cell bores and extended processes. In contrast, astrocytes in white matter were more sparse, often with small cell bodies and beaded processes. Assessment of white matter disruption using Myelin Black Gold staining showed evidence of puncta and irregular thread shaped myelinated fibers. Quantitatively, a Mann Whiney U test showed that power coherence in tissues with a pathological diagnosis of CTE had reduced power coherence (**Figure 4.6**). This finding remained significant after adjusted correction for multiple comparisons ($p_{bonf} = 5.55 \times 10^{-8}$).

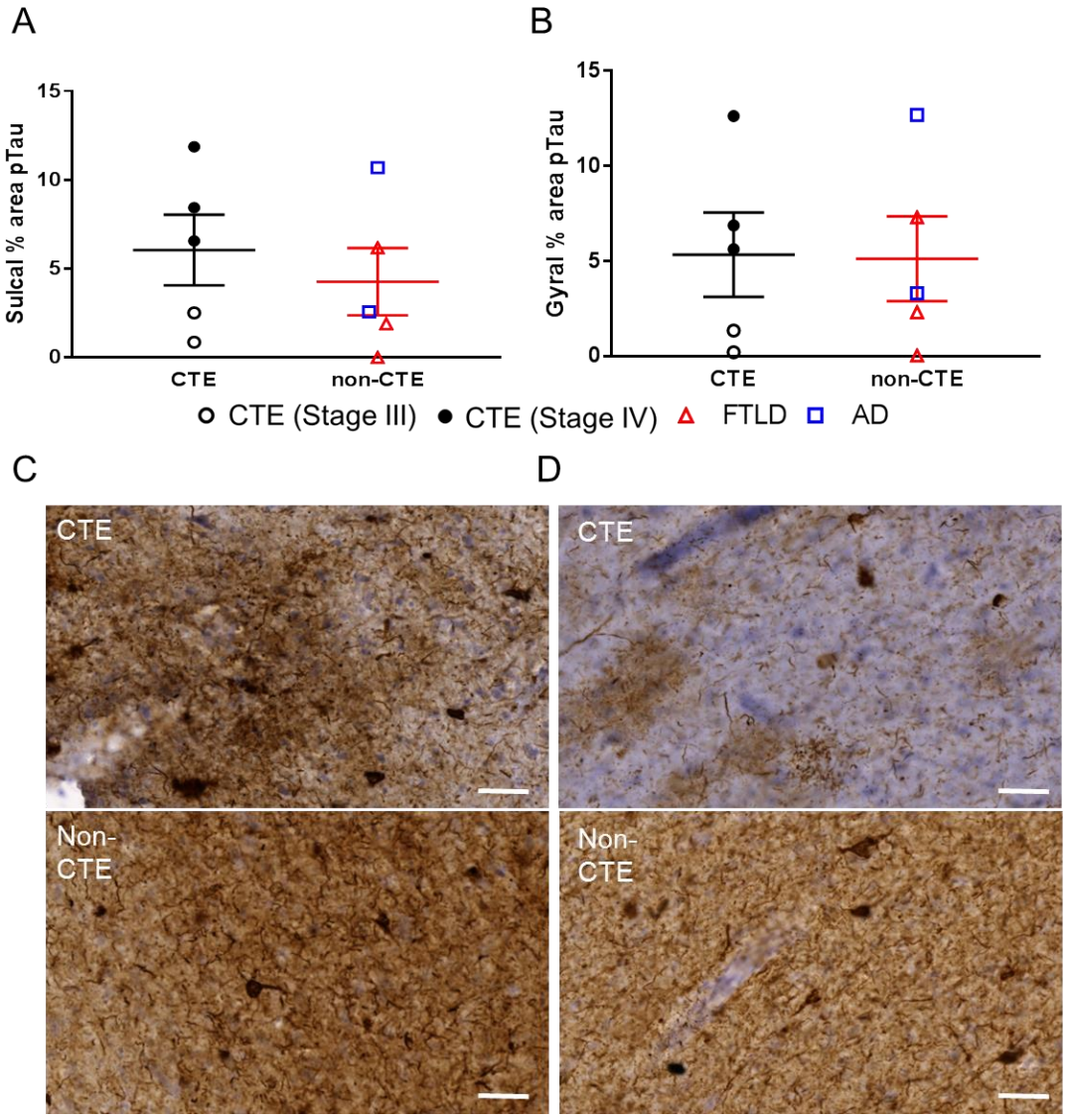

Figure 4.4 No differences of sulcal depth or gyral pTau abundance in CTE and non-CTE tauopathies. A. No differences in percent area of sulcal pTau pathology were observed between CTE and non-CTE tauopathy tissues. **B. C.** AT8 staining in sulcal gray matter shows extensive staining of neurofibrillary tangles and threads in both CTE and non-CTE tauopathy tissues. Each data point represents averages across ROIs for individual tissue blocks. **D.** Tissues with CTE showed positive AT8 staining of neurofibrillary tangles and astroglial tau that, in cases of severe (Stage IV) CTE, were found in superficial gray matter. Non-CTE tauopathy tissues showed varying degrees of AT8 immunoreactive tangles and threads in superficial gray matter. Scale bar = 50 microns.

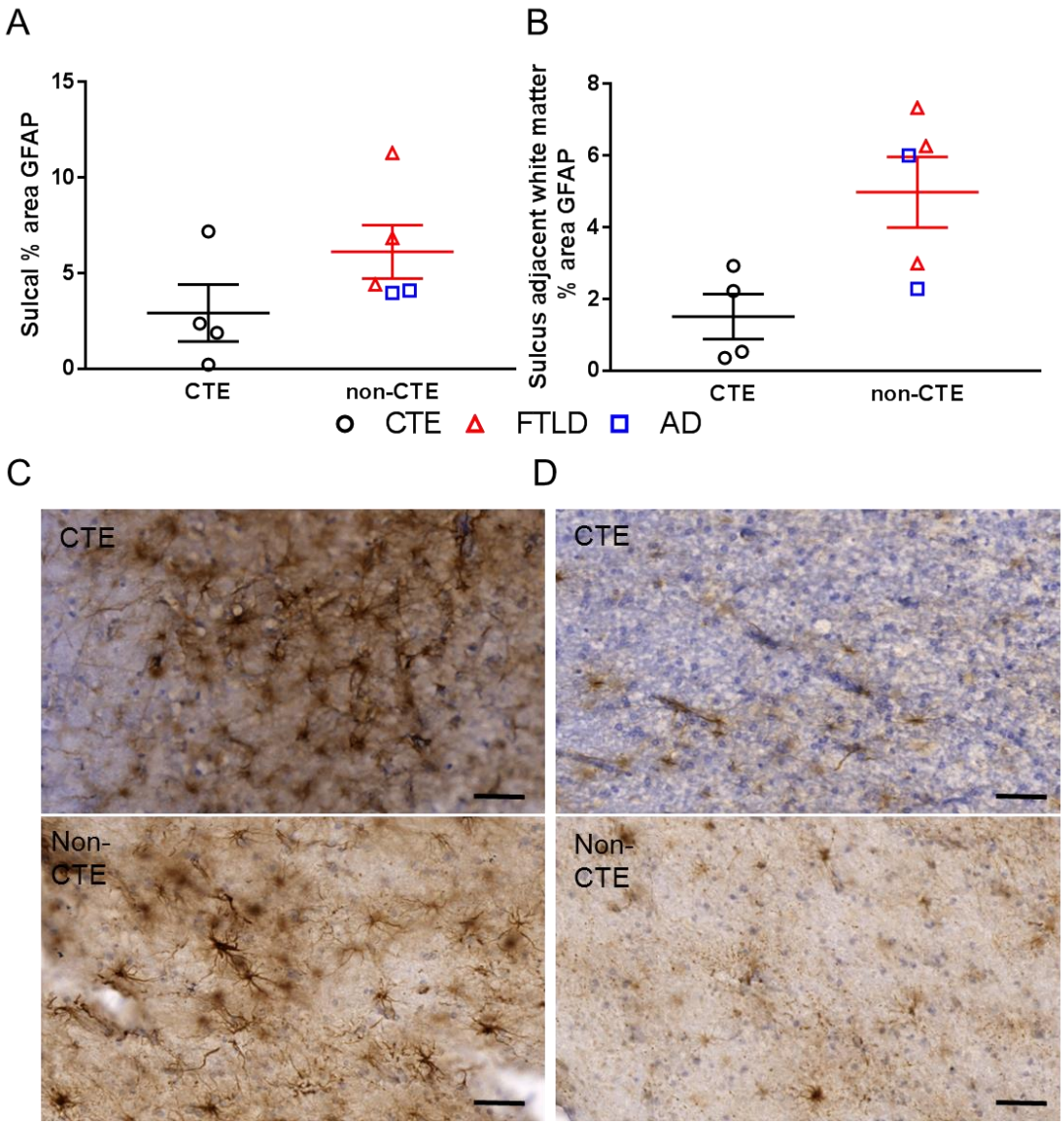

Figure 4.5 No differences in sulcal depth or adjacent white matter astrogliosis. A. In sulcal depths, there was no significant difference between percent area of GFAP staining between CTE and non-CTE tauopathy tissues. **B.** White matter underlying sulcal depths also showed no significant differences in GFAP staining when comparing CTE and non-CTE tauopathy tissues. Each data point represents averages across ROIs for individual tissue blocks. **C.** Gray matter in both CTE and non-CTE tissues tended to have dense GFAP staining, indicating astrocytes with large cell bodies and extended processes. **D.** White matter adjacent to sulcal depths generally showed decreased astrogliosis relative to gray matter, along with astrocytes with beaded processes and small cell bodies. Scale bar = 50 microns.

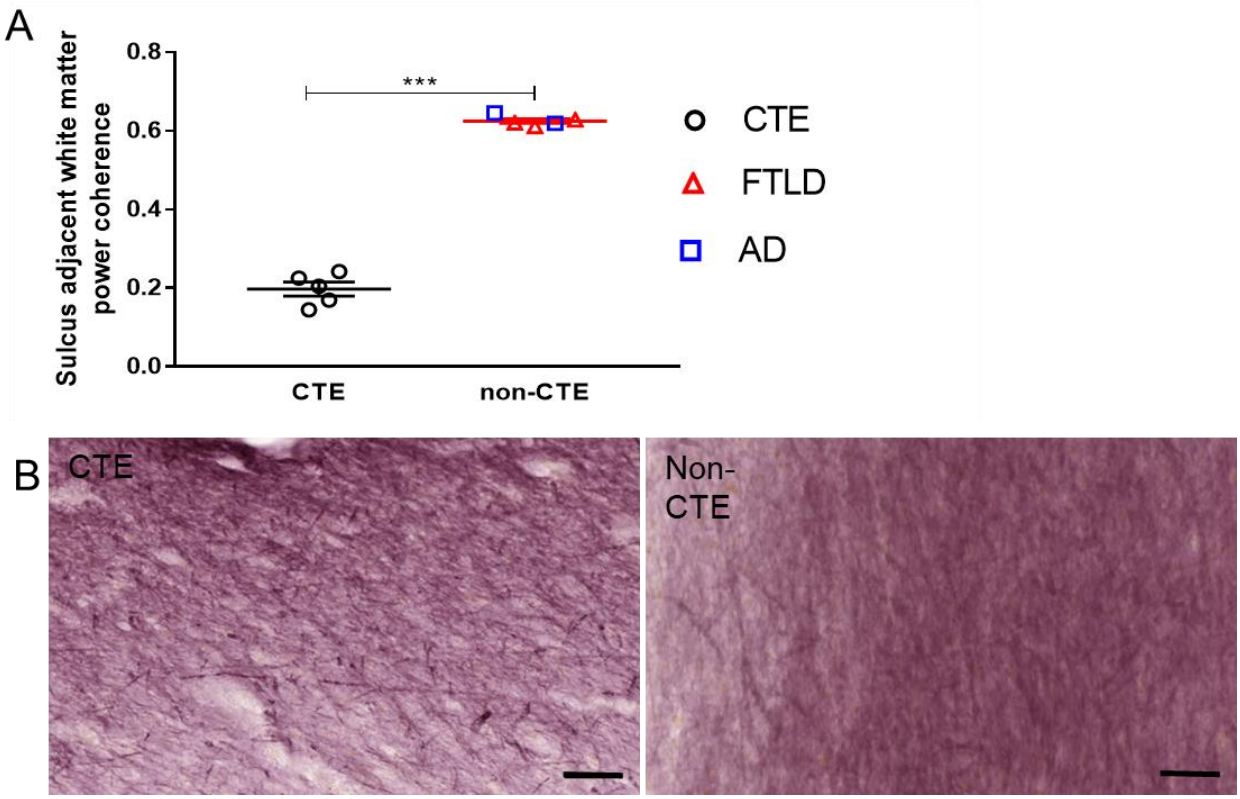

Figure 4.6 CTE tissues have reduced white matter integrity in comparison non-CTE tauopathy tissues. A. Power coherence in white matter adjacent to cortical sulcal depths was significantly reduced in CTE tissues relative to non-CTE tissues ($p = 5.55 \times 10^{-8}$) **.** Each data point represents averages across ROIs for individual tissue blocks. **B.** Myelin Black Gold II staining in CTE tissues does not show severe demyelination, but irregularities such as fragmented and dot-like structures in the myelin are apparent. Non-CTE tissues show crossing and curving fiber architecture in sulcus adjacent white matter but no such irregularities. Scale bar = 50 microns.

We next used Spearman's rank correlations to determine whether there was a correlation between white matter power coherence and pTau pathology that was specific to CTE, or generalized across tauopathies (**Figure 4.7A-B**). In tissues with a pathological diagnosis of CTE, there was a modest, negative correlation between percent area of pTau in cortical sulcal depths and power coherence in adjacent white matter ($r_{(-0.88,0.22)} = -0.517$). Tissues with a diagnosis of FTLD or AD showed weak, negative correlation between percent area of pTau in cortical sulcal depths and power coherence in adjacent white matter ($r_{(-0.71,0.53)} = -0.152$).

These results show that the abundance of phosphorylated tau or astrocytes in sulcal depths is not sufficient to distinguish between CTE and non-CTE tauopathies. Moreover, while Stage III CTE tissues showed localization of staining in sulcal depth regions, tissues with Stage IV CTE showed staining in superficial layers, similar to tissues with a pathological diagnosis of FTLD or AD. Automated thresholding methods could not differentiate between these tissues and non-CTE tauopathies. Furthermore, although sulcus adjacent white matter power coherence in CTE tissues is reduced compared to tissues diagnosed with either AD or FTLD, there does not appear to be sufficiently strong correlation ($r > 0.88$) of power coherence with sulcal pTau, either in CTE or non-CTE tauopathies in this dataset to warrant testing for significance.

4.3.3 Relationship between power coherence and astrogliosis in CTE and non-CTE tauopathies

To determine whether white matter power coherence was related to white matter astrogliosis, we also performed correlations between power coherence and GFAP staining in white matter regions adjacent to cortical sulci. In both CTE ($r_{(-0.42,0.86)} = 0.405$) and non-CTE tauopathy tissues ($r_{(-0.82,0.31)} = -0.394$) the correlation between white matter power coherence and white matter GFAP abundance was weak (**Figure 4.7C-D**). These data show that white matter astrogliosis is not a primary driver of changes in white matter power coherence.

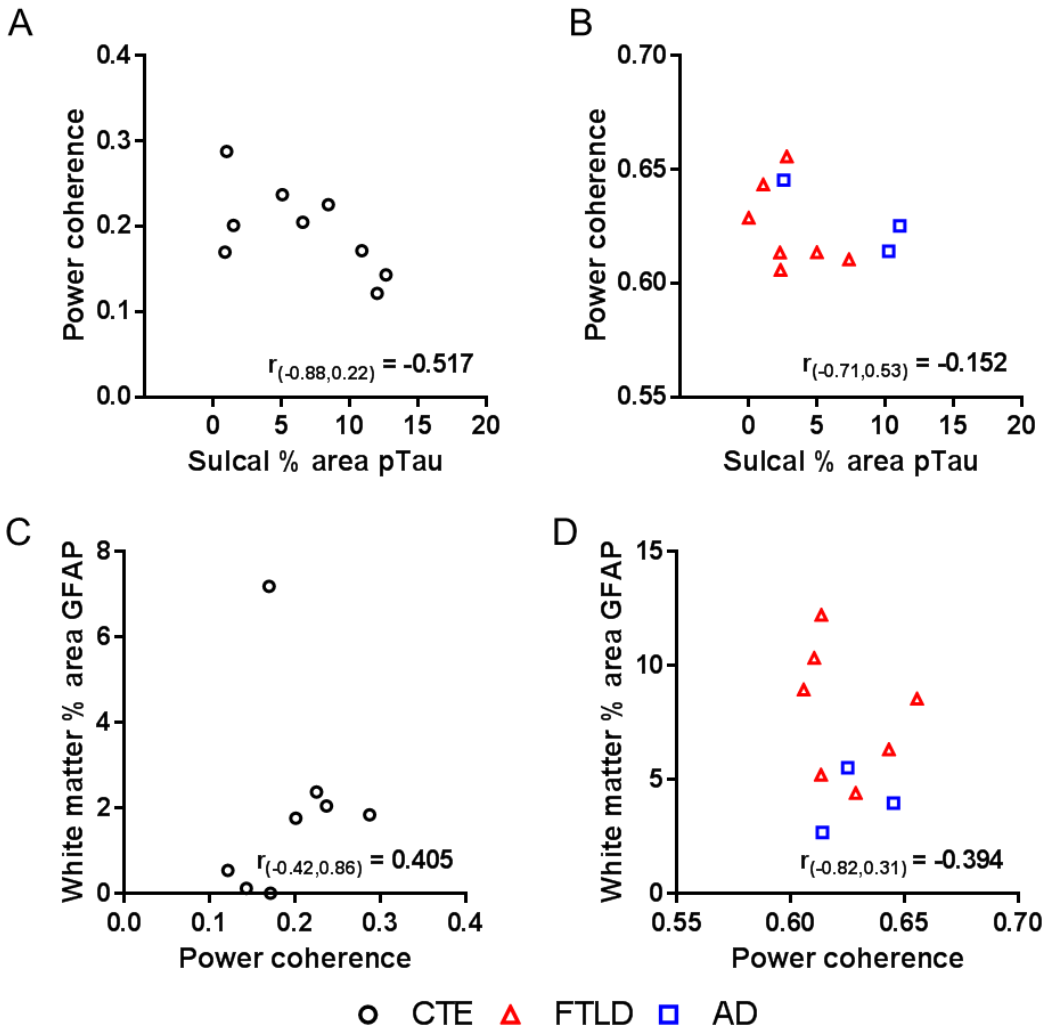

Figure 4.7 Power coherence is weakly correlated with sulcal pTau and white matter GFAP. A. A modest correlation between sulcal pTau and adjacent white matter power coherence was observed in CTE tissues. **B.** In non-CTE tissues, the association between sulcal pTau and adjacent white matter power coherence was weak. **C.** In CTE tissues, there was a weak relationship between power coherence in white matter adjacent to sulcal depths and astrogliosis, measured by percent area of GFAP staining in corresponding regions. **D.** A similar weak relationship between power coherence and astrogliosis was found in non-CTE tauopathy tissues. Each datapoint represents a single region of interest. Subscripts indicate lower and upper 95% confidence intervals.

4.3.4 Diffusion measures in sulcal gray matter do not correlate with hyperphosphorylated tau or astrogliosis

To determine whether diffusion measures were able to indicate the presence of hyperphosphorylated tau in sulcal gray matter, we performed Spearman's rank correlations in all tissue samples with CTE and non-CTE tauopathies. When considering all eighteen regions of

interest together, we found weak to modest correlations of tau in gray matter sulcal depths and diffusion measures in corresponding regions (**Figure 4.8**). We also tested for relationships between sulcal GFAP staining and diffusion measures in sulcal gray matter. Spearman's rank analyses showed weak to modest correlations of astrogliosis in these regions with diffusion measures (**Figure 4.9**). These correlations did not reach sufficient strength ($r > 0.675$) to justify testing for statistical significance. Analyses of the CTE and non-CTE tauopathy groups separately also showed weak to modest associations of phosphorylated tau and astrogliosis in sulcal depths and diffusion measures in associated regions Specifically in CTE tissues, kurtosis measures (mean, axial and radial kurtosis) showed moderate correlations with sulcal depth tau (**Table 4.2**). Interestingly in non-CTE tissues, there were several correlations observed between astrogliosis and gray matter diffusion measures in cortical sulci. Apparent diffusion coefficient, axial diffusivity and radial diffusivity showed negative, moderate to strong correlation with percent area of astrocytes. Isotropic index showed a similar modest and negative relationship. Finally, kurtosis measures of mean, axial and radial kurtosis showed moderate, positive correlations with sulcal astrogliosis (**Table 4.2**). Given the sample size, the correlation values did not reach the specified criteria ($r > 0.88$) to test for statistical significance. These results show that in CTE tissues with reasonably short post mortem intervals, there may be an association between sulcal depth pTau and diffusion measures.

Spearman r	FA	ADC	Axial diffusivity	Radial diffusivity	gFA	Isotropic index	Mean kurtosis	Axial kurtosis	Radial kurtosis
CTE									
Sulcal pTau	-0.371	-0.500	-0.720	-0.512	-0.146	-0.329	0.695	0.781	0.707
Sulcal astrogliosis	-0.494	-0.253	-0.422	-0.229	-0.446	0.060	0.301	0.542	0.398
Non-CTE									
Sulcal pTau	-.281	-.293	-.512	-.159	-.012	-0.195	0.268	0.183	0.268

Sulcal astrogliosis	0.195	-0.768	-0.878	-0.732	0.537	-0.646	0.756	0.744	0.756

Table 4.2 Correlation coefficients of diffusion measures and histopathology in sulcal depths. Analysis of the correlations of sulcal pTau with sulcal diffusion measures and sulcal astrogliosis with diffusion measures showed weak to modest correlations in both CTE and non-CTE tauopathies when analyzed separately.

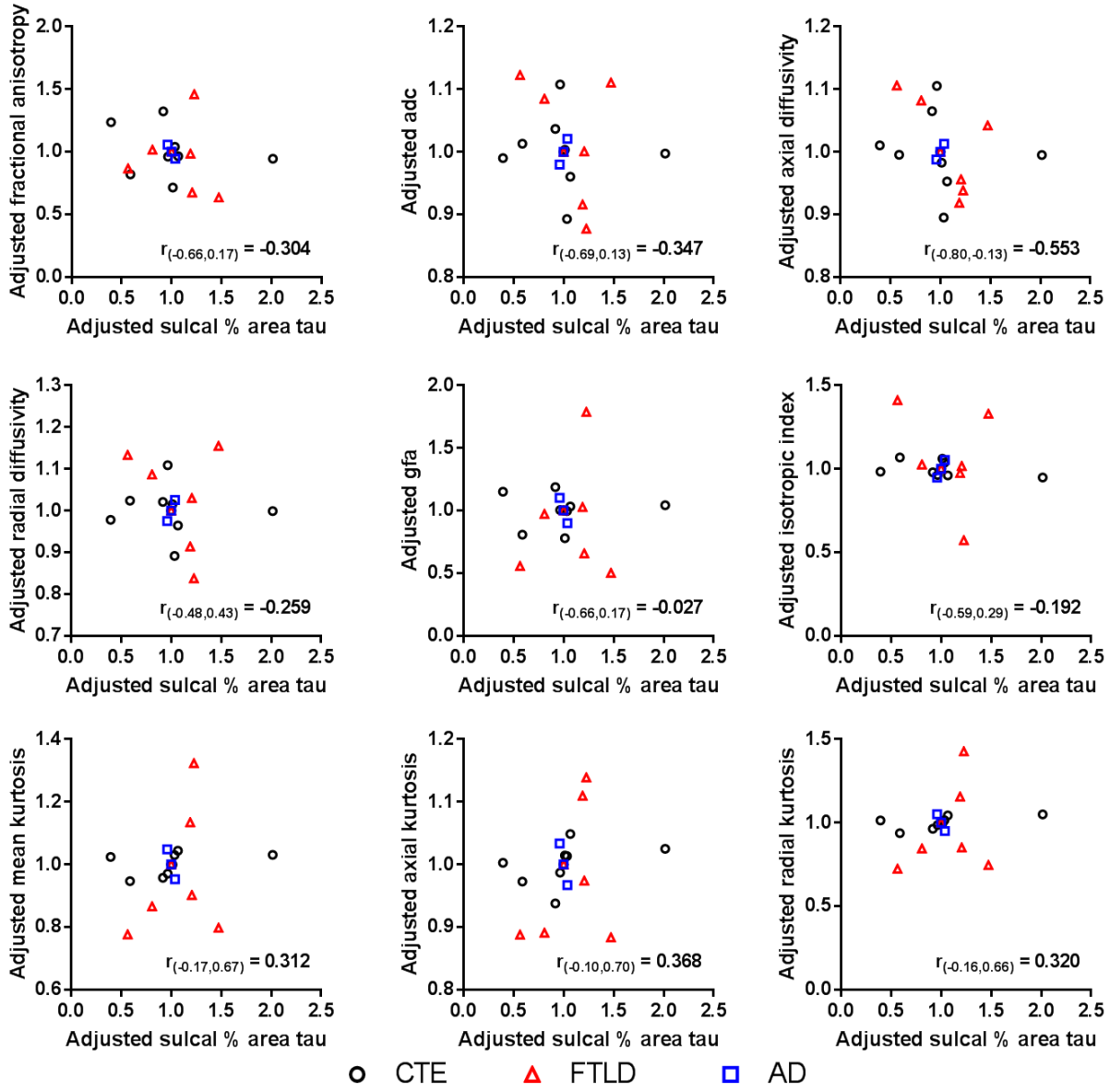

Figure 4.8 No relationship between sulcal pTau and diffusion measures. Percent area of thresholded pTau staining was measured for each sulcal depth and correlated with diffusion measures of gray matter from coregistered data. There was no association between sulcal pTau and any of the diffusion measures. Each datapoint represents a single region of interest. Adjustments of data were performed by dividing the value of ROI by the mean across ROIs for each tissue block. Subscripts indicate lower and upper 95% confidence intervals.

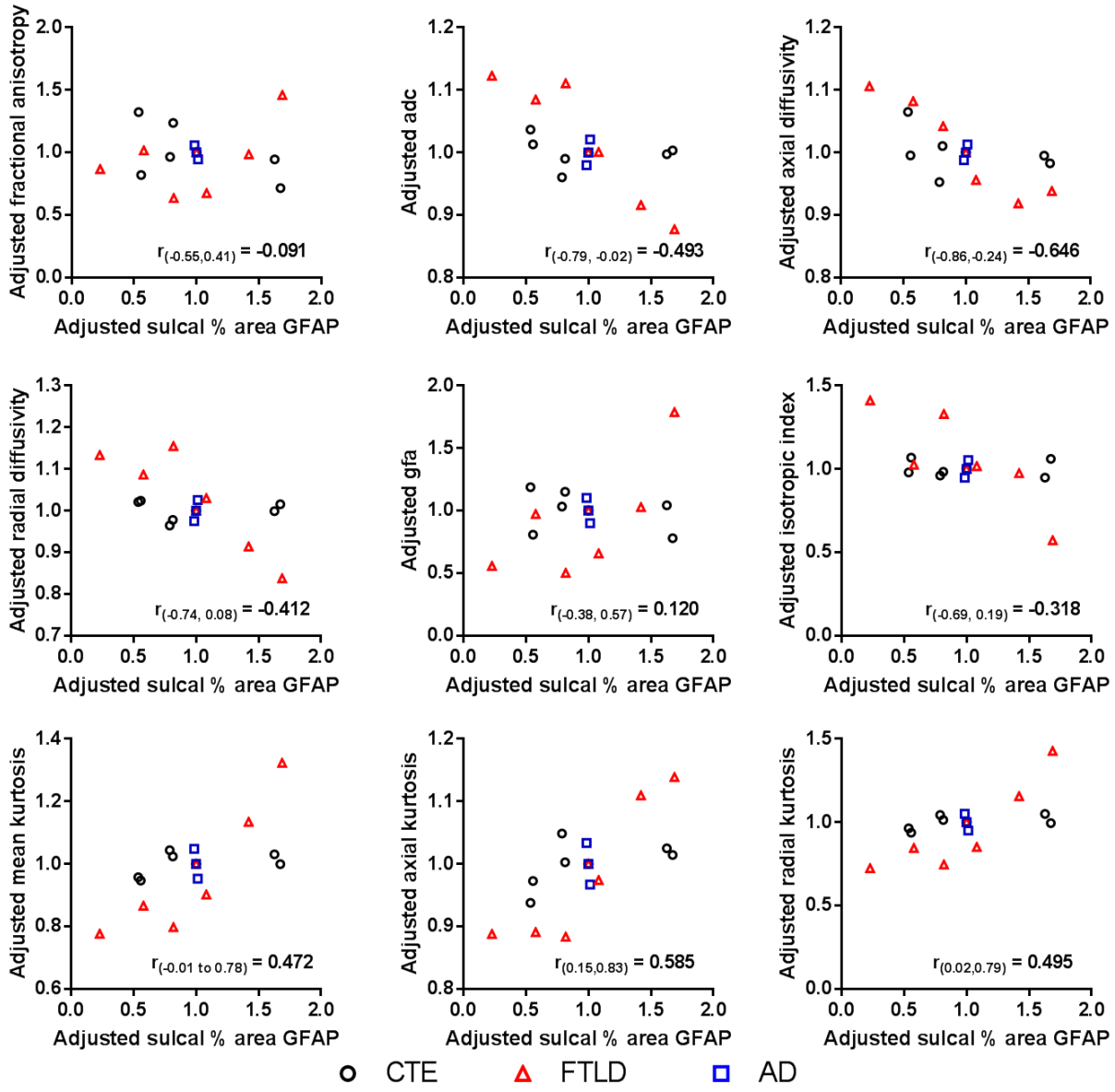

Figure 4.9 No relationship between sulcal GFAP and diffusion measures. Percent area of thresholded GFAP staining was measured for each sulcal depth and correlated with diffusion measures of gray matter from coregistered data. There was no association between sulcal astrogliosis and any of the diffusion measures. Each datapoint represents a single region of interest. Adjustments of data were performed by dividing the value of ROI by the mean across ROIs for each tissue block. Subscripts indicate lower and upper 95% confidence intervals.

4.3.5 Fractional anisotropy shows strong correlation with white matter disruption in CTE tissues

To further support our previous findings in Stage III/IV CTE tissues, we used Spearman's rank correlations followed by adjusted Bonferroni correction for multiple comparisons to determine whether there was a relationship between diffusion derived metrics and phosphorylated tau pathology in both CTE and FTLD/AD tissues. In tissues with a pathological diagnosis of Stage III/IV CTE, there was a modest, negative correlation ($r_{(-0.88,0.22)} = 0.517$) between percent area of pTau in sulcal depths and fractional anisotropy in adjacent white matter (**Figure 4.10A**) that was consistent with the correlation ($r = -0.55$) that we previously observed in a larger dataset of CTE only tissues (Holleran et al., 2017). We found a strong correlation ($r_{(0.84,0.99)} = 0.966$, $p_{bonf} = 7.68 \times 10^{-4}$) between power coherence in sulcus adjacent white matter and fractional anisotropy (**Figure 4.10B**) that remained significant after correction for multiple comparisons. In tissues with a diagnosis of FTLD or AD, the correlations between sulcal pTau and adjacent white matter fractional anisotropy ($r_{(-0.80,0.36)} = -0.341$) as well as sulci adjacent white matter power coherence and fractional anisotropy ($r_{(-0.87,0.14)} = -0.536$) remained modest. (**Figure 4.10C-D**). When considering the relationships between sulcal pTau and the remaining eight diffusion metrics in both CTE and non-CTE tissues, the correlations were weak to modest (**Table 4.3**). Interestingly, while the majority of correlations between white matter power coherence and diffusion parameters remained weak to modest in non-CTE tissues (**Table 4.3**), we found strong correlations of power coherence with adc ($r_{(0.63,0.98)} = 0.902$, $p_{bonf} = 0.011$), radial diffusivity ($r_{(0.76,0.99)} = 0.939$, $p_{bonf} = 0.0018$), and isotropic index ($r_{(0.95,0.99)} = 0.978$, $p_{bonf} =$

3.02 x 10^{-8}). These correlations remained significant after correction for multiple comparisons (**Figure 4.11**).

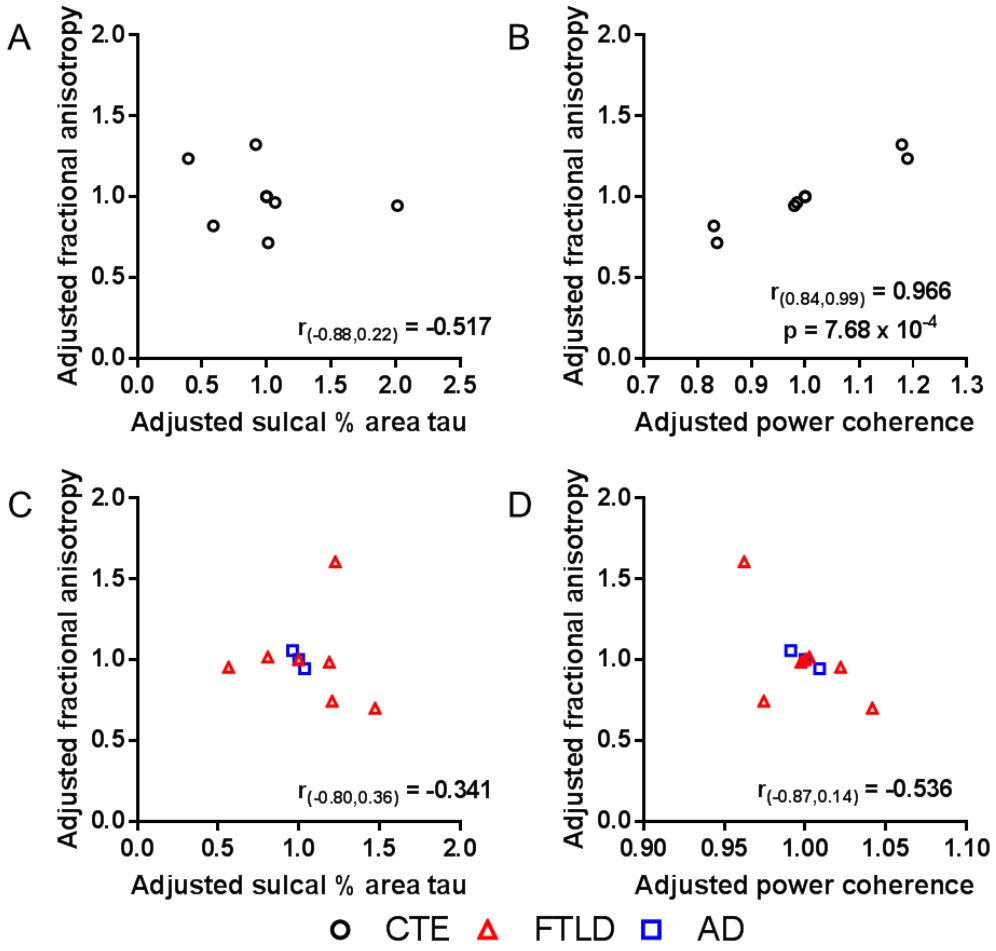

Figure 4.10 Fractional anisotropy correlates with white matter disruption in CTE tissues. A. In CTE tissues, sulcal tau showed modest correlation with fractional anisotropy in adjacent white matter. **B.** There was a strong relationship between white matter fractional anisotropy in tissues with a pathological diagnosis of CTE **C.** In non-CTE tauopathies, the relationship between white matter fractional anisotropy and sulcal pTau was weak. **D.** The relationship between white matter power coherence and fractional anisotropy was modest in non-CTE tissues. Each datapoint represents a single region of interest. Adjustments of data were performed by dividing the value of ROI by the mean across ROIs for each tissue block

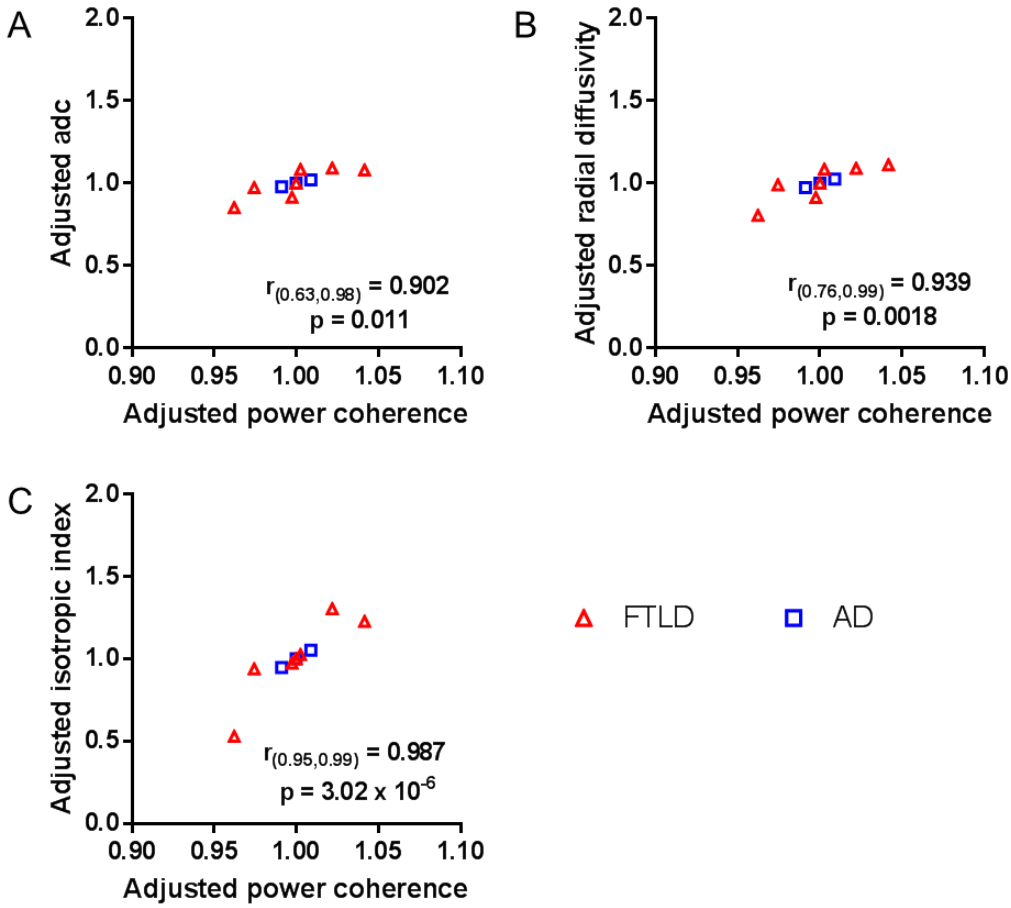

Figure 4.11 Power coherence correlates with diffusion metrics in non-CTE tauopathies. A. Sulcus adjacent white matter power coherence showed strong and significant correlation with apparent diffusion coefficient (ADC) in tissues with non-CTE tauopathies. **B.** Power coherence also showed strong correlation with radial diffusivity in white matter adjacent to sulcal depths. **C.** Power coherence was strongly correlated with isotropic index in non-CTE tauopathies. Each datapoint represents a single region of interest. Adjustments of data were performed by dividing the value of ROI by the mean across ROIs for each tissue block

4.3.6 Astrogliosis has weak to moderate correlation with diffusion in sulcus adjacent white matter

When considering all eighteen sulcal depth regions of interest, Spearman's rank analyses generally showed weak correlations between sulcal percent area GFAP and diffusion measures (**Figure 4.12**). There was a moderate and negative relationship between sulcal astrogliosis and fractional anisotropy in adjacent white matter, driven mainly by values in non-CTE tauopathies (n_{rois} = 10, r = -0.845, **Table 4.3**) and weakened by values from tissues with a pathological

diagnosis of CTE (n_{rois} = 8, r = -0.494). Although the moderate correlation for all sulcal depths (r > 0.675) justified testing for statistical significance, the relationship did not reach statistical significance following adjusted Bonferroni correction for multiple comparisons ($p_{bonf} > 0.05$). Similar Spearman's rank correlations of astrogliosis and diffusion measures in sulcus adjacent white matter showed weak relationships when considering all regions of interest (**Figure 4.13**) and CTE and non-CTE tauopathy groups separately (**Table 4.3**).

Spearman r	FA	ADC	Axial diffusivity	Radial diffusivity	gFA	Isotropic index	Mean kurtosis	Axial kurtosis	Radial kurtosis
CTE									
Sulcal pTau	-0.517	-0.362	-0.741	-0.379	-0.138	-0.396	-0.517	0.707	0.534
Sulcal astrogliosis	-0.494	-0.253	-0.421	-0.229	-0.446	0.060	0.301	0.542	0.398
Power coherence	0.966	-0.172	0.827	-0.293	0.690	-0.362	0.190	-0.259	0.172
White matter astrogliosis	-0.542	-0.108	-0.349	-0.060	-0.518	0.205	0.133	0.398	0.253
Non-CTE									
Sulcal pTau	-0.341	-0.537	-0.512	-0.268	-0.012	-0.354	0.268	0.354	0.268
Sulcal astrogliosis	-0.845	-0.058	-0.156	0.119	-0.512	0.125	-0.265	-0.003	-0.265
Power coherence	-0.537	0.902	0.866	0.939	-0.744	0.988	-0.763	-0.878	-0.768
White matter astrogliosis	-0.277	0.277	0.289	0.252	-0.375	0.179	-0.363	-0.351	-0.363

Table 4.3 Correlation coefficients of white matter diffusion parameters with white matter histopathology. Sulcal pTau and astrogliosis showed weak to modest correlations with metrics derived from DTI, GQI and DKI in adjacent white matter. In CTE tissues, only power coherence in sulcus adjacent white matter showed strong correlation with fractional anisotropy. White matter adjacent to sulcal depths in non-CTE tauopathies showed strong correlations with apparent diffusion coefficient, radial diffusivity and isotropic index. Astrogliosis in sulcus adjacent white matter showed weak to modest correlations with diffusion measures in corresponding regions.

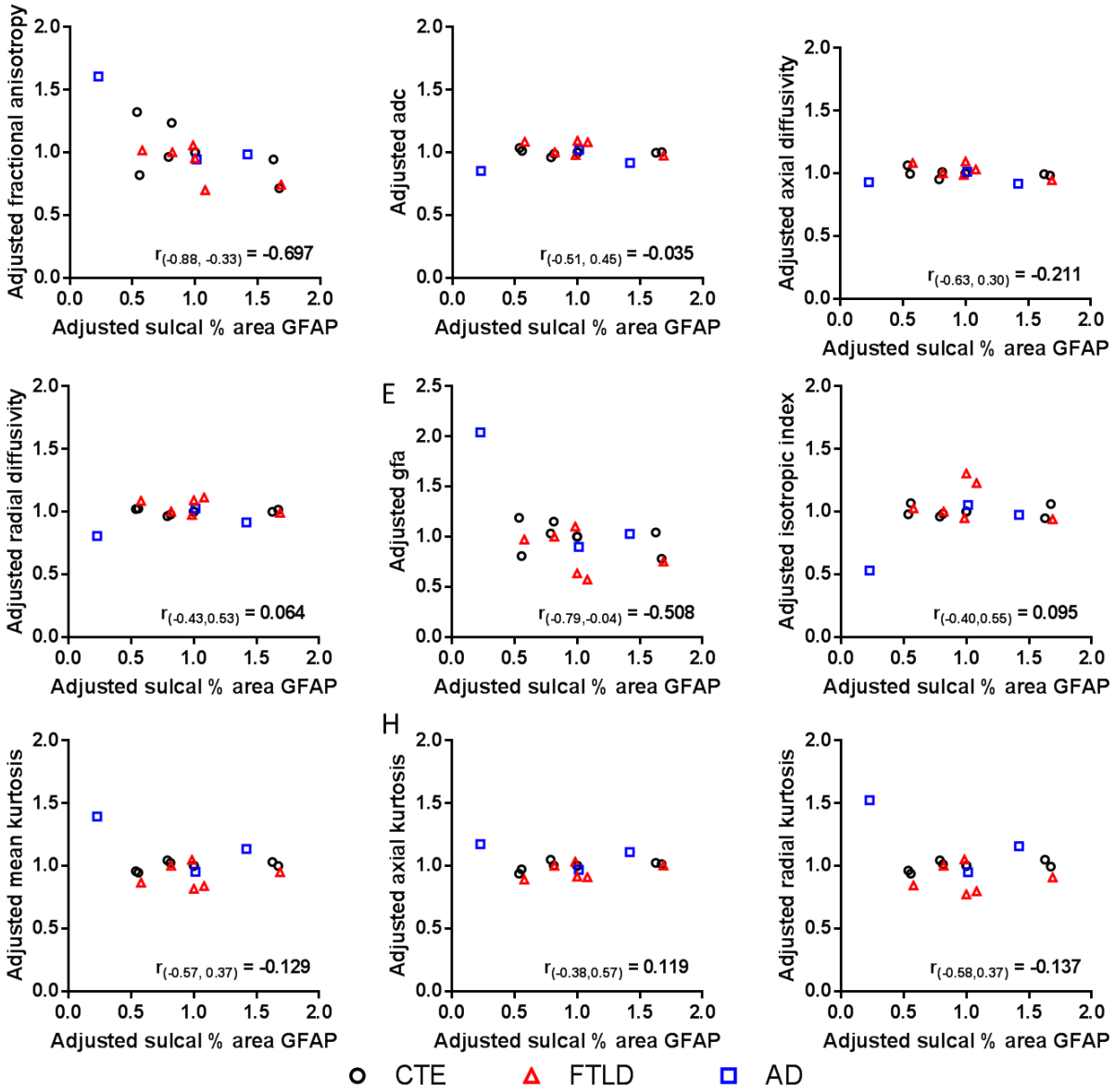

Figure 4.12 No correlation of sulcal astrogliosis with diffusion measures in sulcus adjacent white matter. Percent area of GFAP staining in cortical sulci was correlated with diffusion measures in white matter underlying sulcal depths. There were no correlations with sufficient strength ($r > 0.88$) to test for significance.

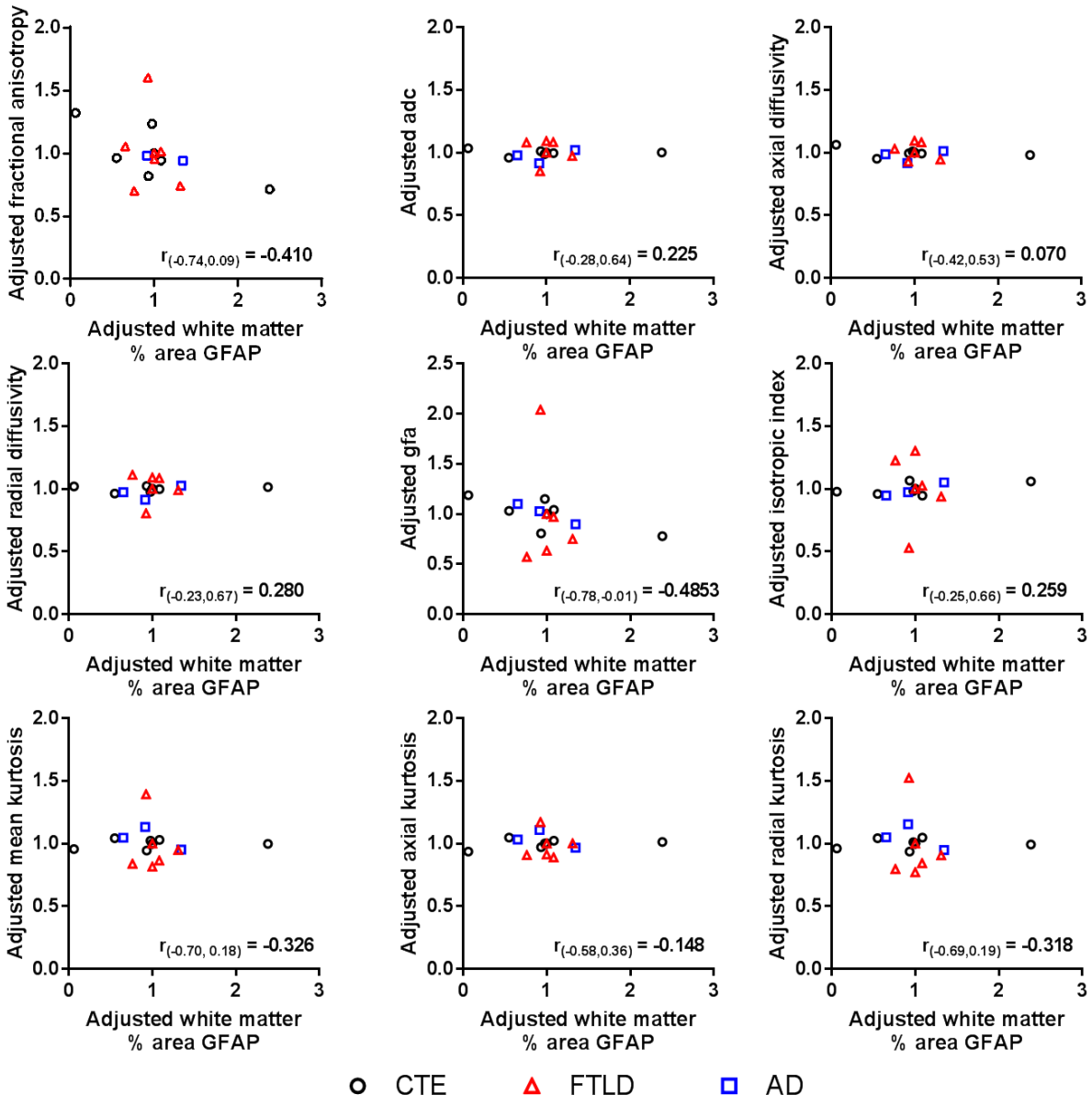

Figure 4.13. No correlation of white matter astrogliosis with diffusion measures in regions adjacent to sulcal depths. Adjusted percent area of GFAP staining was correlated with adjusted DTI, GQI and DKI measures. Spearman's rank analyses did not find sufficiently strong correlations (r>0.88) to test for significance.

4.4 Discussion

In summary, we have implemented quantitative radiological-pathological correlation methods in a blinded sample of tissues with short post mortem intervals diagnosed with either

chronic traumatic encephalopathy (CTE), Alzheimer's disease (AD) or frontotemporal lobar dementia (FTLD). We found that in tissues with CTE, white matter adjacent to sulcal depths showed significantly reduced integrity, which was assessed using power coherence. Moreover, correlation of power coherence with diffusion measures derived from high spatial resolution diffusion data revealed a strong and significant relationship between white matter disruption and fractional anisotropy. In contrast, tissues with non-CTE tauopathies did not show this same pattern of localized white matter disruption, and showed a modest association between fractional anisotropy and power coherence.

This study is complementary to the findings of Holleran et al, which were performed in a larger sample of Stage III/IV CTE tissues (10 tissues, >30 sulcal depths). One major limitation of the previous work was the wide range of post mortem intervals, where the maximum known time between death and sample fixation was 92 hours (Holleran et al., 2017). In contrast, the tissues in this dataset had post mortem intervals of less than twenty-four hours, thereby reducing variability of diffusion measures associated with tissue decomposition (Miller et al., 2011). In the findings of Holleran et al, the relationship between sulcal depth tau and power coherence was modest and negative ($r = -0.55$). In the current study, we also found that this association was modest and negative ($r = -0.517$). Encouragingly, our observations of a relationship between power coherence and fractional anisotropy in CTE tissues also remained consistent with previous findings. Our hypothesis that chronic white matter injury is closely related to sulcal pTau pathology of CTE was supported by the reduced power coherence of sulci adjacent white matter in CTE relative to non-CTE tauopathy tissues. Moreover, power coherence in CTE tissues was strongly and significantly correlated with fractional anisotropy. This correlation did not

generalize to tissues with a diagnosis of AD or FTLD. These results indicate that tau associated white matter disruption is related to fractional anisotropy in CTE tissues.

When considering sulcal depths from both CTE and non-CTE tauopathies, we found that sulcal pTau showed modest, inverse correlation with axial diffusivity. Additionally, gray matter astrogliosis showed modest, inverse correlation with axial diffusivity and modest, positive correlation with axial kurtosis. While none of these correlations were statistically significant, they may be illustrative of changes in diffusion related to cellular responses following injury. In gray matter, microstructural alterations such as neuronal loss and reduced membrane integrity following injury would be expected to increase DTI measures such as mean diffusivity (Rose et al., 2008; Weston et al., 2015). However, the infiltration of cells such as microglia and astrocytes in response to injury would also alter water diffusivity in cortical tissue. While the relationship between pTau and diffusion measures has not been investigated, recent studies have been performed exploring the relationship between astrogliosis and changes in tissue diffusion. In a mouse model of closed headed rotational acceleration injury, gliosis was associated with reduced axial diffusivity (Haber et al., 2017). In contrast, Budde et al found that astroglial scarring following controlled cortical impact (CCI) in a rat contributed to increased axial but not radial diffusivity in the perilesional gray matter, resulting in increased cortical fractional anisotropy (Budde et al., 2011). Blast and controlled cortical impact (CCI) models of TBI in rats have shown changes in measures such as mean kurtosis associated with reactive astrogliosis (Zhuo et al., 2015; Zhuo et al., 2012). These findings of glial associated changes in diffusion measures using animal models, combined with our preliminary findings in sulcal gray matter, may provide an alternative imaging target. Moreover because accumulation of pTau, the basis of CTE staging, is not as strong of a predictor of clinical symptoms compared to concomitant pathological

measures such as microgliosis (Cherry et al., 2016), further investigation of correlates with neuroinflammatory markers such as activated microglia and astrocytes might provide important diagnostic and prognostic information.

One of the primary strengths in this work is our implementation of a histology-MRI coregistration method that allows for correlations of histological measures without being restricted to area fraction of staining. Without such a method, correlations of power coherence with diffusion metrics such as fractional anisotropy would have been impossible. Power coherence as a measure of white matter disruption was integral to this work because we did not observe signs of severe demyelination in any of our tissue samples; white matter quantification using thresholded myelin staining would not have been feasible. Additionally, while neurofilament staining of axonal varicosities has been observed in cases of CTE (McKee et al., 2015b), this histopathological finding has only been reported in limited tissue samples and therefore cannot be considered a definitive marker of CTE. We did not observe positive neurofilament or APP staining in this set of tissues (not shown). Power coherence therefore provided a mode to assess chronic white matter disruption.

We determined that scarring due to accumulation of astrocytes in white matter was not associated with power coherence in either CTE or non-CTE tissues. Interestingly, our data do not show a strong relationship between astrogliosis and changes in associated diffusion measures in sulcus adjacent white matter. Fibrous astrocytes, most commonly found in white matter, have been hypothesized to reduce diffusion in tissue and contribute to changes in white matter anisotropy following injury (Kettenmann H, 2013). Fourier based methods analogous to our measure of power coherence have been used to determine that reduced fractional anisotropy in white matter is associated with demyelination and axonal degeneration but not white matter

astrogliosis (Budde et al., 2011). Furthermore, in an analysis of human corpus callosum white matter, Mollink et al found that astrocytic processes did not significantly contribute to histological measures of orientation dispersion (Mollink et al., 2017).

A clear limitation of this work is the limited sample size of 9-10 sulcal depths per tauopathy group. Power analysis showed that with this sample size, only strong correlations of $r>0.88$ would be sufficient to determine statistical significance. While this study is intended as a follow-up to previous work with a larger sample size, the findings must therefore be cautiously interpreted. In this study, our correlations consisted of sulcal depth and sulcus adjacent regions of interest (1-3 per tissue sample). Consequently there is a potential confound in that regions from one tissue block are not independent of each other. We must also consider the limitation of selection bias. Our dataset was comprised of tissues with Stage III/IV CTE, AD or FTLD. While studies in Stage I/II CTE tissues would be challenging due to the sparse distribution of pTau pathology in the brain, future follow-up studies would be feasible with a larger sample size comprised not only of non-CTE tauopathies but also of chronic TBI cases that do not show CTE pathology. Finally, studies in neurologically healthy, age-matched controls would allow us to make a reasonable interpretation of whether white matter disruption underlying sulcal depths is specific to CTE.

Studies in age-matched controls are also critical when considering the heterogeneity of healthy white matter. While the tissue samples in this study were from superior frontal cortex (Brodmann Area 8/9), we must acknowledge that the white matter tracts being compared are not exactly matched; as is the case with *ex* vivo studies, there is the danger of comparing potential nonequivalent white matter regions (Beaulieu, 2009). We have attributed decreases in power coherence to reduced white matter integrity, but comparisons of equivalent regions would allow

us to determine whether this is indeed the case or whether such regions normally have random fiber organization or more than three fiber paths within a 250 micron isotropic plane. Pierpaoli et al found that in crossing fibers, degeneration of one of the tracts within a voxel would result in increased DTI based fractional anisotropy relative to two crossing, but intact tracts (Pierpaoli et al., 2001). Formation of a glial scar replacing the degenerating crossing white matter tract might contribute to reduced fractional anisotropy, but we found no consistent evidence of astroglial scarring that correlated with power coherence or fractional anisotropy. Therefore, there may be another pathological source of white matter disorganization that we have yet to determine.

Another limitation, just as with other digital histological quantification methods, is the potential of data bias. While we have shown that there is a strong relationship between our thresholding based methods and gold-standard stereology (Holleran et al., 2017), two dimensional sampling is highly vulnerable to underestimation of pathological features (Hsueh et al., 2017). We attempted to address this bias by maintaining a sectioning interval of 250 microns between histological sections, but more accurate estimates of pathology may be feasible using three dimensional imaging techniques such as polarized light microscopy or CLARITY reconstruction methods (Chung and Deisseroth, 2013; Mollink et al., 2017).

Taken together, these findings show that at high spatial resolutions, diffusion MRI has the potential to detect chronic white matter disorganization that is related to chronic traumatic encephalopathy. While such a marker might provide more diagnostic information to patients with suspected CTE, we have not determined that diffusion MRI is yet capable of detecting pTau pathology. Furthermore, subtle alterations in diffusion measures might become undetectable at currently achievable *in vivo* spatial resolutions currently at levels of 1mm isotropic voxel size (Wu et al., 2016). Therefore, further improvements to diffusion imaging methods, or alternative

methods using contrast agents in conjunction with high spatial resolution structural imaging methods might provide a more sensitive and specific diagnosis of CTE.

Chapter 5. Repetitive concussive and subconcussive injury in a human tau mouse model results in chronic cognitive dysfunction and disruption of white matter tracts, but not tau pathology

5.1 Introduction

Chronic traumatic encephalopathy (CTE) is a progressive, neurodegenerative disease that cannot currently be diagnosed in living patients. Individuals with suspected CTE who are diagnosed post-mortem typically have a history of repeated head impacts and often display mood and depressive type symptoms, typically manifesting approximately a decade following the initial impacts, followed by late stage cognitive failure (Bieniek et al., 2015; Mahar et al., 2017; Mez et al., 2017). The distinguishing neuropathological features of CTE, including depositions of phosphorylated tau (pTau) tangles and tau positive astrocytes distributed in depths of cortical sulci and in perivascular regions, are initially observed in the superior and dorsofrontolateral prefrontal cortex. In later stages of CTE, neurofibrillary tangles (NFTs) and astroglial tau are found in the temporal lobe, hippocampus, amygdala, and inferior cortices (McKee et al., 2016; McKee et al., 2015a). Detection of these features is the only means to provide a diagnosis of

CTE, and is performed using immunohistochemical staining of brain tissue. Therefore, an animal model of CTE would provide much needed insight, not only when developing diagnostic biomarkers, but also when testing potential therapeutics *in vivo*.

There have recently been numerous efforts to develop the necessary animal model of CTE using a variety of injury paradigms with mixed results (**Table A.1**). In wild type mice, cognitive and social deficits, accompanied by depressive-like behavior manifest acutely following injury and are present as late as six months post injury (Bajwa et al., 2016; Luo et al., 2014; Mannix et al., 2017; Petraglia et al., 2014a; Petraglia et al., 2014b; Shitaka et al., 2011). For example, Luo et al implemented a repetitive closed head impact model in adult mice that resulted in cognitive deficits during radial arm maze, increased pTau indicated by AT8 immunoreactivity, and astrogliosis indicated by GFAP immunoreactivity (Luo et al., 2014). Concurrent work by Petraglia et al used an increased number and frequency of impacts in adult mice that caused increased risk taking behavior and persistent Morris Water Maze deficits along with increased AT8 and GFAP immunoreactivity at both acute and chronic time points (Petraglia et al., 2014a; Petraglia et al., 2014b). In contrast, an early study by Yoshiyama and colleagues using transgenic mice overexpressing the shortest human isoform (T44) found no significant neurobehavioral differences or histopathological evidence of pTau tangles in injured animals six months following repeated injuries (Yoshiyama et al., 2005). More recent work found that while repetitive closed headed impacts caused progressive behavioral impairments and neuroinflammation, there was no pTau pathology at chronic time points up to six and twelve months post injury using immunohistochemistry methods (Mouzon et al., 2014; Yu et al., 2017). Furthermore, studies of the temporal dynamics of pTau showed an acute increase followed by a return towards baseline at 30 days post injury in wild type mice, a finding paralleled in work by

Tran et al using a single, more severe injury in triple transgenic 3xTG mice (Tran, 2011; Tran et al., 2011; Yang et al., 2015).

The inconsistency of these initial findings raised the question of whether failures of previous attempts to reproduce the chronic and progressive pTau pathology seen in humans was due to the fundamental differences between tau in the human and mouse brain. While wild type mice typically express only the 4R isoforms of tau, the human brain expresses 3R and 4R isoforms in equal amounts (Andorfer et al., 2003; Goedert et al., 1989; Guo et al., 2016) This furthers the motivation to study the chronic effects of repetitive TBI in mice that express the tau isoforms seen in humans (hTau). These mice have been reported to develop age-associated thioflavin S neurofibrillary tangles between nine and 15 months of age, along with cognitive deficits that manifest at twelve months of age (Andorfer et al., 2003; Polydoro et al., 2009). Preliminary work exploring the relationship between brain injury and pTau pathology in the hTau mouse line was performed by Ojo et al, and showed that repetitive impacts in aged (18 months old) mice resulted in increased cortical pTau along with increased neuroinflammation (Ojo et al., 2013). The same group found that adult hTau mice exposed to repeated head injuries also had increased cognitive deficits along with elevated total tau levels at six months following injury (Ojo et al., 2016). These studies provide an initial insight into the role of repeated brain trauma and chronic pTau pathology but do not consistently show progressively worsening neurobehavioral deficits nor the neurofibrillary tangles and tau positive astrocytes that are pathognomonic for CTE.

Of note, all of the previously described models involved primarily impact injuries, whereas a large number of human concussive injuries appear most closely related to rotational acceleration (Zhang et al., 2006). Implementation of a rotational acceleration injury model in

gyrencephalic animals such as pigs has resulted in accumulation of tau colocalized with ßAPP and neurofilament staining indicative of axonal injury, illustrating the need to incorporate such a component in order to better mimic the brain trauma experienced during a concussive or subconcussive event (Smith et al., 1999). The CHIMERA (Closed Head Impact Model of Engineered Rotational Acceleration) is potentially advantageous for this very reason. This model combines high injury reproducibility with the ability to implement a nonsurgical impact plus rotational acceleration injury in small, lower cost animals such as mice (Namjoshi et al., 2014). A recent study using three 0.5J injuries has resulted in chronic cognitive deficits accompanied by increased Iba1 and GFAP levels as late as six months post injury (Chen et al., 2017a).Furthermore, the versatility of impact thresholds at subconcussive and concussive levels has previously been tested and shows neurobehavioral and histopathological changes in the rodent brain (Namjoshi et al., 2017).

We have implemented a repetitive CHIMERA injury paradigm in hTau mice at two energy levels; concussive and subconcussive. The aim of the study is to determine the cumulative effects of repetitive brain trauma in adult mice (4 months of age) at acute (one month), intermediate (three months), and chronic (twelve months) time points post injury. We hypothesized that the repeated impacts plus rotational acceleration would induce tissue shearing, white matter disruption, and in the chronic phase, accumulation of cortical and perivascular neurofibrillary tangles, astrogliosis, and white matter disruption accompanied by progressive neurobehavioral deficits comparable to those exhibited by patients with a diagnosis of CTE. As part of our pre-specified plan, cerebrospinal fluid (CSF) and blood was collected prior to sacrifice for exploration of potential fluid biomarkers of chronic phase repetitive concussive TBI-related tau pathology.

5.2 Methods

5.2.1 Animals

Fifty hTau mice (C57BL/6 Cg-Mapt<tm1(EGFP)Klt>(MAPT), Cat #00549, Jackson Laboratory, Bar Harbor, ME, USA) aged 4-8 weeks were purchased as two cohorts of twenty five animals each. All mice were allowed to acclimate to 12 hour light-dark cycles. Food and water were supplied *ad libitum*.

5.2.2 CHIMERA injury and anesthesia

Injuries were performed using the CHIMERA injury method, which involves a midline closed head impact followed by rotational acceleration. Each animal was anesthetized with 5% isoflurane for 2.5 minutes followed by maintenance at 2.5% isofluorane during positioning on the platform. Total isoflurane exposure did not exceed five minutes and delivery was stopped immediately before impact. Sham animals underwent the same anaesthesia protocol and head positioning on the CHIMERA device but no impact by the piston.

5.2.3 Determination of injury thresholds

Because animals were exposed to twenty daily impacts, the energy levels for subconcussive and concussive impacts were determined empirically (**Figure A.1A**). Latency to right reflex (LRR), defined as the time from impact to regaining consciousness and becoming upright was used as the acute metric of injury. In an initial study, wild type mice (C57Bl6/J, Jackson Laboratory, Bar Harbor, ME) were randomly assigned to receive a single impact with piston pressure set to range between 0 and 2.4 psi. Injuries were performed using the same anesthesia and head placement protocol described above and righting time was recorded and

used to determine the subconcussive threshold. Mice injured with piston pressures greater than 1.9 psi (0.13J energy intensity) all had mean righting times greater than the sham average.

Previous work using the CHIMERA device has determined that a single impact below 0.5J does not result in phenotypic deficits, including any increases in LRR time.(Namjoshi et al., 2017) However, our pilot study with a single impact showed that animals receiving impacts between energy intensities of 0.13J and 0.24J (3.1 psi piston pressure) had increased LRR times (**Figure A.1A**). Furthermore, because we were interested in the cumulative effect of repeated injuries rather than a single impact, a second study was performed using wild type mice. These mice were randomly assigned to receive 20x sham, 20x 0.13J or 20x 0.24J injuries spaced 24 ± 1 hour apart. Righting times were recorded daily. The average righting time over the course of the twenty injuries was then calculated for each group and analyzed using a one way ANOVA followed by a post-hoc Tukey test (**Figure A.1B**). There was a significant effect of injury in this study ($F_{(2,31)} = 28.99$, $\eta^2_p = 0.652$, $p < 0.00001$). Animals in the 0.24J group had increased righting times relative to shams and 20x 0.13J mice (20x sham vs 20x 0.24J, $p = 0.000126$, 20x 0.13J vs 0.24J, $p = 0.000125$). Based on these data we determined a subconcussive energy threshold of 0.13J and a concussive energy threshold of 0.24J.

5.2.4 Injury timeline

At four months of age, hTau mice were assigned to 20x concussive injury, 20x subconcussive injury, or 20x sham groups using a random number generator. Following impact or sham, each animal was placed supine in a warmed chamber (37°C) and monitored by an investigator blinded to injury status in a quiet, separate room until fully upright and ambulatory. LRR was recorded by this investigator. For sham animals, LRR was defined as the time from when isofluorane delivery was stopped to regaining consciousness. After regaining

consciousness, each animal was returned to its home cage. This procedure was repeated for twenty consecutive days with injuries spaced 24 ± 1 hour apart, such that each animal received twenty head impacts or sham procedures (**Figure 5.1A**). A Cox regression for survival analysis was performed to determine the effect of injury on survival post injury (**Figure 5.1B**), and showed that there was a significant effect of injury status on survival (p= 0.0304), with a trend towards more deaths in the 20x concussive injury group.

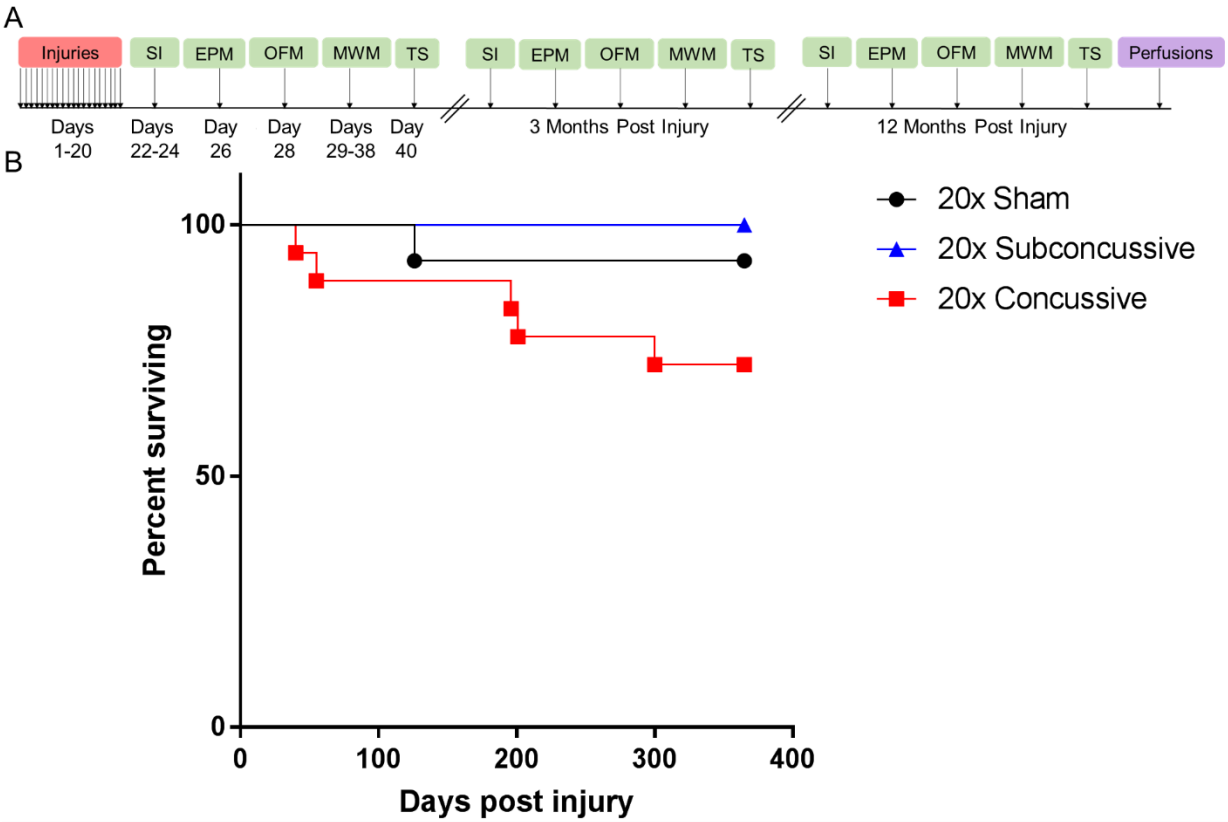

Figure 5.1 Injury timeline and survival post injury. A. Fifty male hTau mice were purchased in two separate cohorts. Animals were randomly assigned to sham, 20x subconcussive (0.13J) or 20x concussive (0.24J) injury groups. Following twenty days of injuries, behavioral outcomes including social interaction (SI), elevated plus maze (EPM), open field maze (OFM), Morris water maze (MWM) and tail suspension (TS) were assessed acutely, at three months, and one year post injury. Following the 12 month behavioral test session, all animals were perfused. **B.** Survival and mortality risk were assessed using a Cox survival and hazard regression analysis. The data showed a modest but significant (p=0.03) effect of subconcussive or concussive injury on mortality rate.

5.2.5 Behavioral testing

All neurobehavioral testing was performed in a specified behavior room isolated from external noise and with light and sound controls. 60 dB white noise (Marpac Dohm-DS, Wilmington, NC, USA) and lighting (40 lux for Morris Water Maze, 20 lux for all other tests) was controlled for all testing. Neurobehavioral tests were performed during the workday (6am-6pm). All equipment was cleaned with 70% ethanol prior to each test to remove scents. Animals were allowed to acclimate in the room for at least one hour before testing. Following injuries, cages were renumbered such that the investigator remained blinded to injury status during the following behavioral testing. Behavioral testing was performed at three time points, acutely, three months and one year following injuries. With the exception of tail suspension, all tests were recorded on video and subsequently analyzed using Panlab SMART (Harvard Bioscience, Holliston, MA, USA).

Social interaction and social novelty: Crawley's three chamber test was used to measure social interaction and social novelty (Nadler et al., 2004). Test mice were singly housed for 24 hours prior to testing. On testing day, the test mouse was placed in a 42 x 70cm three chamber box made of opaque white plastic. Following a five minute habituation session where the mouse was allowed to freely explore all three chambers, the test mouse was then confined to the middle chamber during preparation for the preference for sociability session. A stimulus mouse (male C57BL/6 aged 6-8 weeks) was placed in a wire cage in one chamber while a dummy mouse made of black Legos was placed in a wire cage in the opposite chamber. The test mouse was then allowed to explore all three chambers for ten minutes. The test mouse was then confined again to the middle chamber prior to preference for social novelty testing. The dummy mouse used during sociability testing was replaced with a novel stimulus mouse (male C57BL/6 aged 6-8 weeks). The test mouse was then allowed to explore all three chambers for ten minutes.

Because each testing session required approximately 30 minutes of test time, stimulus mice were used in pairs and allowed to rest while a second pair of stimulus mice was used for the next test mouse. Time spent interacting with each mouse was measured by tracking the time the mouse spent sniffing within a 1.5cm radius around each wire cage. Activity such as climbing on top of the wire cage was not counted as interaction.

Elevated plus maze: A custom maze (30cm high) with arms that were 30cm long and 5cm wide was used for testing. Closed arms were enclosed by 16cm high walls while open arms had a 2mm railing to prevent mice from falling. Mice were placed in a closed arm and allowed to explore the maze for five minutes. A 5cm square was defined as the center zone, requiring the mouse to have all four paws in an arm of the maze to be quantified in SMART as being in that arm. Time spent in all zones (open arms, closed arms, center zone) was quantified using SMART.

Open field test: Mice were placed in a 44.5 x 44.5cm box made of white opaque plastic and allowed to explore for five minutes. Thigmotactic behavior was defined as the average distance away from the wall. Briefly, the time spent moving was measured using Panlab SMART. During video analysis the box was divided into fifteen concentric zones spaced 1.5cm apart. Time spent in each zone was weighted by zone distance from the maze wall and summed to obtain a time-weighted average.

Morris Water Maze: A 120cm diameter pool was filled with 22°C water made opaque using non-toxic white tempera paint. For each day except for probe trial, mice were required to swim for four trials per day, and were inserted into four locations in the pool (NW, SW, SE, NE) and allowed to swim for a maximum of one minute to reach the 11 cm platform. The order of insertion points was changed each day. During the visible platform phase (three days,

Wednesday-Friday), a flag was placed on the platform so that it would be clearly visible. For the hidden platform phase (four days, Monday-Thursday), opaque white curtains were hung to enclose the pool, with prominent visual cues in each quadrant. The platform was then moved to a different quadrant and the water level was increased so that the platform was hidden under 1cm of opaque white water. To control for memory retention between test sessions, the hidden platform was placed in a different quadrant for each test session. For hidden and visible platform testing, the average distance swum, average swim speed, and latency to platform were recorded and calculated using Panlab SMART. Twenty-four hours following the final day of hidden platform testing, the platform was removed from the pool. Mice were then subjected to a single probe trial, where each mouse was inserted at the insertion point furthest from where the hidden platform had previously been and allowed to swim for thirty seconds. The percentage of time spent in the target quadrant as well as mean proximity from the platform were recorded and calculated using Panlab SMART.

Tail Suspension: A white paper cone was placed on each animal's tail to prevent climbing behavior commonly exhibited in C57Bl/6 mice. Mice were then suspended from a rod at a height of 30cm by their tails. The total test time was six minutes. Time immobile, defined as any time the mouse was not moving except swinging from previous movement, was recorded manually by an investigator blinded to injury status.

5.2.6 Cerebrospinal Fluid, Blood, and Tissue collection

Following the one year time point of behavioral testing, mice were sacrificed. Animals were randomly assigned a new identification number to assure blinding during histological analysis. Mice were anesthetized with a 75 mg/kg dose of pentobarbital administered IP. When mice remained unresponsive to tail or toe pinch, they were placed on a pad heated to 37°C, and

CSF was extracted from the cisterna magna (DeMattos et al., 2002). Mice were then transcardially perfused using ice cold 0.3% PBS-heparin solution and approximately 800 microliters of blood was collected using the cardiac bleeding method. Following tissue extraction, the brain was separated into two hemispheres. The left hemisphere was drop fixed overnight in 4% paraformaldehyde and then switched to 30% sucrose solution, stored at 4°C. The right hemisphere was dissected on a chilled aluminum foil plate into cortical and hippocampal regions and stored at -80°C. Blood samples were allowed to clot for a minimum of one hour, and then blood and CSF were centrifuged at 2,000 x g to extract serum samples, which were stored at -80°C. Results from CSF, blood and frozen brain tissue analyses will be reported separately.

5.2.7 Immunohistochemistry

Fixed brain tissue was sectioned coronally into 50 μm thick sections using a freezing sliding microtome (Microm HM 430, ThermoFisher Scientific, Waltham, MA, USA) in a 1:6 series and stored in cryoprotectant (sucrose dissolved in sodium phosphate buffer, pH 7.4 and ethylene glycol) at 4°C. Total human tau was detected using monoclonal HT7 (Cat# MN1000, ThermoFisher Scientific, Waltham, MA, USA). Primary antibodies used to detect phosphorylated tau included monoclonal AT8 (Cat# MN1020, ThermoFisher Scientific, Waltham, MA, USA), CP13 (courtesy of Peter Davies, Albert Einstein College of Medicine, NY, USA) and RZ3 (courtesy of Peter Davies, Albert Einstein College of Medicine, NY, USA). Activated astrocytes were detected with polyclonal GFAP (Cat# AB5541, Millipore Sigma, St Louis, MO) respectively. For tau staining, antigen retrieval was performed using a five minute incubation in 70% formic acid. Sections were then incubated in 0.3% hydrogen peroxide solution to block endogenous peroxidase and then blocked for thirty minutes in 3% serum diluted in TBS-

X. Normal goat serum (Cat# S-1000, Vector Laboratories, Burlingame, CA, USA) was used for tau staining, while normal donkey serum (Cat# 017-000-121, Jackson Immunoresearch, West Grove, PA, USA) was used for GFAP staining. Sections were then incubated overnight at 4°C in primary antibody diluted 1:1000 in 3% serum. Tissue from an uninjured 22 month old 3xTG mouse was used as a positive control for tau pathology, while tissue from a mouse injured using the controlled cortical impact injury model was used as a positive control for GFAP staining (Mac Donald et al., 2007a; Oddo et al., 2003). Negative controls with the primary antibody excluded were performed for all stains. The next day, sections were incubated in secondary antibody diluted 1:1000 in TBS-X for one hour. For AT8 staining, biotinylated goat anti-mouse (Cat# BA-9200, Vector Laboratories, Burlingame, CA, USA) was used while biotinylated donkey anti-chicken (Cat# 703-065-115, Jackson Immunoresearch, West Grove, PA, USA) was used. Sections were incubated for one hour in ABC solution (Cat# PK-6100, Vector Laboratories) diluted 1:400 A and B in 1xTBS, followed by visualization using 3'3' diaminobenzidine (Cat# D5905-100TAB, Sigma Aldrich, St. Louis, MO). Sections were washed three times in 1x TBS between each step.

5.2.8 Myelin Black Gold II staining

Tissue sections were first washed in TBS to remove residual cryoprotectant. Black Gold II solution was prepared by resuspending 150 mg dry Black Gold II powder (Cat# AG400, Millipore Sigma, St. Louis, MO) in 0.9% saline solution. The Black Gold II solution was then heated to 60°C. Free floating tissue sections were incubated in the solution for 8-12 minutes until fibers were completely stained (**Figure A.2**). Following two washes in Milli-Q water, sections were incubated in 0.1% sodium thiosulfate solution heated to 60°C for three minutes. The tissue sections were then washed three times in TBS to remove trace sodium thiosulfate.

5.2.9 Quantification of histology

Following staining, tissue sections were mounted onto positively charged slides, dehydrated in a series of graded ethanols (50%-70%-95%-100%-100%), and cleared in three changes of xylenes before being coverslipped (No. 1.5, Cat # 48393-241, VWR). Images of stained sections were acquired on a Zeiss Axioscan (Carl Zeiss AG, Oberkochen, Germany) using a brightfield 10x objective lens and then exported at their original resolution into tiff format for quantification. Regions of interest (ROIs) in the gray matter included cortical gray matter (4-5 sections/animal), lateral septal nucleus (1 section/animal), and the hippocampus (3-4 sections/animal). White matter intact (>50% of region without folds or tears) ROIs included the corpus callosum (4-5 sections/animal) anterior commissure (1 section/animal), hippocampal commissure (1 section/animal) and fimbria (2 sections/animal).

To quantify GFAP staining, the Renyi entropy thresholding method was applied to all images (**Figure A.3**). Similar to Myelin Black Gold II analysis, ROIs were included and considered intact only if >50% of the region was without folds or tears. To exclude remaining edge and fold artifacts, only particles with an area of 10-500 pixels were included in analysis.

Because there were no signs of severe demyelination in any of the tissue sections, we used power coherence as a measure of white matter integrity as previously described (Gangolli et al., 2017). Briefly, each ROI was subdivided into square regions with an area of 10 pixels^2. This area was used in order to sustain sufficient spatial resolution and prevent artifacts caused by multiple crossing fibers, while also removing noise related artifacts. A two tensor model was then fit to the power spectrum of each subdivided region. Power coherence, a metric ranging from zero to one was calculated by subtracting the ratio of the major and minor axes of the tensors from one.

5.2.10 PCR Confirmation of Genotype

PCR was used to confirm the hTau genotype from one animal selected at random from each cohort of hTau mice. DNA from the leftover regions of the fresh-frozen brain tissue was extracted using the EZ High MW Mouse Tail DNA Isolation Kit (Cat# M1007-100, EZ Bioresearch, St. Louis, MO). Nuclei lysis and Proteinase K solution were added to the tissue sample and incubated overnight at 55°C with gentle shaking until the tissue was completely digested. The next day, protein precipitation solution was added to the mixture. Following a five minute incubation on ice, the solution was centrifuged at 16,000 x g for three minutes at room temperature, separating the protein pellet from supernatant. Isopropanol was added to the supernatant and inverted until DNA was visible as threads. The supernatant and isopropanol solution was then centrifuged 16,000 x g for one minute at room temperature. The supernatant was then removed from the microcentrifuge tube and the remaining DNA pellet was washed with 70% ethanol. The DNA pellet was centrifuged and washed again with 70% ethanol. Any residual supernatant was then removed and the DNA pellet was allowed to air dry for ten minutes. DNA Hydration Solution was added to the pellet and incubated at 65°C for one hour with gentle shaking. The extracted DNA was then stored at 4°C until PCR genotyping. Tail DNA from an hTau mouse was obtained from an independent investigator to use as an external positive control.

Control (htau ctrl R : 5'- GTA GGT GGA AAT TCT AGC ATC ATC C -3', htau ctrl F : 5'- CTA GGC CAC AGA ATT GAA AGA TCT -3') and hTau specific oligonucleotides (htau R : 5'- CTC TGC ATG GCT GTC CAC TAA CCT T -3', htau F : 5'- ACT TTG AAC CAG GAT GGC TGA GCC C -3') were resuspended to 100µM concentration in molecular grade water. The extracted DNA was thawed on ice and diluted to a final concentration of 100 ng/µL. A solution

of DNA, control or hTau oligonucleotides (0.2 µM), GoTaq Flex (Promega, Madison, WI, USA), dNTPs, reaction buffer and enhancer was then prepared in molecular grade water and heated using a thermocycler. Thermocycler conditions were 94°C for 30 seconds, 58°C for one minute, and 72°C for 1 minute for 35 cycles each, with a final extension phase of 72°C for two minutes. PCR was visualized on a 1% agarose gel.

5.2.11 Statistical Methods

All analysis was performed using Statistica (Tibco Software Inc., Palo Alto, CA, USA). All data was tested for normality using the Shapiro-Wilk normality test. Any datasets which violated the assumption of normality were transformed so that parametric analyses could be performed (**Table A.5**). A two-way, repeated measures ANOVA was performed for each neurobehavioral metric to test for the effects of injury and cohort, with test session (acute, three month, one year) being the within-subject factor. Two-way ANOVAs were used to analyze the LRR data and histological data. We prespecified the statistical plan to collapse across the two cohorts of mice for analyses for which there were no significant main effects or cohort of interactions with of other factors with cohort. Statistical power calculations for main effects of injury was 80% at $p<0.05$ with an effect size of 0.50. Animals that died before the end of the experiment were excluded from behavioral and histological analysis. Post-hoc Tukey tests were then used to determine significance for specific pairwise comparisons ($p<0.05$). Because the residuals were not normally distributed, a Spearman's rank correlation was used to determine the relationship between white matter power coherence and Morris water maze measures (four ROIs x five behavioral measures = 20 correlations). This was followed by Bonferroni correction for multiple comparisons, where the effective number of tests was adjusted to account for potential correlation between measures (Cheverud, 2001). Without this adjustment, the Bonferroni

correction at $p<0.05/20 = 0.0025$, however, with the variance of the eigenvalues of the correlation matrix ($v_{\lambda obs} = 1.265$), the adjusted Bonferroni at $p <0.05/18.79 = 0.0027$. Effect sizes were calculated for each test that was performed (**Table A.6**). Graphs were plotted using Prism v7.0 (Graph Pad, La Jolla, CA, USA). All error bars represent standard error of mean (SEM).

5.3 Results

5.3.1 hTau mice show injury dependent differences in righting time

Loss of consciousness, measured by righting time (LRR) was used to measure the immediate effects of injury during the twenty days of impacts (**Figure 5.2**). LRR was calculated by measuring the righting time each day of injury, and averaging across days. A two way ANOVA showed that there was a significant effect of injury ($F_{(2,44)} = 11.8092$, $\eta^2_p = 0.349$, $p < 0.0001$). Animals in the 20x concussive group had elevated righting times compared to 20x shams ($p = 0.00059$) as well as animals in the 20x subconcussive group ($p = 0.00046$) after post hoc Tukey testing. There was no difference in righting times between 20x shams and animals in the 20x subconcussive group ($p = 0.985$). There was no effect of cohort or interaction between injury and cohort. These data show that the higher energy concussive impacts caused a significantly more substantial acute injury than the lower energy subconcussive impacts.

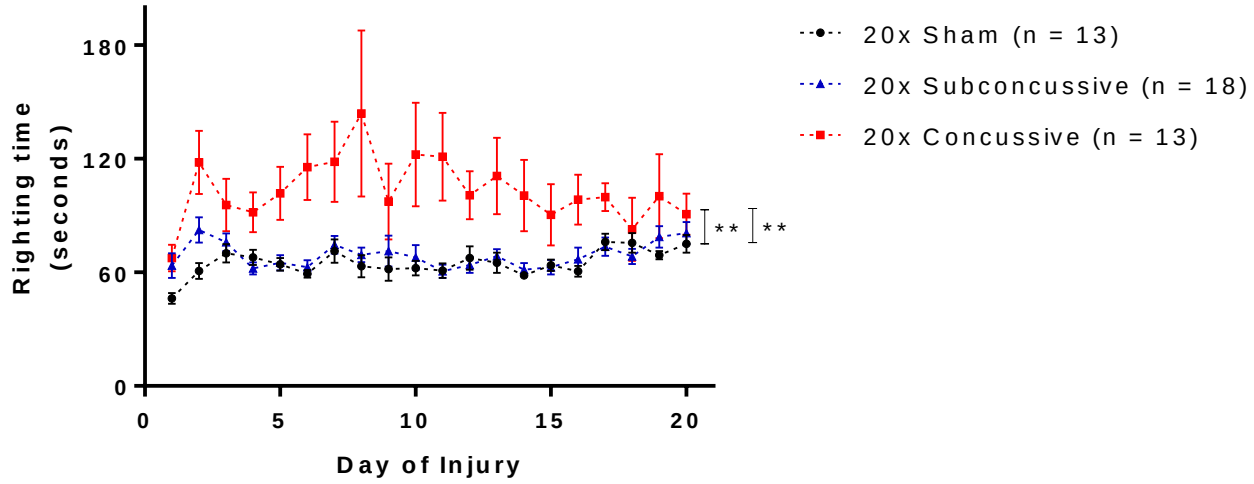

Figure 5.2 Loss of consciousness following injury. Latency righting reflex was used as a measure loss of consciousness. Righting times were measured by an observer blinded to injury status. Animals in the concussive injury group had increased righting times relative to the subconcussive and sham groups, which were indistinguishable. There was a significant effect of concussive injury on righting time, with animals in the 20x concussive group having increased righting times relative to 20x shams ($p = 0.00059$) and 20x subconcussive mice ($p = 0.00046$).

5.3.2 hTau mice subjected to repeated concussive injuries show persistent chronic cognitive deficits

At acute, three month and twelve month time points, animals were tested for learning deficits using the Morris Water Maze task. During the three days of visible platform testing (**Figure 5.3**, **Figure A.4**), the two way, repeated measures ANOVA, showed a main effect of injury on swim speed ($F_{(2,36)} = 29.9335$, $\eta^2_p = 0.624$, $p < 0.00001$). Animals in the 20x concussive group had reduced swim speeds relative to both shams ($p = 0.000127$) and mice in the 20x subconcussive injury group ($p = 0.000128$). There was no interaction between test session (acute, three month, twelve month) and injury. There was also a main effect of injury on distance to the target ($F_{(2,36)} = 25.642$, $\eta^2_p = 0.588$, $p < 0.00001$). Animals in the 20x concussive group had increased swimming distances relative to shams ($p = 0.000127$) and mice in the 20x subconcussive injury group ($p = 0.000127$). There were no differences between subconcussive

injury and sham groups (p = 0.923). There was no effect of test session or interaction between test session and injury on swim speed or distance swum.

At each test session, two days following the final day of visible platform testing, animals underwent hidden platform testing of the Morris Water Maze task for four consecutive days (**Figure 5.4**, **Figure A.5**). Similar to the visible platform phase, the two way repeated measures ANOVA showed an effect of injury on swim speed ($F_{(2,36)} = 36.5009$, $\eta^2_p = 0.663$, $p < 0.00001$) that remained significant after post-hoc testing. Mice in the 20x concussive group had reduced swim speeds relative to 20x shams (p = 0.000125) and mice in the 20x subconcussive group (p = 0.000128). Animals in the in the 20x subconcussive group also had reduced swimming speeds relative to 20x shams (p = 0.028). There was also an effect of injury on swimming distance during the hidden platform phase ($F_{(2,36)} = 6.272$, $\eta^2_p = 0.564$, $p<0.01$) that remained significant following post-hoc Tukey testing. Animals in the 20x concussive group had increased swimming distances relative to 20x shams (p = 0.044) and animals in the 20x subconcussive group (p = 0.009). There was no difference in swimming distance between subconcussive injury and sham groups (p = 0.867). There was no effect of test session on either swim speed or swimming distance. There was also no interaction between test session and injury on either of these measures.

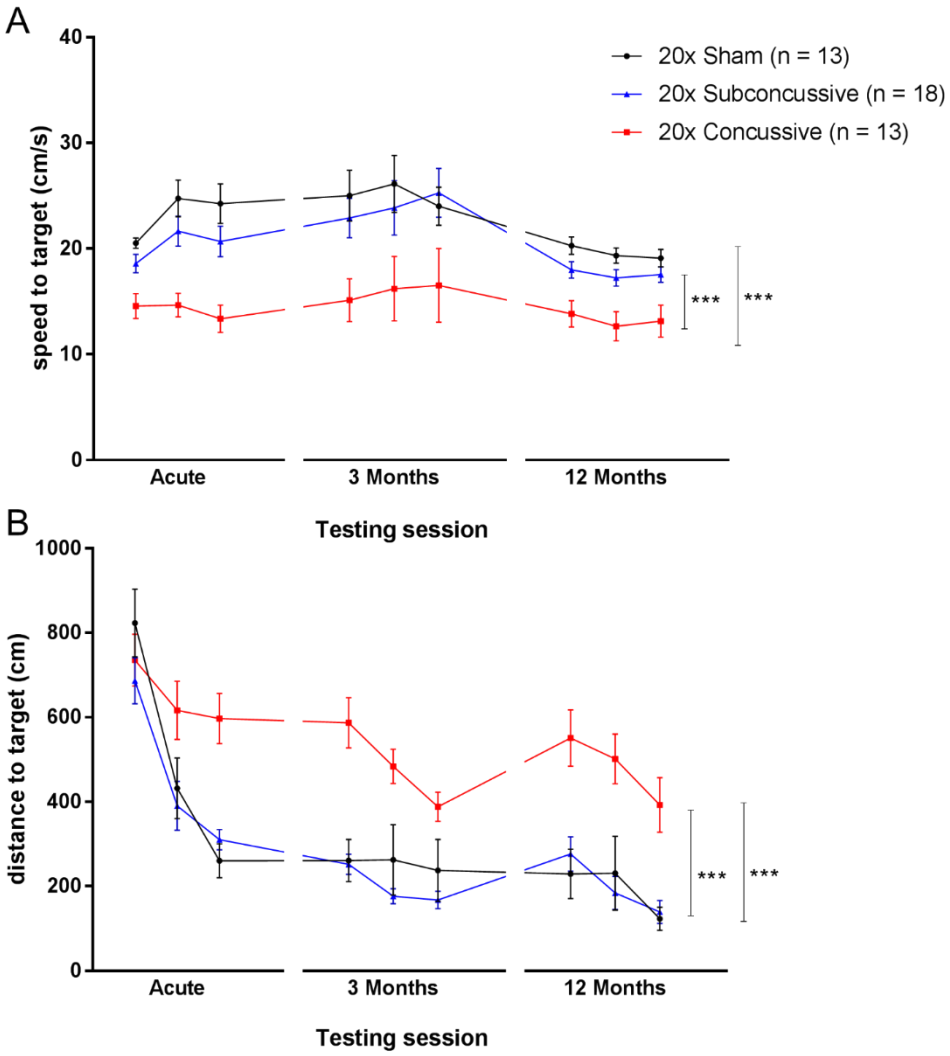

Figure 5.3 Effects of injury on visible platform phase of the Morris water maze. A. Average swimming speeds for each day of the visible phase of the Morris water maze during each of the three test sessions. There was a significant effect of injury on swim speed (0.24J vs sham: $p = 0.000127$, 20x concussive vs 20x subconcussive: $p = 0.000128$). There was no interaction between test session and injury. **B.** Total distance to the target platform during three days of visible platform testing. There was a significant effect of repetitive concussive injury (20x concussive vs sham: $p = 0.000127$, 20x concussive vs 20x subconcussive: $p = 0.000127$).

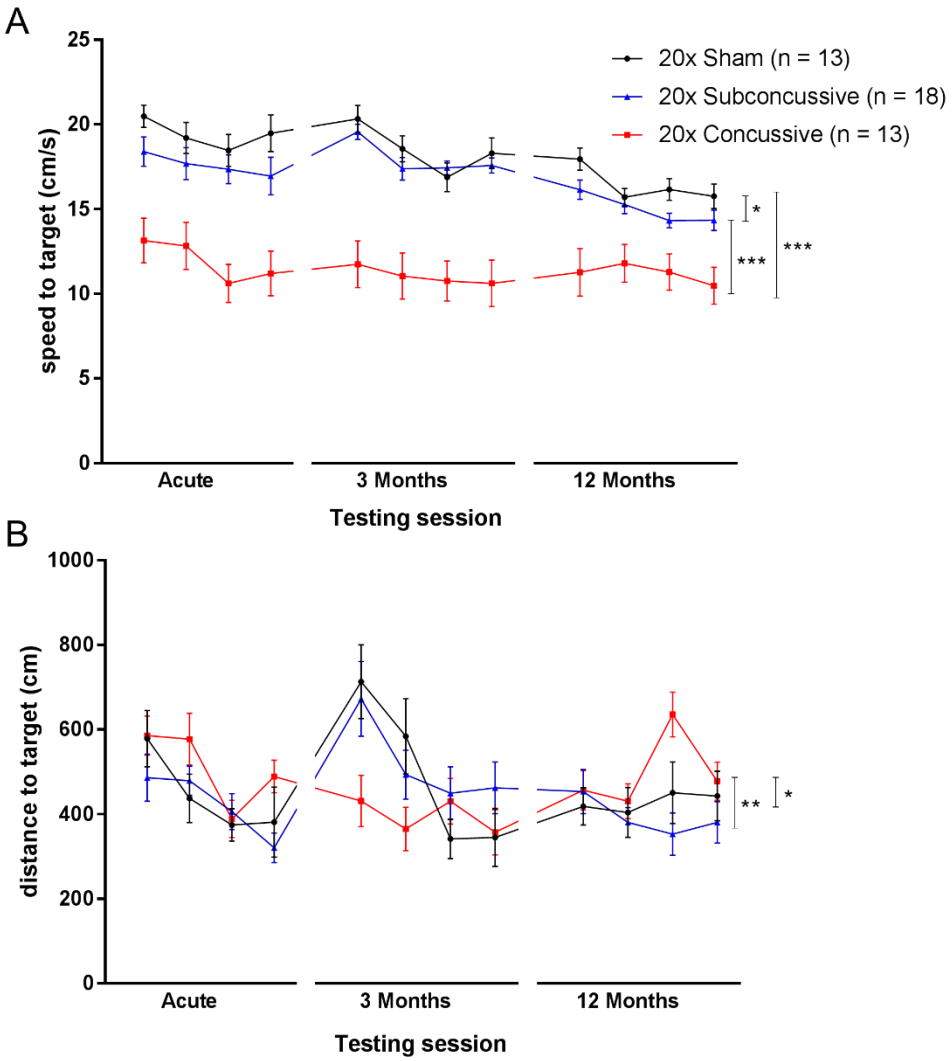

Figure 5.4 Effects of injury on hidden platform phase of the Morris water maze. A. Average swimming speeds for each of the four days of the hidden platform task during each of the three test sessions. There was a significant effect of injury (20x concussive vs sham, p = 0.000125, 20x concussive vs subconcussive, p = 0.000128). Mice in the 20x subconcussive group also had reduced swimming speeds relative to shams (p = 0.028). **B.** Total distance to the target platform during four days of hidden platform testing. There was a significant effect of concussive injury (20x concussive vs sham: p = 0.044, 20x concussive vs 20x subconcussive: p = 0.009). There was no interaction of test session and injury.

Twenty four hours after the final day of hidden platform testing, hTau mice were tested for memory retention using the probe trial of the Morris Water Maze task (**Figure 5.5**, **Figure A.6**). Mean proximity to platform and percent time spent in the target quadrant were used as metrics of memory retention for each test session. For the measure of mean proximity to

platform, there was an effect of injury ($F_{(2,36)} = 23.173$, $\eta^2_p = 0.570$, $p < 0.00001$) and time ($F_{(2,70)} = 6.9935$, $\eta^2_p = 0.167$, $p < 0.01$) on mean proximity to platform that remained significant after post-hoc testing. Animals in the 20x concussive injury group were further away from where the hidden platform had previously been placed relative to both shams ($p = 0.000124$) and 20x subconcussive animals ($p = 0.000126$). Animals also had increased proximity to the target platform during the three month test session ($p = 0.000280$) relative to the acute test session. There was also an effect of injury on percent time in the target quadrant ($F_{(2,36)} = 22.851$, $\eta^2_p = 0.566$, $p < 0.00001$) that remained significant after post-hoc testing. These same animals also spent significantly less time in the target quadrant relative to shams ($p = 0.000124$) and 20x subconcussive animals ($p = 0.000123$). There were no significant differences between animals in the 20x subconcussive group or 20x sham group for either proximity to platform or percent time spent in the target quadrant. There was no interaction between time and injury for either parameter.

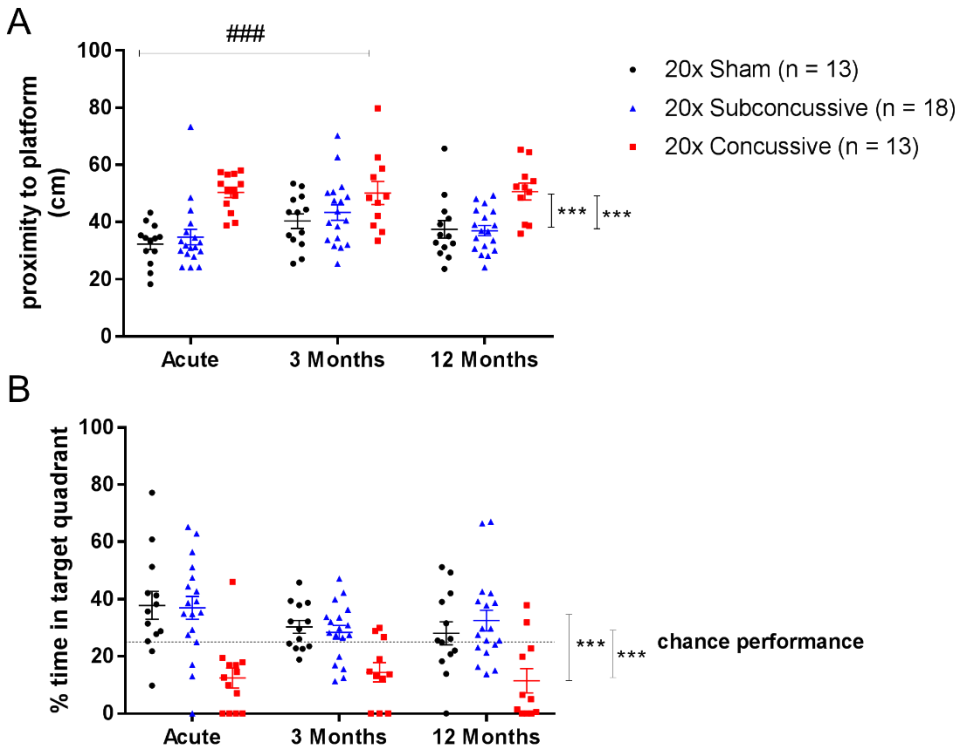

Figure 5.5 Effects of injury on Morris water maze probe trial performance. A. There was a significant effect of concussive injury on average proximity to platform during probe trial; 20x concussive vs 20x sham: p =0.000124, 20x concussive vs 20x subconcussive: p = 0.000126). There was also an effect of time, where animals were significantly further away from the platform at the 3 month test session (p = 0.000280) relative to the acute session (###). Animals in the repetitive concussive injury group were on average further away from the location of the target platform. **B.** There was a significant effect of concussive injury on the percent time spent in the quadrant where the platform had previously been placed (20x concussive vs sham: p =0.000124, 20x concussive vs 20x subconcussive: p = 0.000123). Animals in the repetitive concussive injury group tended to spend less than 25% of their time (chance performance, dotted line) in the target quadrant. There was no interaction between test session and injury.

In summary, repetitive concussive injury resulted in reduced swim speed during both visible and hidden platform phases of Morris Water Maze, a possible indication of reduced motor function or motivation following injury. Furthermore, repetitive concussive injury also caused an increase in distance swum to the target. This effect indicates an impairment in ability to learn the platform location. Moreover, repetitive concussive injury resulted in impaired memory, demonstrated by increased proximity to platform and reduced percent time in target quadrant during the probe trial. These findings, combined with the effect of time on proximity to the platform during only intermediate session of probe trial indicates that the 20x concussive

injury method implemented in this study causes acute cognitive deficits that neither progressively worsen nor resolve at one year post injury. Instead, these changes in learning and memory appear to remain sustained at a reduced level relative to shams and animals in the 20x subconcussive group.

5.3.3 No social interaction deficits, anxiety or depressive-like behaviors detected after repeated injury in hTau mice

The sociability and social novelty phases of Crawley's three chamber social interaction test were used to measure both acute and chronic social behaviors (**Figure 5.6**, **Figure A.7**). For the sociability test, the ratio of time spent interacting with the stimulus mouse to time spent interacting with the novel object was used as an index of sociability. For the social novelty test, the ratio of time spent interacting with the novel mouse to time spent interacting with the previous stimulus mouse was used as an index of social novelty. The two way repeated measures ANOVA showed no effect of injury on either sociability index ($F_{(2,37)} = 0.300$, $p = 0.74$) or social novelty testing index ($F_{(2,37)} = 2.729$, $p = 0.78$). There was also no effect of test session on either index.

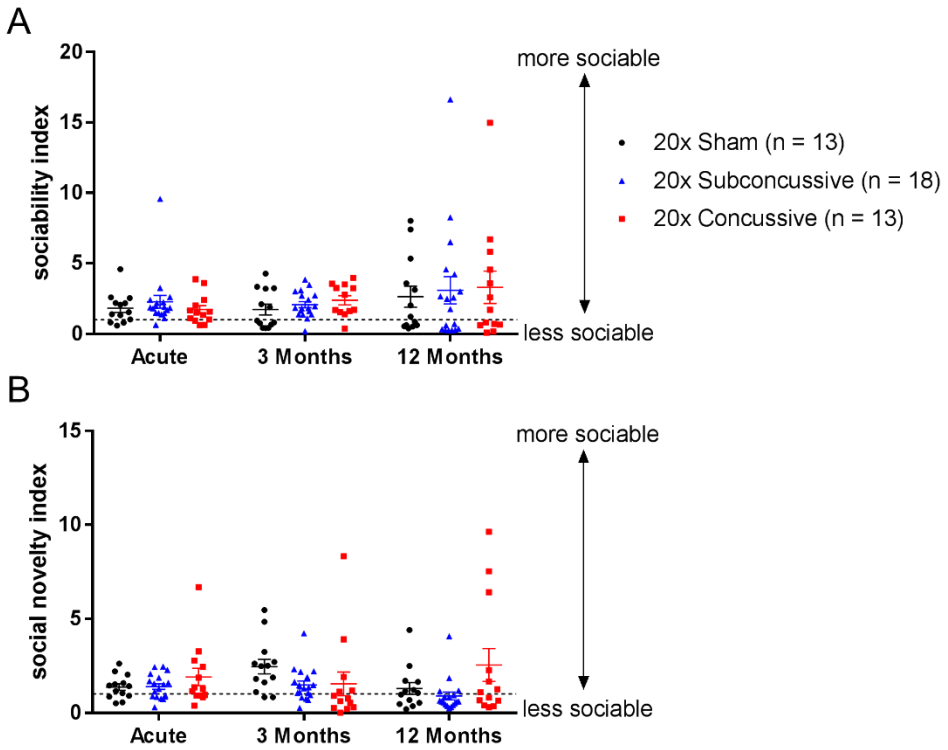

Figure 5.6 No change in social interaction following injury. A. Injured animals did not show any significant changes in sociability compared to shams. Dotted line indicates a sociability index of one. Points above this line indicate that the animal showed preference for the stimulus mouse rather than the novel inanimate object. **B.** Injured animals did not show any significant changes in social novelty compared to shams. Dotted line indicates a social novelty index of one. Points above this line indicate that the animal showed preference for the novel mouse rather than the stimulus mouse from the previous sociability session.

Anxiety-like behavior was measured using two behavioral measures, open arm time during the elevated plus maze task, and thigmotaxis during the open field maze task (**Figure 5.7**, **Figure A.8**). Animals displaying increased risk taking and anxious behavior would be expected to have increased open arm time and elevated thigmotaxis scores. There was no effect of injury on open arm time ($F_{(2,37)} = 0.195$, $p = 0.98$). While the two way repeated measures ANOVA did show an effect of injury on open field thigmotaxis ($F_{(2,37)} = 3.610$, $p = 0.0367$) there were no significant differences between groups following post-hoc testing. There was no effect of test session on open arm time or thigmotaxis.

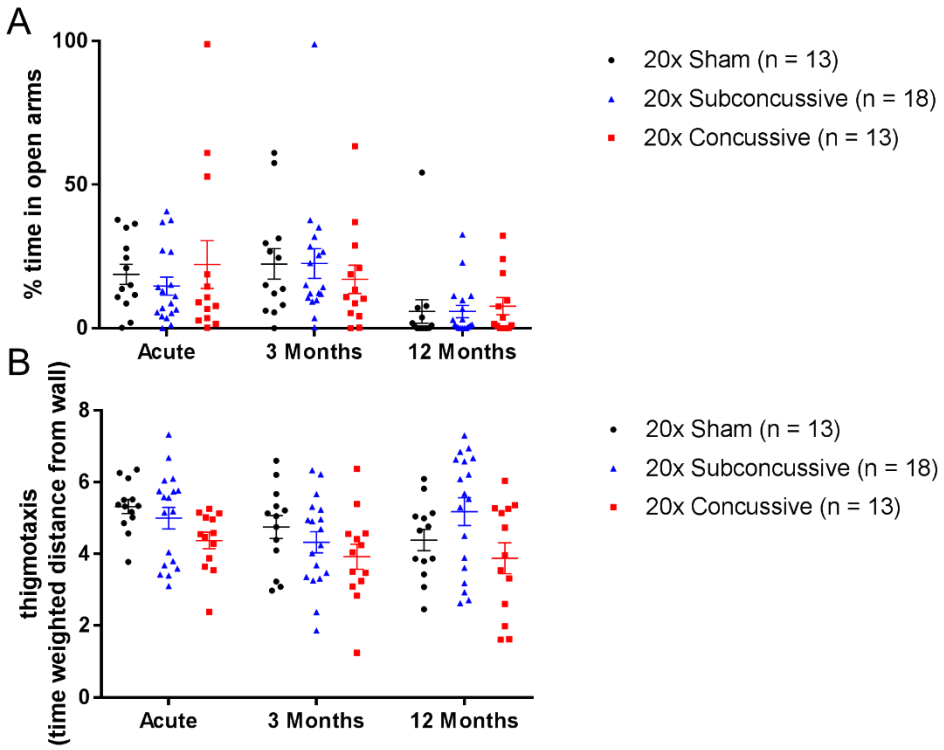

Figure 5.7 No changes in anxiety related behavior following injury. A. Animals in the 20x concussive and 20x subconcussive did not show any changes in percent time spent in open arms of the elevated plus maze relative to shams. **B.** Injured animals did not show any changes in open field thigmotaxis (time weighted distance from the wall) relative to sham animals.

Time immobile during the tail suspension test was used as a metric of depressive-like behavior (**Figure 5.8**, **Figure A.9**). The two way repeated measures ANOVA showed an effect of injury on immobility time ($F_{(2,37)} = 12.954$, $p < 0.0001$) that remained significant after post-hoc testing. hTau mice in the 20x concussion group showed reduced immobility times rather than the expected increased immobility times relative to shams ($p = 0.00427$) and relative to mice in the subconcussive group ($p = 0.000212$). The interpretation of this result is not clear (see discussion). There was no significant difference between animals in the 20x subconcussive group and 20x shams ($p = 0.546$). There was also no significant effect of test session on time spent immobile, though it appeared that the effect was less apparent at the 3 month test session.

These findings show that repetitive concussive or subconcussive injury does not result in acute social, anxiety related, or depressive-like deficits. Furthermore, based on the lack of an effect of test session, deficits in these domains do not manifest during the chronic stages following injury.

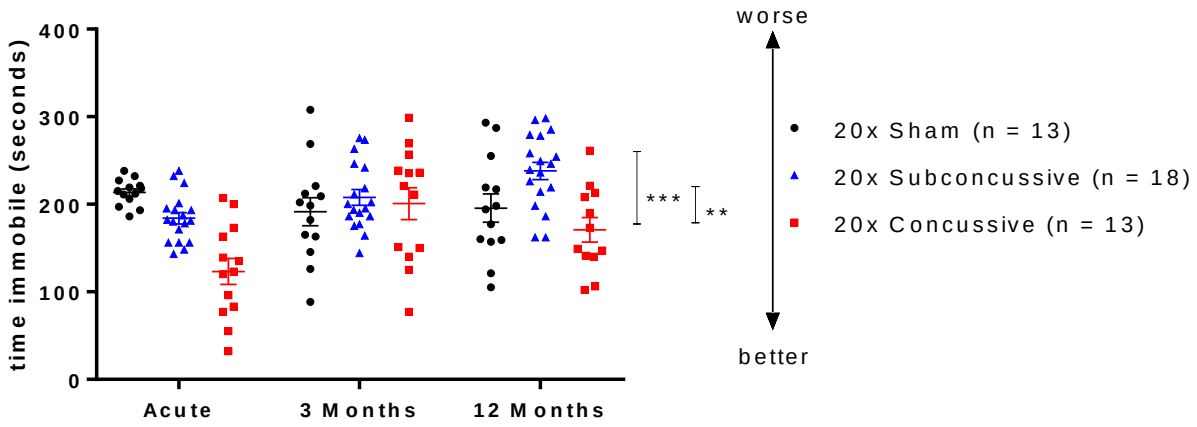

Figure 5.8 Effects of injury on depressive-type behavior. The tail suspension test was used to assess depressive-type behavior in animals. There was a significant effect of injury (20x concussive vs sham: p = 0.00427, 20x concussive vs 20x subconcussive: p = 0.000212) with less immobility in the 20x concussive group.

5.3.4 Repetitive brain injury does not result in chronic astrogliosis

GFAP staining was used to assess the effect of repetitive head injury on chronic astrogliosis. Regions of interest were drawn in the gray matter (cortex, lateral septal nucleus and hippocampus) and white matter (corpus callosum, anterior commissure, hippocampal commissure and fimbria). Percent area of positive staining was used as a measure of astrogliosis. The two way ANOVA showed no effect of injury ($p > 0.05$ all regions, details in Table A.6) on percent area of GFAP staining in any of the regions of interest (**Figure 5.9**). In summary, our analysis of activated astrocytes shows that our 20x concussion model does not result in chronic astrogliosis.

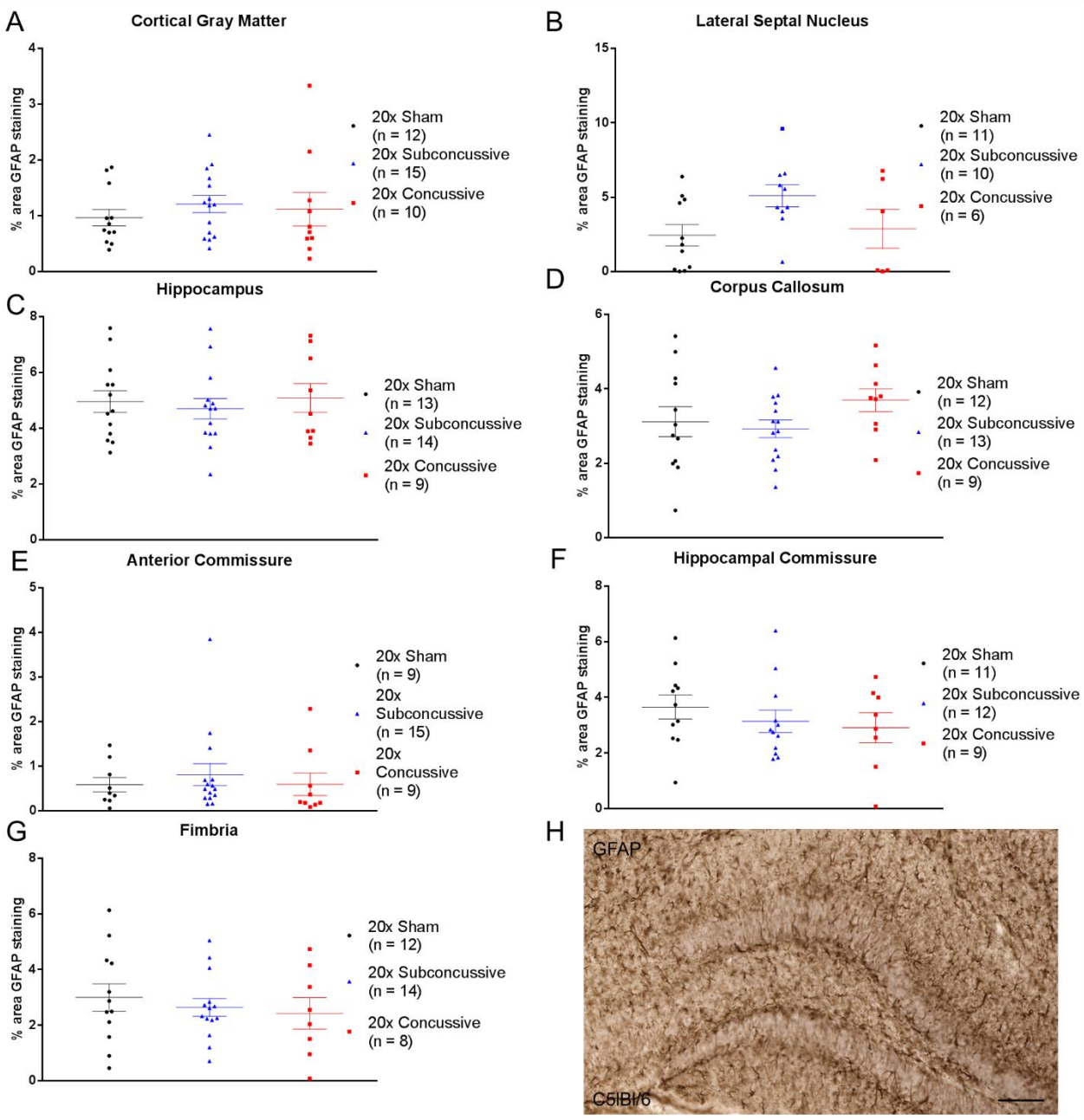

Figure 5.9 No effects of injury on chronic astrogliosis. A. Percent area of GFAP staining was measured in cortical gray matter. There were no differences in staining between injury groups. **B.** There was no difference in GFAP staining between injury groups in the lateral septal nucleus. **C.** No differences in GFAP staining were detected in the hippocampus **D.** No differences in GFAP staining were detected in the corpus callosum **E.** There were no differences between injury groups detected in the anterior commissure. **F.** No differences in GFAP staining were detected in the hippocampal commissure. **G.** No differences in GFAP staining were detected in the fimbria. **H.** GFAP staining in a positive control wild type mouse injured using CCI shows extensive astrogliosis in the hippocampus contralateral to the injury site. Scale bar = 100 microns.

5.3.5 No evidence of phosphorylated tau pathology in hTau mice

PCR genotyping confirmed that mice from both cohorts were positive for human tau (**Figure A.10**). However, hTau mice did not show any substantive staining for HT7 (total tau), AT8 (pTau, ser202/thr205), CP13 (pTau, ser202) or RZ3 (pTau, thr231) (**Figure 5.10A**). A 22 month old 3xTG mouse, used as a positive control for total tau and pTau staining, showed extensive positive staining for total tau and phosphorylated tau epitopes **(Figure 5.10B**).

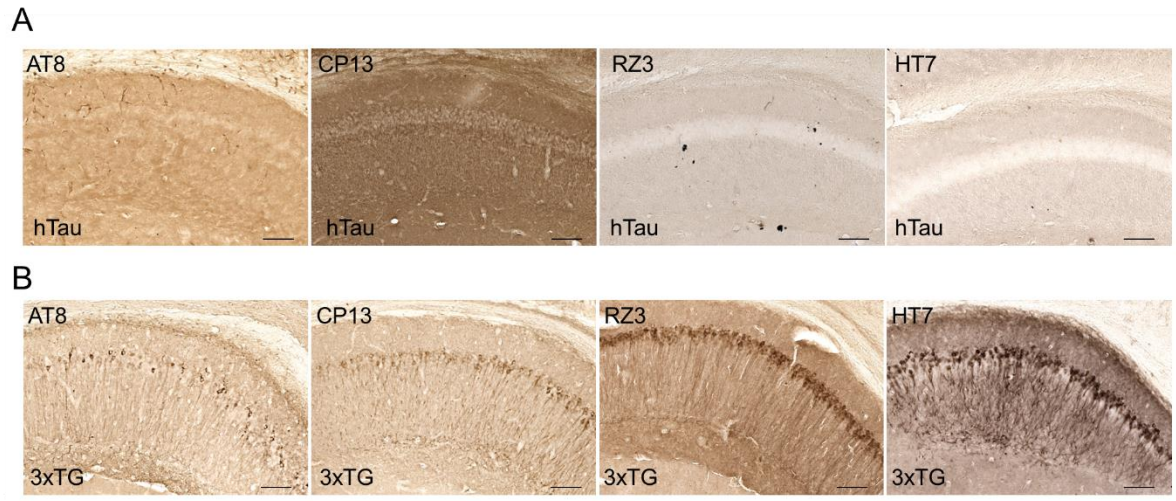

Figure 5.10 No detection of tau pathology using immunohistochemistry in any of the hTau mice. A. Monoclonal AT8 (pTau, ser202/thr205), CP13 (pTau, ser202), RZ3 (pTau, Thr231) and HT7 (total tau) were tested to detect phosphorylated and total tau in the hTau mice line. No positive staining was observed for any of the antibodies in any of the groups. **B.** Tissue from a 22 month old 3xTG mouse was used as a positive control. When stained with AT8, CP13, RZ3 and HT7 there is extensive positive staining in the hippocampal neurons. Scale bar = 100 microns.

5.3.6 Repetitive injury results in chronic white matter disruption

Power coherence analysis of Myelin Black Gold II stained images was used to measure chronic white matter disruption (**Figure 5.11**). White matter regions of interest included the corpus callosum, anterior commissure, hippocampal commissure and fimbria. The two way ANOVA showed an effect of injury on power coherence in the corpus callosum ($F_{(2,37)} = 28.048$, $\eta^2_p = 0.644$, $p < 0.00001$), hippocampal commissure ($F_{(2,37)} = 34.015$, $\eta^2_p = 0.687$, $p < 0.00001$)

and fimbria ($F_{(2,37)} = 17.262$, $\eta^2_p = 0.527$, $p < 0.00001$) that remained significant following post hoc Tukey testing (**Figure 5.12**). hTau animals in the 20x concussive group had reduced power coherence in the corpus callosum ($p = 0.000125$), hippocampal commissure ($p = 0.000125$) and fimbria ($p = 0.000136$) relative to shams. Animals in the 20x subconcussive group also showed more modestly reduced power coherence only in the corpus callosum ($p = 0.0091$) and hippocampal commissure ($p = 0.027$) relative to shams. Power coherence was also significantly reduced in the corpus callosum ($p = 0.000367$), hippocampal commissure ($p = 0.000150$), and fimbria ($p = 0.000189$) in the 20x concussive group relative to animals in the 20x subconcussive group. The injury dependent reduction in power coherence suggests that repetitive brain injuries cause acute white matter disruption that remains unresolved in the chronic phase of injury. The difference in effect sizes when comparing power coherence in white matter indicates that the corpus callosum and hippocampal commissure may be especially useful regions to assess chronic histological outcomes.

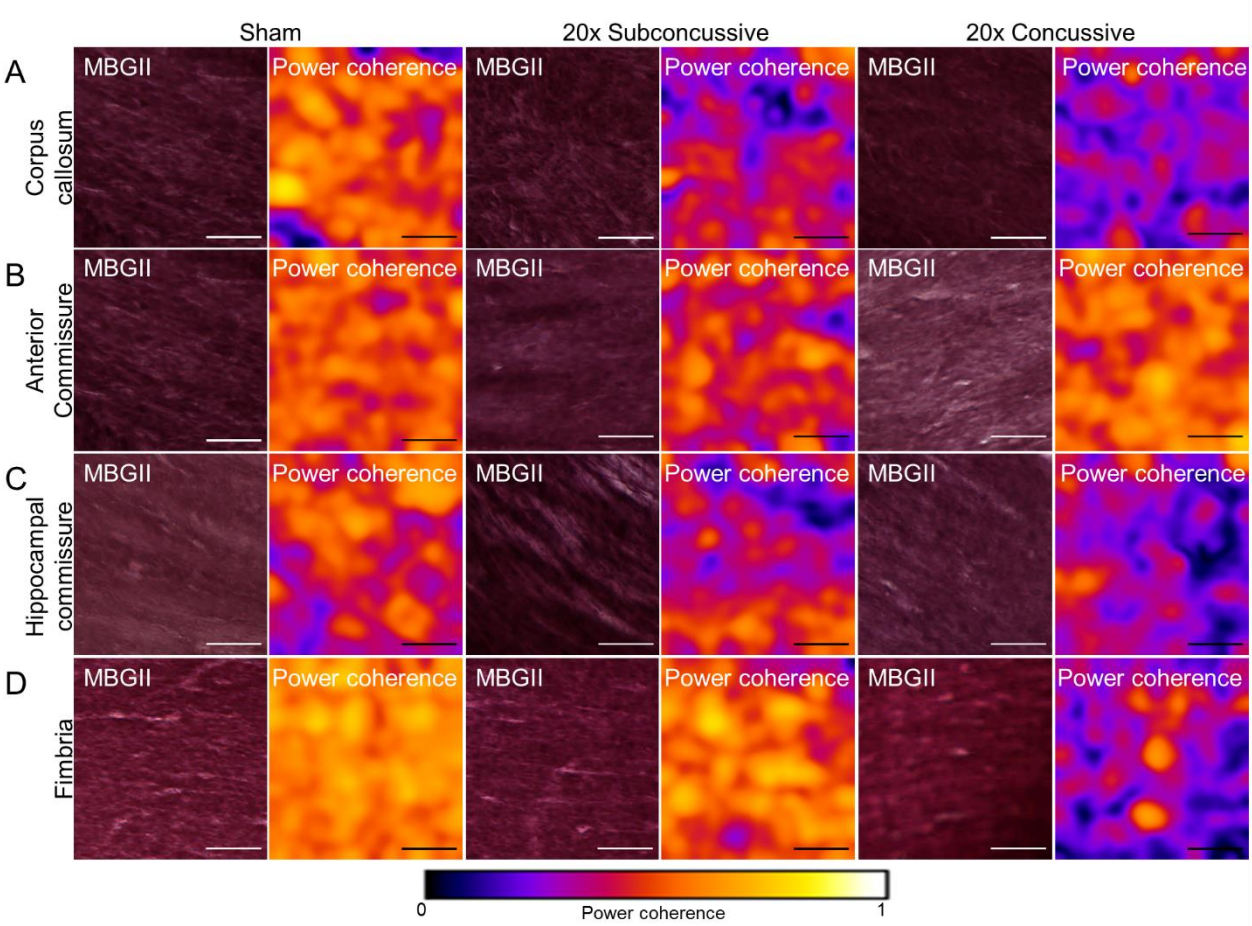

Figure 5.11 Effects of injury on chronic white matter disruption, assessed using power coherence. A. Power coherence was measured in the corpus callosum of tissue sections stained with Myelin Black Gold II. Fibers in sham animals have high coherence, indicating that fibers are aligned and intact. However, white matter fibers in injured animals show reduced power coherence, indicating white matter disruption. **B.** Fibers in the anterior commissure do not show any differences in power coherence, indicating intact white matter. **C.** Similar to the corpus callosum, white matter in the hippocampal commissure has reduced power coherence, indicating fiber disruption. **D.** White matter in the fimbria of sham and 20x subconcussive animals shows high power coherence, while the fimbria of 20x concussive animals shows reduced power coherence. Because the fimbria had a tendency to stain more heavily relative to other regions, brightness and contrast levels were uniformly adjusted adjusted for the exemplars so fibers could be better visualized. Scale bars = 50 microns.

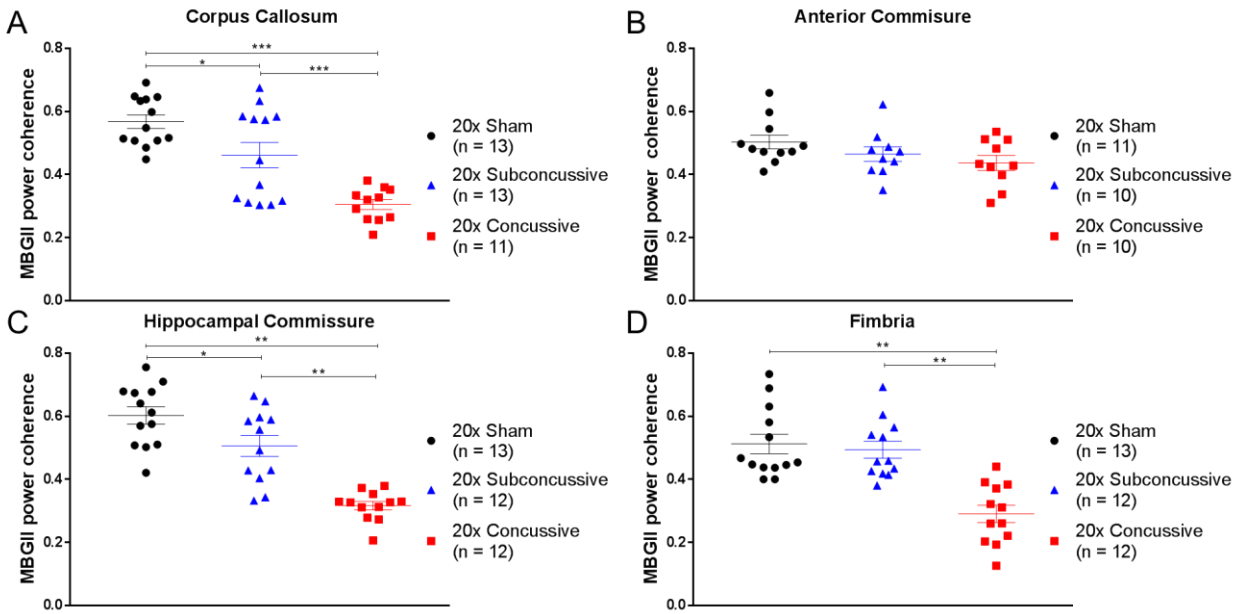

Figure 5.12 Reduced white matter integrity following repetitive injury. A. Power coherence in the corpus callosum was significantly reduced in injured animals (20x concussive vs sham, p = 0.000125, 20x subconcussive vs sham, p = 0.0091). There was also a significant difference in power coherence between animals in the 20x concussive and 20x subconcussive groups (p = 0.000367). **B.** Power coherence in the anterior commissure showed no effect of injury. **C.** There was a significant effect of injury on power coherence in the hippocampal commissure of hTau animals (20x concussive vs sham, p = 0.000125, 20x subconcussive vs sham, p = 0.027). There was also a significant difference between animals in the 20x concussive and 20x subconcussive groups (p = 0.000150). **D.** Power coherence in the fimbria was significantly reduced in animals in the 20x concussive group (20x concussive vs sham, p= 0.000136, 20x concussive vs. 20x subconcussive, p = 0.000189).

5.3.7 Correlation between white matter disruption and behavioral performance deficits

To address the question of whether there was a relationship between white matter disruption and the cognitive and motor deficits observed during the Morris water maze task, we performed Spearman's rank correlations between white matter power coherence data collected from the chronic test session of Morris water maze (**Figure 5.13; Table 5.1**). This was followed by Bonferroni correction for multiple comparisons where the effective number of tests was adjusted by the variance of the eigenvalues of the correlation matrix.(Cheverud, 2001) We found a modest but significant relationship between power coherence in the corpus callosum and swimming speed during both visible and hidden phases. When analyzing the 20x concussive

group in isolation, this correlation remained moderate and significant. There was also a moderate correlation between white matter power coherence in the hippocampal commissure and swimming speed during both visible and hidden phases. However, when considering the 20x concussive injury group in isolation, this relationship was weak and not significant. There were no significant correlations between white matter damage and distance to platform measures. Finally, we found a modest but significant relationship between power coherence in the fimbria and proximity to platform during probe trial. This relationship weakened and was not significant when considering the 20x concussive group in isolation. These results indicate that white matter damage in the corpus callosum, hippocampal commissure, and fimbria is related to behavioral deficits exhibited during the Morris water maze.

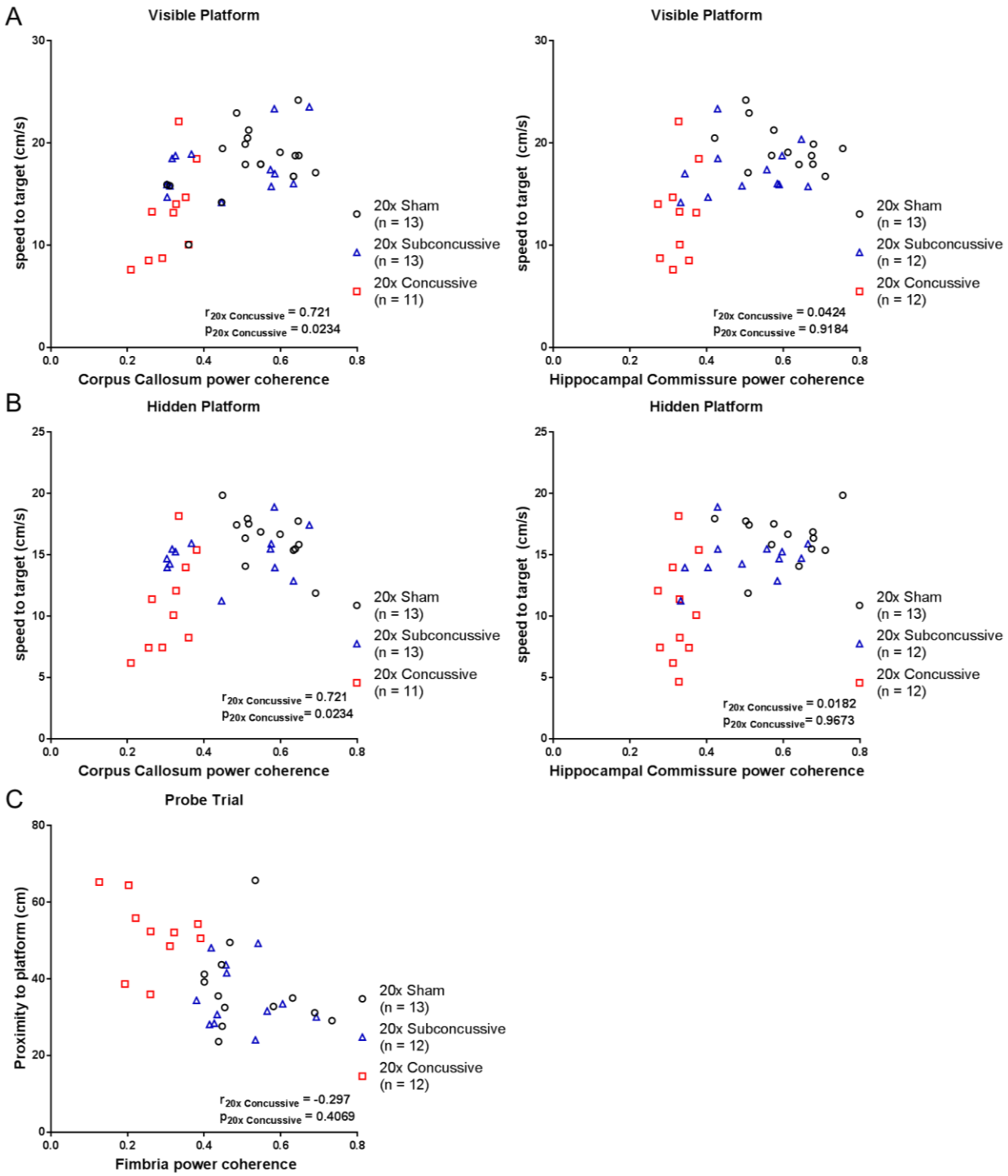

Figure 5.13 Relationship between white matter disruption and Morris water maze deficits. A. There was a modest, significant relationship between power coherence in the corpus callosum and swimming speed during the visible platform phase. When considering the 20x concussive group alone, this relationship remained consistent. In the hippocampal commissure, animals in the 20x concussive groups had weak, insignificant correlation of power coherence and swim speed. **B.** A similar trend was observed in both the corpus callosum and hippocampal commissure during the hidden platform phase. **C.** Animals that were further away from the platform during probe

trial had a tendency to sustain more severe chronic white matter damage in the fimbria. There was a modest but significant relationship between power coherence in this region and proximity to platform. However, in the 20x concussive group, this relationship was weak and no significant relationship between power coherence in the fimbria and proximity to platform during probe trial.

Behavioral measure	White matter region	$p_{full\ sample}$	$r_{full\ sample}$	$p_{20x\ Sham}$	$r_{20x\ Sham}$	$p_{20x\ Subconcussive}$	$r_{20x\ Subconcussive}$	$p_{20x\ Concussive}$	$r_{20x\ Concussive}$
Visible swim speed	Corpus Callosum	$2.22x10^{-4}$	0.578	0.193	0.312	0.182	0.396	0.023	0.721
Hidden swim speed	Corpus Callosum	$2.69x10^{-3}$	0.485	0.101	-0.478	0.505	0.203	0.023	0.721
Visible swim speed	Hippocampal Commissure	$2.62x10^{-3}$	0.493	0.146	-0.429	0.417	0.259	0.918	0.042
Hidden swim speed	Hippocampal Commissure	$4.09x10^{-4}$	0.558	0.630	-.148	0.147	0.448	0.967	0.018
Probe trial: proximity to platform	Fimbria	$2.28x10^{-3}$	-0.499	0.448	-0.231	0.991	-.007	0.407	-0.297

Table 5.1. Correlations of Morris water maze behavior and white matter integrity. A Spearman's correlation followed by adjusted Bonferroni correction for multiple comparisons was used to determine whether there were any significant correlations between white matter power coherence and the cognitive and motor dysfunctions observed during Morris water maze.

5.4 Discussion

We have implemented a repetitive subconcussive and concussive brain injury paradigm and reported acute, subacute, and chronic behavioral outcomes, as well as histological outcomes at one year following injury. We found that repetitive concussive injuries in adult mice result in acute cognitive and motor dysfunction that remains unresolved at up to one year post injury. Furthermore, repetitive concussive injuries caused chronic white matter disruption in several regions of the brain that was moderately correlated with deficits in swimming speed and memory during Morris water maze testing.

Our findings show some consistencies with previous repetitive brain injury models. Multiple repetitive injury models have shown that daily injuries result in cognitive deficits that manifest acutely and persist as late as six months to one year following injury (Luo et al., 2014; Mannix et al., 2013; Petraglia et al., 2014a). These results show some relevance to the manifestation of behavioral symptoms in patients diagnosed with CTE post-mortem. These patients can be classified into two categories: the first group of patients present with mood and behavioral disturbances at an early age (~ 35 years old) followed by later cognitive deterioration, while the second group presents with cognitive symptoms at an older age (~60 years old) followed by further progression into dementia (Stern et al., 2013). The robust findings of persistent cognitive impairment are most clearly relevant to the second group.

When studying other behavioral domains, such as anxiety, social, or depressive behavior, the results become more challenging to reproduce in animal models. For example, mice injured using repetitive injury paradigms do not consistently show deficits when assayed using the open field maze or elevated plus maze, a result paralleled in our work. This could be explained by the

sensitivity of these tests to external conditions, such as background noise, lighting conditions and time of day. In particular, tests such as open field maze lack a standardized metric, instead often using distance traveled or time in a user defined periphery zone of the testing box. We attempted to address this deficiency by using time-weighted distance from the maze center as a measure of thigmotaxis, but still found no differences in anxiety related behavior following injury. Our findings in relation to depressive behavior using the tail suspension test proved to be counterintuitive. Although injured animals showed impaired swimming speed during Morris water maze, injured animals had greater mobility times during the tail suspension task, a finding contradicted by previous work using the same behavioral assay (Bajwa et al., 2016; Klemenhagen et al., 2013). The increased mobility may indicate increased hyperactivity following injury. However, sham hTau animals also had surprisingly long immobility times compared to wild type animals of comparable age (Shoji et al., 2016). The findings are therefore difficult to interpret without additional data from other tests of depressive behavior such as sucrose preference or the forced swim test, as well as testing tail suspension in the absence of prior stressors such as Morris water maze testing (Castagne et al., 2011; Strekalova et al., 2004).

Interpretation of our histological findings in the context of previous work shows mixed results. Our data show injury related differences in white matter integrity measured using power coherence. Furthermore, there were region specific correlations of white matter disruption and impairments in swimming speed and spatial memory, specifically in the corpus callosum, hippocampal commissure, and fimbria. The large effect sizes in both the corpus callosum and hippocampal commissure indicate that these regions may be useful targets when assessing chronic histological outcomes following therapeutic trials. Previous repetitive injury paradigms have shown reduced white matter volume in the intermediate period following injury (Mannix et

al., 2017) but detected no changes in SMI31 immunoreactivity at 6 months post injury (Mannix et al., 2013). We have previously observed reduced white matter integrity measured by power coherence in the regions adjacent to tau laden sulcal depths in ex vivo Stage III/Stage IV CTE human cortical tissue (Holleran et al., 2017). However, it remains uncertain whether this white matter disruption is a consequence of acute axonal injury, myelin degeneration, or an increased microglial or astrocytic response. Furthermore, our findings of correlations of fiber integrity in the corpus callosum and hippocampal commissure with swim speed were surprising and indicate a need for further investigation into the microstructural changes in gray matter in the chronic phase following brain injury, as these may be better predictors of cognitive outcomes such as swimming distance. Our attempt to address this question by measuring chronic astrogliosis showed no differences in GFAP immunoreactivity between sham and injured groups. We used percent area of GFAP staining as our metric, which is not sensitive to morphological differences in astrocytes. Quantification of changes in astrocyte process and cell body shape would be an alternative method, but would require the use of fluorescent markers and image acquisition at high magnifications for optimal analysis (Soltys et al., 2003). However, with the growing interest in the relationship between astrocytes and pTau in neurodegenerative disease, such experiments may be worth exploring (Kovacs et al., 2017). Additionally, because microgliosis may have an important role in many tauopathies including CTE, exploration of microglial morphology using CD68 or Iba1 staining could provide further insight into the sequence of neurodegeneration (Cherry et al., 2016). A further area requiring future investigations will be analysis of synapse loss and its relationship with behavioral deficits.

The main strength of this study is that it is one of a few that has followed a population of mice out to 16 months of age and recorded behavioral data from the same mice at acute,

intermediate (three month) and chronic (one year) time points post injury. Importantly, the injury related deficits in learning and memory we observed are apparent at the chronic time point, while previous studies have shown cognitive and behavioral deficits acutely that either resolve by the intermediate phase, or do not use a more long term time point (9-12 months post injury) when measuring chronic behavioral outcomes. There are also several strengths when considering the design on the study. First, the use of the transgenic hTau mouse line allowed us to eliminate potential confounds of the differences in tau isoforms between mice and humans. Second, mice were injured at four months of age, when phosphorylated tau tangles are not yet present in the hippocampus or cortex. This age at time of injury was selected to better parallel the age at which many patients with CTE sustain repetitive injuries (McKee et al., 2009a; Mez et al., 2017). Third, our choice of the non-surgical CHIMERA model allowed for increased number and frequency of injuries that combined both direct impact and rotational acceleration components experienced during a traumatic brain injury.

The negative outcomes of this study reveal several limitations. The first and perhaps most important, is the choice of energy level for repeated concussive and subconcussive impacts. Our LRR data used to inform the selection of 0.13J and 0.24J for subconcussive and concussive injuries showed that animals injured with at least one impact had increased righting times relative to shams. Moreover, we found that animals injured twenty times with 0.24J impacts had increased righting times relative to animals in the 20x subconcussive group and shams, as well as a significantly reduced survival rate in the intermediate and chronic phases following injury. These findings are inconsistent with previous studies using the CHIMERA device, which defined injuries with energy levels below 0.4J as “subthreshold” (Namjoshi et al., 2017). However, these assessments were performed after a maximum of two impacts and did not address the question of

cumulative effects of repetitive subthreshold injuries (Namjoshi et al., 2017; Namjoshi et al., 2016). Previous work in the field of repetitive subthreshold injuries in a rat model has shown that while a single subthreshold impact does not result in pathology, repeated injuries can acutely result in histological abnormalities such as increases in microtubule associated protein, phosphorylated neurofilament, and increased pTau immunoreactivity (Kanayama et al., 1996). In humans, a combination of number of injuries as well as impact velocity shows a threshold-dose response when predicting late-life cognitive dysfunction and mood dysregulation (Montenigro et al., 2017). One possible future direction would be to increase the energy intensities, using 0.4J as the concussive threshold while maintaining the same frequency and number of injuries. This might better address the question of the differences in neurobehavioral and neuropathological trajectory following repetitive subconcussive and concussive injuries.

A second limitation is the use of a lissencephalic animal when attempting to develop an animal model of CTE, where the formation and distribution of pTau pathology is attributed to injury of cortical tissue. In humans, these structures are highly folded, and the curvature of fibers may result in increased vulnerability to mechanical insult and subsequent aggregation of pTau tangles and astroglial tau (Ghajari et al., 2017). Additionally, the composition of the rodent brain, which has a substantially lower white:gray matter ratio relative to humans could also be a reason for the lack of replication of pTau pathology found in CTE (Zhang and Sejnowski, 2000). Future studies in animals with gyrencephalic brain architecture, such as ferrets or pigs, would be more relevant when understanding the relationship between repetitive brain injury and chronic histopathological and behavioral deficits found in humans (Barnette et al., 2009; Hutchinson et al., 2016; Schwerin et al., 2017; Smith et al., 1999).

An unexpected limitation of this work is the lack of tau pathology in the hTau mice. Previous studies in the hTau mouse line have shown that uninjured animals are expected to develop neurofibrillary tangles in the hippocampus and cortex starting at nine months of age, verified using immunohistochemistry, Western blot, and ELISA assays (Andorfer et al., 2003; Polydoro et al., 2009). PCR confirmed the hTau genotype of the two cohorts of mice used in this study. However, an array of monoclonal antibodies specific for both total tau and pTau showed minimal staining in hTau mice compared to a 22 month old 3xTG positive control. While the positive control would be expected to have increased tau staining because of the triple transgene, this does not explain the lack of positive staining in the hTau line. This could instead be attributed to genetic drift in the mouse line. However, the role of mature neurofibrillary tangles as a driver of neurotoxicity as recently come into question. Tagge et al demonstrated that repeated closed head impacts in wild-type mice resulted in increased cis-pTau histopathology as late as five months post injury, while CP13 levels measured using immunoblot analysis were elevated at two weeks post injury (Tagge et al., 2018).These findings indicate that there is indeed an upregulation of pTau proteoforms in the months following injury that may precede the formation of tangles. Additionally, recent work has shown that soluble tau oligomers may have increased toxicity relative to fully mature neurofibrillary tangles that potentially have a neuroprotective effect for neurons (d'Orange et al., 2018). Analysis of soluble tau species may therefore provide a better correlate with injury and the cognitive dysfunction that we observed.

The choice of pentobarbital as anesthesia during CSF collection and tissue extraction is also a potential confound of this study. The reduction in respiratory rate during this mode of anesthesia could result in unexpected histopathological effects, such as an altered inflammatory or astrocytic response.(DeWalt et al., 2017; Soltys et al., 2003) While we did not see any

differences in astrocytosis as evidenced by GFAP staining in any region, an acute astroglial response following pentobarbital injection would explain the levels of astrocytes observed in the gray and white matter regions of both injured and sham hTau mice. This would be best addressed by performing GFAP staining in animals perfused using an alternative method of anesthesia, such as isofluorane, on littermates.

Additional future directions of this study include analysis of the CSF and blood samples for tau, GFAP, and other brain proteins. These will allow us to explore the question of whether repetitive brain injury results in changes of soluble tau species or impairs long-term blood brain barrier integrity. Furthermore, ELISAs and other assays of the fresh-frozen tissue samples collected from the hTau mice will provide an alternative to histopathology to determine whether there is evidence of phosphorylated tau in the brain.

In summary, a repetitive CHIMERA injury paradigm implemented in adult mice results in persistent behavioral dysfunction that is linked to disruption of specific white matter tracts. This disruption, detected by calculation of power coherence from myelin staining, shows that white matter damage occurs in a graded manner based on the intensity of repeated impacts, coinciding with behavioral deficits. These outcomes show that impacts previously considered "subthreshold" do result in lasting tissue damage in the brain.

Chapter 6. Conclusions and Future Directions

6.1 Conclusions

In summary, we have developed and implemented quantitative radiological-pathological correlations to determine whether high spatial resolution diffusion MRI techniques are capable of detecting pathology related to chronic traumatic encephalopathy (CTE). To do so, it was essential to optimize diffusion MRI data acquisition in human *ex vivo* tissues to obtain high quality data with maximal signal to noise ratio (SNR) in both gray and white matter. Manually placed landmarks on histological tissue sections were used as the bases to apply a nonlinear least squares transformation to coregister high power histological images to MRI data. We found that manual landmark placement produced voxel-based coregistered grids with excellent reproducibility within raters (intra-rater) and between raters (inter-rater). Extensive validation of the accuracy of the grids gemerated using these methods included (1) testing agreement between MRI histological when classifying voxels as gray matter, white matter, and gray/white matter boundary voxels and (2) a radiological-pathological correlation of diffusion derived and histologically derived fiber orientation in complex white matter. Using the assumption of a maximum of two in-plane fiber populations, we found excellent agreement ($r_{spearman} > 0.85$) when testing correlations in both primary and secondary fiber orientations. An important outcome of this method was our ability to perform comparisons of fiber orientation using high resolution histological data; typical histological quantification methods using amount of thresholded staining would not have provided fiber directionality information, making voxel-based validations impossible. An additional important outcome of this study was the use of power

coherence to distinguish between crossing fibers and disorganized white matter fibers. For future hypothesis testing, power coherence would be a useful metric particularly in complex human cortical white matter that is adjacent to gray matter regions where the pTau pathology of CTE is most commonly observed. Furthermore, we used power coherence to quantify the heterogeneity of white matter sampled at spatial resolutions ranging from 0.25 mm to 1mm. As expected, the variance of power coherence at spatial resolutions with increased in-plane voxel size was reduced, indicating the limited capability of clinically achievable spatial resolutions to capture underlying white matter heterogeneity. These findings drive the need for improved imaging methodologies to better quantify complex white matter and associated pathological changes that occur following brain injury.

Our next study was intended as a follow-up to our pilot study in tissues with a known diagnosis of Stage III/IV CTE all with post mortem intervals greater than 24 hours. In the pilot study, we found a modest, negative relationship between sulcal pTau and adjacent white matter power coherence (Holleran et al., 2017). Furthermore, while sulcal pTau had a weak relationship with adjacent white matter diffusion measures, power coherence showed modest, positive correlations with fractional anisotropy (Holleran et al., 2017). While these findings were encouraging, further testing was required in tissues both with short post mortem intervals and in tissues with non-CTE tauopathies. Therefore, I performed blinded radiological-pathological correlations in tissues with a diagnosis of CTE (III/IV), AD or FTLD, all with post mortem intervals of less than 24 hours. While the sample size of this study was too small to detect modest correlations ($r = 0.55$) and significant correlations ($p < 0.05$) previously observed, there were still several important findings. First, when comparing white matter disorganization in CTE and non-CTE tauopathies, white matter adjacent to sulcal depths in CTE showed significant

reduced power coherence compared to non-CTE tauopathies (AD or FTLD tissues). Second, in CTE tissues, power coherence in white matter underlying sulcal depths showed strong, positive correlation with fractional anisotropy that was significant ($r_{spearman} = 0.966$, $p = 7.68 \times 10^{-4}$). In non-CTE tissues, this relationship was modest, and negative but not significant. Furthermore, no relationship was found between white matter power coherence and astrogliosis. While the findings in CTE tissues recapitulate those from Holleran et al, correlations in more non-CTE tauopathies are necessary to determine whether the correlation of white matter power coherence with fractional anisotropy is indeed specific to CTE. Additionally, correlations are essential in healthy, age-matched controls in tissues ideally studying corresponding white matter tracts to determine whether our observations are not a natural consequence of random fiber organization in cortical white matter tracts. White matter in the fundus has been shown to have complex architecture such as crossing and fanning fibers (Kleinnijenhuis, 2014) and our use of a two tensor fit to define power coherence may not be sufficient to account for white matter heterogeneity in such regions. Furthermore, we observed several interesting correlations between gray matter astrogliosis and diffusion measures in associated regions that would benefit from studies in additional tissues.

Finally, I used a closed headed model of engineered rotational acceleration (CHIMERA) injury platform to study the chronic effects of repetitive concussive and subconcussive injuries on human tau (hTau) transgenic mice. The primary outcome of this study was that hTau mice injured with repetitive concussive injuries showed persistent cognitive deficits associated with histopathological alterations, including reduced power coherence in white matter tracts including the corpus callosum and hippocampal commissure. Surprisingly, these animals did not show signs of tau pathology, assessed using immunohistochemistry to detect total and phosphorylated

tau. Furthermore, there were no behavioral deficits manifested in anxiety, depressive or social behaviors. While the findings of this study were mostly negative, they did serve as an important test of whether chronic, "subthreshold" white matter injury can be assessed using white matter power coherence. Moreover, this was one of the first studies that has studied behavior and pathology following head injury at a truly chronic time point (one year post injury), which is most relevant when studying CTE.

6.2 Future Directions

Repetitive head injuries may result in chronic histopathological and neurobehavioral deficits, including the pTau pathology used to diagnose CTE and the associated clinical presentation of mood, rage and cognitive deficits (Mez et al., 2016; Stern et al., 2013). Without a noninvasive, *in vivo* metric of pTau or related pathology, CTE will continue to remain a post-mortem diagnosis. The data presented here provide some evidence for the claim that diffusion MRI is capable of detecting white matter injury related to CTE. However, there are several important lines work necessary to support this conclusion. First, and perhaps most importantly, we have not shown that diffusion measures in gray matter robustly correlate with pTau pathology. Determining this relationship, if any, between gray matter diffusion and pTau pathology would provide the most direct diagnostic measure of CTE. Support vector machine (SVM) approaches have used to classify Alzheimer's patients using DTI and DKI based measures (Chen et al., 2017b). Furthermore, an SVM classifier was used to detect diffusion abnormalities related to traumatic axonal injury and show that these were predictors of processing speed and executive function deficits (Hellyer et al., 2013). In the context of

radiological-pathological correlations, Haber et al used random forest analysis to perform unsupervised classification of CHIMERA injured mice vs sham animals using DTI and histological measures (Haber et al., 2017). Such analyses would be highly advantageous in determining whether diffusion measures are predictive of pTau pathology and can be used to distinguish CTE from healthy controls and non-CTE tauopathies.

Second, while attempts at developing an animal model of CTE have been focused on the mouse or rat, implementation of a repetitive head injury paradigm in a gyrencephalic animal would be a more useful model when assessing changes in imaging measures following injury. Studies in mice appear to show a relationship between axonal injury and abnormalities in diffusion tensor imaging (Bennett et al., 2012; Mac Donald et al., 2007a; Mac Donald et al., 2007b), but white matter tracts in small rodents do not have the complex white matter architecture that comprises 63% of white matter in the human brain (Jeurissen et al., 2013). Therefore, assessment of axonal injury in an animal with curving and crossing white matter fiber tracts would be more appropriate in answering the question of whether diffusion metrics are capable of detecting axonal injury in cortical white matter. Recent work in the ferret brain has shown white matter abnormalities following controlled cortical impact are detected by diffusion and T2 imaging (Hutchinson et al., 2016). Long-term studies following repetitive head injuries of the ferret brain would answer the questions of (1) whether power coherence is genuinely a reflection of residual white matter disruption in complex white matter tracts and (2) whether white matter pathological changes in these regions can be detected at chronic time points.

Finally, this work highlights a need for imaging methodologies with improved spatial resolution that are sensitive to TBI related pathology. Currently, clinically achievable voxel sizes are on the order of 1mm (Wu et al., 2016), while the pathology most indicative of CTE is often

in sulcal depths, perivascular regions and gray-white matter boundaries, all regions that are prone to volume averaging (Im et al., 2008; Shimony et al., 1999; Van Essen, 2005; Zacharopoulos and Narayana, 1998). To circumvent the limitation of large voxel sizes, alternative approaches such as molecular contrast agents with binding affinity to pTau, GFAP or neurofilament would provide the high spatial resolutions of T1 or T2 MRI along with the presumed microstructural sensitivity of diffusion MRI. Factors that must be considered when using this approach would be potential toxicity of the contrast agent (Ramalho and Ramalho, 2017), and blood brain barrier permeability (Ichikawa et al., 2010).

Concluding Remarks:

While traumatic brain injury has been increasingly linked to the development of neurodegenerative diseases such as chronic traumatic encephalopathy, a noninvasive mode of diagnosis has yet to be determined. In this work, I have attempted to address the question of whether diffusion MRI is able to detect microstructural white matter changes in human cortical white matter, and whether these changes are related to CTE. I also studied the chronic consequences of repetitive TBI in a mouse model. The major outcome of this work was that while compromised white matter integrity following repetitive head impacts may be closely related to CTE pathology and correlates with DTI derived fractional anisotropy in *ex vivo* tissues, further advancements in imaging methods are necessary to sensitively measure these changes *in vivo*. This work therefore not only provides the motivation to further refine diffusion MRI approaches, but also furthers the rationale for investigations into alternative modes of imaging to detect CTE pathology.

Appendix

Table A.1: Animal models of repetitive head injury

Authors	Animal type	Age at time of injury	Injury model	Injury number	Inter-injury interval	Acute behavioral outcomes	Acute pathology	Chronic behavioral outcomes	Chronic pathology
(Kanayama et al., 1996)	Rat	N/A	FPI	7	24 hours	1 week: impaired habituation to novel environment	1 week: Accumulation of MAP2 and NFH spreading to the contralateral cortex and hippocampus. pTau immunoreactivity in cortical neurons	N/A	N/A
(Creeley et al., 2004)	C57BL/6	7-8 weeks	Weight drop	3	24 hours	Impaired spatial learning during MWM	Silver staining abnormalities in olfactory and optic tracts	N/A	N/A
(Shitaka et al., 2011)	C57BL/6	2-3 months	Closed head impact	2	24 hours	MWM deficits	Abnormal APP swellings, argyrophylic abnormalities	7 weeks: MWM deficits	Persistent microglial activation, white matter silver staining
(Ojo et al., 2013)	hTau mice	18 months	Closed head CCI	5	48 hours	N/A	Increased pTau immunoreactivity no perivascular or astroglial tau. Increased microglial and astrocytic reactivity	N/A	N/A
(Mannix et al., 2013)	C57BL/6	2-3 months	Weight drop	7	24 hours	Impaired balance and MWM deficits	N/A	12 months: Impaired balance and MWM deficits	6 months: elevated microgliosis and astrogliosis
(Petraglia et al., 2014a; Petraglia et al., 2014b)	C57BL/6	3 months	Closed head CCI with acceleration/deceleration (no anesthesia)	42	2 hours	Elevated NSS, increased anxiety like behavior, MWM deficits, sleep disturbances, depressive behavior	Reactive astrocytosis elevated pTau immunoreactivity	Increased risk taking behavior at 6 months persistent MWM deficits	6 months; astrogliosis and microgliosis, increased pTau immunoreactivity
(Luo et al., 2014)	C57BL/6	2-3 months	Closed head CCI	3	24 hours	Spatial learning and memory deficits	N/A	6 months post injury; spatial learning and memory deficits	6 months post injury; increased astrogliosis, increased pTau immunoreactivity
(Turner et al., 2015a)	Sprague-Dawley rats	N/A	Blast injury	6	48 hours	Increased open arm time in EPM, MWM deficits	Increased pTau immunoreactivity	N/A	N/A

(Bajwa et al., 2016)	C57BL/6	3 months	Unrestrained closed head CCI	2	72 hours	No differences	N/A	90 days post injury; increased depressive like behavior Reduced social activity	N/A
(Ojo et al., 2016)	hTau mice	3 months	Closed head CCI	24 or 32	72 or 96 hours	N/A	N/A	6 months post injury; impaired MWM performance, increased risk taking behavior	Increased total tau levels, mild increase in pTau.
(Chen et al., 2017a)	C57BL/6	12 weeks	0.5J CHIMERA	3	24 hours	Motor deficits, MWM deficits	APP deposition, reduced by 1 month	6 months post injury; impaired MWM deficits	Increased GFAP, Iba1 levels

Table A.1 Preclinical animal models of repetitive traumatic brain injury. Multiple groups have implemented repetitive head injury paradigms in rodent models (mouse and rat) in an attempt to study chronic phosphorylated tau pathology commonly found in human patients diagnosed with chronic traumatic encephalopathy.

Table A.2: DTI diffusion sensitized gradients

b value (s/mm^2)	b_x	b_y	b_z
4000	1	0	0
4000	0.166	0.986	0
4000	-0.11	0.664	0.74
4000	0.901	-0.419	-0.11
4000	-0.169	-0.601	0.781
4000	-0.815	-0.386	0.433
4000	0.656	0.366	0.66
4000	0.582	0.8	0.143
4000	0.9	0.259	0.35
4000	0.693	-0.698	0.178
4000	0.357	-0.924	-0.14
4000	0.543	-0.488	-0.683
4000	-0.525	-0.396	0.753
4000	-0.639	0.689	0.341
4000	-0.33	-0.013	-0.944
4000	-0.524	-0.783	0.335
4000	0.609	-0.065	-0.791
4000	0.22	-0.233	-0.947
4000	-0.004	-0.91	-0.415
4000	-0.511	0.627	-0.589
4000	0.414	0.737	0.535
4000	-0.679	0.139	-0.721
4000	0.884	-0.296	0.362
4000	0.262	0.432	0.863
4000	0.088	0.185	-0.979
4000	0.294	-0.907	0.302
4000	0.887	-0.089	-0.453
4000	0.257	-0.443	0.859
4000	0.086	0.867	-0.491
4000	0.863	0.504	-0.025

Table A.2 b-matrix used to collect diffusion tensor data. A diffusion scheme with four unweighted diffusion images (b = 0 s/mm^2), 30 directions, and b-value of 4000 s/mm^2 was used to acquire data for diffusion tensor imaging.

Table A.3: GQI diffusion sensitized gradients

b-value (s/mm^2)	b_x	b_y	b_x
50.29395	0	0	0
50.29395	0	0	0
50.29395	0	0	0
50.29395	0	0	0
50.29395	0	0	0
50.29395	0	0	0
50.29395	0	0	0
50.29395	0	0	0
50.29395	0	0	0
50.29395	0	0	0
606.8971	-1	0	0
606.8971	0	1	0
843.9749	0	0	1
369.8193	0	0	-1
606.8971	0	-1	0
606.8971	1	0	0
1163.5	-0.70711	0.707107	0
1400.578	-0.70711	0	0.707107
926.4224	-0.70711	0	-0.70711
1163.5	-0.70711	-0.70711	0
1400.578	0	0.707107	0.707107
926.4224	0	0.707107	-0.70711
1400.578	0	-0.70711	0.707107
926.4224	0	-0.70711	-0.70711
1163.5	0.707107	0.707107	0
1400.578	0.707107	0	0.707107
926.4224	0.707107	0	-0.70711
1163.5	0.707107	-0.70711	0
1957.181	-0.57735	0.57735	0.57735
1483.026	-0.57735	0.57735	-0.57735
1957.181	-0.57735	-0.57735	0.57735
1483.026	-0.57735	-0.57735	-0.57735
1957.181	0.57735	0.57735	0.57735
1483.026	0.57735	0.57735	-0.57735
1957.181	0.57735	-0.57735	0.57735
1483.026	0.57735	-0.57735	-0.57735
2276.706	-1	0	0
2276.706	0	1	0
2750.862	0	0	1

1802.551	0	0	-1
2276.706	0	-1	0
2276.706	1	0	0
2833.31	-0.89443	0.447214	0
3070.387	-0.89443	0	0.447214
2596.232	-0.89443	0	-0.44721
2833.31	-0.89443	-0.44721	0
2833.31	-0.44721	0.894427	0
3307.465	-0.44721	0	0.894427
2359.154	-0.44721	0	-0.89443
2833.31	-0.44721	-0.89443	0
3070.387	0	0.894427	0.447214
2596.232	0	0.894427	-0.44721
3307.465	0	0.447214	0.894427
2359.154	0	0.447214	-0.89443
3307.465	0	-0.44721	0.894427
2359.154	0	-0.44721	-0.89443
3070.387	0	-0.89443	0.447214
2596.232	0	-0.89443	-0.44721
2833.31	0.447214	0.894427	0
3307.465	0.447214	0	0.894427
2359.154	0.447214	0	-0.89443
2833.31	0.447214	-0.89443	0
2833.31	0.894427	0.447214	0
3070.387	0.894427	0	0.447214
2596.232	0.894427	0	-0.44721
2833.31	0.894427	-0.44721	0
3626.991	-0.8165	0.408248	0.408248
3152.835	-0.8165	0.408248	-0.40825
3626.991	-0.8165	-0.40825	0.408248
3152.835	-0.8165	-0.40825	-0.40825
3626.991	-0.40825	0.816497	0.408248
3152.835	-0.40825	0.816497	-0.40825
3864.068	-0.40825	0.408248	0.816497
2915.757	-0.40825	0.408248	-0.8165
3864.068	-0.40825	-0.40825	0.816497
2915.757	-0.40825	-0.40825	-0.8165
3626.991	-0.40825	-0.8165	0.408248
3152.835	-0.40825	-0.8165	-0.40825
3626.991	0.408248	0.816497	0.408248
3152.835	0.408248	0.816497	-0.40825

3864.068	0.408248	0.408248	0.816497
2915.757	0.408248	0.408248	-0.8165
3864.068	0.408248	-0.40825	0.816497
2915.757	0.408248	-0.40825	-0.8165
3626.991	0.408248	-0.8165	0.408248
3152.835	0.408248	-0.8165	-0.40825
3626.991	0.816497	0.408248	0.408248
3152.835	0.816497	0.408248	-0.40825
3626.991	0.816497	-0.40825	0.408248
3152.835	0.816497	-0.40825	-0.40825
4503.119	-0.70711	0.707107	0
4977.275	-0.70711	0	0.707107
4028.963	-0.70711	0	-0.70711
4503.119	-0.70711	-0.70711	0
4977.275	0	0.707107	0.707107
4028.963	0	0.707107	-0.70711
4977.275	0	-0.70711	0.707107
4028.963	0	-0.70711	-0.70711
4503.119	0.707107	0.707107	0
4977.275	0.707107	0	0.707107
4028.963	0.707107	0	-0.70711
4503.119	0.707107	-0.70711	0
5059.722	-1	0	0
5296.8	-0.66667	0.666667	0.333333
4822.644	-0.66667	0.666667	-0.33333
5533.878	-0.66667	0.333333	0.666667
4585.566	-0.66667	0.333333	-0.66667
5533.878	-0.66667	-0.33333	0.666667
4585.566	-0.66667	-0.33333	-0.66667
5296.8	-0.66667	-0.66667	0.333333
4822.644	-0.66667	-0.66667	-0.33333
5533.878	-0.33333	0.666667	0.666667
4585.566	-0.33333	0.666667	-0.66667
5533.878	-0.33333	-0.66667	0.666667
4585.566	-0.33333	-0.66667	-0.66667
5059.722	0	1	0
5770.956	0	0	1
4348.489	0	0	-1
5059.722	0	-1	0
5533.878	0.333333	0.666667	0.666667
4585.566	0.333333	0.666667	-0.66667

5533.878	0.333333	-0.66667	0.666667
4585.566	0.333333	-0.66667	-0.66667
5296.8	0.666667	0.666667	0.333333
4822.644	0.666667	0.666667	-0.33333
5533.878	0.666667	0.333333	0.666667
4585.566	0.666667	0.333333	-0.66667
5533.878	0.666667	-0.33333	0.666667
4585.566	0.666667	-0.33333	-0.66667
5296.8	0.666667	-0.66667	0.333333
4822.644	0.666667	-0.66667	-0.33333
5059.722	1	0	0
5616.325	-0.94868	0.316228	0
5853.403	-0.94868	0	0.316228
5379.247	-0.94868	0	-0.31623
5616.325	-0.94868	-0.31623	0
5616.325	-0.31623	0.948683	0
6327.559	-0.31623	0	0.948683
4905.092	-0.31623	0	-0.94868
5616.325	-0.31623	-0.94868	0
5853.403	0	0.948683	0.316228
5379.247	0	0.948683	-0.31623
6327.559	0	0.316228	0.948683
4905.092	0	0.316228	-0.94868
6327.559	0	-0.31623	0.948683
4905.092	0	-0.31623	-0.94868
5853.403	0	-0.94868	0.316228
5379.247	0	-0.94868	-0.31623
5616.325	0.316228	0.948683	0
6327.559	0.316228	0	0.948683
4905.092	0.316228	0	-0.94868
5616.325	0.316228	-0.94868	0
5616.325	0.948683	0.316228	0
5853.403	0.948683	0	0.316228
5379.247	0.948683	0	-0.31623
5616.325	0.948683	-0.31623	0
6410.006	-0.90453	0.301511	0.301511
5935.851	-0.90453	0.301511	-0.30151
6410.006	-0.90453	-0.30151	0.301511
5935.851	-0.90453	-0.30151	-0.30151
6410.006	-0.30151	0.904534	0.301511
5935.851	-0.30151	0.904534	-0.30151

6884.162	-0.30151	0.301511	0.904534
5461.695	-0.30151	0.301511	-0.90453
6884.162	-0.30151	-0.30151	0.904534
5461.695	-0.30151	-0.30151	-0.90453
6410.006	-0.30151	-0.90453	0.301511
5935.851	-0.30151	-0.90453	-0.30151
6410.006	0.301511	0.904534	0.301511
5935.851	0.301511	0.904534	-0.30151
6884.162	0.301511	0.301511	0.904534
5461.695	0.301511	0.301511	-0.90453
6884.162	0.301511	-0.30151	0.904534
5461.695	0.301511	-0.30151	-0.90453
6410.006	0.301511	-0.90453	0.301511
5935.851	0.301511	-0.90453	-0.30151
6410.006	0.904534	0.301511	0.301511
5935.851	0.904534	0.301511	-0.30151
6410.006	0.904534	-0.30151	0.301511
5935.851	0.904534	-0.30151	-0.30151
7203.687	-0.57735	0.57735	0.57735
6255.376	-0.57735	0.57735	-0.57735
7203.687	-0.57735	-0.57735	0.57735
6255.376	-0.57735	-0.57735	-0.57735
7203.687	0.57735	0.57735	0.57735
6255.376	0.57735	0.57735	-0.57735
7203.687	0.57735	-0.57735	0.57735
6255.376	0.57735	-0.57735	-0.57735
7286.135	-0.83205	0.5547	0
7760.29	-0.83205	0	0.5547
6811.979	-0.83205	0	-0.5547
7286.135	-0.83205	-0.5547	0
7286.135	-0.5547	0.83205	0
7997.368	-0.5547	0	0.83205
6574.901	-0.5547	0	-0.83205
7286.135	-0.5547	-0.83205	0
7760.29	0	0.83205	0.5547
6811.979	0	0.83205	-0.5547
7997.368	0	0.5547	0.83205
6574.901	0	0.5547	-0.83205
7997.368	0	-0.5547	0.83205
6574.901	0	-0.5547	-0.83205
7760.29	0	-0.83205	0.5547

6811.979	0	-0.83205	-0.5547
7286.135	0.5547	0.83205	0
7997.368	0.5547	0	0.83205
6574.901	0.5547	0	-0.83205
7286.135	0.5547	-0.83205	0
7286.135	0.83205	0.5547	0
7760.29	0.83205	0	0.5547
6811.979	0.83205	0	-0.5547
7286.135	0.83205	-0.5547	0

Table A.3 b-matrix used to collect generalized q-sampling data. A diffusion scheme with 10 unweighted diffusion images (b = 0 s/mm^2), 202 directions, and a maximum b-value of 8000 s/mm^2 was used to acquire data for generalized q-sampling imaging.

Table A.4: DKI diffusion sensitized gradients

b-value (s/mm^2)	b_x	b_y	b_x
50.2395	0	0	0
50.2395	0	0	0
50.2395	0	0	0
50.2395	0	0	0
50.2395	0	0	0
50.2395	0	0	0
50.2395	0	0	0
50.2395	0	0	0
50.2395	0	0	0
50.2395	0	0	0
2000	1	0	0
2000	0.166	0.986	0.000
2000	-0.110	0.664	0.740
2000	0.901	-0.419	-0.110
2000	-0.169	-0.601	0.781
2000	-0.815	-0.386	0.433
2000	0.656	0.366	0.660
2000	0.582	0.800	0.143
2000	0.900	0.259	0.350
2000	0.693	-0.698	0.178
2000	0.357	-0.924	-0.140
2000	0.543	-0.488	-0.683
2000	-0.525	-0.396	0.753

2000	-0.639	0.689	0.341
2000	-0.330	-0.013	-0.944
2000	-0.524	-0.783	0.335
2000	0.609	-0.065	-0.791
2000	0.220	-0.233	-0.947
2000	-0.004	-0.910	-0.415
2000	-0.511	0.627	-0.589
2000	0.414	0.737	0.535
2000	-0.679	0.139	-0.721
2000	0.884	-0.296	0.362
2000	0.262	0.432	0.863
2000	0.088	0.185	-0.979
2000	0.294	-0.907	0.302
2000	0.887	-0.089	-0.453
2000	0.257	-0.443	0.859
2000	0.086	0.867	-0.491
2000	0.863	0.504	-0.025
4000	1	0	0
4000	0.166	0.986	0.000
4000	-0.110	0.664	0.740
4000	0.901	-0.419	-0.110
4000	-0.169	-0.601	0.781
4000	-0.815	-0.386	0.433
4000	0.656	0.366	0.660
4000	0.582	0.800	0.143
4000	0.900	0.259	0.350
4000	0.693	-0.698	0.178
4000	0.357	-0.924	-0.140
4000	0.543	-0.488	-0.683
4000	-0.525	-0.396	0.753
4000	-0.639	0.689	0.341
4000	-0.330	-0.013	-0.944
4000	-0.524	-0.783	0.335
4000	0.609	-0.065	-0.791
4000	0.220	-0.233	-0.947
4000	-0.004	-0.910	-0.415
4000	-0.511	0.627	-0.589

4000	0.414	0.737	0.535
4000	-0.679	0.139	-0.721
4000	0.884	-0.296	0.362
4000	0.262	0.432	0.863
4000	0.088	0.185	-0.979
4000	0.294	-0.907	0.302
4000	0.887	-0.089	-0.453
4000	0.257	-0.443	0.859
4000	0.086	0.867	-0.491
4000	0.863	0.504	-0.025
6000	1	0	0
6000	0.166	0.986	0.000
6000	-0.110	0.664	0.740
6000	0.901	-0.419	-0.110
6000	-0.169	-0.601	0.781
6000	-0.815	-0.386	0.433
6000	0.656	0.366	0.660
6000	0.582	0.800	0.143
6000	0.900	0.259	0.350
6000	0.693	-0.698	0.178
6000	0.357	-0.924	-0.140
6000	0.543	-0.488	-0.683
6000	-0.525	-0.396	0.753
6000	-0.639	0.689	0.341
6000	-0.330	-0.013	-0.944
6000	-0.524	-0.783	0.335
6000	0.609	-0.065	-0.791
6000	0.220	-0.233	-0.947
6000	-0.004	-0.910	-0.415
6000	-0.511	0.627	-0.589
6000	0.414	0.737	0.535
6000	-0.679	0.139	-0.721
6000	0.884	-0.296	0.362
6000	0.262	0.432	0.863
6000	0.088	0.185	-0.979
6000	0.294	-0.907	0.302
6000	0.887	-0.089	-0.453

6000	0.257	-0.443	0.859
6000	0.086	0.867	-0.491
6000	0.863	0.504	-0.025
8000	1	0	0
8000	0.166	0.986	0.000
8000	-0.110	0.664	0.740
8000	0.901	-0.419	-0.110
8000	-0.169	-0.601	0.781
8000	-0.815	-0.386	0.433
8000	0.656	0.366	0.660
8000	0.582	0.800	0.143
8000	0.900	0.259	0.350
8000	0.693	-0.698	0.178
8000	0.357	-0.924	-0.140
8000	0.543	-0.488	-0.683
8000	-0.525	-0.396	0.753
8000	-0.639	0.689	0.341
8000	-0.330	-0.013	-0.944
8000	-0.524	-0.783	0.335
8000	0.609	-0.065	-0.791
8000	0.220	-0.233	-0.947
8000	-0.004	-0.910	-0.415
8000	-0.511	0.627	-0.589
8000	0.414	0.737	0.535
8000	-0.679	0.139	-0.721
8000	0.884	-0.296	0.362
8000	0.262	0.432	0.863
8000	0.088	0.185	-0.979
8000	0.294	-0.907	0.302
8000	0.887	-0.089	-0.453
8000	0.257	-0.443	0.859
8000	0.086	0.867	-0.491
8000	0.863	0.504	-0.025
10000	1	0	0
10000	0.166	0.986	0.000
10000	-0.110	0.664	0.740
10000	0.901	-0.419	-0.110

10000	-0.169	-0.601	0.781
10000	-0.815	-0.386	0.433
10000	0.656	0.366	0.660
10000	0.582	0.800	0.143
10000	0.900	0.259	0.350
10000	0.693	-0.698	0.178
10000	0.357	-0.924	-0.140
10000	0.543	-0.488	-0.683
10000	-0.525	-0.396	0.753
10000	-0.639	0.689	0.341
10000	-0.330	-0.013	-0.944
10000	-0.524	-0.783	0.335
10000	0.609	-0.065	-0.791
10000	0.220	-0.233	-0.947
10000	-0.004	-0.910	-0.415
10000	-0.511	0.627	-0.589
10000	0.414	0.737	0.535
10000	-0.679	0.139	-0.721
10000	0.884	-0.296	0.362
10000	0.262	0.432	0.863
10000	0.088	0.185	-0.979
10000	0.294	-0.907	0.302
10000	0.887	-0.089	-0.453
10000	0.257	-0.443	0.859
10000	0.086	0.867	-0.491
10000	0.863	0.504	-0.025

Table A.4 b-matrix used to collect diffusion kurtosis data. A diffusion scheme with five shells (b = 2000, 4000, 6000, 8000, 10000 s/mm^2) and 10 unweighted (b = 0 s/mm^2) was used to collect data long 30 collinear directions.

Table A.5: Transformations applied to hTau data

Dataset	Normally distributed? (Shapiro Wilk ($p < 0.05$)	Transformation applied	Effect of Cohort
Three chamber social interaction: sociability index	No	Rank (no ties)	No
Three chamber social interaction: social novelty index	No	Rank (no ties)	No
Open field maze: thigmotaxis	Yes	N/A	No
Elevated plus maze: % time in open arms	No	Rank (no ties)	No
Morris Water Maze visible platform: speed to target	No	Averaged across test session	No

Morris Water Maze visible platform: distance to target	No	Averaged across test session	No
Morris Water Maze hidden platform: speed to target	No	Square root	No
Morris Water Maze hidden platform: speed to target	No	Rank transformed averaged across test session (no ties)	No
Morris Water Maze probe trial: proximity to platform	No	Inverse (1/x)	No
Morris Water Maze probe trial: % time in target quadrant	No	Rank	No
Astrogliosis: % area GFAP staining	Yes	N/A	No

Table A.5 List of transformations applied for statistical analysis of data. Datasets where the residuals were not normally distributed (Shapiro Wilkes, $p<0.05$), were transformed so that residuals would be normally distributed. A two way (repeated measures for behavioral data) ANOVA was then used to test for effects of injury and cohort. Once transformed, there was no effect of cohort, allowing us to collapse the datasets for the two cohorts. Post-hoc Tukey testing was then used to test for significant effects of repetitive subconcussive and concussive injury.

Table A.6: Effects sizes for hTau data

Behavioral/Histological Test	$F_{(df,error)}$	Effect Size (η^2_p)
Latency righting reflex	$F_{(2,44)} = 11.8092$	0.349
MWM visible platform: swim speed	$F_{(2,36)} = 29.9335$	0.624
MWM visible platform: swimming distance	$F_{(2,36)} = 25.642$	0.588
MWM hidden platform: swim speed	$F_{(2,36)} = 36.5009$	0.663
MWM hidden platform: swimming distance	$F_{(2,36)} = 6.272$	0.564
MWM probe trial: proximity to platform	$F_{(2,36)} = 23.173$ (Injury) $F_{(2,70)} = 6.9935$ (Time)	0.570 (Injury) 0.167 (Time)
MWM probe trial: % time in target quadrant	$F_{(2,36)} = 22.851$	0.566
Three chamber social interaction: sociability	$F_{(2,37)} = 0.300$	0.0159
Three chamber social interaction: social novelty	$F_{(2,37)} = 2.729$	.0860
Open field maze: thigmotaxis	$F_{(2,37)} = 3.610$	0.0243
Elevated plus maze: % time in open arms	$F_{(2,37)} = 0.195$	0.00102
Tail suspension: time immobile	$F_{(2,37)} = 12.954$	0.412
Astrogliosis: % area GFAP staining cortical gray matter	$F_{(2,31)} = 135.77$	0.125
Astrogliosis: % area GFAP staining lateral septal nucleus	$F_{(2,21)} = 62.55$	0.368
Astrogliosis: % area GFAP staining hippocampus	$F_{(2,30)} = 474.92$	0.00868
Astrogliosis: % area GFAP staining corpus callosum	$F_{(2,29)} = 349.54$	0.0156
Astrogliosis: % area GFAP staining anterior commissure	$F_{(2,27)} = 17.53$	0.0138
Astrogliosis: % area GFAP staining hippocampal commissure	$F_{(2,25)} = 116.08$	0.0126
Astrogliosis: % area GFAP staining fimbria	$F_{(2,28)} = 136.95$	0.0778
White matter integrity: power coherence corpus callosum	$F_{(2,37)} = 28.048$	0.644
White matter integrity: power coherence anterior commissure	$F_{(2,25)} = 183.19$	0.144
White matter integrity: power coherence hippocampal commissure	$F_{(2,37)} = 34.015$	0.687
White matter integrity: power coherence fimbria	$F_{(2,37)} = 17.262$	0.527

Table A.6 List of effect sizes for ANOVAs. The F distribution, described by the degrees of freedom and error, along with effect sizes (η^2_p) were calculated for each behavioral and histological parameter assessed.

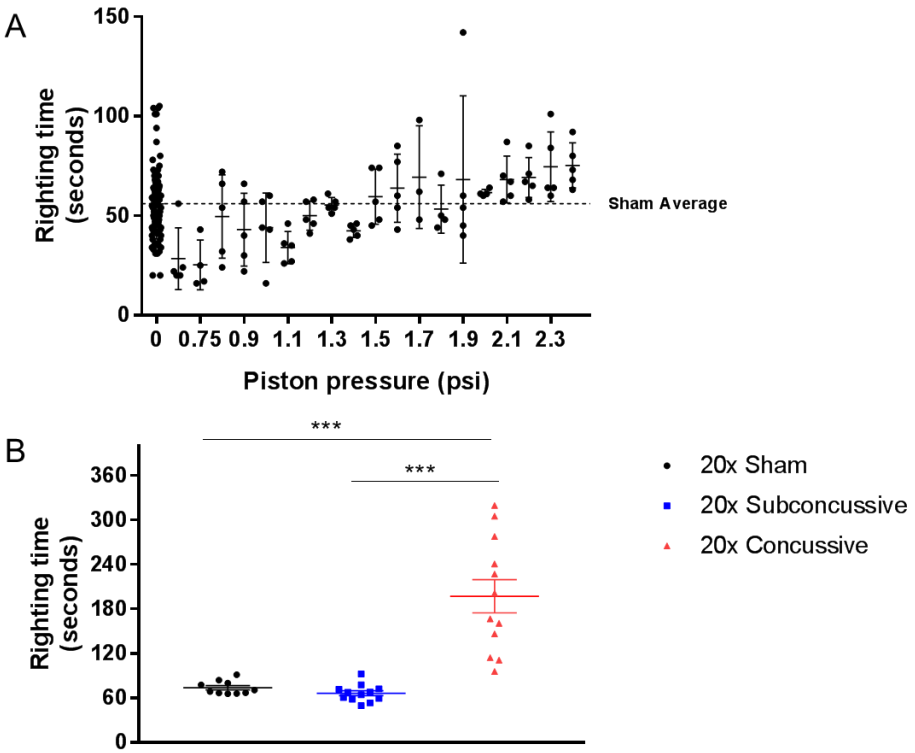

Figure A.1 Determination of impact thresholds. A. Wild type mice were randomly assigned to receive a single impact with the CHIMERA piston pressure set to a value between 0 (sham) and 2.4 psi. Latency to righting reflex (righting time) was measured following impact for each animal. Mice in groups receiving an impact of 2.0 psi or higher had mean righting times greater than the sham average (56 seconds), with standard deviations that did not overlap with the sham average righting time. **B.** In a separate experiment, mice (n = 10-12 per group) received daily concussive (3.1 psi) or subconcussive (2.0 psi) injuries for twenty consecutive days. Mice in the 20x concussive group had increased righting times averaged over the course of the twenty days relative to shams ($p = 0.000126$) and animals in the 20x subconcussive group ($p = 0.000125$). There was no difference between sham animals and 20x subconcussive animals.

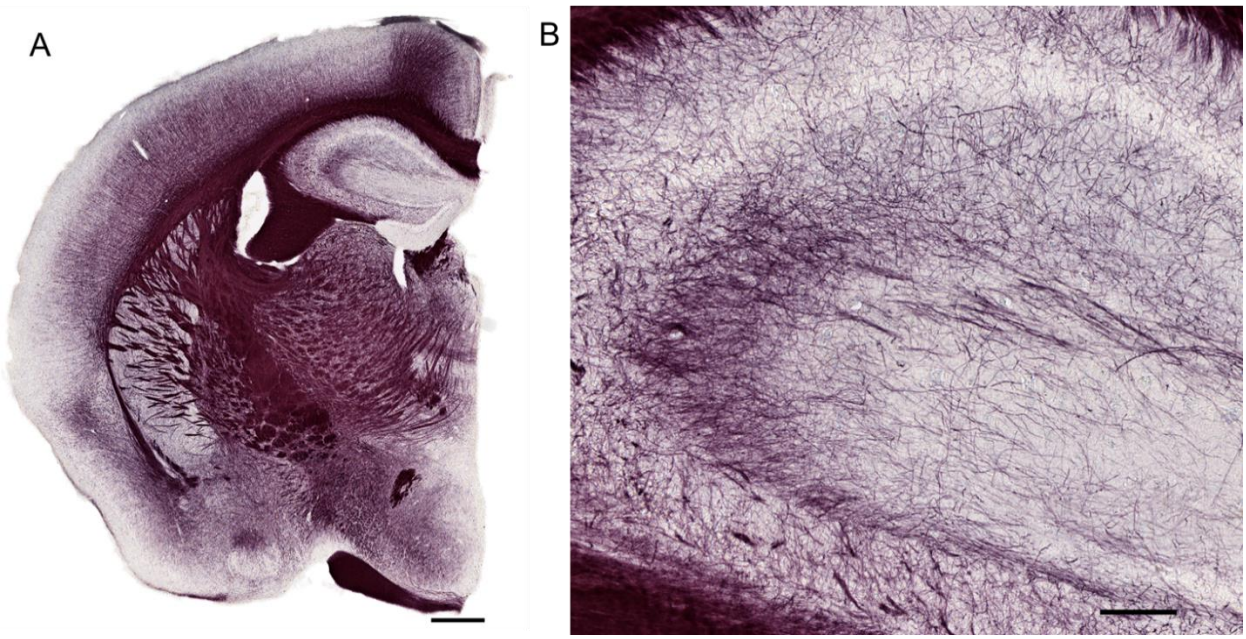

Figure A.2 Myelin Black Gold II staining. A. 50 µm free floating sections were incubated in Black Gold II solution for 8-12 minutes. Scale bar = 500 microns. **B.** Staining was completed once the mossy fibers of the hippocampus were stained. Scale bar = 100 microns.

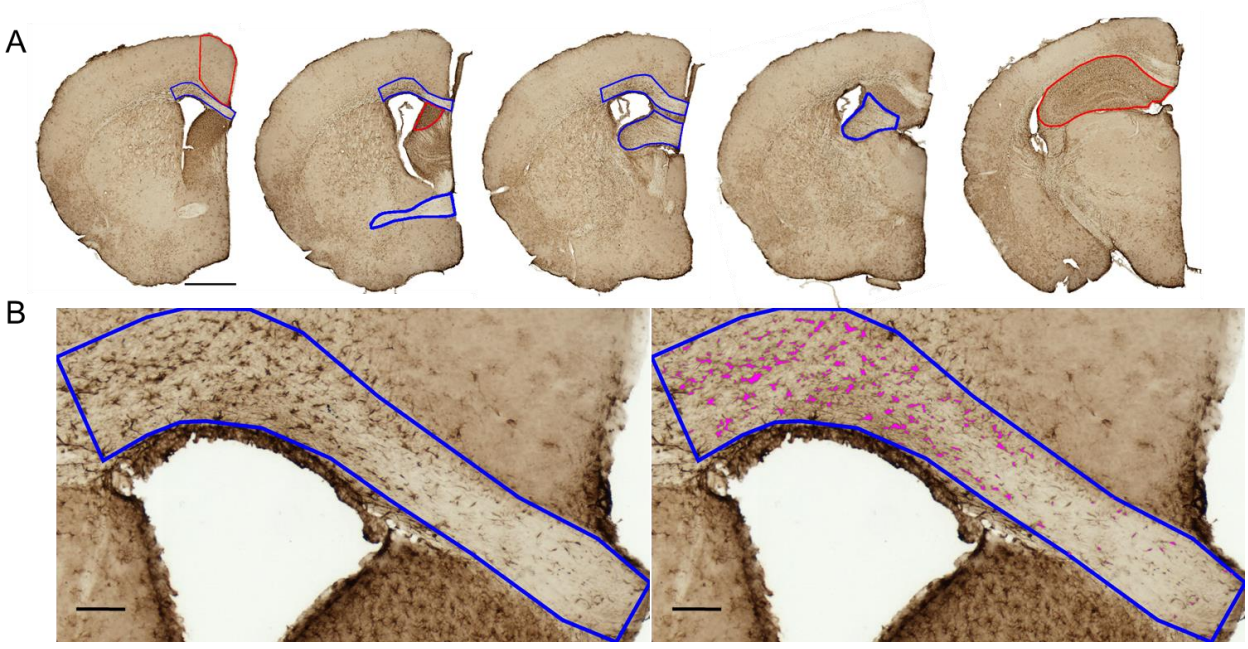

Figure A.3 Quantification of astrogliosis. A. Regions of interest were drawn to include the corpus callosum, cortical gray matter, lateral septal nucleus, anterior commissure, hippocampal commissure, fimbria, and hippocampus (red line = gray matter, blue line = white matter). Scale bar = 500 microns. **B.** Astrogliosis was quantified by thresholding images of the GFAP stained sections in FIJI, followed by size exclusion to remove edge artifacts and out of focus cell bodies. Scale bar = 100 microns.

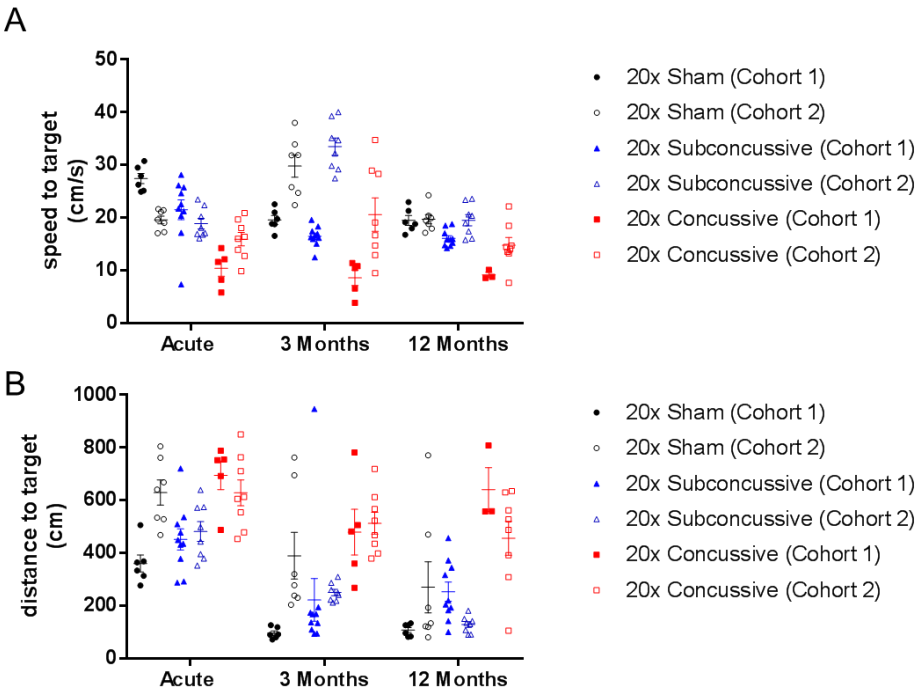

Figure A.4 Raw data of visible phase of Morris Water Maze. A. Swimming speeds during the visible phase of Morris Water Maze. Speeds represent the mean for each subject across the three days of visible platform for each test session. **B.** Distance to the target platform during the visible phase of Morris Water Maze. Distances represent the mean for each subject across the three days of visible platform for each test session.

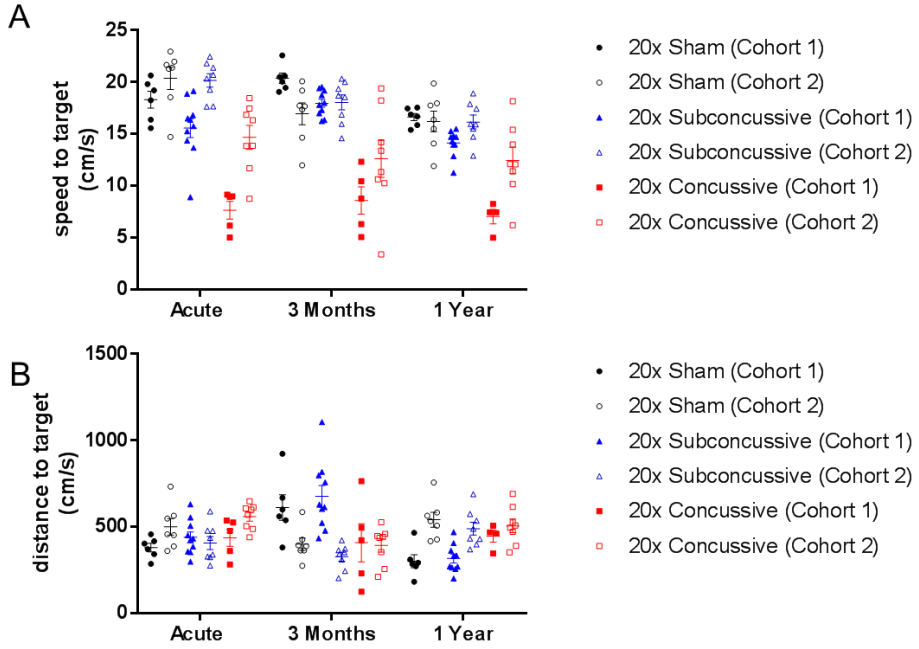

Figure A.5 Raw data of hidden phase of Morris Water Maze. A. Swimming speeds during the hidden phase of Morris Water. Speeds represent the mean for each subject across the four days of hidden platform for each test

session **B.** Distance swum to platform during the hidden phase of Morris Water Maze. Distances represent the mean for each subject across the four days of hidden platform for each test session.

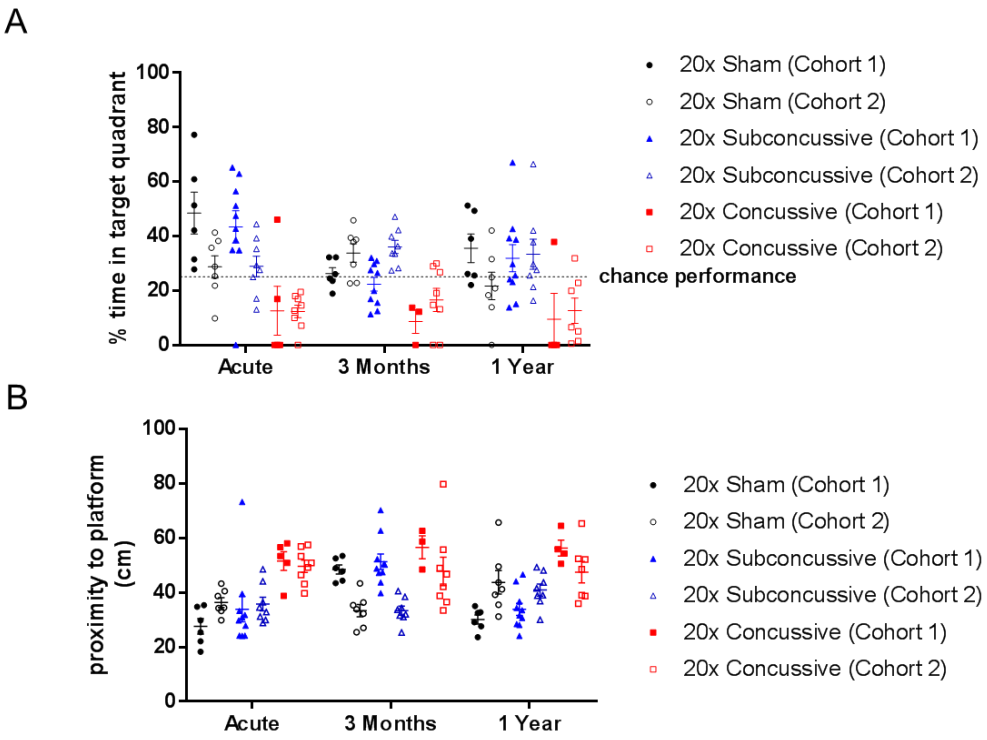

Figure A.6 Raw data of probe trial performance. A. Raw data of percent time spent in the target quadrant during probe trial. Dotted line indicates chance performance, where mice spending less than 25% of their time in the target quadrant show impaired memory. **B.** Raw data of the mean proximity to the location of where the platform had been placed during the preceding hidden platform phase. Increased proximity to platform indicates worse performance and impaired memory of the platform location.

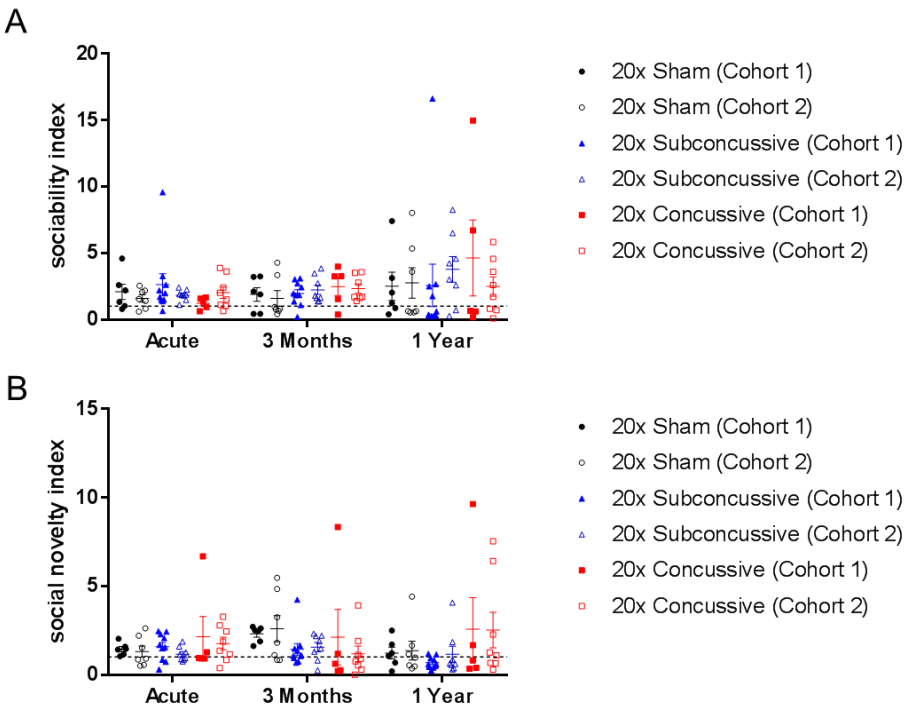

Figure A.7 Raw data of social interaction task. A. Raw data of sociability index during the three chamber social interaction test. Sociability index was calculated as the ratio of time interacting with the stimulus mouse to time spent with the novel object. The dotted line marks an index of one. Points above this line indicate that the animal preferred to interact with the stimulus mouse. **B.** Raw data of social novelty index during the three chamber social interaction test. Social novelty index was calculated as the ratio of time interacting with the novel mouse to time spent with the first stimulus mouse. The dotted line marks an index of one. Points above this line indicate that the animal preferred to interact with the novel mouse.

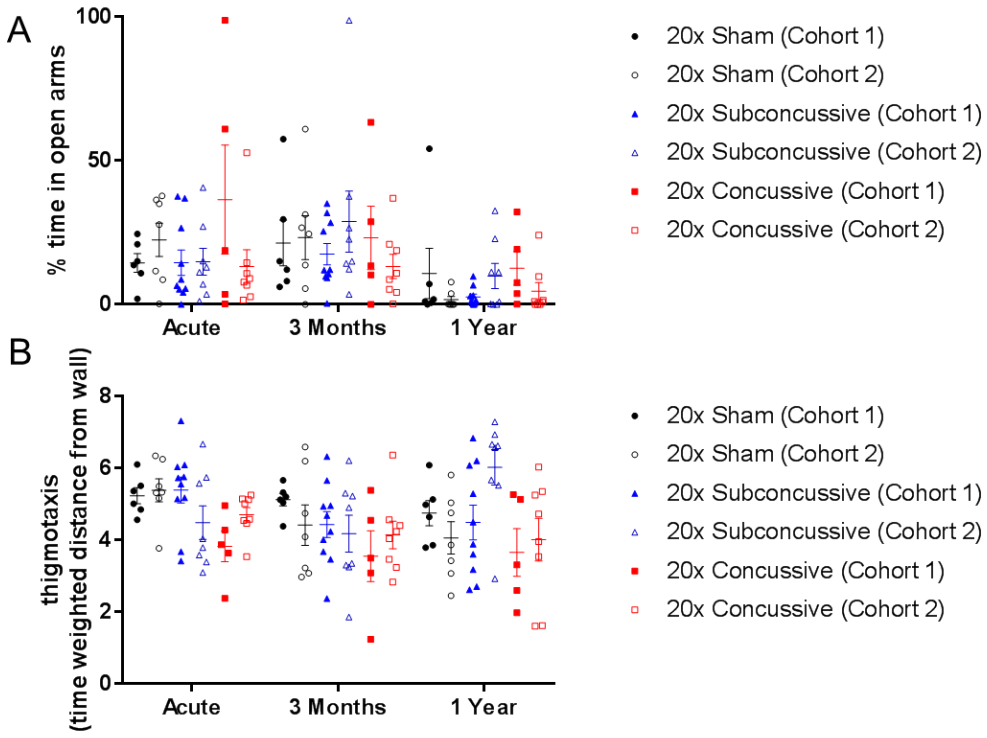

Figure A.8 Raw data of elevated plus maze and open field maze. A. Percent time spent in the open arms of the elevated plus maze. **B.** Raw data of open field maze thigmotaxis, measured as the time weighted distance from the maze wall.

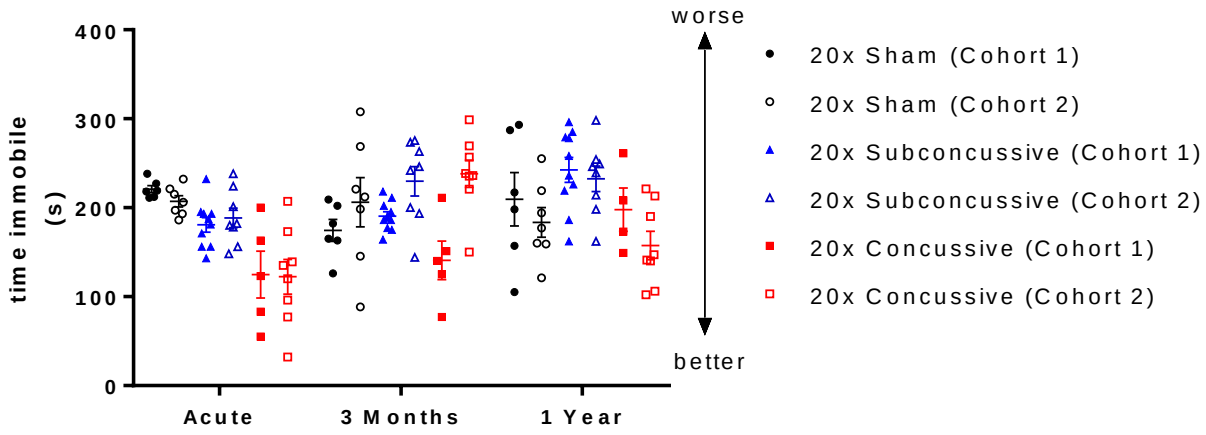

Figure A.9 Raw data of tail suspension test. Raw data of time immobile during a six minute tail suspension test was measured for each animal during each test session.

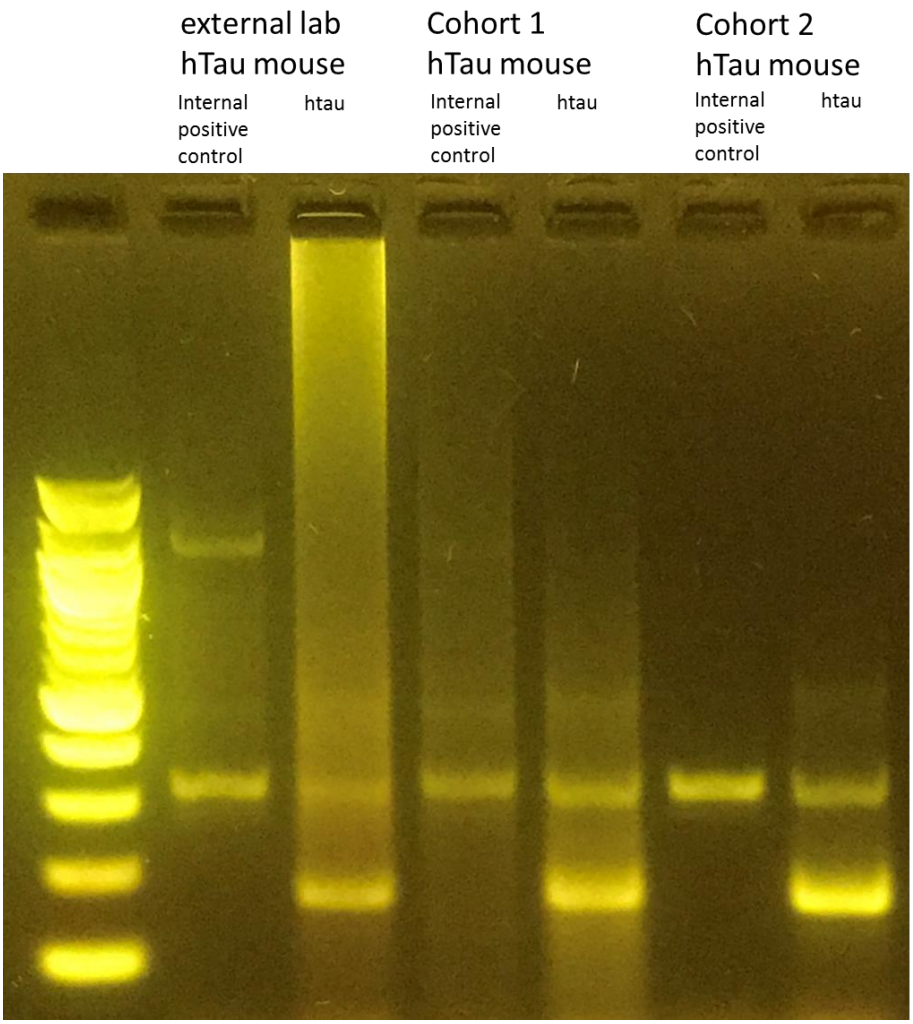

Figure A.10 PCR genotyping of hTau mice PCR was performed by DNA extraction from fresh-frozen brain tissue of one hTau mouse randomly selected from each cohort of animals purchased from Jackson Laboratory. As a positive control, tail DNA from an hTau mouse was obtained from an independent investigator. The animals from each cohort tested positive for the hTau transgene.

References

Absinta, M., Nair, G., Filippi, M., Ray-Chaudhury, A., Reyes-Mantilla, M.I., Pardo, C.A., Reich, D.S., 2014. Postmortem magnetic resonance imaging to guide the pathologic cut: individualized, 3-dimensionally printed cutting boxes for fixed brains. J Neuropathol Exp Neurol 73, 780-788.

Adams, J.H., Doyle, D., Ford, I., Gennarelli, T.A., Graham, D.I., McLellan, D.R., 1989. Diffuse axonal injury in head injury: definition, diagnosis and grading. Histopathology 15, 49-59.

Alexander, M.P., 1995. Mild traumatic brain injury: pathophysiology, natural history, and clinical management. Neurology 45, 1253-1260.

Amato, S.P., Pan, F., Schwartz, J., Ragan, T.M., 2016. Whole Brain Imaging with Serial Two-Photon Tomography. Front Neuroanat 10, 31.

Andorfer, C., Kress, Y., Espinoza, M., de Silva, R., Tucker, K.L., Barde, Y.A., Duff, K., Davies, P., 2003. Hyperphosphorylation and aggregation of tau in mice expressing normal human tau isoforms. Journal of neurochemistry 86, 582-590.

Arfanakis, K., Haughton, V.M., Carew, J.D., Rogers, B.P., Dempsey, R.J., Meyerand, M.E., 2002. Diffusion tensor MR imaging in diffuse axonal injury. AJNR Am J Neuroradiol 23, 794-802.

Bajwa, N.M., Halavi, S., Hamer, M., Semple, B.D., Noble-Haeusslein, L.J., Baghchechi, M., Hiroto, A., Hartman, R.E., Obenaus, A., 2016. Mild Concussion, but Not Moderate Traumatic Brain Injury, Is Associated with Long-Term Depression-Like Phenotype in Mice. PLoS One 11, e0146886.

Barnette, A.R., Neil, J.J., Kroenke, C.D., Griffith, J.L., Epstein, A.A., Bayly, P.V., Knutsen, A.K., Inder, T.E., 2009. Characterization of brain development in the ferret via MRI. Pediatric research 66, 80-84.

Barrio, J.R., Small, G.W., Wong, K.P., Huang, S.C., Liu, J., Merrill, D.A., Giza, C.C., Fitzsimmons, R.P., Omalu, B., Bailes, J., Kepe, V., 2015. In vivo characterization of chronic traumatic encephalopathy using [F-18]FDDNP PET brain imaging. Proc Natl Acad Sci U S A 112, E2039-2047.

Basser, P.J., 2002. Relationships between diffusion tensor and q-space MRI. Magnetic resonance in medicine 47, 392-397.

Basser, P.J., Özarslan, E., 2014. Chapter 1 - Introduction to Diffusion MR. Diffusion MRI (Second Edition). Academic Press, San Diego, pp. 3-9.

Beaulieu, C., 2009. CHAPTER 6 - The Biological Basis of Diffusion Anisotropy A2 - Johansen-Berg, Heidi. In: Behrens, T.E.J. (Ed.), Diffusion MRI. Academic Press, San Diego, pp. 105-126.

Behrens, T.E.J., Sotiropoulos, S.N., Jbabdi, S., 2014. Chapter 19 - MR Diffusion Tractography. Diffusion MRI (Second Edition). Academic Press, San Diego, pp. 429-451.

Bennett, R.E., Mac Donald, C.L., Brody, D.L., 2012. Diffusion tensor imaging detects axonal injury in a mouse model of repetitive closed-skull traumatic brain injury. Neuroscience letters 513, 160-165.

Benveniste, H., Kim, K., Zhang, L., Johnson, G.A., 2000. Magnetic resonance microscopy of the C57BL mouse brain. Neuroimage 11, 601-611.

Bieniek, K.F., Ross, O.A., Cormier, K.A., Walton, R.L., Soto-Ortolaza, A., Johnston, A.E., DeSaro, P., Boylan, K.B., Graff-Radford, N.R., Wszolek, Z.K., Rademakers, R., Boeve, B.F., McKee, A.C., Dickson, D.W., 2015. Chronic traumatic encephalopathy pathology in a neurodegenerative disorders brain bank. Acta neuropathologica 130, 877-889.

Bishara, A.J., Hittner, J.B., 2017. Confidence intervals for correlations when data are not normal. Behavior research methods 49, 294-309.

Blumbergs, P.C., Jones, N.R., North, J.B., 1989. Diffuse axonal injury in head trauma. J Neurol Neurosurg Psychiatry 52, 838-841.

Blumbergs, P.C., Scott, G., Manavis, J., Wainwright, H., Simpson, D.A., McLean, A.J., 1994. Staining of amyloid precursor protein to study axonal damage in mild head injury. Lancet 344, 1055-1056.

Bogoslovsky, T., Wilson, D., Chen, Y., Hanlon, D., Gill, J., Jeromin, A., Song, L., Moore, C., Gong, Y., Kenney, K., Diaz-Arrastia, R., 2016. Increases of Plasma Levels of Glial Fibrillary Acidic Protein, Tau, and Amyloid beta up to 90 Days after Traumatic Brain Injury. Journal of Neurotrauma.

Braak, H., Braak, E., 1995. Staging of Alzheimer's disease-related neurofibrillary changes. Neurobiology of aging 16, 271-278; discussion 278-284.

Breen, M.S., Lancaster, T.L., Wilson, D.L., 2005a. Correcting spatial distortion in histological images. Comput Med Imaging Graph 29, 405-417.

Breen, M.S., Lazebnik, R.S., Wilson, D.L., 2005b. Three-dimensional registration of magnetic resonance image data to histological sections with model-based evaluation. Ann Biomed Eng 33, 1100-1112.

Brody, D.L., Mac Donald, C., Kessens, C.C., Yuede, C., Parsadanian, M., Spinner, M., Kim, E., Schwetye, K.E., Holtzman, D.M., Bayly, P.V., 2007. Electromagnetic controlled cortical impact device for precise, graded experimental traumatic brain injury. Journal of Neurotrauma 24, 657-673.

Budde, M.D., Annese, J., 2013. Quantification of anisotropy and fiber orientation in human brain histological sections. Front Integr Neurosci 7, 3.

Budde, M.D., Frank, J.A., 2012. Examining brain microstructure using structure tensor analysis of histological sections. Neuroimage 63, 1-10.

Budde, M.D., Janes, L., Gold, E., Turtzo, L.C., Frank, J.A., 2011. The contribution of gliosis to diffusion tensor anisotropy and tractography following traumatic brain injury: validation in the rat using Fourier analysis of stained tissue sections. Brain 134, 2248-2260.

Cairns, N.J., Bigio, E.H., Mackenzie, I.R., Neumann, M., Lee, V.M., Hatanpaa, K.J., White, C.L., 3rd, Schneider, J.A., Grinberg, L.T., Halliday, G., Duyckaerts, C., Lowe, J.S., Holm, I.E., Tolnay, M., Okamoto, K., Yokoo, H., Murayama, S., Woulfe, J., Munoz, D.G., Dickson, D.W., Ince, P.G., Trojanowski, J.Q., Mann, D.M., 2007. Neuropathologic diagnostic and nosologic criteria for frontotemporal lobar degeneration: consensus of the Consortium for Frontotemporal Lobar Degeneration. Acta neuropathologica 114, 5-22.

Castagne, V., Moser, P., Roux, S., Porsolt, R.D., 2011. Rodent models of depression: forced swim and tail suspension behavioral despair tests in rats and mice. Current protocols in neuroscience Chapter 8, Unit 8 10A.

Chen, H., Desai, A., Kim, H.Y., 2017a. Repetitive Closed-Head Impact Model of Engineered Rotational Acceleration Induces Long-Term Cognitive Impairments with Persistent Astrogliosis and Microgliosis in Mice. Journal of Neurotrauma 34, 2291-2302.

Chen, Y., Sha, M., Zhao, X., Ma, J., Ni, H., Gao, W., Ming, D., 2017b. Automated detection of pathologic white matter alterations in Alzheimer's disease using combined diffusivity and kurtosis method. Psychiatry research. Neuroimaging 264, 35-45.
Cherry, J.D., Tripodis, Y., Alvarez, V.E., Huber, B., Kiernan, P.T., Daneshvar, D.H., Mez, J., Montenigro, P.H., Solomon, T.M., Alosco, M.L., Stern, R.A., McKee, A.C., Stein, T.D., 2016. Microglial neuroinflammation contributes to tau accumulation in chronic traumatic encephalopathy. Acta neuropathologica communications 4, 112.
Cheverud, J.M., 2001. A simple correction for multiple comparisons in interval mapping genome scans. Heredity 87, 52-58.
Choe, A.S., Gao, Y., Li, X., Compton, K.B., Stepniewska, I., Anderson, A.W., 2011. Accuracy of image registration between MRI and light microscopy in the ex vivo brain. Magn Reson Imaging 29, 683-692.
Chung, K., Deisseroth, K., 2013. CLARITY for mapping the nervous system. Nature methods 10, 508-513.
Coughlin, J.M., Wang, Y., Munro, C.A., Ma, S., Yue, C., Chen, S., Airan, R., Kim, P.K., Adams, A.V., Garcia, C., Higgs, C., Sair, H.I., Sawa, A., Smith, G., Lyketsos, C.G., Caffo, B., Kassiou, M., Guilarte, T.R., Pomper, M.G., 2015. Neuroinflammation and brain atrophy in former NFL players: An in vivo multimodal imaging pilot study. Neurobiology of disease 74, 58-65.
Creeley, C.E., Wozniak, D.F., Bayly, P.V., Olney, J.W., Lewis, L.M., 2004. Multiple episodes of mild traumatic brain injury result in impaired cognitive performance in mice. Academic emergency medicine : official journal of the Society for Academic Emergency Medicine 11, 809-819.
D'Arceuil, H., de Crespigny, A., 2007. The effects of brain tissue decomposition on diffusion tensor imaging and tractography. Neuroimage 36, 64-68.
D'Arceuil, H.E., Westmoreland, S., de Crespigny, A.J., 2007. An approach to high resolution diffusion tensor imaging in fixed primate brain. Neuroimage 35, 553-565.
d'Orange, M., Auregan, G., Cheramy, D., Gaudin-Guerif, M., Lieger, S., Guillermier, M., Stimmer, L., Josephine, C., Herard, A.S., Gaillard, M.C., Petit, F., Kiessling, M.C., Schmitz, C., Colin, M., Buee, L., Panayi, F., Diguet, E., Brouillet, E., Hantraye, P., Bemelmans, A.P., Cambon, K., 2018. Potentiating tangle formation reduces acute toxicity of soluble tau species in the rat. Brain : a journal of neurology 141, 535-549.
Dauguet, J., Delzescaux, T., Conde, F., Mangin, J.F., Ayache, N., Hantraye, P., Frouin, V., 2007. Three-dimensional reconstruction of stained histological slices and 3D non-linear registration with in-vivo MRI for whole baboon brain. J Neurosci Methods 164, 191-204.
de Guzman, A.E., Wong, M.D., Gleave, J.A., Nieman, B.J., 2016. Variations in post-perfusion immersion fixation and storage alter MRI measurements of mouse brain morphometry. Neuroimage.
Delannoy, J., Chen, C.N., Turner, R., Levin, R.L., Le Bihan, D., 1991. Noninvasive temperature imaging using diffusion MRI. Magnetic resonance in medicine 19, 333-339.
DeMattos, R.B., Bales, K.R., Parsadanian, M., O'Dell, M.A., Foss, E.M., Paul, S.M., Holtzman, D.M., 2002. Plaque-associated disruption of CSF and plasma amyloid-beta (Abeta) equilibrium in a mouse model of Alzheimer's disease. Journal of neurochemistry 81, 229-236.

Deroulers, C., Ameisen, D., Badoual, M., Gerin, C., Granier, A., Lartaud, M., 2013. Analyzing huge pathology images with open source software. Diagnostic pathology 8, 92.

DeWalt, G.J., Mahajan, B., Foster, A.R., Thompson, L.D.E., Marttini, A.A., Schmidt, E.V., Mansuri, S., D'Souza, D., Patel, S.B., Tenenbaum, M., Brandao-Viruet, K.I., Thompson, D., Duong, B., Smith, D.H., Blute, T.A., Eldred, W.D., 2017. Region-specific alterations in astrocyte and microglia morphology following exposure to blasts in the mouse hippocampus. Neuroscience letters 664, 160-166.

Donahue, C.J., Sotiropoulos, S.N., Jbabdi, S., Hernandez-Fernandez, M., Behrens, T.E., Dyrby, T.B., Coalson, T., Kennedy, H., Knoblauch, K., Van Essen, D.C., Glasser, M.F., 2016. Using Diffusion Tractography to Predict Cortical Connection Strength and Distance: A Quantitative Comparison with Tracers in the Monkey. The Journal of neuroscience : the official journal of the Society for Neuroscience 36, 6758-6770.

Donovan, V., Kim, C., Anugerah, A.K., Coats, J.S., Oyoyo, U., Pardo, A.C., Obenaus, A., 2014. Repeated mild traumatic brain injury results in long-term white-matter disruption. Journal of cerebral blood flow and metabolism : official journal of the International Society of Cerebral Blood Flow and Metabolism 34, 715-723.

Drechsel, D.N., Hyman, A.A., Cobb, M.H., Kirschner, M.W., 1992. Modulation of the dynamic instability of tubulin assembly by the microtubule-associated protein tau. Molecular biology of the cell 3, 1141-1154.

Edgar, J.M., Griffiths, I.R., 2014. Chapter 7 - White Matter Structure: A Microscopist's View. Diffusion MRI (Second Edition). Academic Press, San Diego, pp. 127-153.

Fan, Q., Nummenmaa, A., Witzel, T., Zanzonico, R., Keil, B., Cauley, S., Polimeni, J.R., Tisdall, D., Van Dijk, K.R., Buckner, R.L., Wedeen, V.J., Rosen, B.R., Wald, L.L., 2014. Investigating the capability to resolve complex white matter structures with high b-value diffusion magnetic resonance imaging on the MGH-USC Connectom scanner. Brain connectivity 4, 718-726.

Gangolli, M., Holleran, L., Hee Kim, J., Stein, T.D., Alvarez, V., McKee, A.C., Brody, D.L., 2017. Quantitative validation of a nonlinear histology-MRI coregistration method using generalized Q-sampling imaging in complex human cortical white matter. Neuroimage 153, 152-167.

Gangolli, M., Kim, J., Holleran, L., Stein, T., Alvarez, V., McKee, A., Brody, D., 2015. Advanced Diffusion MRI Methods to Quantitatively Distinguish Between Complex White Matter and Traumatic Axonal Injury. National Neurotrauma Symposium. Mary Ann Liebert, Santa Fe, NM, p. A54.

Gennarelli, T.A., Graham, D.I., 1998. Neuropathology of the Head Injuries. Semin Clin Neuropsychiatry 3, 160-175.

Gerson, J., Castillo-Carranza, D.L., Sengupta, U., Bodani, R., Prough, D.S., DeWitt, D.S., Hawkins, B.E., Kayed, R., 2016. Tau Oligomers Derived from Traumatic Brain Injury Cause Cognitive Impairment and Accelerate Onset of Pathology in Htau Mice. Journal of Neurotrauma 33, 2034-2043.

Ghajari, M., Hellyer, P.J., Sharp, D.J., 2017. Computational modelling of traumatic brain injury predicts the location of chronic traumatic encephalopathy pathology. Brain : a journal of neurology 140, 333-343.

Goedert, M., Spillantini, M.G., Jakes, R., Rutherford, D., Crowther, R.A., 1989. Multiple isoforms of human microtubule-associated protein tau: sequences and localization in neurofibrillary tangles of Alzheimer's disease. Neuron 3, 519-526.

Goshtasby, A., 1988. Image Registration by Local Approximation Methods. Image and Vision Computing 6, 255-261.

Goubran, M., Crukley, C., de Ribaupierre, S., Peters, T.M., Khan, A.R., 2013. Image registration of ex-vivo MRI to sparsely sectioned histology of hippocampal and neocortical temporal lobe specimens. Neuroimage 83, 770-781.

Goubran, M., de Ribaupierre, S., Hammond, R.R., Currie, C., Burneo, J.G., Parrent, A.G., Peters, T.M., Khan, A.R., 2015. Registration of in-vivo to ex-vivo MRI of surgically resected specimens: a pipeline for histology to in-vivo registration. J Neurosci Methods 241, 53-65.

Grossman, E.J., Ge, Y., Jensen, J.H., Babb, J.S., Miles, L., Reaume, J., Silver, J.M., Grossman, R.I., Inglese, M., 2012. Thalamus and cognitive impairment in mild traumatic brain injury: a diffusional kurtosis imaging study. Journal of Neurotrauma 29, 2318-2327.

Guo, J.L., Narasimhan, S., Changolkar, L., He, Z., Stieber, A., Zhang, B., Gathagan, R.J., Iba, M., McBride, J.D., Trojanowski, J.Q., Lee, V.M., 2016. Unique pathological tau conformers from Alzheimer's brains transmit tau pathology in nontransgenic mice. The Journal of experimental medicine 213, 2635-2654.

Guzman-Martinez, L., Farias, G.A., Maccioni, R.B., 2013. Tau oligomers as potential targets for Alzheimer's diagnosis and novel drugs. Frontiers in neurology 4, 167.

Haber, M., Hutchinson, E.B., Sadeghi, N., Cheng, W.H., Namjoshi, D., Cripton, P., Irfanoglu, M.O., Wellington, C., Diaz-Arrastia, R., Pierpaoli, C., 2017. Defining an Analytic Framework to Evaluate Quantitative MRI Markers of Traumatic Axonal Injury: Preliminary Results in a Mouse Closed Head Injury Model. eNeuro 4.

Hagmann, P., Jonasson, L., Deffieux, T., Meuli, R., Thiran, J.P., Wedeen, V.J., 2006. Fibertract segmentation in position orientation space from high angular resolution diffusion MRI. Neuroimage 32, 665-675.

Hales, C., Neill, S., Gearing, M., Cooper, D., Glass, J., Lah, J., 2014. Late-stage CTE pathology in a retired soccer player with dementia. Neurology 83, 2307-2309.

Hellyer, P.J., Leech, R., Ham, T.E., Bonnelle, V., Sharp, D.J., 2013. Individual prediction of white matter injury following traumatic brain injury. Annals of neurology 73, 489-499.

Helpern, J.A., Adisetiyo, V., Falangola, M.F., Hu, C., Di Martino, A., Williams, K., Castellanos, F.X., Jensen, J.H., 2011. Preliminary evidence of altered gray and white matter microstructural development in the frontal lobe of adolescents with attention-deficit hyperactivity disorder: a diffusional kurtosis imaging study. Journal of magnetic resonance imaging : JMRI 33, 17-23.

Henriksen, K., Wang, Y., Sorensen, M.G., Barascuk, N., Suhy, J., Pedersen, J.T., Duffin, K.L., Dean, R.A., Pajak, M., Christiansen, C., Zheng, Q., Karsdal, M.A., 2013. An enzyme-generated fragment of tau measured in serum shows an inverse correlation to cognitive function. PLoS One 8, e64990.

Herrera, J.J., Bockhorst, K., Kondraganti, S., Stertz, L., Quevedo, J., Narayana, P.A., 2016. Acute White Matter Tract Damage after Frontal Mild Traumatic Brain Injury. J Neurotrauma.

Hof, P.R., Bouras, C., Buee, L., Delacourte, A., Perl, D.P., Morrison, J.H., 1992. Differential distribution of neurofibrillary tangles in the cerebral cortex of dementia pugilistica and Alzheimer's disease cases. Acta neuropathologica 85, 23-30.
Holleran, L., Kim, J., Gangolli, M., Stein, T., Alvarez, V., McKee, A., Brody, D., 2015. Advanced Diffusion MRI-Based Radiological Pathological Correlations in Chronic Traumatic Encephalopathy. National Neurotrauma Symposium. Mary Ann Liebert, Santa Fe, NM, p. A9.
Holleran, L., Kim, J.H., Gangolli, M., Stein, T., Alvarez, V., McKee, A., Brody, D.L., 2017. Axonal disruption in white matter underlying cortical sulcus tau pathology in chronic traumatic encephalopathy. Acta neuropathologica 133, 367-380.
Hoult, D.I., Richards, R.E., 2011. The signal-to-noise ratio of the nuclear magnetic resonance experiment. 1976. Journal of magnetic resonance 213, 329-343.
Hsueh, B., Burns, V.M., Pauerstein, P., Holzem, K., Ye, L., Engberg, K., Wang, A.C., Gu, X., Chakravarthy, H., Arda, H.E., Charville, G., Vogel, H., Efimov, I.R., Kim, S., Deisseroth, K., 2017. Pathways to clinical CLARITY: volumetric analysis of irregular, soft, and heterogeneous tissues in development and disease. Sci Rep 7, 5899.
Hubbard, P.L., Parker, G.J.M., 2014. Chapter 20 - Validation of Tractography. Diffusion MRI (Second Edition). Academic Press, San Diego, pp. 453-480.
Hutchinson, E.B., Schwerin, S.C., Radomski, K.L., Irfanoglu, M.O., Juliano, S.L., Pierpaoli, C.M., 2016. Quantitative MRI and DTI Abnormalities During the Acute Period Following CCI in the Ferret. Shock 46, 167-176.
Ichikawa, H., Ishikawa, M., Fukunaga, M., Ishikawa, K., Ishiyama, H., 2010. Quantitative evaluation of blood-cerebrospinal fluid barrier permeability in the rat with experimental meningitis using magnetic resonance imaging. Brain research 1321, 125-132.
Im, K., Lee, J.M., Lyttelton, O., Kim, S.H., Evans, A.C., Kim, S.I., 2008. Brain size and cortical structure in the adult human brain. Cerebral cortex 18, 2181-2191.
Jensen, J.H., Helpern, J.A., 2010. MRI quantification of non-Gaussian water diffusion by kurtosis analysis. NMR in biomedicine 23, 698-710.
Jensen, J.H., Helpern, J.A., Ramani, A., Lu, H., Kaczynski, K., 2005. Diffusional kurtosis imaging: the quantification of non-gaussian water diffusion by means of magnetic resonance imaging. Magn Reson Med 53, 1432-1440.
Jeurissen, B., Leemans, A., Tournier, J.D., Jones, D.K., Sijbers, J., 2013. Investigating the prevalence of complex fiber configurations in white matter tissue with diffusion magnetic resonance imaging. Human brain mapping 34, 2747-2766.
Johnson, V.E., Stewart, J.E., Begbie, F.D., Trojanowski, J.Q., Smith, D.H., Stewart, W., 2013. Inflammation and white matter degeneration persist for years after a single traumatic brain injury. Brain 136, 28-42.
Jones, D.K., Cercignani, M., 2010. Twenty-five pitfalls in the analysis of diffusion MRI data. NMR in biomedicine 23, 803-820.
Jones, D.K., Horsfield, M.A., Simmons, A., 1999. Optimal strategies for measuring diffusion in anisotropic systems by magnetic resonance imaging. Magnetic resonance in medicine 42, 515-525.
Kanayama, G., Takeda, M., Niigawa, H., Ikura, Y., Tamii, H., Taniguchi, N., Kudo, T., Miyamae, Y., Morihara, T., Nishimura, T., 1996. The effects of repetitive mild brain

injury on cytoskeletal protein and behavior. Methods and findings in experimental and clinical pharmacology 18, 105-115.
Kashluba, S., Paniak, C., Blake, T., Reynolds, S., Toller-Lobe, G., Nagy, J., 2004. A longitudinal, controlled study of patient complaints following treated mild traumatic brain injury. Archives of clinical neuropsychology : the official journal of the National Academy of Neuropsychologists 19, 805-816.
Kettenmann H, R.B.R., 2013. Neuroglia, 3 ed.
Kier, E.L., Staib, L.H., Davis, L.M., Bronen, R.A., 2004. Anatomic dissection tractography: a new method for precise MR localization of white matter tracts. AJNR Am J Neuroradiol 25, 670-676.
Kim, J.H., Trinkaus, K., Ozcan, A., Budde, M.D., Song, S.K., 2007. Postmortem delay does not change regional diffusion anisotropy characteristics in mouse spinal cord white matter. NMR in biomedicine 20, 352-359.
Kleinnijenhuis, M., 2014. Imaging fibres in the brain.
Klemenhagen, K.C., O'Brien, S.P., Brody, D.L., 2013. Repetitive concussive traumatic brain injury interacts with post-injury foot shock stress to worsen social and depression-like behavior in mice. PLoS One 8, e74510.
Kovacs, G.G., Lee, V.M., Trojanowski, J.Q., 2017. Protein astrogliopathies in human neurodegenerative diseases and aging. Brain pathology 27, 675-690.
Lazebnik, R.S., Lancaster, T.L., Breen, M.S., Lewin, J.S., Wilson, D.L., 2003. Volume registration using needle paths and point landmarks for evaluation of interventional MRI treatments. IEEE Trans Med Imaging 22, 653-660.
Le Bihan, D., 1995. Molecular diffusion, tissue microdynamics and microstructure. NMR Biomed 8, 375-386.
Le Bihan, D., Poupon, C., Amadon, A., Lethimonnier, F., 2006. Artifacts and pitfalls in diffusion MRI. Journal of magnetic resonance imaging : JMRI 24, 478-488.
Luo, J., Nguyen, A., Villeda, S., Zhang, H., Ding, Z., Lindsey, D., Bieri, G., Castellano, J.M., Beaupre, G.S., Wyss-Coray, T., 2014. Long-term cognitive impairments and pathological alterations in a mouse model of repetitive mild traumatic brain injury. Frontiers in neurology 5, 12.
Mac Donald, C.L., Barber, J., Andre, J., Evans, N., Panks, C., Sun, S., Zalewski, K., Elizabeth Sanders, R., Temkin, N., 2017. 5-Year imaging sequelae of concussive blast injury and relation to early clinical outcome. NeuroImage. Clinical 14, 371-378.
Mac Donald, C.L., Dikranian, K., Bayly, P., Holtzman, D., Brody, D., 2007a. Diffusion tensor imaging reliably detects experimental traumatic axonal injury and indicates approximate time of injury. The Journal of neuroscience : the official journal of the Society for Neuroscience 27, 11869-11876.
Mac Donald, C.L., Dikranian, K., Song, S.K., Bayly, P.V., Holtzman, D.M., Brody, D.L., 2007b. Detection of traumatic axonal injury with diffusion tensor imaging in a mouse model of traumatic brain injury. Exp Neurol 205, 116-131.
Mahar, I., Alosco, M.L., McKee, A.C., 2017. Psychiatric phenotypes in chronic traumatic encephalopathy. Neuroscience and biobehavioral reviews 83.
Manning, K.Y., Schranz, A., Bartha, R., Dekaban, G.A., Barreira, C., Brown, A., Fischer, L., Asem, K., Doherty, T.J., Fraser, D.D., Holmes, J., Menon, R.S., 2017. Multiparametric

MRI changes persist beyond recovery in concussed adolescent hockey players. Neurology 89, 2157-2166.
Mannix, R., Berkner, J., Mei, Z., Alcon, S., Hashim, J., Robinson, S., Jantzie, L., Meehan, W.P., 3rd, Qiu, J., 2017. Adolescent Mice Demonstrate a Distinct Pattern of Injury after Repetitive Mild Traumatic Brain Injury. Journal of Neurotrauma 34, 495-504.
Mannix, R., Meehan, W.P., Mandeville, J., Grant, P.E., Gray, T., Berglass, J., Zhang, J., Bryant, J., Rezaie, S., Chung, J.Y., Peters, N.V., Lee, C., Tien, L.W., Kaplan, D.L., Feany, M., Whalen, M., 2013. Clinical correlates in an experimental model of repetitive mild brain injury. Annals of neurology 74, 65-75.
Margulies, S.S., Thibault, L.E., Gennarelli, T.A., 1990. Physical model simulations of brain injury in the primate. Journal of biomechanics 23, 823-836.
Maroon, J.C., Winkelman, R., Bost, J., Amos, A., Mathyssek, C., Miele, V., 2015. Chronic traumatic encephalopathy in contact sports: a systematic review of all reported pathological cases. PLoS One 10, e0117338.
Martland, H.S., 1928. Punch drunk. Journal of the American Medical Association 91, 1103-1107.
McCrory, P., Meeuwisse, W., Johnston, K., Dvorak, J., Aubry, M., Molloy, M., Cantu, R., 2009. Consensus statement on concussion in sport: the 3rd International Conference on Concussion in Sport held in Zurich, November 2008. Journal of athletic training 44, 434-448.
McKee, A.C., Cairns, N.J., Dickson, D.W., Folkerth, R.D., Keene, C.D., Litvan, I., Perl, D.P., Stein, T.D., Vonsattel, J.P., Stewart, W., Tripodis, Y., Crary, J.F., Bieniek, K.F., Dams-O'Connor, K., Alvarez, V.E., Gordon, W.A., 2016. The first NINDS/NIBIB consensus meeting to define neuropathological criteria for the diagnosis of chronic traumatic encephalopathy. Acta neuropathologica 131, 75-86.
McKee, A.C., Cantu, R.C., Nowinski, C.J., Hedley-Whyte, E.T., Gavett, B.E., Budson, A.E., Santini, V.E., Lee, H.S., Kubilus, C.A., Stern, R.A., 2009a. Chronic traumatic encephalopathy in athletes: progressive tauopathy after repetitive head injury. Journal of neuropathology and experimental neurology 68, 709-735.
McKee, A.C., Cantu, R.C., Nowinski, C.J., Hedley-Whyte, E.T., Gavett, B.E., Budson, A.E., Santini, V.E., Lee, H.S., Kubilus, C.A., Stern, R.A., 2009b. Chronic traumatic encephalopathy in athletes: progressive tauopathy after repetitive head injury. J Neuropathol Exp Neurol 68, 709-735.
McKee, A.C., Stein, T.D., Kiernan, P.T., Alvarez, V.E., 2015a. The neuropathology of chronic traumatic encephalopathy. Brain pathology 25, 350-364.
McKee, A.C., Stein, T.D., Kiernan, P.T., Alvarez, V.E., 2015b. The neuropathology of chronic traumatic encephalopathy. Brain Pathol 25, 350-364.
McKee, A.C., Stern, R.A., Nowinski, C.J., Stein, T.D., Alvarez, V.E., Daneshvar, D.H., Lee, H.S., Wojtowicz, S.M., Hall, G., Baugh, C.M., Riley, D.O., Kubilus, C.A., Cormier, K.A., Jacobs, M.A., Martin, B.R., Abraham, C.R., Ikezu, T., Reichard, R.R., Wolozin, B.L., Budson, A.E., Goldstein, L.E., Kowall, N.W., Cantu, R.C., 2013. The spectrum of disease in chronic traumatic encephalopathy. Brain : a journal of neurology 136, 43-64.
McNab, J.A., Jbabdi, S., Deoni, S.C., Douaud, G., Behrens, T.E., Miller, K.L., 2009. High resolution diffusion-weighted imaging in fixed human brain using diffusion-weighted steady state free precession. Neuroimage 46, 775-785.

Mez, J., Daneshvar, D.H., Kiernan, P.T., Abdolmohammadi, B., Alvarez, V.E., Huber, B.R., Alosco, M.L., Solomon, T.M., Nowinski, C.J., McHale, L., Cormier, K.A., Kubilus, C.A., Martin, B.M., Murphy, L., Baugh, C.M., Montenigro, P.H., Chaisson, C.E., Tripodis, Y., Kowall, N.W., Weuve, J., McClean, M.D., Cantu, R.C., Goldstein, L.E., Katz, D.I., Stern, R.A., Stein, T.D., McKee, A.C., 2017. Clinicopathological Evaluation of Chronic Traumatic Encephalopathy in Players of American Football. JAMA 318, 360-370.

Mez, J., Solomon, T.M., Daneshvar, D.H., Stein, T.D., McKee, A.C., 2016. Pathologically Confirmed Chronic Traumatic Encephalopathy in a 25-Year-Old Former College Football Player. JAMA Neurol 73, 353-355.

Miller, K.L., Stagg, C.J., Douaud, G., Jbabdi, S., Smith, S.M., Behrens, T.E., Jenkinson, M., Chance, S.A., Esiri, M.M., Voets, N.L., Jenkinson, N., Aziz, T.Z., Turner, M.R., Johansen-Berg, H., McNab, J.A., 2011. Diffusion imaging of whole, post-mortem human brains on a clinical MRI scanner. Neuroimage 57, 167-181.

Mitsis, E.M., Riggio, S., Kostakoglu, L., Dickstein, D.L., Machac, J., Delman, B., Goldstein, M., Jennings, D., D'Antonio, E., Martin, J., Naidich, T.P., Aloysi, A., Fernandez, C., Seibyl, J., DeKosky, S.T., Elder, G.A., Marek, K., Gordon, W., Hof, P.R., Sano, M., Gandy, S., 2014. Tauopathy PET and amyloid PET in the diagnosis of chronic traumatic encephalopathies: studies of a retired NFL player and of a man with FTD and a severe head injury. Translational psychiatry 4, e441.

Mollink, J., Kleinnijenhuis, M., Cappellen van Walsum, A.V., Sotiropoulos, S.N., Cottaar, M., Mirfin, C., Heinrich, M.P., Jenkinson, M., Pallebage-Gamarallage, M., Ansorge, O., Jbabdi, S., Miller, K.L., 2017. Evaluating fibre orientation dispersion in white matter: Comparison of diffusion MRI, histology and polarized light imaging. Neuroimage 157, 561-574.

Montenigro, P.H., Alosco, M.L., Martin, B.M., Daneshvar, D.H., Mez, J., Chaisson, C.E., Nowinski, C.J., Au, R., McKee, A.C., Cantu, R.C., McClean, M.D., Stern, R.A., Tripodis, Y., 2017. Cumulative Head Impact Exposure Predicts Later-Life Depression, Apathy, Executive Dysfunction, and Cognitive Impairment in Former High School and College Football Players. Journal of Neurotrauma 34, 328-340.

Mouzon, B.C., Bachmeier, C., Ferro, A., Ojo, J.O., Crynen, G., Acker, C.M., Davies, P., Mullan, M., Stewart, W., Crawford, F., 2014. Chronic neuropathological and neurobehavioral changes in a repetitive mild traumatic brain injury model. Annals of neurology 75, 241-254.

Multani, N., Goswami, R., Khodadadi, M., Ebraheem, A., Davis, K.D., Tator, C.H., Wennberg, R., Mikulis, D.J., Ezerins, L., Tartaglia, M.C., 2016. The association between white-matter tract abnormalities, and neuropsychiatric and cognitive symptoms in retired professional football players with multiple concussions. Journal of neurology 263, 1332-1341.

Nadler, J.J., Moy, S.S., Dold, G., Trang, D., Simmons, N., Perez, A., Young, N.B., Barbaro, R.P., Piven, J., Magnuson, T.R., Crawley, J.N., 2004. Automated apparatus for quantitation of social approach behaviors in mice. Genes, brain, and behavior 3, 303-314.

Naess-Schmidt, E.T., Blicher, J.U., Eskildsen, S.F., Tietze, A., Hansen, B., Stubbs, P.W., Jespersen, S., Ostergaard, L., Nielsen, J.F., 2017. Microstructural changes in the thalamus

after mild traumatic brain injury: A longitudinal diffusion and mean kurtosis tensor MRI study. Brain injury 31, 230-236.
Namjoshi, D.R., Cheng, W.H., Bashir, A., Wilkinson, A., Stukas, S., Martens, K.M., Whyte, T., Abebe, Z.A., McInnes, K.A., Cripton, P.A., Wellington, C.L., 2017. Defining the biomechanical and biological threshold of murine mild traumatic brain injury using CHIMERA (Closed Head Impact Model of Engineered Rotational Acceleration). Experimental neurology 292, 80-91.
Namjoshi, D.R., Cheng, W.H., Carr, M., Martens, K.M., Zareyan, S., Wilkinson, A., McInnes, K.A., Cripton, P.A., Wellington, C.L., 2016. Chronic Exposure to Androgenic-Anabolic Steroids Exacerbates Axonal Injury and Microgliosis in the CHIMERA Mouse Model of Repetitive Concussion. PLoS One 11, e0146540.
Namjoshi, D.R., Cheng, W.H., McInnes, K.A., Martens, K.M., Carr, M., Wilkinson, A., Fan, J., Robert, J., Hayat, A., Cripton, P.A., Wellington, C.L., 2014. Merging pathology with biomechanics using CHIMERA (Closed-Head Impact Model of Engineered Rotational Acceleration): a novel, surgery-free model of traumatic brain injury. Molecular neurodegeneration 9, 55.
Nazaran, A., Wisco, J.J., Hageman, N., Schettler, S.P., Wong, A., Vinters, H.V., Teng, C.C., Bangerter, N.K., 2016. Methodology for computing white matter nerve fiber orientation in human histological slices. Journal of neuroscience methods 261, 75-84.
Niogi, S.N., Mukherjee, P., Ghajar, J., Johnson, C., Kolster, R.A., Sarkar, R., Lee, H., Meeker, M., Zimmerman, R.D., Manley, G.T., McCandliss, B.D., 2008. Extent of microstructural white matter injury in postconcussive syndrome correlates with impaired cognitive reaction time: a 3T diffusion tensor imaging study of mild traumatic brain injury. AJNR Am J Neuroradiol 29, 967-973.
Nolte, U.G., Finsterbusch, J., Frahm, J., 2000. Rapid isotropic diffusion mapping without susceptibility artifacts: whole brain studies using diffusion-weighted single-shot STEAM MR imaging. Magnetic resonance in medicine 44, 731-736.
Oddo, S., Caccamo, A., Shepherd, J.D., Murphy, M.P., Golde, T.E., Kayed, R., Metherate, R., Mattson, M.P., Akbari, Y., LaFerla, F.M., 2003. Triple-transgenic model of Alzheimer's disease with plaques and tangles: intracellular Abeta and synaptic dysfunction. Neuron 39, 409-421.
Ojo, J.O., Mouzon, B., Algamal, M., Leary, P., Lynch, C., Abdullah, L., Evans, J., Mullan, M., Bachmeier, C., Stewart, W., Crawford, F., 2016. Chronic Repetitive Mild Traumatic Brain Injury Results in Reduced Cerebral Blood Flow, Axonal Injury, Gliosis, and Increased T-Tau and Tau Oligomers. Journal of neuropathology and experimental neurology 75, 636-655.
Ojo, J.O., Mouzon, B., Greenberg, M.B., Bachmeier, C., Mullan, M., Crawford, F., 2013. Repetitive mild traumatic brain injury augments tau pathology and glial activation in aged hTau mice. Journal of neuropathology and experimental neurology 72, 137-151.
Perrone, D., Aelterman, J., Pizurica, A., Jeurissen, B., Philips, W., Leemans, A., 2015. The effect of Gibbs ringing artifacts on measures derived from diffusion MRI. Neuroimage 120, 441-455.
Petraglia, A.L., Plog, B.A., Dayawansa, S., Chen, M., Dashnaw, M.L., Czerniecka, K., Walker, C.T., Viterise, T., Hyrien, O., Iliff, J.J., Deane, R., Nedergaard, M., Huang, J.H., 2014a. The spectrum of neurobehavioral sequelae after repetitive mild traumatic brain injury: a

novel mouse model of chronic traumatic encephalopathy. Journal of neurotrauma 31, 1211-1224.
Petraglia, A.L., Plog, B.A., Dayawansa, S., Dashnaw, M.L., Czerniecka, K., Walker, C.T., Chen, M., Hyrien, O., Iliff, J.J., Deane, R., Huang, J.H., Nedergaard, M., 2014b. The pathophysiology underlying repetitive mild traumatic brain injury in a novel mouse model of chronic traumatic encephalopathy. Surgical neurology international 5, 184.
Pfefferbaum, A., Sullivan, E.V., Adalsteinsson, E., Garrick, T., Harper, C., 2004. Postmortem MR imaging of formalin-fixed human brain. Neuroimage 21, 1585-1595.
Pierpaoli, C., Barnett, A., Pajevic, S., Chen, R., Penix, L.R., Virta, A., Basser, P., 2001. Water diffusion changes in Wallerian degeneration and their dependence on white matter architecture. Neuroimage 13, 1174-1185.
Pierpaoli, C., Jezzard, P., Basser, P.J., Barnett, A., Di Chiro, G., 1996. Diffusion tensor MR imaging of the human brain. Radiology 201, 637-648.
Pipe, J., 2014. Chapter 2 - Pulse Sequences for Diffusion-Weighted MRI. Diffusion MRI (Second Edition). Academic Press, San Diego, pp. 11-34.
Polydoro, M., Acker, C.M., Duff, K., Castillo, P.E., Davies, P., 2009. Age-dependent impairment of cognitive and synaptic function in the htau mouse model of tau pathology. The Journal of neuroscience : the official journal of the Society for Neuroscience 29, 10741-10749.
Povlishock, J.T., Katz, D.I., 2005. Update of neuropathology and neurological recovery after traumatic brain injury. J Head Trauma Rehabil 20, 76-94.
Prevention, C.f.D.C.a., 2015. Report to Congress on Traumatic Brain Injury in the

United States: Epidemiology and Rehabilitation. National Center for Injury Prevention and Control; Division of Unintentional

Injury Prevention., Atlanta, GA.
Ramalho, J., Ramalho, M., 2017. Gadolinium Deposition and Chronic Toxicity. Magnetic resonance imaging clinics of North America 25, 765-778.
Reveley, C., Seth, A.K., Pierpaoli, C., Silva, A.C., Yu, D., Saunders, R.C., Leopold, D.A., Ye, F.Q., 2015. Superficial white matter fiber systems impede detection of long-range cortical connections in diffusion MR tractography. Proceedings of the National Academy of Sciences of the United States of America 112, E2820-2828.
Rissman, R.A., Poon, W.W., Blurton-Jones, M., Oddo, S., Torp, R., Vitek, M.P., LaFerla, F.M., Rohn, T.T., Cotman, C.W., 2004. Caspase-cleavage of tau is an early event in Alzheimer disease tangle pathology. The Journal of clinical investigation 114, 121-130.
Rose, S.E., Janke, A.L., Chalk, J.B., 2008. Gray and white matter changes in Alzheimer's disease: a diffusion tensor imaging study. J Magn Reson Imaging 27, 20-26.
Rutgers, D.R., Toulgoat, F., Cazejust, J., Fillard, P., Lasjaunias, P., Ducreux, D., 2008. White matter abnormalities in mild traumatic brain injury: a diffusion tensor imaging study. AJNR Am J Neuroradiol 29, 514-519.
Ryu, J., Horkayne-Szakaly, I., Xu, L., Pletnikova, O., Leri, F., Eberhart, C., Troncoso, J.C., Koliatsos, V.E., 2014. The problem of axonal injury in the brains of veterans with histories of blast exposure. Acta Neuropathol Commun 2, 153.
Savaskan, N.E., Weinmann, O., Heimrich, B., Eyupoglu, I.Y., 2009. High resolution neurochemical gold staining method for myelin in peripheral and central nervous system at the light- and electron-microscopic level. Cell Tissue Res 337, 213-221.

Schilling, K., Janve, V., Gao, Y., Stepniewska, I., Landman, B.A., Anderson, A.W., 2016. Comparison of 3D orientation distribution functions measured with confocal microscopy and diffusion MRI. Neuroimage 129, 185-197.
Scholl, M., Lockhart, S.N., Schonhaut, D.R., O'Neil, J.P., Janabi, M., Ossenkoppele, R., Baker, S.L., Vogel, J.W., Faria, J., Schwimmer, H.D., Rabinovici, G.D., Jagust, W.J., 2016. PET Imaging of Tau Deposition in the Aging Human Brain. Neuron 89, 971-982.
Schwerin, S.C., Hutchinson, E.B., Radomski, K.L., Ngalula, K.P., Pierpaoli, C.M., Juliano, S.L., 2017. Establishing the ferret as a gyrencephalic animal model of traumatic brain injury: Optimization of controlled cortical impact procedures. Journal of neuroscience methods 285, 82-96.
Shahim, P., Linemann, T., Inekci, D., Karsdal, M.A., Blennow, K., Tegner, Y., Zetterberg, H., Henriksen, K., 2016. Serum Tau Fragments Predict Return to Play in Concussed Professional Ice Hockey Players. Journal of Neurotrauma 33, 1995-1999.
Shahim, P., Mattsson, N., Macy, E.M., Crimmins, D.L., Ladenson, J.H., Zetterberg, H., Blennow, K., Tegner, Y., 2015. Serum visinin-like protein-1 in concussed professional ice hockey players. Brain injury 29, 872-876.
Shattuck, D.W., Leahy, R.M., 2002. BrainSuite: an automated cortical surface identification tool. Medical image analysis 6, 129-142.
Shepherd, T.M., Flint, J.J., Thelwall, P.E., Stanisz, G.J., Mareci, T.H., Yachnis, A.T., Blackband, S.J., 2009. Postmortem interval alters the water relaxation and diffusion properties of rat nervous tissue--implications for MRI studies of human autopsy samples. Neuroimage 44, 820-826.
Shimony, J.S., McKinstry, R.C., Akbudak, E., Aronovitz, J.A., Snyder, A.Z., Lori, N.F., Cull, T.S., Conturo, T.E., 1999. Quantitative diffusion-tensor anisotropy brain MR imaging: normative human data and anatomic analysis. Radiology 212, 770-784.
Shitaka, Y., Tran, H.T., Bennett, R.E., Sanchez, L., Levy, M.A., Dikranian, K., Brody, D.L., 2011. Repetitive closed-skull traumatic brain injury in mice causes persistent multifocal axonal injury and microglial reactivity. Journal of neuropathology and experimental neurology 70, 551-567.
Shively, S.B., Edgerton, S.L., Iacono, D., Purohit, D.P., Qu, B.X., Haroutunian, V., Davis, K.L., Diaz-Arrastia, R., Perl, D.P., 2017. Localized cortical chronic traumatic encephalopathy pathology after single, severe axonal injury in human brain. Acta neuropathologica 133, 353-366.
Shoji, H., Takao, K., Hattori, S., Miyakawa, T., 2016. Age-related changes in behavior in C57BL/6J mice from young adulthood to middle age. Molecular brain 9, 11.
Siman, R., Shahim, P., Tegner, Y., Blennow, K., Zetterberg, H., Smith, D.H., 2015. Serum SNTF Increases in Concussed Professional Ice Hockey Players and Relates to the Severity of Postconcussion Symptoms. Journal of Neurotrauma 32, 1294-1300.
Smith, D.H., Chen, X.H., Nonaka, M., Trojanowski, J.Q., Lee, V.M., Saatman, K.E., Leoni, M.J., Xu, B.N., Wolf, J.A., Meaney, D.F., 1999. Accumulation of amyloid beta and tau and the formation of neurofilament inclusions following diffuse brain injury in the pig. Journal of neuropathology and experimental neurology 58, 982-992.
Soltys, Z., Janeczko, K., Orzylowska-Sliwinska, O., Zaremba, M., Januszewski, S., Oderfeld-Nowak, B., 2003. Morphological transformations of cells immunopositive for GFAP,

TrkA or p75 in the CA1 hippocampal area following transient global ischemia in the rat. A quantitative study. Brain research 987, 186-193.
Srinivasan, M., Sedmak, D., Jewell, S., 2002. Effect of fixatives and tissue processing on the content and integrity of nucleic acids. Am J Pathol 161, 1961-1971.
Stejskal, E.O., Tanner, J.E., 1965. Spin Diffusion Measurements: Spin Echoes in the Presence of a Time-Dependent Field Gradient. The Journal of Chemical Physics 42, 288-292.
Stern, R.A., Daneshvar, D.H., Baugh, C.M., Seichepine, D.R., Montenigro, P.H., Riley, D.O., Fritts, N.G., Stamm, J.M., Robbins, C.A., McHale, L., Simkin, I., Stein, T.D., Alvarez, V.E., Goldstein, L.E., Budson, A.E., Kowall, N.W., Nowinski, C.J., Cantu, R.C., McKee, A.C., 2013. Clinical presentation of chronic traumatic encephalopathy. Neurology 81, 1122-1129.
Strekalova, T., Spanagel, R., Bartsch, D., Henn, F.A., Gass, P., 2004. Stress-induced anhedonia in mice is associated with deficits in forced swimming and exploration. Neuropsychopharmacology : official publication of the American College of Neuropsychopharmacology 29, 2007-2017.
Strich, S.J., 1956. Diffuse degeneration of the cerebral white matter in severe dementia following head injury. J Neurol Neurosurg Psychiatry 19, 163-185.
Stulemeijer, M., van der Werf, S., Borm, G.F., Vos, P.E., 2008. Early prediction of favourable recovery 6 months after mild traumatic brain injury. Journal of neurology, neurosurgery, and psychiatry 79, 936-942.
Suri, S., Topiwala, A., Mackay, C.E., Ebmeier, K.P., Filippini, N., 2014. Using structural and diffusion magnetic resonance imaging to differentiate the dementias. Current neurology and neuroscience reports 14, 475.
Tabesh, A., Jensen, J.H., Ardekani, B.A., Helpern, J.A., 2011. Estimation of tensors and tensor-derived measures in diffusional kurtosis imaging. Magnetic resonance in medicine 65, 823-836.
Tagge, C.A., Fisher, A.M., Minaeva, O.V., Gaudreau-Balderrama, A., Moncaster, J.A., Zhang, X.L., Wojnarowicz, M.W., Casey, N., Lu, H., Kokiko-Cochran, O.N., Saman, S., Ericsson, M., Onos, K.D., Veksler, R., Senatorov, V.V., Jr., Kondo, A., Zhou, X.Z., Miry, O., Vose, L.R., Gopaul, K.R., Upreti, C., Nowinski, C.J., Cantu, R.C., Alvarez, V.E., Hildebrandt, A.M., Franz, E.S., Konrad, J., Hamilton, J.A., Hua, N., Tripodis, Y., Anderson, A.T., Howell, G.R., Kaufer, D., Hall, G.F., Lu, K.P., Ransohoff, R.M., Cleveland, R.O., Kowall, N.W., Stein, T.D., Lamb, B.T., Huber, B.R., Moss, W.C., Friedman, A., Stanton, P.K., McKee, A.C., Goldstein, L.E., 2018. Concussion, microvascular injury, and early tauopathy in young athletes after impact head injury and an impact concussion mouse model. Brain : a journal of neurology 141, 422-458.
Thelwall, P.E., Shepherd, T.M., Stanisz, G.J., Blackband, S.J., 2006. Effects of temperature and aldehyde fixation on tissue water diffusion properties, studied in an erythrocyte ghost tissue model. Magnetic resonance in medicine 56, 282-289.
Tournier, J.D., Mori, S., Leemans, A., 2011. Diffusion tensor imaging and beyond. Magnetic resonance in medicine 65, 1532-1556.
Tran, H.T., 2011. The Association Between Traumatic Brain Injury and Alzheimer's Disease: Mouse Models and Potential Mechanisms. Biology and Biomedical Sciences: Neuroscience. Washington University in St. Louis, St. Louis.

Tran, H.T., Sanchez, L., Esparza, T.J., Brody, D.L., 2011. Distinct temporal and anatomical distributions of amyloid-beta and tau abnormalities following controlled cortical impact in transgenic mice. PLoS One 6, e25475.

Turner, R.C., Lucke-Wold, B.P., Logsdon, A.F., Robson, M.J., Dashnaw, M.L., Huang, J.H., Smith, K.E., Huber, J.D., Rosen, C.L., Petraglia, A.L., 2015a. The Quest to Model Chronic Traumatic Encephalopathy: A Multiple Model and Injury Paradigm Experience. Frontiers in neurology 6, 222.

Turner, R.C., Lucke-Wold, B.P., Logsdon, A.F., Robson, M.J., Lee, J.M., Bailes, J.E., Dashnaw, M.L., Huber, J.D., Petraglia, A.L., Rosen, C.L., 2015b. Modeling Chronic Traumatic Encephalopathy: The Way Forward for Future Discovery. Frontiers in neurology 6, 223.

Van Essen, D.C., 2005. A Population-Average, Landmark- and Surface-based (PALS) atlas of human cerebral cortex. Neuroimage 28, 635-662.

Veraart, J., Fieremans, E., Jelescu, I.O., Knoll, F., Novikov, D.S., 2016. Gibbs ringing in diffusion MRI. Magnetic resonance in medicine 76, 301-314.

Verwer, R.W., Hermens, W.T., Dijkhuizen, P., ter Brake, O., Baker, R.E., Salehi, A., Sluiter, A.A., Kok, M.J., Muller, L.J., Verhaagen, J., Swaab, D.F., 2002. Cells in human postmortem brain tissue slices remain alive for several weeks in culture. FASEB J 16, 54-60.

Wang, Y., Sun, P., Wang, Q., Trinkaus, K., Schmidt, R.E., Naismith, R.T., Cross, A.H., Song, S.K., 2015. Differentiation and quantification of inflammation, demyelination and axon injury or loss in multiple sclerosis. Brain : a journal of neurology 138, 1223-1238.

Weiss, M., Alkemade, A., Keuken, M.C., Muller-Axt, C., Geyer, S., Turner, R., Forstmann, B.U., 2015. Spatial normalization of ultrahigh resolution 7 T magnetic resonance imaging data of the postmortem human subthalamic nucleus: a multistage approach. Brain Struct Funct 220, 1695-1703.

Weston, P.S., Simpson, I.J., Ryan, N.S., Ourselin, S., Fox, N.C., 2015. Diffusion imaging changes in grey matter in Alzheimer's disease: a potential marker of early neurodegeneration. Alzheimer's research & therapy 7, 47.

White, E., Woolley, M., Bienemann, A., Johnson, D.E., Wyatt, M., Murray, G., Taylor, H., Gill, S.S., 2011. A robust MRI-compatible system to facilitate highly accurate stereotactic administration of therapeutic agents to targets within the brain of a large animal model. Journal of neuroscience methods 195, 78-87.

Wiegell, M.R., Larsson, H.B., Wedeen, V.J., 2000. Fiber crossing in human brain depicted with diffusion tensor MR imaging. Radiology 217, 897-903.

Wu, W., Poser, B.A., Douaud, G., Frost, R., In, M.H., Speck, O., Koopmans, P.J., Miller, K.L., 2016. High-resolution diffusion MRI at 7T using a three-dimensional multi-slab acquisition. Neuroimage 143, 1-14.

Yang, Z., Wang, P., Morgan, D., Lin, D., Pan, J., Lin, F., Strang, K.H., Selig, T.M., Perez, P.D., Febo, M., Chang, B., Rubenstein, R., Wang, K.K., 2015. Temporal MRI characterization, neurobiochemical and neurobehavioral changes in a mouse repetitive concussive head injury model. Scientific reports 5, 11178.

Yeh, F.C., Wedeen, V.J., Tseng, W.Y., 2010. Generalized q-sampling imaging. IEEE Trans Med Imaging 29, 1626-1635.

Yoshiyama, Y., Uryu, K., Higuchi, M., Longhi, L., Hoover, R., Fujimoto, S., McIntosh, T., Lee, V.M., Trojanowski, J.Q., 2005. Enhanced neurofibrillary tangle formation, cerebral

atrophy, and cognitive deficits induced by repetitive mild brain injury in a transgenic tauopathy mouse model. Journal of Neurotrauma 22, 1134-1141.
Yu, F., Shukla, D.K., Armstrong, R.C., Marion, C.M., Radomski, K.L., Selwyn, R.G., Dardzinski, B.J., 2017. Repetitive Model of Mild Traumatic Brain Injury Produces Cortical Abnormalities Detectable by Magnetic Resonance Diffusion Imaging, Histopathology, and Behavior. Journal of Neurotrauma 34, 1364-1381.
Zacharopoulos, N.G., Narayana, P.A., 1998. Selective measurement of white matter and gray matter diffusion trace values in normal human brain. Medical physics 25, 2237-2241.
Zagorchev, L., Goshtasby, A., 2006. A comparative study of transformation functions for nonrigid image registration. IEEE transactions on image processing : a publication of the IEEE Signal Processing Society 15, 529-538.
Zarow, C., Kim, T.S., Singh, M., Chui, H.C., 2004. A standardized method for brain-cutting suitable for both stereology and MRI-brain co-registration. J Neurosci Methods 139, 209-215.
Zemlan, F.P., Rosenberg, W.S., Luebbe, P.A., Campbell, T.A., Dean, G.E., Weiner, N.E., Cohen, J.A., Rudick, R.A., Woo, D., 1999. Quantification of axonal damage in traumatic brain injury: affinity purification and characterization of cerebrospinal fluid tau proteins. Journal of neurochemistry 72, 741-750.
Zemmoura, I., Serres, B., Andersson, F., Barantin, L., Tauber, C., Filipiak, I., Cottier, J.P., Venturini, G., Destrieux, C., 2014. FIBRASCAN: a novel method for 3D white matter tract reconstruction in MR space from cadaveric dissection. Neuroimage 103, 106-118.
Zetterberg, H., Hietala, M.A., Jonsson, M., Andreasen, N., Styrud, E., Karlsson, I., Edman, A., Popa, C., Rasulzada, A., Wahlund, L.O., Mehta, P.D., Rosengren, L., Blennow, K., Wallin, A., 2006. Neurochemical aftermath of amateur boxing. Archives of neurology 63, 1277-1280.
Zhang, J., Yoganandan, N., Pintar, F.A., Gennarelli, T.A., 2006. Role of translational and rotational accelerations on brain strain in lateral head impact. Biomedical sciences instrumentation 42, 501-506.
Zhang, K., Sejnowski, T.J., 2000. A universal scaling law between gray matter and white matter of cerebral cortex. Proceedings of the National Academy of Sciences of the United States of America 97, 5621-5626.
Zhuo, J., Keledjian, K., Xu, S., Pampori, A., Gerzanich, V., Simard, J.M., Gullapalli, R.P., 2015. Changes in Diffusion Kurtosis Imaging and Magnetic Resonance Spectroscopy in a Direct Cranial Blast Traumatic Brain Injury (dc-bTBI) Model. PLoS One 10, e0136151.
Zhuo, J., Xu, S., Proctor, J.L., Mullins, R.J., Simon, J.Z., Fiskum, G., Gullapalli, R.P., 2012. Diffusion kurtosis as an in vivo imaging marker for reactive astrogliosis in traumatic brain injury. Neuroimage 59, 467-477.